UNIVERSITÀ
DEGLI STUDI
FIRENZE

DIEF - Dipartimento di Ingegneria Industriale

PhD School: *Energetica e Tecnologie Industriali e Ambientali Innovative*

Scientific Area: ING-IND/09

EXPERIMENTAL INVESTIGATION ON A HIGH PRESSURE NGV CASCADE IN THE PRESENCE OF A REPRESENTATIVE LEAN BURN AERO-ENGINE COMBUSTOR OUTFLOW

PhD Candidate: Ing. Tommaso Bacci

Tutor: Prof. Ing. Bruno Facchini

Co-Tutor: Ing. Alessio Picchi

PhD School Coordinator: Prof. Ing. Maurizio De Lucia

PhD School Cycle: XXX (2014-2017)

To my family...

Aknowledgment

Coming towards the end of such a challenging and satisfying journey, I feel that there are quite a lot of people that really helped me to get here. First of all, I want to thank Prof. Bruno Facchini, for the the opportunity to join his research group: looking back at the very beginning of this path, I realize how it made me grow, both from a professional and from a human point of view. Thank you also for the trust that you constantly showed to me and for your precious advices.

I also want to thank all the people that, with different roles, work in the HTC family. Even if we didn't constantly live side by side, a special thank goes to all the guys working at Santa Marta. I'll name some of you with the goal of really thank everyone, since you made me feel part of a great team: Antonio, for the help that he provided any time I asked for, Stefano and Sabrina, my Ph.D. course mates, with whom I share the struggles of this final deadline. A special acknowledgement goes to Lorenzo (Mazze), for all the time that he spent running CFD for the sake of this work: thanks for making everything easier to me, both with your expertise and your attitude. Speaking about the people that helped me carrying out this work, how not to mention Charlie, my main reference point in the FACTOR project, and Martin. Coming to the THT Lab mates, I'll begin by thanking Gianlu, that started this work: thank you for having put the basis for all of this and for having taken me under your wings. I also feel grateful to all the ones that joined the THT group during these years. Daniele, Tommaso F., Tommaso L. and Valter: I really couldn't have asked for better people to work and spend time together. Finally, I want to spend a few words for the two people that I

had beside me since the very beginning of this path and up to now. Ricca, one year ahead of me in your course, I feel lucky to have had you as a reference for all the challenges that I found; thank you also for all the time that we spent joking of everything and everyone we could. Ale, I don't even know how to call you: I could say lab-mate, mentor or even just friend.... I'll use Technical Supervisor because I know it's the term you like the most! Thank you for always having helped me in all the challenges that we had to face; it's hard to explain how your advices and our discussions and overthinking made me grow in these years.

My thoughts also go to the people that, outside of the academic world, have influenced my life. First of all, I want to thank my lifelong friends. Cecco, Fede, Bibo, Pepo, Scihari, Papo, Edo, Nicco and all the others... Together we grew up, played, studied, did wonderful and stupid things (more stupid ones probably...), shared the struggles of our first professional experiences. Wherever our lives will bring us, I know I'll never be alone.

I left the last part of these few lines for the most important acknowledgement, the one that goes to my family. I really couldn't have arrived here without your help, support and teachings. Thank you for having allowed me to go after my dreams and for enjoying them with me. Thanks for having taught me to try to put my best in everything I do.

This Ph.D thesis was carried out within the research projects FACTOR (Full Aerothermal Combustor-Turbine interactiOns Research) and INSIDE (Aerothermal Investigation of cooled Stage turbine: Design optimization and Experimental analysis). FACTOR is a Collaborative Project co-funded by the European Commission within the Seventh Framework Programme (2010-2016) under the Grant Agreement n° 265985. INSIDE is a Research National Program (PRIN 2010-11) financed by MIUR (Italian Office for University and Research). I gratefully acknowledge both consortia for the permission to publish and especially for the opportunity to take part in such a challenging work.

≪With respect, Professor, we've tried that hundreds of times...≫

≪It only has to work once, Murph.≫

Interstellar

Contents

List of Figures

List of Tables

Abstract

The current growth in the global civil air traffic has led to new and more severe limitations on aero-engines pollutant emissions, especially regarding NO_x. To overcome these limits, the control of the combustion temperature through the introduction of lean combustion has been widely recognized as the most promising solution. In addition to enforcing challenges related to flame stabilization and fuel/air mixing, the introduction of lean combustion led to a completely different flow field evolution inside the combustion chamber. Up to 70% of the total air flow is generally headed to the injection system, for fuel/air mixture preparation; consequently, new and more efficient liners cooling concepts, such as effusion cooling, must be adopted and dilution holes, that are typical of traditional RQL combustors, are not present. Therefore the highly swirling structures created by the injectors, in order to improve fuel/air mixing and combustion process stability in the primary zone, as well as the hot spots, due to discrete fuel injection, hardly interact with cooling flows and live up to the chamber exit. As a result, the typical outflow of these modern combustors is characterized by enhanced temperature distortions, called hot streaks, an aggressive degree of swirl and, consequently, a highly unsteady behaviour. Despite the effect of pressure and temperature non-uniformity on the high pressure turbine behaviour has been widely documented in the last fourty years, very little literature and industrial experience exist when it comes to evaluate the effect of these enhanced distortions and swirling flows. Moreover, these kind of highly unsteady flow fields significantly challenge the reliability of numerical codes and modelling strategies, mainly based on Reynolds-Averaged Navier-Stokes (RANS) models, that are generally adopted for the prediction of the turbine module per-

formance. Therefore, new experimental studies have been promoted, in order to deepen the knowledge of the combustor-turbine interaction behaviour, validate CFD codes dedicated to its design and promote an integrated design philosophy for turbine and combustor modules.

From an experimental point of view, a few studies have been carried out in recent years to evaluate the effects of either swirling flows or enhanced temperature distortions separately on the turbine performance. No relevant literature is nowadays available regarding the study of both phenomena together, since severe challenges arise in the design of non-reactive lean combustor simulators aimed at reproducing both aspects. In non reactive, highly swirling flows, in fact, different phenomena that are damped in reactive conditions by the heat release effect, can significantly affect the overall flow field, making the achieved results far from the target.

Within this research framework, a three-sector rig made by a combustor simulator and a nozzle guide vane cascade, was installed at THT Lab (*Laboratory of Technologies for High Temperature*) of University of Florence. In the combustor simulator, representative temperature distortions and swirl field are generated through the mixing of a heated swirling mainflow, passing through three axial swirlers, and liner cooling flows at ambient temperature. The nozzle guide vane geometry and film-cooling system were designed in order to adapt to the expected inlet flow field, according to preliminary measurements at the combustor exit; tangentially averaged radial profiles were used as inlet conditions, as it is common for this kind of procedures. In the present study the the combustor simulator flow field has been characterized, without the NGV cascade, thanks to PIV measurements carried out inside the chamber. Afterwards the test rig has been upgraded by adding the film-cooled NGV module at its exit. A thorough experimental campaign has been then carried out with the goal of evaluating both the effect of the distorted combustor outflow on the NGV module and the flow field and temperature pattern migration through the cascade. In particular, five hole probe and temperature measurements have been carried out upstream and downstream of the NGV in order to characterize the hot streaks migration and the aerodynamic behaviour of the cascade; hot wire measurements have

also been carried out in the same positions to evaluate the turbulence intensity pattern at combustor exit and its modification through the cascade. Furthermore adiabatic effectiveness measurements have been performed on the cooled airfoils, in order to assess the impact of the highly swirling combustor outflow on the film cooling capabilities.

The characterization of the combustor simulator, through both PIV measurements inside the chamber and aerothermal and turbulence measurements at combustor exit, demonstrated that the test rig was a useful test case for the study of combustor-turbine interaction problems for modern aero-engines. An aggressive swirl field was, in fact, detected at the combustor simulator exit, together with significant turbulence intensities in its core. Marked temperature distortions were found as well. The second part of the campaign has highlighted several phenomena induced in the NGV behaviour by the combustor outflow. The focus was placed first on the evaluation of the aerodynamic field and of the turbulence pattern in isothermal conditions. This information was also used as boundary conditions for the investigation of the film-cooling performance, through the adiabatic effectiveness measurements. Finally the hot streaks migration within the highly swirling flow was evaluated through measurements in design point conditions, heating up the swirling flow. This investigation constitutes one of the first of its kind and complements the large amount of data regarding hot streaks migration within uniform flow fields. The residual swirl convected in the cascade was found to be the driving force that influenced all the investigated aspects: significantly different outcomes, with respect with the ones that are normally expected for uniform inflows were evidenced. This research provides a deep overview of the effects induced by a representative lean-burn combustor outflow on a high-pressure nozzle guide vane. Results have been used to highlight where and how such a complex flow field can challenge the reliability of a traditional design procedure; they also constitute a large experimental dataset that can be exploited to tune CFD codes and, in turn, validate modelling strategies and influence design practices.

The activities of this Ph.D. course has been carried out within the European FACTOR (*Full Aerothemal Combustor-Turbine interactiOn Research*)

collaborative project (Grant Agreement FP7-265985) and the National Interest Project, promoted by the Italian Ministry of Education, Universities and Research ($MIUR$), called INSIDE (*aerothermal INvestigation of cooled Stage turbIne: Design optimization and Experimental analysis*).

Nomenclature

Symbols

A	Area	$[m^2]$
BR	Blowing ratio	$[-]$
C	Mass fraction	$[-]$
C_{ax}	Axial chord	$[m]$
C_p	Pressure loss coefficient	$[-]$
C_w	Mass fraction close to wall	$[-]$
d	Diameter	$[m]$
DR	Density ratio	$[-]$
E	Voltage	$[V]$
FAR	Fuel air ratio	$[-]$
f	Frequency	$[Hz]$
G	Mass flux per unit of area	$[kg/(m^2 s)]$
h	Local height	$[m]$
h_{conv}	Adiabatic heat transfer coefficient	$[W/(m^2 K)]$
I	Momentum ratio	$[-]$
k	Thermal conductivity	$[W/(mK)]$
K	Turbulent kinetic energy	$[m^2/s^2]$
Kn	Knudsen number	$[-]$
l,L	Length	$[m]$
Le	Lewis number	$[-]$
M	Mach number	$[-]$
NGV_{0-4}	Test rig NGV	$[-]$
Nu	Nusselt number	$[-]$
P	Pressure	$[Pa]$
p	Tangential NGV pitch	$[^\circ]$

Pr	Prandtl number	$[-]$
PS_{1-5}	Pressure side film-cooling rows	$[-]$
q	Dynamic pressure	$[Pa]$
R	Radial coordinate	$[m]$
Re	Reynolds number	$[-]$
R_w	wire resistance	$[Ohm]$
S	Linear NGV pitch	$[-]$
Sc	Schmidt number	$[m]$
S_N	Swirl number	$[-]$
SS_{1-3}	Suction side film-cooling rows	$[-]$
St	Stokes number	$[-]$
S_x	Streamwise hole pitch	$[m]$
S_y	Spanwise hole pitch	$[m]$
t	Tangential coordinate	$[^\circ]$
T	Temperature	$[K]$
Tu	Turbulence intensity	$[-]$
u,U,V	Velocity	$[m/s]$
u'	Fluctuating Velocity	$[m/s]$
u_{ax}	Axial Velocity	$[m/s]$
u_x	x-Velocity	$[m/s]$
u_y	y-Velocity	$[m/s]$
VR	Velocity Ratio	$[-]$
V_{tg}	Boroscope Tangential Velocity	$[m/s]$
W	Coolant-mainstream mass flow ratio	$[\%]$
x,y,z	Cartesian coordinates	$[m]$
y_a, y_b	Pressure loss coefficients	$[-]$

Greeks

α	Hole inclination angle	$[^{\circ}]$
ϵ_T	Turbulent diffusivity	$[-]$
ϵ_C	Turbulent mass diffusivity	$[-]$
η_{ad}	Adiabatic effectiveness	$[-]$
η_p	Peak effectiveness level	$[-]$
η_r	Recovery factor	$[-]$
μ	Dynamic viscosity	$[Pa \cdot s]$
ρ	Density	$[kg/m^3]$
τ	Time	$[s]$
ϕ	Equivalence ratio	$[-]$

Subscripts-Superscripts

$\bar{\cdot}$	Time-averaged quantity
0	Total
40	Plane 40
41	Plane 41
ad	Adiabatic
air	Air
ax	Axial
$cool$	Coolant
d	Down
$dark$	Dark image
f	Fluid
fg	Foreign gas
$kolm$	Kolmogorov
l	Left
M	Mainstream
$mean$	Mass/Area-averaged quantity
nd	Non-dimensional
O_2	Oxygen
p	Particle

r	Right
rad	Radial
ref	Reference
rms	Root-Mean-Square
sf	Secondary Flows
$swirler$	Swirler
t	Total
T	Turbulent
tan	Tangential
u	Up
w	Wire
x	x-direction
y	y-direction

Acronyms

CCD	Couple Charged Device
CFD	Computational Fluid Dynamics
CTA	Constant Temperature Anemometry
$DMLS$	Direct Metal Laser Sintering
DP	Design Point
HWA	hot Wire Anemometry
IOP	Isothermal Operating Point
IOP_2	Isothermal Operating Point 2
LDI	Lean Direct Ignition
LES	Large Eddy Simulation
$LOTDF$	Local Overall Temperature Distortion Factor
LPP	Lean Premixed Prevaporised
$LRTDF$	Local Radial Temperature Distortion Factor
LTO	Landing Take-Off
NGV	Nozzle Guide Vane

OPR	Overall Pressure Ratio	[–]
$OTDF$	Overall Temperature Distortion Factor	
$PERM$	Partially Evaporated and Rapid Mixing	
PID	Proportional Integral Derivative	
PIV	Particle Image Velocimetry	
PS	Pressure Side	
PSP	Pressure Sensitive Paint	
PVC	Precessing Vortex Core	
$RANS$	Reynolds Averaged Navier-Stokes Equations	
RCZ	Recirculation Zone	
RQL	Rich Quench Lean	
$RTDF$	Radial Temperature Distortion Factor	
SAS	Scale Adaptive Simulation	
SFC	Specific Fuel Consumption	
SS	Suction Side	
TE	Trailing Edge	
TIT	Turbine Inlet Temperature	
TKE	Turbulent Kinetic Energy	
TLC	Thermocromic Liquid Crystals	
TRL	Technology Readiness Level	
TSP	Temperature Sensitive Paint	
UHC	Unburned Hydro-Carbons	
ULN	Ultra Low NO_x	
UV	Ultra-Violet	

Chapter 1

Technical Background

Contents

1.1 Development of Modern Aero-engine

One of the greatest impacts of gas turbines development is related to aircraft propulsion. Turbine jet propulsion was introduced during the 1930s, thanks to two separated studies carried out by Hans von Ohain, who was granted a patent for his turbojet engine in 1936, and English Royal Air Force engineer Frank Whittle, who was the first to register a patent for a turbojet engine in 1930 (Fig. 1.1). Hans von Ohain's turbojet engine was the first to fly in 1939, followed by Frank Whittle's one in 1941.

Since then, gas turbine engines have rapidly became the standard for aircraft propulsion, allowing higher flight speeds and increased efficiency and power/weight ratios. Even if the operating principles have been kept substantially unchanged from the prototype of Whittle and von Ohain, gas turbine aero-engine have experienced a rapid growth in the last decades, mainly

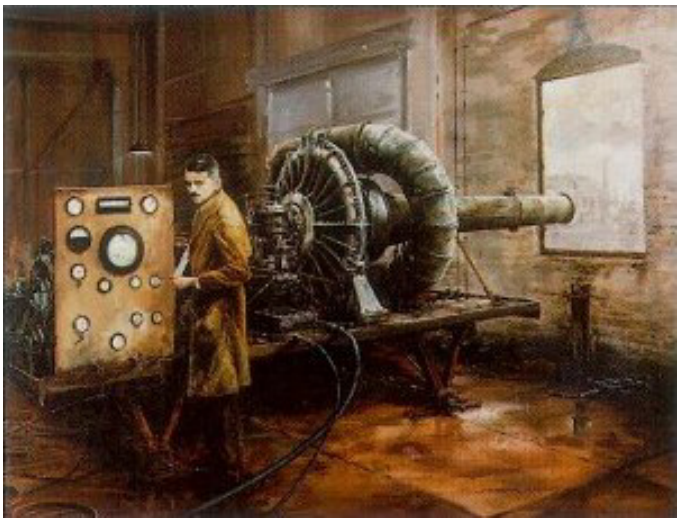

Figure 1.1: Whittle's first experimental jet engine (painting by Rod Lovesey - Midland Air Museum)

aimed at increasing reliability and performance, in the form of specific fuel consumption (SFC) and thrust/weight ratios: almost seven times superior thrust/weight ratios have been achieved [1] (Fig. 1.2)

The standard for modern civil aero-engines has been set to turbofan en-

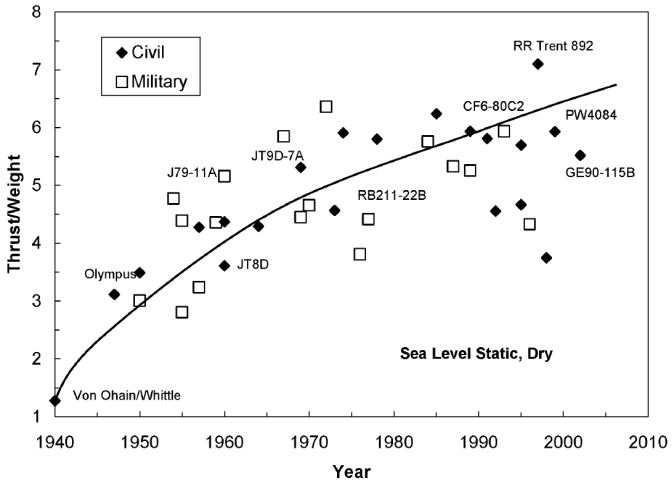

Figure 1.2: Thrust/Weight ratio advancements for aero-engines [1]

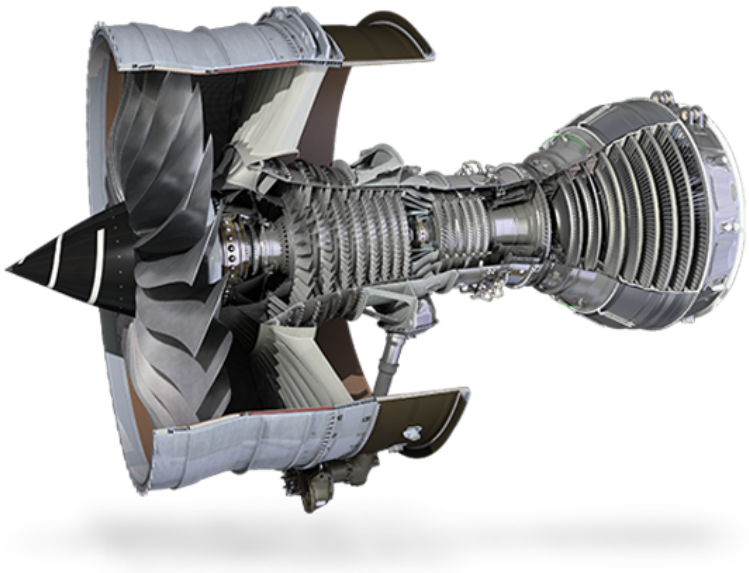

Figure 1.3: Sketch of Rolls Royce Trent XWB (*www.rolls-royce.com*)

gines, which make use of a large fan at the intake to obtain a high by-pass ratio and a reduced SFC. In order to increase efficiency and specific power of this configuration, the advances in blade cooling technologies and high-temperature materials have allowed to increase the turbine inlet temperature (TIT) beyond $2000K$; at the same time, overall pressure ratios (OPR) have been increased, thanks to the improved performance of modern fan and compressors. Moreover multi-shaft configurations have been adopted to take advantage of various rotational speeds of the shaft for different parts of the engine. Figure 1.3 depicts a sketch of the *Rolls Royce Trent XWB* , a large turbofan engine, powering aircraft Airbus A350, featuring a three-shaft configuration and OPR and bypass ratio of 50 and 9.6 respectively.

Despite aero-engines have nowadays reached a highly advanced level, a lot of research fields still exist. In the next twenty years the global air traffic is forecast to grow at an expected annual rate of about 4.1% [2]. This forecast makes the environmental impact of civil aviation one of the most relevant challenge related to its further development, with the aim of matching the goals set by ACARE (Advisory Council for Aeronautical Research in Europe

[3]) by 2020. In details, the following targets have been set:

- reduction of fuel consumption and CO_2 emissions by 50% per pkm
- reduction of fuel consumption and NO_x emissions by 80%
- reduction of perceived noise by 80%
- reduction of the environmental impact of the manufacture, maintenance and disposal of aircraft and related products

In order to strict these requirements, aero-engine manufacturers have been forced to either try to increase the engine SFC or explore improved technologies to damp pollutant emissions.

In recent years the European Community has prmoted several research projects, such as NEWAC [1] and LEMCOTEC [2], aimed at developing and validating novel core engine configurations. Most of these configurations make use of intercooled compression and regeneration, in order to significantly increase the thermodynamic cycle efficiency, as sketched in Fig. 1.4. Among the first ones, the *Variable Flow-Path Intercooler* [4], which uses a set of valves that allows to either use the intercooler or bypass it to adapt to the operating condition, and the *Reverse-flow Core Intercooler Turbofan* [5] have been investigated.

Another configuration worth of note is the *Composite Cycle Engine* [7], aimed at combining the benefits of piston engine and turbofan architecture, by replacing the high pressure section with a piston system. The turbo components deliver thrust and pressurize the piston system, so to use the superior power-to-weight ratio and reliability of turbo engines; at the same time, during the combustion in the piston engine, pressure rises and very high temperature peaks are reached due to short exposure times [8]. A schematics is shown in Fig. 1.5.

Nevertheless, all the mentioned solutions, having to cope with drawbacks and limitations, such as the increase in size and weight and reliability issues, are not fully mature and necessitate further research and development; none

[1] NEW Aero-Engine Core concepts

[2] Low EMissions COre-engine TEChnologies

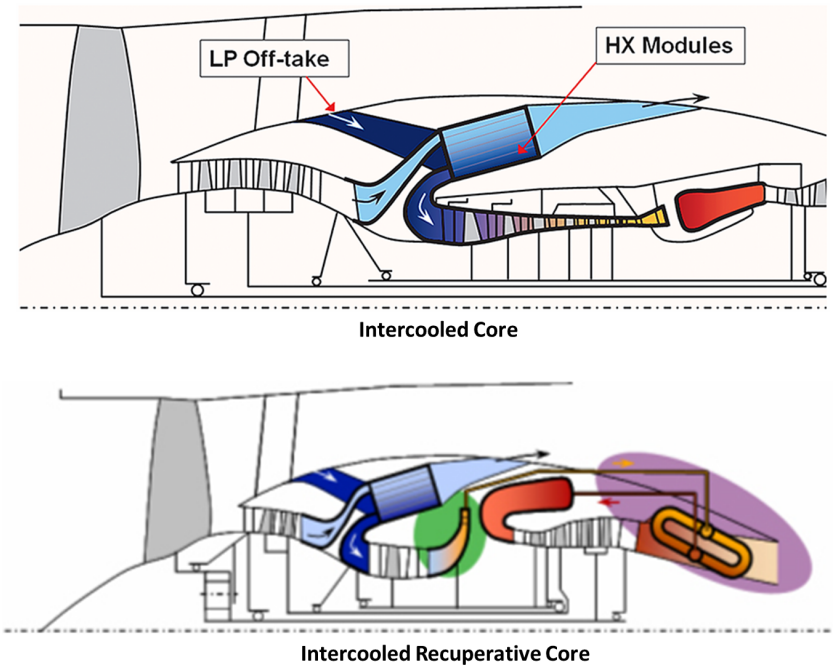

Figure 1.4: Schematics of intercooled and recuperative core-engine concepts [6]

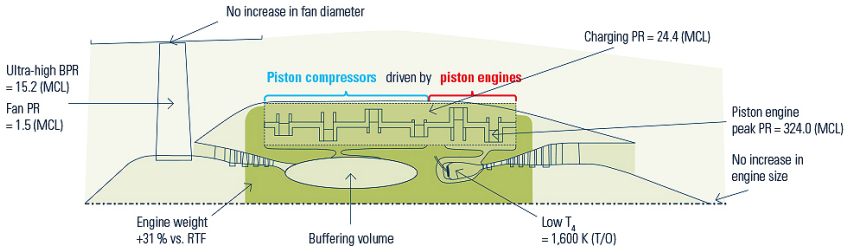

Figure 1.5: Schematics of composite cycle engine concept (*www.bauhaus-luftfahrt.net*)

of them is foreseen to entry into service before 2030-2035. Therefore, in order to increase the engine thermal efficiency in the short terms, the same research goals that have allowed the aero-engine development in the last decades are still pursued, even if nowadays they allow reduced improvements. The increase in OPR, up to 70 for large turbofan, and the development and

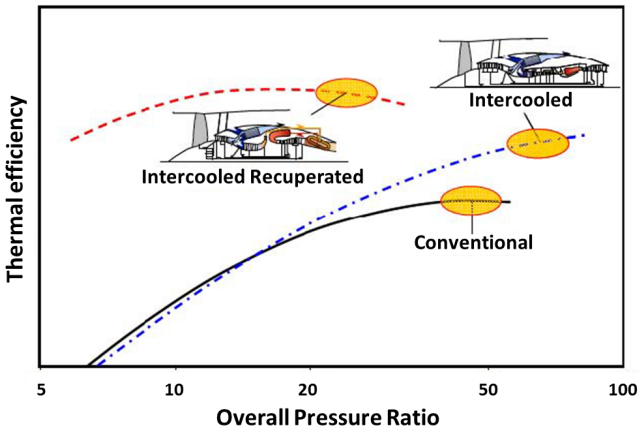

Figure 1.6: Effect of OPR on thermal efficiency for conventional and innovative core-engine [6]

optimization of cooling systems, in order to either increase the TIT or reduce the coolant mass flow rate, are still among the main development trends. In a second phase, around 2030 and later, when novel technologies like intercooling will be ready, it could be possible to integrate them in high OPR thermodynamic cycles, in order to achieve a significant improvement in fuel consumption, as reported in Fig. 1.6.

On the other hand, new combustion technologies for pollutant emissions reduction have been widely explored in recent years; in the next sections a brief account of both the most important aero-engine sources of emission and of their combustion systems characteristics can be found.

1.2 Pollutant emissions for aero-engines

In general, the exhaust gases of a turbine aero-engine are composed of particulate material and different gaseous species, depending on the fuel composition and on the portion of air that doesn't take part in the combustion process. In order to quantify the weight of the different species to the global emissions, the following composition can be considered as a typical one, in abstract terms and without referring to specific engines or technologies:

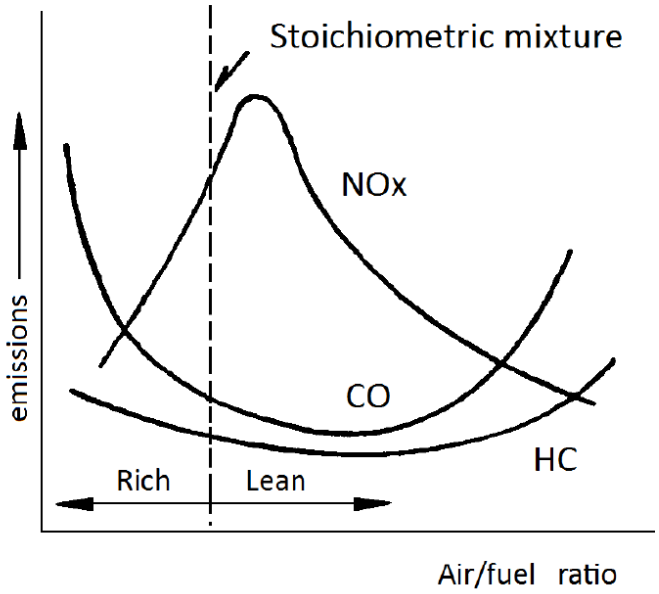

Figure 1.7: Dependence of NO_x, UHC and CO emissions with the air/fuel ratio

- CO: below 50 ppm
- UHC: below 10 ppm
- NO_x: 200-300 ppm (for combustors without NO_x reduction technologies)

NO_x emission is considered the main threat to civil air traffic growth; ICAO-CAEP standards impose a nitric oxides emissions reduction of 80% by 2020. Apart from the fuel composition, CO and NO_x emissions mainly depend on the fuel/air ratio and on the combustion temperature. As sketched in Fig. 1.7, they have an opposite trend: CO emissions, as well as UHC ones, reach their maximum for either very lean or very rich mixtures, due to incomplete combustion; on the other hand NO_x emissions have their maximum impact for air/fuel ratios slightly higher than the stoichiometric value, due to their generation mechanism.

In general different "typologies" of NO_x can be produced depending on their generation mechanism; they are commonly divided in the following

cathegories:

- *Prompt* NO_x: generated in the very first part of the combustion process by the reaction of atmospheric nitrogen, N_2, with radicals such as C, CH, and CH_2 fragments derived from fuel

- NO_2 *pathway*: starting from nitrous oxide (N_2O), or *Fuel* NO_x, due to the fuel nitrogen content [9]

- *Zeldovich Thermal* NO_x *mechanism*: an endothermic process that brings to the formation of NO_x in quantities that exponentially depend on the combustion temperature

The predominant generation mechanism, as demonstrated by Zeldovich et al. [10], is the last one; as a consequence, the maximum of NO_x emissions is achieved for slightly leaner than stoichiometric fuel/air mixtures, where combustion temperatures are high and residual oxygen is available for nitrogen oxidation. Due to the opposite behaviour of NO_x and CO emissions, in terms of combustion temperature that maximizes their production (Fig. 1.7), the design of NO_x abatement technologies has to take care not to increase CO emissions. The most followed way to pursue this necessity is to realize combustion systems able to operate at a trade-off temperature, where both species emissions are limited, as sketched in Fig. 1.8.

In the next section the most used technologies adopted to contain NO_x emissions will be discussed. It must be also reminded that the evolution trends described in the previous section, in order to increase the cycle thermal efficiency and indirectly reduce pollutant emissions, are somehow in contrast with the necessity to keep the combustion process within certain temperature limits: both an increase in OPR, due to the enhanced compressor delivery temperature, and in TIT would led to higher combustion temperatures, and so to an increase in thermal NO_x, without proper adjustments. These aspects place significant challenges in the pollutant emission abatement criteria and led to the necessity of developing innovative concepts to strict the goal.

1.3 Combustors for aero-engines

Combustion chambers are located in the very core of the Brayton-Joule thermodynamic cycle and are subjected to the harshest conditions both in terms of pressure and temperatures. Therefore, their design is a crucial part of the engine design process and a lot of engineering field, such as chemistry, fluid dynamics, heat transfer and structural mechanics, are involved. Furthermore, when considering the global engine performance, additional requirements such as minimizing weight, front area and pressure losses, as well as the amount of cooling air, must be considered.

Despite that, the development of aero-engine combustors, has reached very high standards, with combustion efficiencies close to 100% and life expectancy up to many tens of thousands of hours [11]. By around 1950, the most important features of conventional aero-engine combustors, as they are known today, were already established. Due to the similar pressing needs that characterize their design, most of the combustors that are currently in

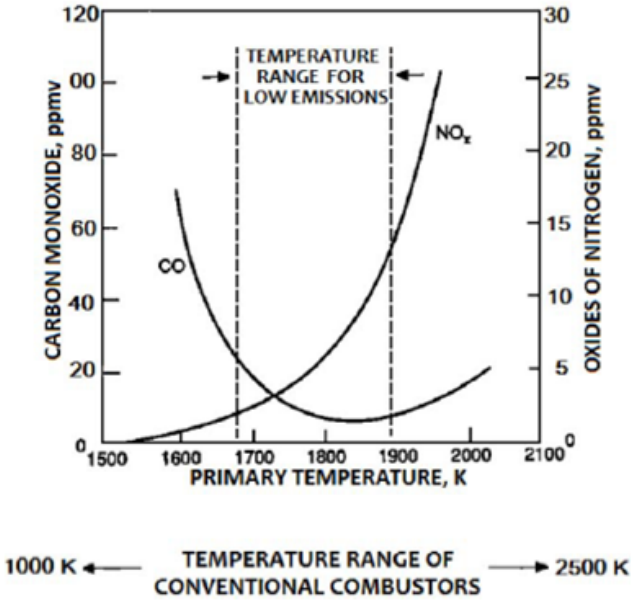

Figure 1.8: Temperature range to reduce both NO_x and CO emissions [11]

service tend to resemble each other in several characteristics. In particular, the standard has rapidly set to annular combustors, since they allow to minimize pressure losses, front area and weight, with respect to can and can-annular combustors. As sketched in Fig. 1.9, the main components that characterize this common architecture can be summarized in: the *diffuser*,

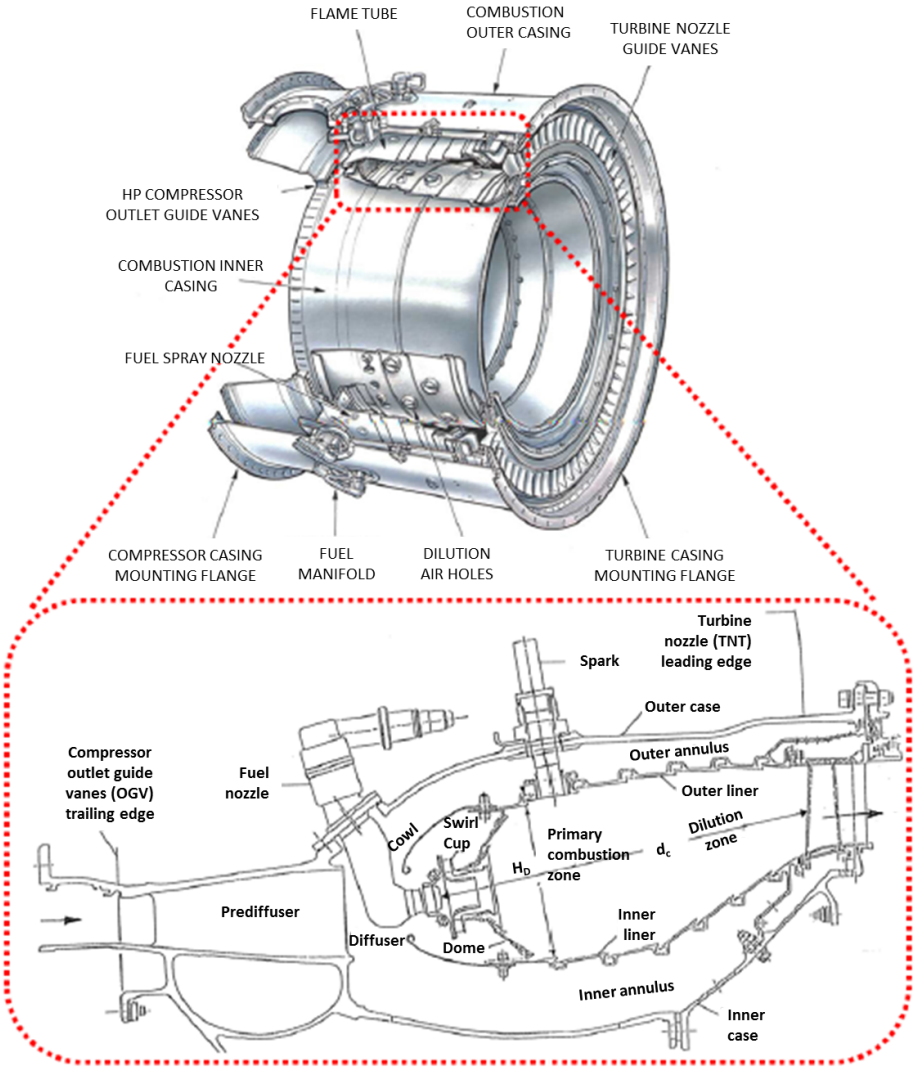

Figure 1.9: Example of an annular combustor chamber [12] and detailed view on a general layout [13]

with the goal of decreasing the inlet air flow velocity in order to minimize the pressure losses; the *cowl*, a shaped structure that split the inlet flow into the main flow and the cooling flow; the *dome*, which is the front end of the combustor and acts as a shield, protecting the injectors from the burning gases; the *inner/outer liners*, made of a thin metal sheet and cooled through different techniques, they delimit the flame tube and protect the surroundings from the burning gases; the *casing*, which bonds the inner and outer annuli (i.e. the passages for the liner cooling air) and is the structural shell of the combustor. Other components, arguably the most important ones, that characterize the combustion chamber architecture are the fuel injectors, that have the goals of delivering the fuel and promoting the dominant flow field structures, useful for air/fuel mixing and flame stabilization. Since they can strongly differ from combustor to combustor, some details of their behaviour will be deepened in the next sections.

Despite the overall standardisation of these components, the need for always new requirements have pushed the manufacturer to recurrently adapt combustors characteristics and design procedures. Regarding the need for NO_x emissions reduction, that has been the main guideline in the last 30 years, two main possibilities have been explored. Referring to Fig. 1.8, in order to avoid the condition of peak temperature (i.e. maximum NO_x formation) designers can either choose to move towards high equivalence ratios, as in the RQL (Rich-Quench-Lean) concept, which has been the standard for a long time, or to opt for values of ϕ significantly below the unity (lean combustion), as it has been explored in recent years. A brief account of both configurations will be given in the following.

1.3.1 RQL combustors

The state of the art for $Low - NO_x$ aero-engine combustors has been constituted for a long time by the so called RQL (*Rich-Quench-Lean*) combustors; a sketch of a RQL combustor is reported in Fig. 1.10. They make use of a rich primary zone (equivalence ratio $\phi = 1.2 - 1.6$ at high load) where fuel is directly injected and it mixes via turbulent and molecular diffusion with part of the air flow from the compressor. The NO_x formation is con-

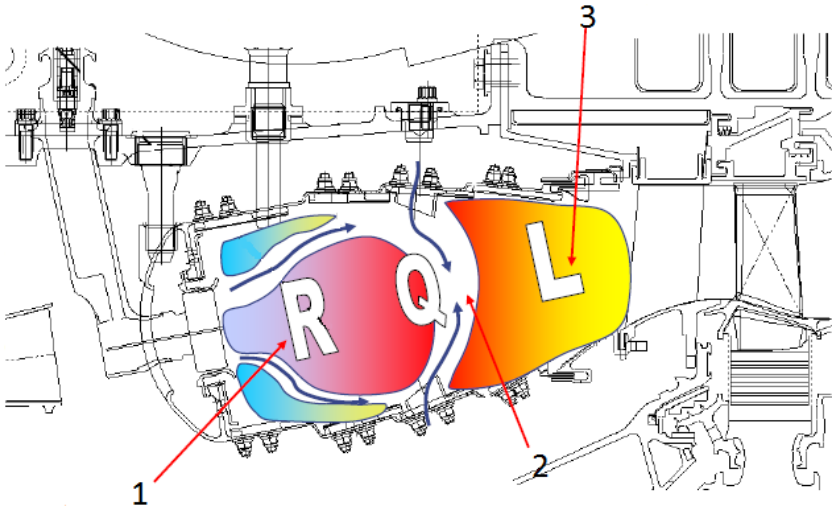

Figure 1.10: Sketch of a Rolls Royce Trent XWB combustor

trolled thanks to both the limited flame temperature and to the low oxygen concentration, without compromising the flame stability in a wide operation range. This primary zone has also the goal of generating a recirculating flow that anchors the flame and provides sufficient resident time for fuel-air mixture to carry on the combustion process. After the primary zone the burning gases, rich in partially oxidized hydrocarbon species, hydrogen, and carbon monoxide, encounter a dilution zone, where a big quantity of air is injected through wall jets ("dilution holes") in order to achieve a quick shift in the air/fuel composition and to let the combustion process to be completed in lean conditions ($\phi = 0.5 - 0.7$).

The critical passage in the process stays in the switch between rich and lean conditions, since, due to the not ideal mixing between the burning gases from the primary zone and the dilution air, some local zone with close to stoichiometric conditions are generally created. As a result an enhancement of the thermal NOx production rate occurs. Another drawback of this solution stays in the fact that the secondary air used for liners cooling must be reduced as more as possible, in order to prevent the formation of stoichiometric spots in the rich primary zone. Fig. 1.11 shows the differences between the ideal RQL combustors behaviour and the real one, characterized by a more intense production of NO_x. Even if RQL combustors behaviour allows to contain

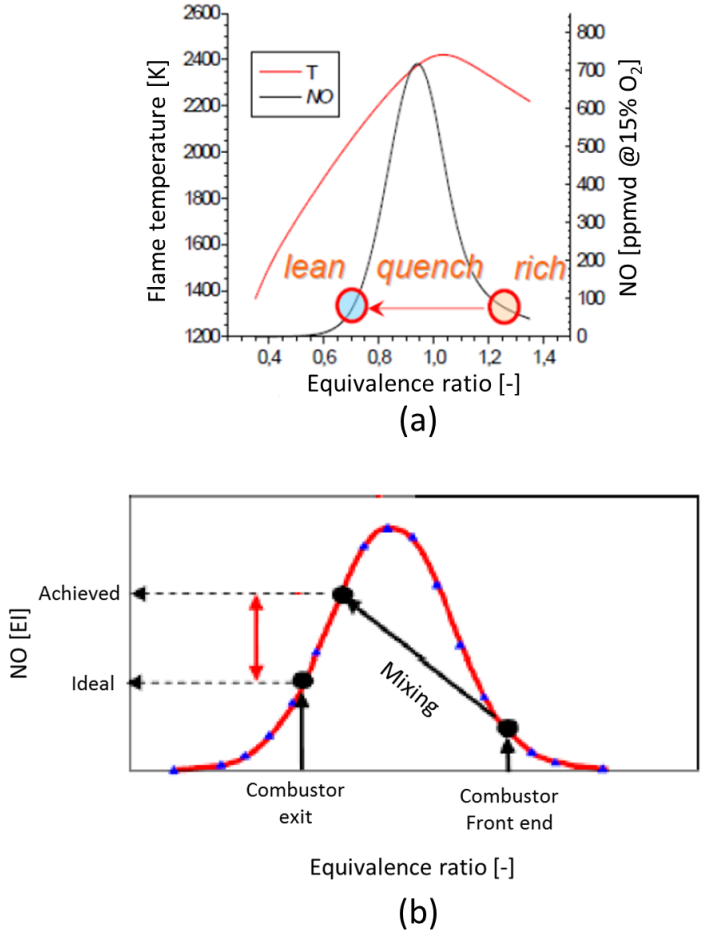

Figure 1.11: Comparison between (a) ideal and (b) real behaviour of a RQL combustor

pollutant emissions, their intrinsic characteristics represent a severe limitation and prevent them to reach NO_x concentrations below 30-50 ppm [11]. Therefore, in order to strict the goals set by ACARE, manufacturers have been pushed to explore lean combustion as a mean to reach lower emissions, despite increasing issues in terms of flame stability and reliability.

1.3.2 Lean Burn combustors

The idea of a lean burn combustor is to operate with a premixed lean mixture in order to keep the combustion temperature at a lower level and

therefore to inhibit the formation of NO_x. In parallel with this benefit, there are several issues that designers have to deal with: first of all, the lower combustion temperature leads to increased conversion times, that become similar to residence times for CO and UHC, and so to higher emissions for these species [14]. Furthermore, lean combustors work closer to the flame extinction limit, so relevant issues in terms of flame stability arise. These issues become even more pressing when considering that aero-engine combustors are subjected to different operating regimes, from the idle to the take off conditions, and that efficiency, stability and polluting emissions limitation must be always guaranteed through the whole Landing-Take Off (LTO) cycle. Therefore, a big effort has been put, in recent years, in trying to introduce lean combustion in the aero-engine combustors market.

The most used way to overcome the problem related to flame stability is the so called *fuel staging*: it consists in turning off individual or groups of burners, and thus increasing the equivalence ratio in the remaining ones. While this technique is widely used also on *Dry-Low-Nox* industrial gas turbine combustors, the more pressing needs in terms of stability for aero-engine applications, led to modifications and refinements. In a staged combustor two separated zones are designed to improve the combustion performance: the first zone operates at fairly high equivalence ratio, even if lower than stoichiometric, to achieve a good combustion efficiency and to minimize the production of CO and UHC. This "primary" zone guarantees the stability of combustion during idle and low power conditions. At higher power level, it acts as a pilot source of heat for the second "main" combustion zone, which is supplied with premixed fuel-air mixture. In this way, the engine globally works in lean conditions and still the combustion process results efficient and stable for a wide range of operative conditions. Examples of axially and radially staged combustors are reported in Fig. 1.12.

The drawback of these configuration stays in the large surface to be cooled and, for radially staged combustors, the relevant front area; moreover, CO and UHC emissions are slightly higher than in single annular chambers. Therefore the research was aimed at developing single annular technologies with internally staged injectors; the idea is to combine the two domes into one

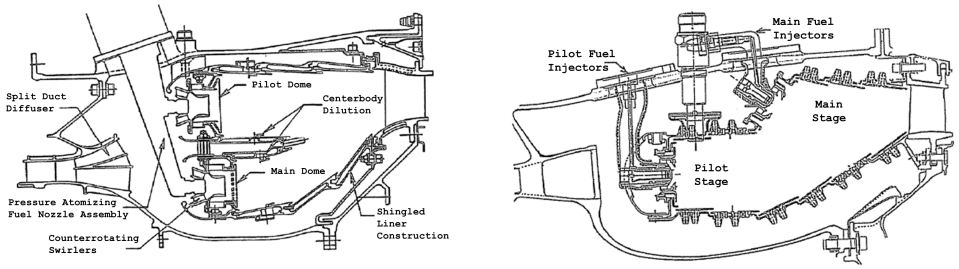

(a) General Electric dual-annular combustor

(b) Pratt and Whitney axially staged combustor

Figure 1.12: Axially and radially staged combustors [11]

with fuel staging, using two fuel manifolds. Emission performance characteristics have shown this approach to be highly promising, making it possible to reduce all types of emissions compared with a double annular combustor. Despite some drawbacks, mainly related to CO and UHC emissions and complexity, this architecture is nowadays considered as the most viable technology to be exploited [15], as current research heads towards the development of *Ultra Low* NO_x (ULN) combustors with single digit emissions of NO_x. Fig. 1.13 shows a scheme of the *GE Taps* (Twin Annular Premix System) combustor, a single annular combustor currently mounted on $GEnx$ engines which power Boeing 787 aircraft.

Particular attention must be paid to the injector design, not to erode the benefits achieved with the implementation of lean combustion and prevent from the formation of nearly stoichiometric zones within the lean mixture. Such a component plays a key role since it is responsible for both liquid atomization into small droplets, in order to favour liquid fuel evaporation, and for air/fuel mixing. Furthermore the injection system must be designed in order to create the dominant flow structures in the primary air flow, that are responsible for flame stabilization and for the completion of the combustion processes. For a given injector geometry, the combustor working pressure strongly affects the fuel atomization performance and, therefore, the efficiency of the whole combustion process. As a consequence, a single injector technology is very difficult to scale to various engine sizes and working conditions. To overcome this issue, several injector technologies have

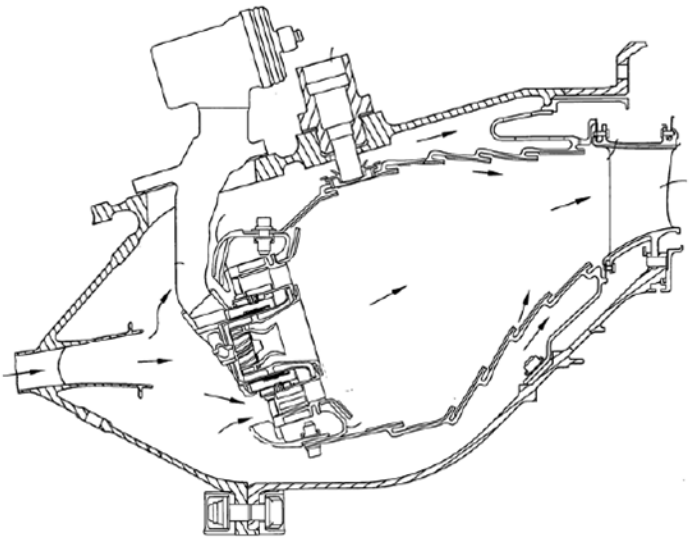

Figure 1.13: Scheme of GE Taps combustor (*Patent US20070028618*)

been developed; three different typologies have been developed within the NEWAC project, showing promising capabilities within their own range of application [6]:

- *Lean Premixed Prevaporized* (LPP): the working principles is based on

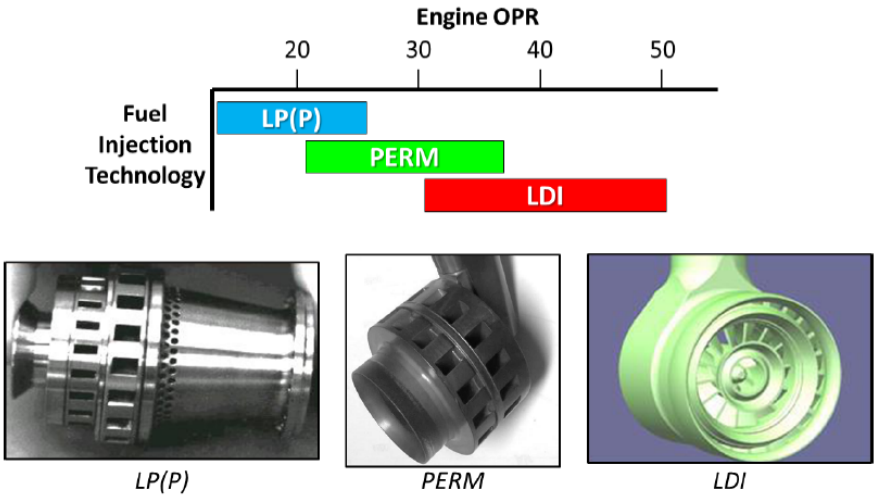

Figure 1.14: Lean burn injector technologies [6]

the action of two distinct air flow: the first is used primarily to get a good liquid fuel atomization, while the second is devoted to mix the fuel with air stream promoting the fuel evaporation and creating a mixture as uniform as possible. The main drawbacks are related to combustion instabilities and flashback issues, especially at high pressures; for these reasons its use is limited to engines that work at low OPR conditions.

- *Partially Evaporated and Rapid Mixing* ($PERM$): with a design aimed at overcoming the risk of autoignition, the concept is based on swirler technology development and it is addressed to achieve partial evaporation inside the inner duct and a rapid mixing within the combustor, optimising the location of the flame and the stability of the lean system [16, 17].

- *Lean Direct Injection* (LDI): the fuel is directly introduced in the combustion test section where it is subjected to rapid mixing with the combustor air. Internally staged injector are generally used, with no premixing ducts, and the mixing is promoted by means of concentric axial swirlers. In addition to its ability to limit flashback, studies have shown low level of NO_x emission and higher combustion efficiency compared to the LPP injector, making this technology attractive for high OPR aircraft applications.

These configurations, as well as their typical application range in terms of OPR are reported in Fig. 1.14.

Once traditional (RQL) low-NOx combustors and modern lean burn ones have been briefly introduced, it is useful to summarize their differences, in order to understand how they can affect the flow field evolution inside the chamber and the performance of the whole engine.

The main difference stays in the air flow split distribution; while for RQL combustors, most of the airflow (65-70%) is headed to dilution and cooling flows, as a limited amount of air is needed in the rich burning primary zone, in order to create the desired conditions, in lean burn combustors, almost 70% of the air mass flow is injected in the primary zone, for air/fuel preparation. As a consequence, a reduced amount of air is available for liner cooling,

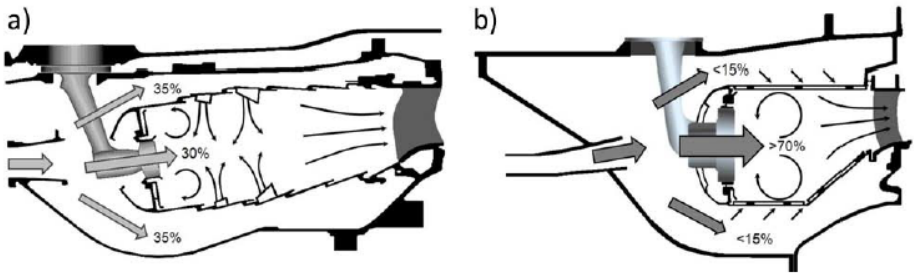

Figure 1.15: Air flow split and main flow field structures for RQL (a) and lean combustors (b) [18]

so the research has to be headed to different and more efficient cooling concepts. Another distinction stays in the flow field promoted by the injection system. Even if in both configurations the swirling structures generated by the injection system play an important role in the primary zone combustion performance, for RQL combustors, where diffusive flames are adopted, the crucial part of the process stays in the rich-lean switch promoted by the dilution flows. Therefore these flow structures are the dominant ones within the combustion chamber flow field evolution and where most of the design efforts are focused. On the other hand, for lean combustors, the cooling flows interaction with mainflow is much more limited, due to the reduced cooling mass flow; the flow structures created by the injection systems, thus, play the main role in the swirl-stabilized combustion process and propagate through the chamber without being significantly altered. Fig. 1.15 summarizes the differences in air split and flow field evolution between the two low-NOx technologies.

Once lean burn combustion has been identified as the most effective technology to damp NOx emissions, and proper injection systems have been designed, a review of the entire combustor arrangement becomes necessary in order to both meet the new specific requirements and to obtain an efficient integration with the following parts of the engine. In particular it must be assessed how the different flow field evolution and the generated flow features affect the behaviour of the high pressure turbine, in order to promote an in-

tegrated design philosophy of the two modules. An extensive account of this innovative trend of development is provided in the next chapter.

Chapter 2

Combustor-Turbine Interaction

Contents

As anticipated in the previous chapter, in comparing traditional RQL combustors to modern lean burn ones, relevant differences can be found, not only in their intrinsic behaviour, but also in the chamber flow field evolution and in how it affects the turbine module. In order to treat this problem, which is the final goal of this work, brief insights on lean combustors and high pressure turbine vanes flow field characteristics will be separately provided

first.

2.1 Flow Field in Lean Combustors

The investigation of the flow field structures that are generated and evolve inside the combustion chamber is a crucial part of the core-engine design process for at least three main reasons: first of all it is important to investigate the flow field structures generated by the injection systems in order to understand if they fulfil the design goals in terms of fuel/air mixing and flame stabilization and to improve the injection system design itself; secondly, the flow field characterization is important in order to understand the interaction between mainflow structures and cooling flows, so that a well-performing cooling scheme for the liners can be reached, with the goal of minimizing losses and maximizing the durability of the components; furthermore, if the focus is extended to the whole engine, it is necessary to understand how these structures affect the flow field at combustor outlet, in the view of optimizing the high pressure turbine module design.

Several works focused on the characterization of the flow structures generated by swirling flows coming from combustor injectors, have been carried out. A first extensive review dealing with swirling flows in combustion chambers was given by Lilley [19]. The main outcome of this work stays in the fact that it put the basis for the characterization of the degree of swirl of an injector, through the *swirl number* (S_N): it was defined by Beer and N.A.Chigier [20] as the ratio between the axial flux of angular momentum and the axial thrust of the flow. It was found that, when $S_N > 0.6$, strong radial and axial pressure gradients are set up near the nozzle exit, resulting in a central toroidal recirculation zone (RCZ) and a vortex breakdown [21]. These phenomena play an important role in both fuel/air mixing and combustion process completion, by increasing turbulence and residence time. Another structure, that is often related to vortex breakdown is the PVC (*Precessing Vortex Core*). As stated by Hall et al. [22], the specific conditions that bring to the formation of a PVC are not fully understood yet, but it is usually identified as an asymmetric, large scale, coherent flow feature, generally as-

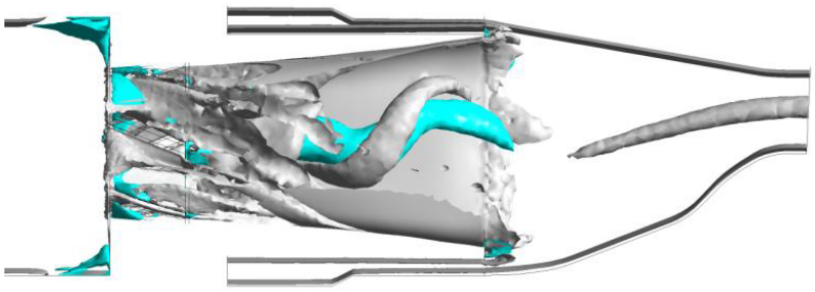

Figure 2.1: URANS calculation results: highlight of RCZ (blue) and PVC (grey) [22]

suming a corkscrew shape, with the potential to cause large-scale flow field instability within a swirling flow. Fig. 2.1 shows RCZ and PVC, highlighted by Hall et al. [22], through URANS calculation in preliminary steps of a lean burn combustor simulator design.

In the last years, with the growing interest in developing and optimizing lean injectors, several authors have carried out flow field measurements on the novel injector technologies (Section 1.3.2), in order to detail problems related to combustion instabilities [23] and interaction between swirling flows and liner cooling schemes [24, 25, 26]. Berrino et al. [27, 28] carried out experimental investigations of the flow field downstream of an ultra low NOx injection system in order to highlight both the overall field and unsteady phenomena. It was also highlighted that, in these kind of higly swirling flows, the chemical combustion process, in the form of heat release, play an important role in flow field stabilization. Unsteady phenomena like PVC were found to be damped or erased when experiments shifted from non-reactive flows to combustion tests, on same injector geometries [29, 30, 31]; a reduction in the extent of the RCZ was also found[16, 17]. Therefore, from a purely experimental point of view, differences between the reacting and non-reacting cases exist and, if no adjustment are made in the design phase, they can affect the combustor exit profiles obtained in experiments with non-reactive simulators [22].

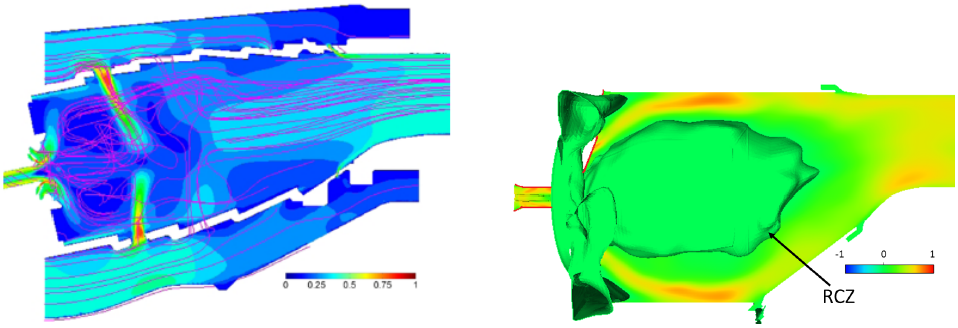

(a) (b)

Figure 2.2: Evolution of the flow field in the combustor chamber: comparison between (a) RQL [32] and (b) Lean-Burn [33] arrangements

2.2 Combustor Exit Non-Uniformities

Starting from what have been described in the previous sections, it is possible to add some details about the flow field that should be expected at the exits of modern lean combustors. Generally speaking, the flow field at the exit of a swirl-stabilized annular combustor is by nature highly unsteady, due to the turbulent combustion, the mixing processes and the aggressive swirl angles; it is also non-uniform in temperature, both on the circumferential direction, because of the discrete position of fuel injectors and dilution holes, and on the radial one, due to liner cooling and core flow mixing. All these aspects, as it will be explained in the following, have a relevant impact on the turbine behaviour. This issue, as already mentioned, is emphasised in lean combustors, since a reduced amount of air is used for liner cooling and it hardly interacts with the mainflow coming from the primary combustion zone. Fig. 2.2 summarizes the differences in flow field evolution between RQL and lean combustors.

As a result, modern combustors outlets are generally characterized by enhanced non-uniformity in terms of both total temperature, with marked hot spots called *hot streaks*, and flow angles, with an aggressive swirling flow that is also responsible for significant turbulence intensities [22] and for a highly unsteady behaviour.

As an example, the measured combustor exit temperature field of a mod-

ern Rolls-Royce engine is shown in Fig. 2.3a [34]; it was used by Povey and Qureshi [35] as the target profile for the design of an enhanced temperature distortions simulator: both circumferential and radial temperature gradient can be observed, due the hot streak issuing from the burner, visible in the central region and apparently centred on the NGV passage, and to the mixing with liner coolant. Fig. 2.3b shows the combustor exit flow field chosen as a target by Qureshi and Povey [36], for the design of a modern lean burn combustor simulator, with peak swirl angles exceeding ±40°.

2.2.1 Temperature Distortion Characterization

In order to quantify and characterize the degree of non-uniformity of the temperature field at combustor exit, lots of different parameters have been defined. In particular, two coefficients, called *Overall Temperature Distribution (or Distortion) Factor* (*OTDF*) and *Radial Temperature Distortion Factor* (*RTDF*) have been proposed by Povey and Qureshi [34] ; the first one considers the difference between maximum and mean temperature, over the whole combustor exit section, while the latter considers the difference between the maximum circumferentially averaged temperature and mean temperature:

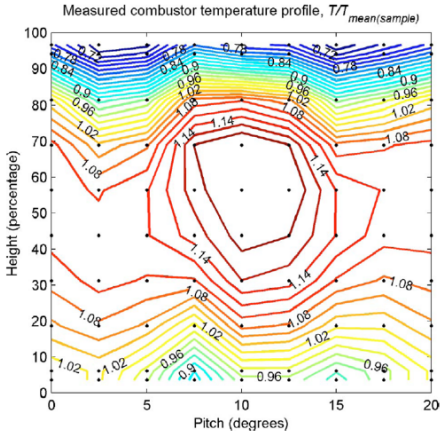

(a) Combustor exit temperature field measured across one burner pitch (Rolls Royce engine) [34]

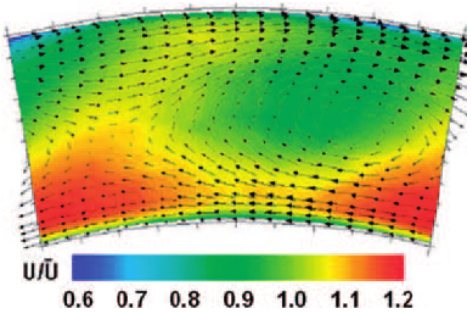

(b) Exit swirl conditions for a modern low-NOx combustor. [36]

Figure 2.3: Examples of temperature non-uniformities and swirl field at combustor exit

$$OTDF = PatternFactor = \frac{T_{4,max} - T_{4,mean}}{\Delta T_{comb}} \tag{2.1a}$$

$$RTDF = ProfileFactor = \frac{T^{circ}_{4,max} - T_{4,mean}}{\Delta T_{comb}} \tag{2.1b}$$

where subscript 4 refers to the combustor exit plane and ΔT_{comb} is the difference between mean temperatures at combustor exit and inlet.
At the same time it is possible to define the correspondent local parameters (*Local Overall Temperature Distortion Factor* and *Local Radial Temperature Distortion Factor*), if a full description of the profile shape is necessary, substituting the maximum temperature with the local one, in a certain position of the exit plane.

$$LOTDF = \frac{T_4 - T_{4,mean}}{\Delta T_{comb}} \tag{2.2a}$$

$$LRTDF = \frac{T^{circ}_4 - T_{4,mean}}{\Delta T_{comb}} \tag{2.2b}$$

It's not uncommon, however, to refer also to the local parameters as OTDF and RTDF. In the context of non-reactive test rigs, these definitions are not easy to use. Therefore, alternate definitions of Eq. 2.1 and Eq. 2.2 are preferentially used to describe the flow at the combustor exit plane [34]:

$$LOTDF' = \frac{T_4}{T_{4,mean}} \tag{2.3a}$$

$$LRTDF' = \frac{T^{circ}_4}{T_{4,mean}} \tag{2.3b}$$

or, to directly take into account for cooling flows temperature:

$$LOTDF'' = \frac{T_4 - T_{4,mean}}{T_{4,mean} - T_{cool}} \tag{2.4a}$$

$$LRTDF'' = \frac{T_4^{circ} - T_{4,mean}}{T_{4,mean} - T_{cool}} \tag{2.4b}$$

2.3 Flow Field Characteristics in Turbine Nozzle Guide Vanes

In an axial flow turbine, nozzle guide vanes (NGV) are the first stage stator blades and have the goal of directing the airflow onto the turbine blades while, at the same time, converting pressure energy into kinetic energy. Gases coming from the combustion chamber pass through the nozzle guide vanes, where they are forced to accelerate. In general, the design of nozzle guide vane should follow a lot of necessities and many aspects, mainly related to aerodynamics, structural mechanics and heat transfer, must be taken into account. Even if a detailed description of nozzle guide vanes design procedures and criteria goes beyond the aim of this work, it is possible to state that one of the main goal that a design procedure should be headed to is minimizing the pressure losses across the vanes; moreover, since NGVs are invested by the hot gases coming from the combustion chamber, another important design goal is the definition of an efficient cooling system. It must be also considered that both requirements interact with each other, since cooling flows are responsible for aerodynamic losses, in the form of turbulent mixing and momentum balance, but, also, a detailed knowledge of the flow field is necessary for an accurate design of the cooling scheme.

2.3.1 Pressure Losses in Turbine NGV

Aerodynamic losses in turbine NGV are generally described in terms of total pressure drop across the cascade; even so, a lot of parameters have been used for the goal, mainly differing from each other by the quantities used to

make the values non-dimensional. Ligrani [37] provided a full review of many used parameters; among them the most used ones are expressed as:

$$Y_A = \frac{P_{0,i,mean} - P_{0,e}}{P_{0,i,mean} - P_{s,e}} \tag{2.5}$$

or:

$$Y_P = \frac{P_{0,i,mean} - P_{0,e}}{q_e} \tag{2.6}$$

where subscripts i and e indicate cascade inlet and exit positions respectively, q is the dynamic pressure contribution and the subscript *mean* stands for either mass or area averaging within a certain axial position. For each parameter a correspondent integral one can be achieved simply by averaging $P_{0,e}$, $P_{s,e}$ and q_e.

In general it is not easy to classify and summarize all the sources of pressure losses in axial turbine vanes, since the different phenomena interact with each other and sometimes a fine line exists between one and another. Nevertheless it is common to simplify the treatment by diving them into three main sources [38]:

- *Profile losses*: due to skin friction or separation which take place on the airfoil with a uniform two-dimensional flow across a cascade
- *Annulus losses* or *Endwall losses*: due to skin friction on the endwalls
- *Secondary losses*: due non-uniformity of the three-dimensional flow through a row of blades (or due to *secondary flows*)

Profile losses are generally expressed in terms of momentum thickness at blade trailing edge and, since they increase with blade load, they strongly depend on the parameters that influence blade load such as pitch/chord ratio and flow deflection. Different methods [40, 41] exist to evaluate this source

of losses and to find optimum values for these parameters. Other sources of profile losses are due to the finite thickness of the blade TE, which creates a low-pressure wake region behind it and mixing between PS ans SS boundary layers.

Secondary losses are the more complex, since they depend on particular flow structures as the secondary flows, which may be defined as the difference between the actual and an idealized axisymmetric flow [42]. The fundamental features of secondary flow patterns in nozzle guide vane passages were proposed by Langston [43], through the characterization of a linear cascade; even if it is acknowledged that several differences between annular and linear cascade flow fields exist, its work is recognized as highly significant in establishing the basic mechanisms that apply in all cascades [44]. The main secondary flow is the so called *passage vortex*: the reduced velocity in the boundary layers causes an overturning of the flow towards the suction side, which creates two counter-rotating vortexes close to the inner and outer endwalls. An outline of the passage vortex structures can be found in Fig. 2.4, that also shows the endwall streamlines measured by Langston et al. [39].

A second contribution is due to the *horseshoe vortex*, generated by the pressure gradient caused by the endwall boundary layer in correspondence

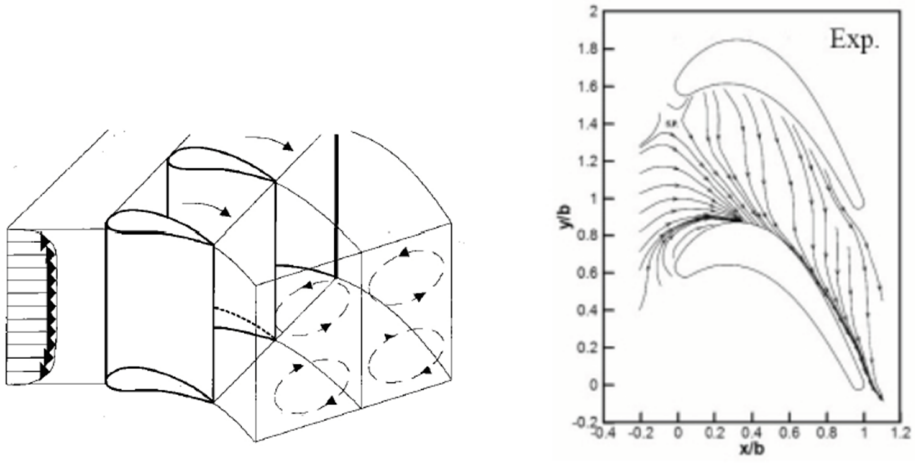

Figure 2.4: Schematics of passage vortex structures and measured endwall streamlines [39]

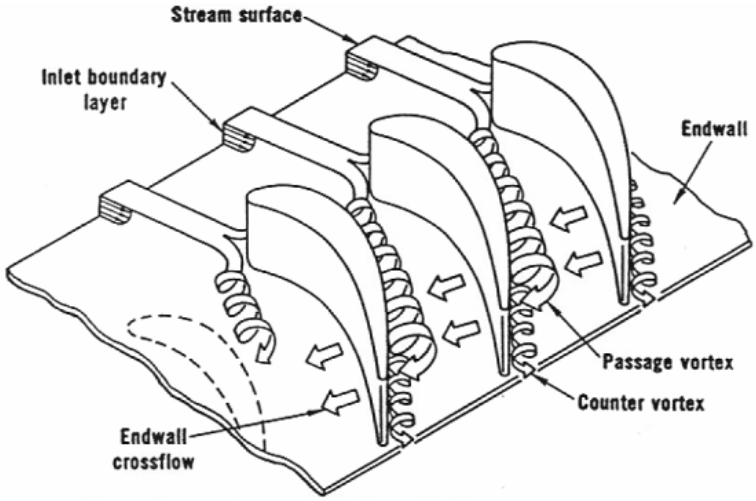

Figure 2.5: Three-dimensional separation of a boundary layer entering a turbine vane [45]

of the stagnation point at the blade LE. Such a vortex is then split in a *pressure* and a *suction leg* and convected inside the passage. The pressure leg is "fed" by the passage pressure-to-suction endwall flow and enforces the passage vortex; the suction leg, on the other hand, has an opposite sense of rotation and is sometimes labelled as *counter vortex* [43]. The resulting three-dimensional flow configuration is depicted in Fig. 2.5 [45].

All the parameters that affect the blade load and, in general, the flow field evolution have an impact on the pressure losses. Among others, Ligrani [37] investigated the influence of exit Mach number and inlet turbulence intensity: enhanced pressure losses were found with increases of both parameters. Same conclusions were found when investigating the effect of film cooling: Fig. 2.6 summarizes how higher coolant mass flow rates bring to higher pressure loss coefficients; the definition of the used pressure loss parameter can be found in the referenced work. An increase in pressure losses due to film-cooling flows was also detailed by Day et al. [46], that also evidenced the importance of matching the main-coolant momentum flux ratio, for the evaluation of this aspect and the correct scaling of the results.

A typical pressure loss coefficient contour, for uniform axial inflow, is reported in Fig. 2.7, as measured by Giller and Schiffer [47]. Important

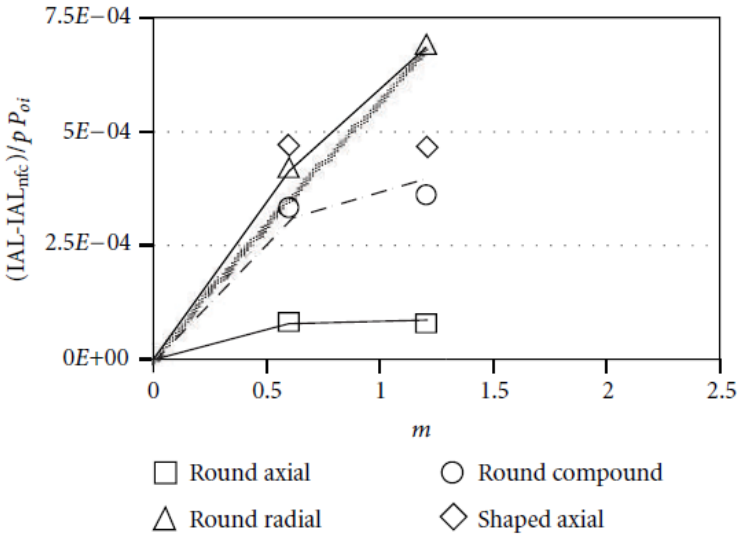

Figure 2.6: Effect of film cooling mass flow rate on pressure losses [37]

contributions of profile losses (red circles) and, in particular, of endwall secondary losses (white circles) can be appreciated. Similar patterns were found in several studies related to the evaluation of pressure losses and secondary flows in both linear and annular NGV cascades [48, 49, 50]. Due to this typical behaviour several studies have been carried out, in recent years, to find contoured endwall shapes able to reduce these source of losses [51, 52].

2.3.2 Film Cooling in Turbine Nozzle Guide Vanes

Typically, cooling is provided by extracting some of the compressed air and bypassing the combustor directly into the turbine. The extraction of the working fluid imposes a penalty to system efficiency, as work has been done on the fluid to compress it. Also, the addition of the coolant back into the hot mainstream imposes further thermodynamic penalties. The turbine components cooling is, in general, achieved both from inside and outside. Internal cooling typically involves impingement, turbulated serpentine passages and flow through pin-fin arrays. External cooling consists in allowing the coolant from inside the blade to eject out onto the hot gas path side of

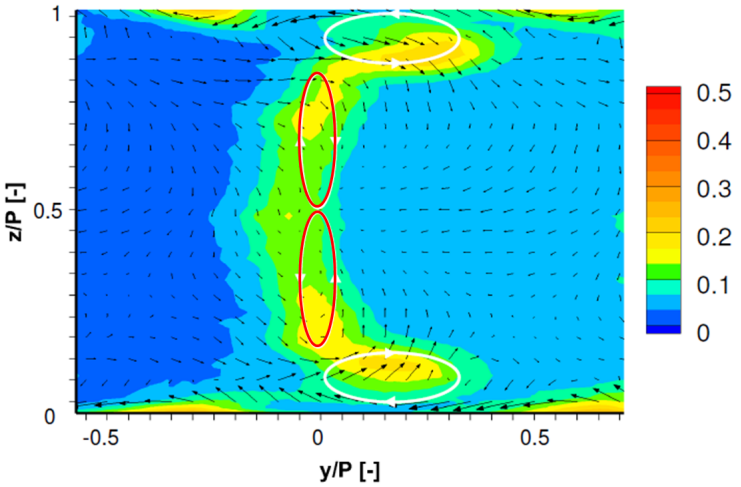

Figure 2.7: Pressure loss coefficient measured on a linear cascade with axial inflow [47]

the surface through discrete holes. This method is called film cooling [53]. From a design point of view it is necessary to understand the impact of different flow parameters and phenomena on film-cooling behaviour itself. Four of the most important ones, that are commonly considered in the evaluation of a film-cooling system performance, are the following:

$$BlowingRatio(BR) = \frac{(\rho V)_{cool}}{(\rho V)_{main}} \tag{2.7a}$$

$$VelocityRatio(VR) = \frac{V_{cool}}{V_{main}} \tag{2.7b}$$

$$DensityRatio(DR) = \frac{\rho_{cool}}{\rho_{main}} \tag{2.7c}$$

$$MomentumRatio(I) = \frac{(\rho V^2)_{cool}}{(\rho V^2)_{main}} \tag{2.7d}$$

For a single row of holes, the film-cooling behaviour can be described by the correlation developed by L'Ecuyer and Soechting [54]. They defined three regimes for characterizing the film effectiveness distribution on any surface:

- *Mass addition regime*: Effectiveness increases with BR due to increased thermal capacity of the coolant, but the effectiveness is independent of DR and VR.

- *Mixing regime*: Effectiveness distribution depends on BR, DR due to opposing influence of increased thermal capacity and increased coolant/free-stream mixing and penetration.

- *Penetration regime*: Effectiveness distribution is completely dominated by a complex interaction of excessive coolant penetration and augmented turbulent diffusivity of the coolant.

The basic phenomenology can be described through the behaviour of a flat plate (i.e. no curvature and mainstream flow acceleration effects). In this case, for an angle of injection of $\alpha = 35°$, a *pitch-diameter* ratio $p/D = 3$ and for a single row of cylindrical holes, the above mentioned regimes occur within the following range of VR:

- *Mass addition regime*: $VR < 0.25$

- *Mixing regime*: $0.25 < VR < 0.8$

- *Penetration regime*: $VR > 0.8$

The equation that relates the velocity ratio threshold value, at which the shift to penetration regime occurs, to the injection angle is the following:

$$VR_{pen} = \frac{0.45887}{sin(\alpha)} \tag{2.8}$$

According to these findings, the peak effectiveness level (η_p) is a function of geometric parameters and of VR and DR in the form reported in Fig. 2.8a; L'Ecuyer and Soechting [54] also developed a correlation capable of representing the effectiveness distribution for all the above regimes. A typical shape of this curve, for fixed values of all the above mentioned parameters except for injection angle, is reported in Fig. 2.8b.

In turbine nozzles and blades applications the treatment becomes more complex. Typically, coolant from within the airfoil is injected through several rows of discrete holes to protect the surface and reduce heat-transfer rates.

The interaction between the mainstream gases and coolant jets varies from zone to zone, as local mainstream velocity and pressure increase and decrease depending on the curvature of the airfoil. Therefore coolant-mainstream interaction varies with several geometric and aerodynamic factors also affecting the heat-transfer [53] and, often, ad hoc analyses for specific configurations must be carried out. Still, some conclusions from the above cited work can be utilized, in terms of both influencing parameters and qualitative behaviour.

Mick and Mayle [55] studied the stagnation region as a semicircular leading edge with a flat afterbody. They presented heat-transfer coefficient and film effectiveness results for two rows of holes. They varied the coolant blowing rate from BR=0.38 to 0.97. Results showed (Fig. 2.9a) that effectiveness values decreased with increasing blowing ratio, as coolant protection at higher injection rates suffers from excessive mainstream boundary layer penetration, jet interference, and mixing. Mehendale and Han [56] studied the effect of high free-stream turbulence on a film-cooled leading-edge model, similar to the one used by Mick and Mayle [55]. Higher free-stream turbulence was generated using passive grids (Tu=9.67%) and air jets injections (Tu=12.9%). Results (Fig. 2.9b) showed that, at BR=0.4, free-stream turbulence caused reduced film effectiveness over the entire surface, as coolant jets tend to dissipate faster into the mainstream; with an increase in blowing ratio, the jet momentum is stronger and the diffusion of the jets in the mainstream is reduced, resulting in a lower impact of the free-stream turbulence. In other studies [57] at higher blowing ratios, spanwise averaged effective-

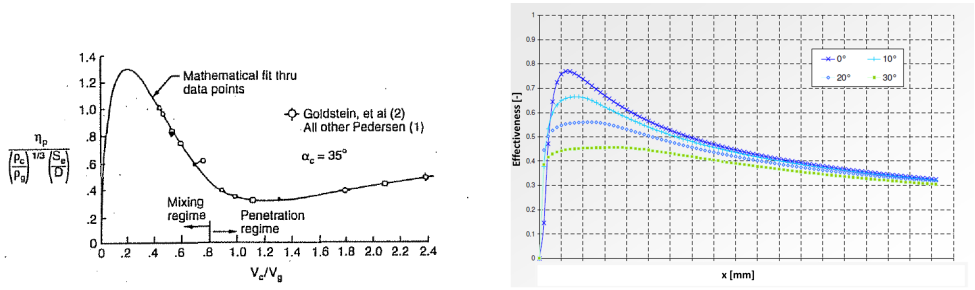

(a) (b)

Figure 2.8: Peak effectiveness level (a) and spanwise averaged effectiveness (b) trends [54]

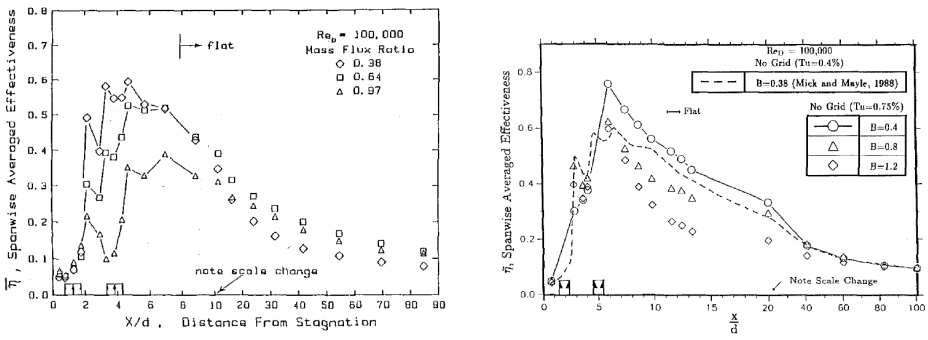

(a) (b)

Figure 2.9: Adiabatic effectiveness results on a leading-edge model for different blowing ratio (a) and free-stream turbulence (b) [55, 56]

ness has been also found to increase due to higher free-stream turbulence, due to the promoted lateral diffusion of the coolant. Similar results were found by Ekkad et al. [58]. The effect of free-stream turbulence was studied for blowing ratios of 0.4, 0.8, and 1.2: an increase in free-stream turbulence reduced film effectiveness significantly at low blowing ratios while a reduced effect was appreciated at higher values of BR. The effect of the density ratio was also evaluated in the same study: it was found that an increase in DR generally brings the maximum effectiveness to be reached for higher blowing ratios. A strong influence of coolant-to-mainstream density ratio was found also by Narzary et al. [59], who studied these effect on a prismatic blade geometry, and found that effectiveness was enhanced with higher DRs. They also found an important influence of secondary flows on their results, since coolant wakes on the suction side are driven away from the endwalls due to the effect of the passage vortex, as depicted in Fig. 2.10.

Concerning the study of adiabatic effectiveness on nozzle guide vane profiles, two additional parameters have been recognized as important ones; as, in part, already anticipated, both the mainstream pressure gradient and the surface curvature play an important role in defining the film-cooling performance. A lot of studies have been carried out to assess how film-cooling behaves in case it is applied to either concave (i.e. pressure side) or convex (suction side) surfaces [60, 61, 62]. According to Han et al. [53], results

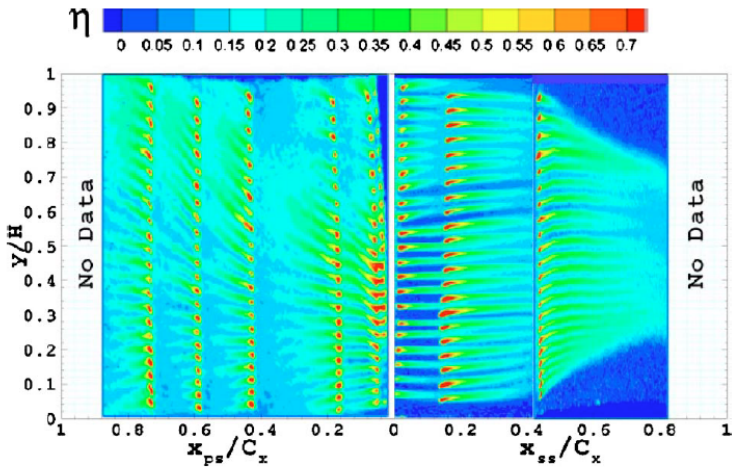

Figure 2.10: Adiabatic effectiveness results on a 2D blade geometry [59]

demonstrated that it is fairly reasonable to state that a convex surface enhances cooling effectiveness at low momentum flux ratios as does a concave surface at higher momentum flux ratios. In particular, a concave surface is generally characterized by lower adiabatic effectiveness, than a flat plate, due to the static pressure force acting on the jets that moves them away from the surface. Increasing the momentum ratio leads to a reduced coverage in the very proximity of the holes, but the area downstream of it is generally characterized by an improved effectiveness, as a stronger reattachment occurs, since the curvature is along the direction of the liftoff. For convex surfaces, on the other hand, effectivenss is generally higher than for flat plates, but an important drop-off in performance occurs as the momentum ratio overcomes threshold values: these values were found to be slightly higher than for flat plates, due to the greater turning of the jet, by the favorable pressure gradient, that shifts the detachment to higher momentum ratios [63]. The adiabatic effectiveness is always higher in the proximity of the holes, as the surface curvature works against the reattachment.

Barigozzi et al. [64] also showed that an increase in Mach number (i.e. flow acceleration), from 0.2 to 0.6, could be beneficial to the film coverage, as the positive stream-wise pressure gradient creates higher velocities in the bound-

ary layer and keeps the jets closer to the surface. On the other hand, when an acceleration does not lead to a further boundary layer thickness reduction, it was found to increase the rate at which the jets are mixed out by the freestream, resulting in faster stream-wise decay of the laterally averaged effectiveness [63].

2.4 Review of Combustor-Turbine Interaction Researches

Once brief accounts of the behaviours of both modern combustors and nozzle guide vanes have been provided, it is necessary to understand how they influence each other. As explained in the last section, the flow field at the exit of annular aero-engine combustors is intrinsically non-uniform, due to the complex flow field evolution occurring in the chamber; on the other hand, the design of the high pressure turbine NGV has to take into account several phenomena and parameters, most of them depending on the inlet flow conditions, to fulfil the requirements in terms of both aerodynamics and heat transfer. Therefore, several research activities have been carried out since 1980s, in order to deepen the knowledge of the impact of hot-streaks and flow field distortions on the high pressure turbine. Still, despite the tight link between the combustor and the turbine due to these non-uniformities, the design of the two modules historically relied on separated approaches: experts in combustor and turbine aerothermal have always been two separate teams in both industrial and academic fields. This has influenced the definition of design criteria for the high pressure module: combustor and turbine are studied separately, leading to the establishment of a standard interface between the two components, commonly referred to as “Plane 40”, through which information is passed forward between the design teams. The gap of knowledge on the mutual interaction was bridged by the industrial experience and by the application of safety margins that are detrimental to the engine efficiency. With the introduction of lean combustors, significant issues can arise in the traditional design procedures. Industrial applications,

in fact, usually relies on 1D, circumferentially-averaged profiles of pressure, velocity and temperature at the combustor-turbine interface, in conjunction with Reynolds-Averaged Navier-Stokes (RANS) models, for the characterization of the turbine behaviour. In the presence of highly unsteady and non-uniform combustor outflows, the complexities related to the knowledge of their behaviour and to their modelling can lead to significant inaccuracies in the prediction of both aerothermal performance and heat loads. The investigation of combustor-turbine interactions has assumed mandatory importance, due to the lack of literature data and industrial experience in predicting the impact of these enhanced distortions on the turbine behaviour. Therefore, innovative test rigs have been developed, in recent years, in order to provide additional data, evidence the limits of current design procedures and promote an integrated design approach of the two modules together. In the following, a quick overview of the test rigs developed throughout the last fourty years will be given, before shifting the focus to the recent test rigs aimed at simulating lean burn combustors behaviour. An important goal of experimental data, in addition to describe the physics of a certain phenomenon, is to validate numerical tools, especially when the focus is placed on improving design practices; despite that, in the following, the focus will be almost exclusively limited to experimental characterizations of the relevant phenomena, without any reference to how common numerical tools are able to characterize them. CFD results will be only used, in the next sections, to deepen the description of the knowledge of some aspects when reduced or no experimental surveys are available yet.

2.4.1 First generation hot-streaks simulators

Povey and Qureshi [34] provided an exhaustive review of the hot streak simulators for turbine testing. The first one, in chronological order is the *Combustor Exit Radial Temperature Simulator* (*CERTS*), set up in 1983 in the Warm Core Turbine Test Facility at NASA Lewis Research Center [65]. This rig, used to test a scaled model of a constant speed engine, is able to reproduce only radial temperature non-uniformities, achieved by injecting colder air from four slots. Figure 2.11 shows the rig layout. Results showed

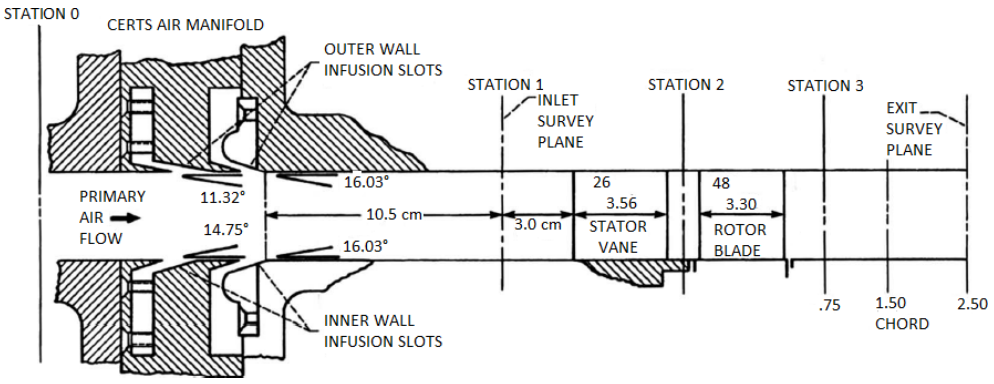

Figure 2.11: CERTS rig layout [66]

that the only radial distortion, despite it alters the secondary flows inside the cascade, doesn't have effect on the engine efficiency, with respect to the uniform profile.

The *Large Scale Rotating Rig*, consisting in a low speed turbine, was assembled at the United Technologies Research Center (East Hartford, Connecticut) [67]. Thanks to a nozzle that injected air together with a tracer gas (CO_2), a single hot streak was reproduced. The flow containing CO_2 could be heated up to a temperature twice as high as the ambient air that passes through the rig. Fig. 2.12a shows its layout: it's possible to note that the nozzle position made the CO_2 flow pass through a vane instead of impinging on the leading edge. The same rig, in the following years, was upgraded with five concentric rings, each one with 144 injectors, in order to simulate a full annular profile with hot streaks, as shown in Fig. 2.12. Since in this new configuration the CO_2 flow could not be heated, the new rig allowed to evaluate the effect of the generated secondary flows but not the heat transfer aspects.

The *Rotating Blow-Down Facility* (*BDF*) was set up at MIT (Massachusetts Institute of Technology) in 1989 [69]. This rig allowed to reproduce both radial and circumferential non-uniformities. As shown by Fig. 2.13, the first ones were achieved thanks to a stainless steel honeycomb heater, crossed by the mainflow that passed through the rig; for the latter ones some air was bypassed in a duct provided with another heather and then re-injected from four injectors distributed on one third of the annulus.

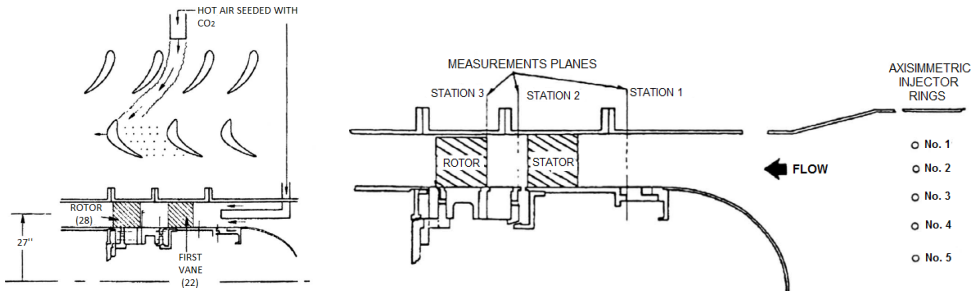

(a) (b)

Figure 2.12: United Technologies Research Center test rigs: layout of LSRR [67] (a) and upgraded temperature profile simulator [68] (b)

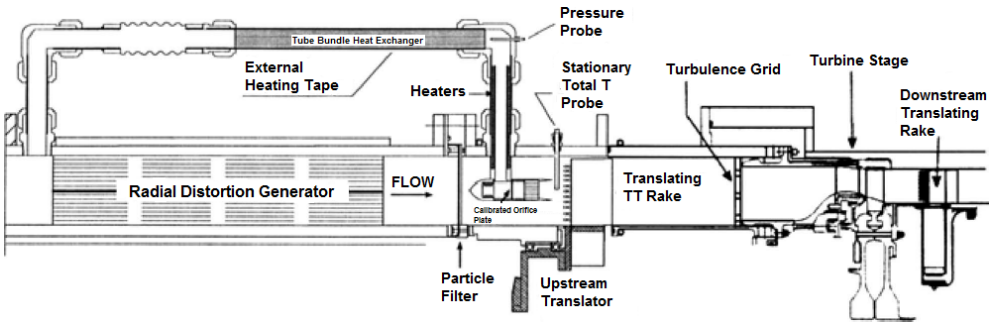

Figure 2.13: BDF rig layout [69]

These three, first generation rigs, were designed for proof-of-concept investigations, aiming only at the simulation of temperature distortion, without specifically referring to particular engine conditions. In the following years, more complex test rigs were developed; most of them were able to control both the temperature distribution and the pressure profiles, in order to explore the impact of both phenomena.

2.4.2 Recent studies of combustor-turbine interface

An important investigation has been carried out at the *Turbine Research Facility* (*TRF*) of the Wright Patterson Air Force Base (Dayton, Ohio). TRF is a facility realized in order to perform short duration tests on turbines, allowing to set some parameters of interest like Mach and Reynolds numbers, turbulence intensity, corrected speed and gas-blades temperature ratio

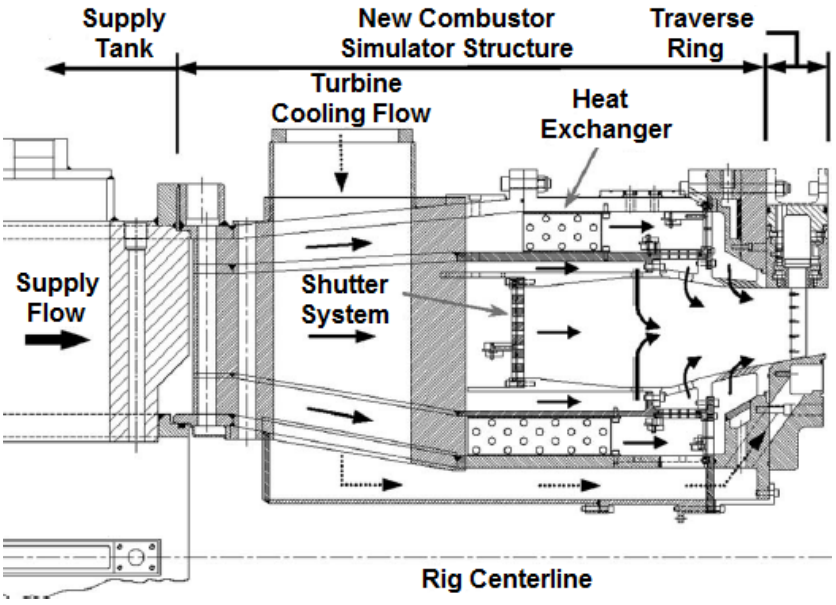

Figure 2.14: TRF combustor simulator section [70]

[70]. To study combustor-turbine interaction phenomena, the test facility was equipped with a combustor simulator. The sketch reported in Fig. 2.14 shows that the simulator is made by five annular concentric paths. The outer path hosts heat exchangers used to cool down the flow passing through them: this flow is, then, injected through primary dilution holes, useful to increase the turbulence intensity, and secondary ones, used to reproduce radial temperature non-uniformity. Moreover the simulator is provided with grids that allow to control the total pressure of the different flows.

With this instrumentation Barringer et al. [70] studied temperature and pressure profiles interactions with the turbine first stage. The investigated effects were mainly the modification of such profiles due to the high pressure vanes [71] and the vane heat transfer and aerodynamic behaviour [72].
For the first aspect, it was noted that the radial profiles distortion, downstream of the vanes, was damped by turbulence and secondary flows that promote the mixing. For the second aspect surface pressure and heath transfer measurements were performed on vanes and endwalls, using respectively miniaturized pressure transducers and thin film heath transfer gauges. Results showed the thermal field mainly affected the heath transfer only by

altering gases-blades temperature difference; the pressure field, on the other hand, influenced both the aerodynamic load and the heath transfer, altering the Nusselt numbers due to its influence on the secondary flows.

Several studies aimed at the characterization of a hot spot migration throuh a turbine cascade were also carried out. Most of them were conducted at Texas University, where several guidelines for the hot streaks migration analysis and scaling criteria were set [74, 73]. A linear cascade with a hot streak generator at its inlet (Fig. 2.15) was employed for the analysis; a metal duct and electrical resistance heating elements was adopted to create a well-bounded hot spot in the mainflow. The mainstream temperature was kept at 300K, while the NGV coolant and the hot streak flow were regulated at 187.5 and 330K respectively. It was found that a coherent hot spot was still recognizable on the exit plane, even if its entity was much reduced by the passage through the cascade. The mainstream turbulence, that determined a spreading of the hot spot and a consequent weakening in its strength, and film cooling injection were found to play a very important role in the quantification of such a reduction. The clocking with the hot streak aligned with the vane leading edge was not found to further diminish its strength, compared

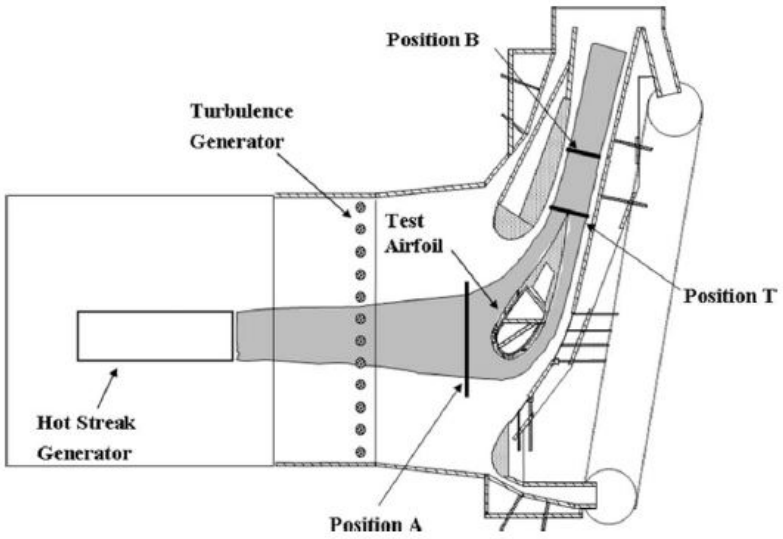

Figure 2.15: Scheme of the linear cascade used by Jenkins and Bogard [73]

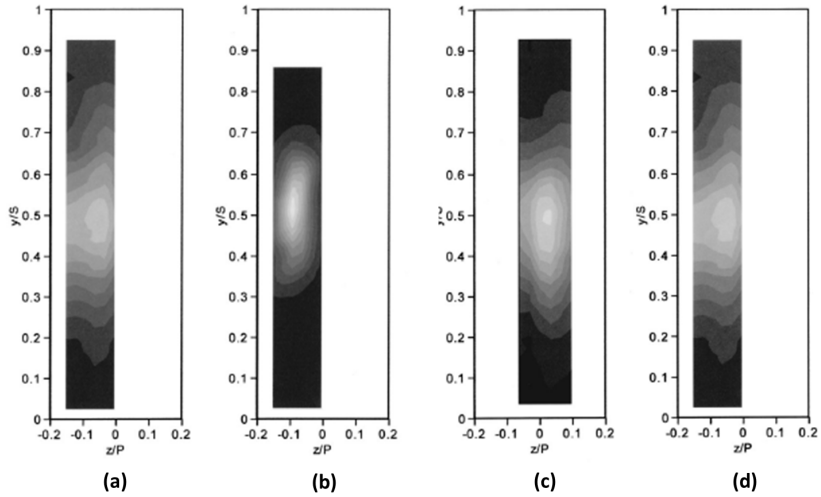

Figure 2.16: Normalized temperature ratio downstream of NGV cascade: hot streak through the mid-passage with (a) high turbulence, (b) low turbulence; high inlet turbulence with hot streak (c) impacting the stagnation point and (d) through the mid-passage [74]

to the passage clocking, due to the suppression of the mainstream turbulence near the surface of the vane. A similar conclusion was drawn by Barigozzi et al. [75]. Fig. 2.16 shows results from the work of Jenkins et al. [74], where the effect of turbulence and clocking is reported; as stated above, once a high level of turbulence is set at the cascade inlet, no predominant effect of the clocking can be appreciated. It was also found that the evaluation of the temperature field at NGV exit, by using a simple superposition principle, created an overestimation of the migrated hot streak of about 20% [73].

Similar phenomena were investigated by Mathison et al. [76], at the *Gas Turbine Laboratory* of the Ohio State University, on a test rig made by a combustor simulator and a full-scale model of a turbine first stage with cooled NGVs and not cooled rotor blades; the combustor simulator was made by a set of heat exchangers that could be independently powered in order to create a uniform temperature field or hot streaks. Tests with and without coolant injection were carried out in order to highlight their differences. The results showed that coolant tends to move towards the rotor suction side, bringing to a heath transfer reduction on such side. Moreover the goal of the test was

to evaluate the effect of the clocking position between hot streaks and NGV leading edges. The conclusions were not completely in line with what was found in the above described studies: if the hot streaks were aligned with NGV leading edges, the temperature profile was severely altered, due to the mixing that occurred after the impingement of the flow on the leading edge; on the other hand, if the hot streaks were aligned with the passages, the temperature profile was slightly altered and markedly non-uniform approaching the rotor. Moreover it's necessary to consider that, in the first case, the heath transfer between gases and nozzles was enhanced, resulting in a lower mean temperature at rotor inlet. No details of the inlet turbulence intensity were provided in this work.

Despite all these works offered detailed insights of temperature and pressure distortions effects on the high pressure turbine, none of them was aimed at simulating typical modern combustor flow fields; as described above, no realistic swirling flows were created and turbulence and pressure profiles were mainly achieved by means of grids or dilution holes. The necessities driven by the introduction of lean combustors (Section 2.4), have pushed to the development of specific experimental facilities for this goal. The most important ones will be described in the next section.

2.4.3 Tests on lean burn combustor simulators

As described earlier, the main features of lean burn combustors outflow are a high degree of swirl, and consequently highly unsteady behaviour, and hot streaks. A number of works dealt with the first aspect; results, mainly aimed at evidencing the influence of residual swirl on secondary flows and pressure losses, are not always in agreement with each other, as they strongly depend on the specific configuration. In the following a brief review of the main findings is provided. The problem was extensively studied at the Large Scale Turbine Rig (LSTR) of Darmstadt University, a scaled-up 1.5-stage low Mach number turbine, together with a lean combustor simulator [77]. A sketch of the test rig is shown in Fig. 2.17. Angles of $\pm 15^{\circ}$ can be achieved at the turbine inlet. CFD calculations carried out on this test case [78] showed that, for a certain NGV geometry, shifting from either 0D (i.e. average

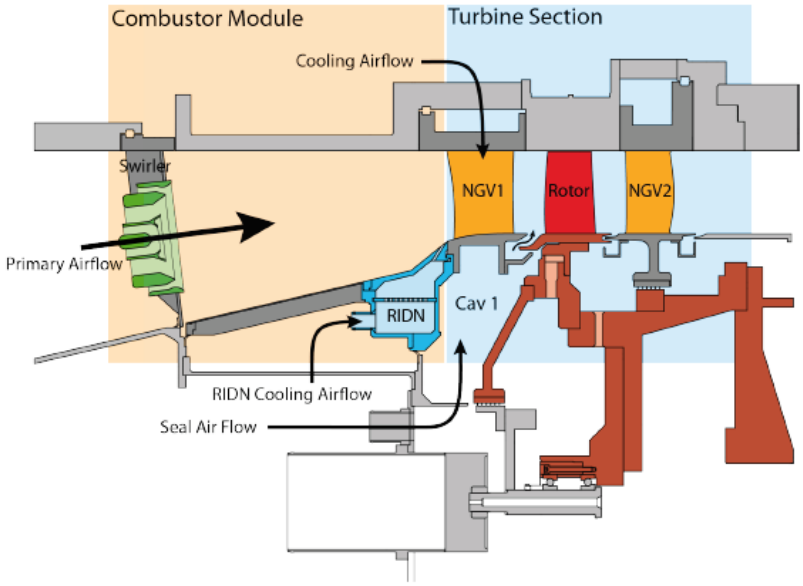

Figure 2.17: Darmstadt University annular test rig [78]

quantities) or 1D (i.e. tangentially averaged radial profiles) inlet conditions to actual 2D conditions, where both swirl and turbulence are considered, can lead to a stage efficiency reduction up to 2%. In particular, a significant effect of the swirling flow on the secondary flows and pressure loss pattern was evidenced. Residual swirl was found to create spots with high pressure losses close to either the hub or the casing, due to the interaction with end-wall secondary flows. The outcome depends on the clocking configuration (swirling structure aligned wih either the vane LE or passage) and on the sense of rotation of the swirling structure.

Results, reported in Fig. 2.18, showed that for a positive (i.e. counter-clockwise) orientation, higher pressure losses are registered close to the casing, while the opposite appears for negative (i.e. clockwise) orientation (black circles). Moreover, for a passage (PA) clocking configuration, relevant differences arise in the pressure losses in the central part of the two passages, with the one where the residual swirl is convected showing higher values (red circle). A more similar outcome is achieved in the leading edge (LE) clocking. A following experimental campaign confirmed these findings in the case of positive swirl [79]. The focus was also placed on the evaluation of the trajectory

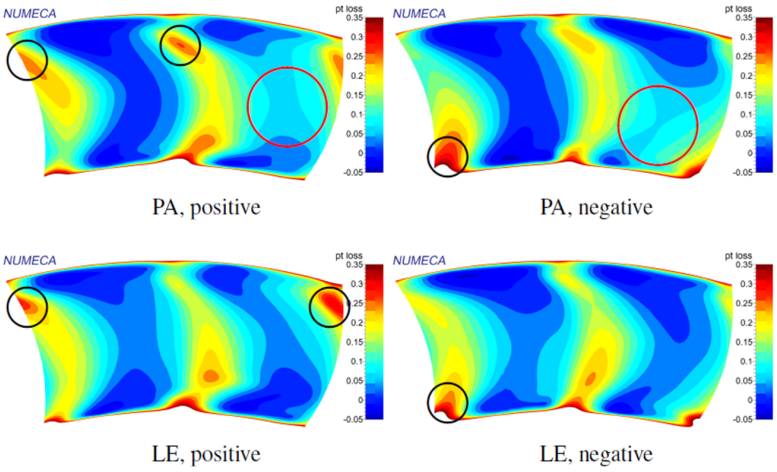

Figure 2.18: Pressure loss distribution for different clocking configurations and swirl orientation [78]

of coolant flows and pressure losses either in the presence of axial or swirled inflow. Results showed that, while for axial inflow, the cooling system layout is mainly responsible for the resulting pressure loss pattern, the presence of swirl determines a global smoothing due to a promoted mixing; therefore, the swirling flow characteristics, instead of the coolant injection, becomes the driving force for the measured pressure losses. Finally, the impact of the swirling flow on endwall effectiveness and heat transfer was detailed, for different swirler-vane clocking positions. Results showed relevant differences between swirling and axial inflows, mainly leading to heat transfer enhancement and adiabatic effectiveness reduction for the combustor representative case [80].

A linear cascade rig was also exploited for the investigation of the influence of residual swirl on leading edge film-cooling effectiveness [47]. The test section of the facility, operated at ambient conditions, sketched in Fig. 2.19a, consisted of six swirl generators and five linear cascade vanes.

The three middle vanes were equipped with film cooling holes at the leading edges. The swirler nozzles were aligned with the center of the cascade passages. Swirl angles above 30° were measured by means of a five hole probe at the cascade inlet. A strong influence was found on the leading

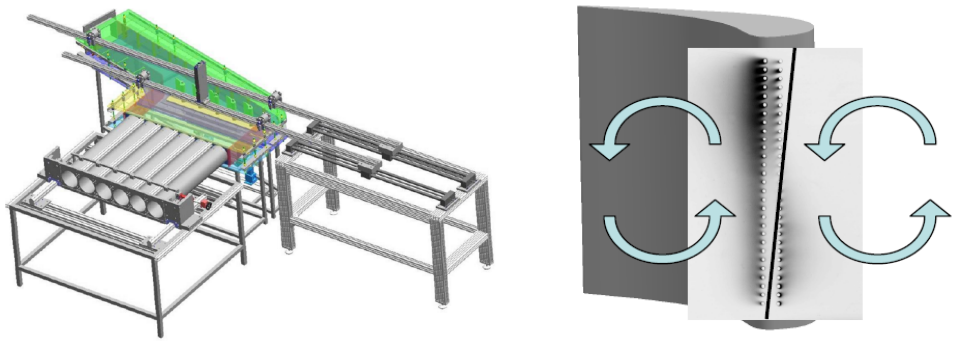

(a) (b)

Figure 2.19: (a) Sketch of the linear cascade rig layout (*www.glr.tu-darmstadt.de*) and (b) film cooling behaviour under swirling inflow [47]

edge film cooling behaviour, mainly due to the alteration of the stagnation line position; their investigation of swirling flow effects on the film-cooling performance was, anyway, limited to the leading edge region (Fig. 2.19b).

A large amount of work has been also carried out at the *Oxford Turbine Research Facility* (OTRF), in order to investigate both swirl and hot streaks. The OTRF is a short-duration wind tunnel capable of testing an engine-scale high-pressure turbine stage at non-dimensionally representative conditions. Compressed air is heated and forced into the test section by the action of a piston; steady conditions are reached for about 500ms, as test run ends when the piston reaches the end of the piston tube, allowing for short duration transient measurements. A sketch of the facility is reported in Fig. 2.20a.

Over the years, the OTRF has been provided with different combustor simulator sections, depending on the flow field phenomena that had to be investigated. In 2011, the facility was provided with a lean-burn combustor representative swirl generator. The design process, summarized by Qureshi and Povey [36], led to swirler able to generate maximum pitch and yaw angles of about $\pm 50°$ at the combustor simulator exit, with approximately constant temperature field. Fig. 2.20b, shows a picture of the inlet swirl simulator module. Qureshi et al. [44] carried out an experimental and numerical investigation on this test case aimed at evaluating NGV aerodynamics and heat transfer in the presence of this aggressive swirl. CFD calculations showed

that the swirling structure is divided, by the vane LE, in two vortexes that are convected into the passages and are responsible for the measured non-uniformities in heat transfer and aerodynamic load. Fig. 2.21a, reports secondary flows, calculated by CFD, both 0.25 axial chords downstream the NGV inlet and at the NGV exit plane; it is evident how the vortex has been divided by the LE of vane C1 into a main part, that fills the right passage (pressure side end of C1) and a smaller vortex in the left one. At the exit of the cascade, the main contribution is still recognizable, while only a residual ascending motion is present in the left passage.

The resulting pressure losses (reported in Fig. 2.21b in terms of differences with respect to a uniform inflow case) were enhanced on the suction side hub region of the vane invested by the swirling flow (C1); the downwash of flow on the surface, causing the boundary layer fluid to collect in this area, was found as the cause of this phenomenon. A similar behaviour, with much reduced intensities was detected in the pressure side casing area. The adjacent vane (C2) presented a similar picture, but with reduced magnitude of most of the features. Similar results in terms of pressure losses were found by Jacobi et al. [81], on a can combustor simulator rig, with a correspondent configuration; they attributed the loss core in the suction side region to unsteady structures, generated by the interaction between the pressure pattern of the swirling flow and the potential field of the vane, as they affected the passage and horseshoe vortexes development. An opposite behaviour was

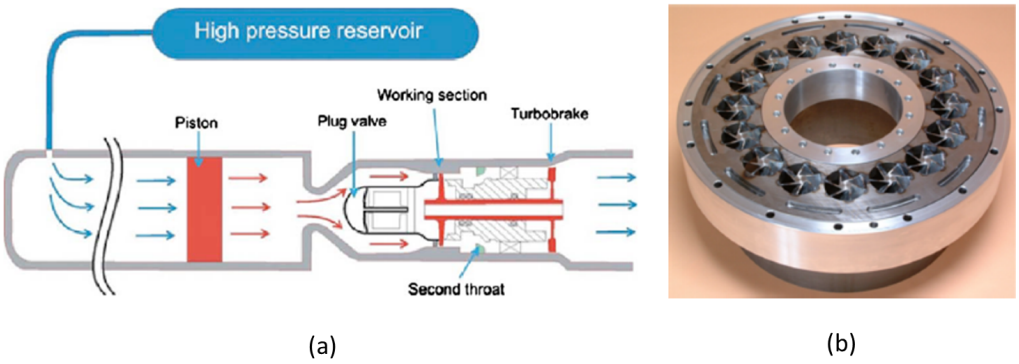

Figure 2.20: OTRF wind tunnel [36] (a) and picture of swirler simulator module (b) [44]

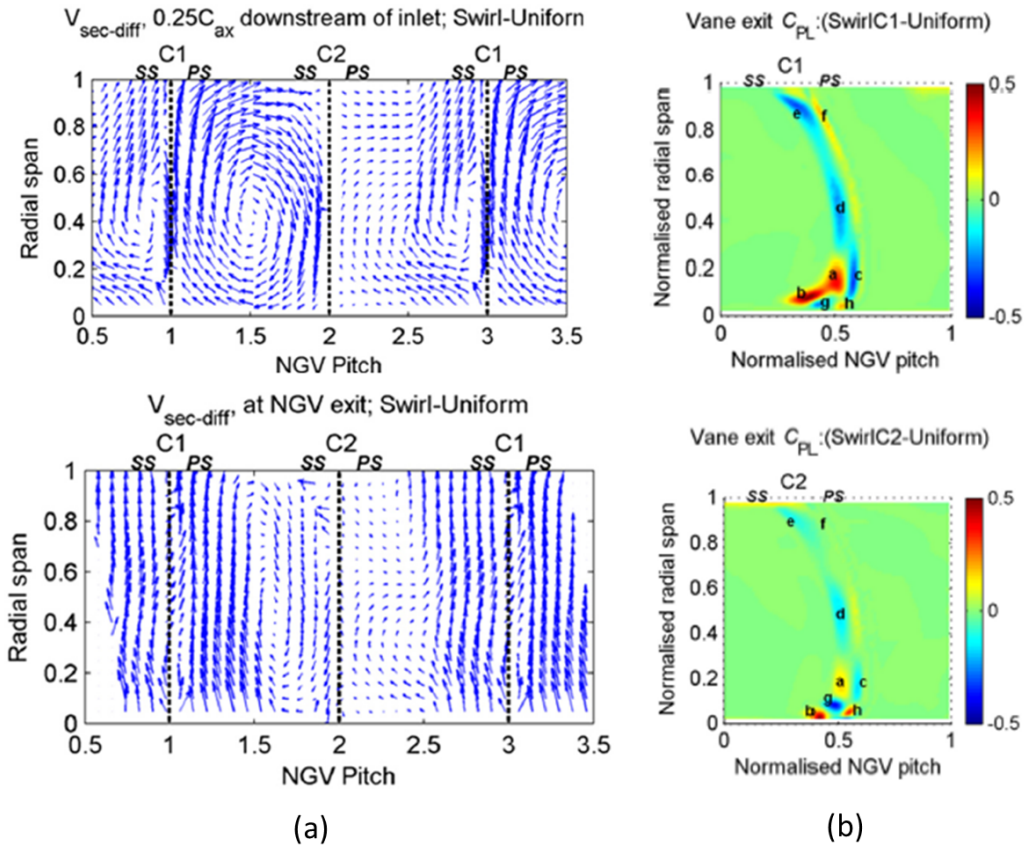

Figure 2.21: Secondary flow evolution (a) and pressure losses (b) measured by [44]

found, on the other hand, by Turrell et al. [82] on a different test case. They validated CFD calculations, with experimental streamline visualization: the swirling structure, colliding with a vane LE, was found to be convected in the passage to the suction side end and migrated towards the low pressure zone close to the hub. The analysis was, anyway, conducted on a can lean-premixed combustor and included features, like the transition duct, that are not present in aero-engine combustors.

To detail the hot streaks effect on the NGV heat transfer, an inlet temperature distortion generator was designed in 2002 by Chana et al. [83]; in 2008 it was upgraded to produce an enhanced and more realistic temperature distortion pattern (*EOTDF generator*) [35]. Both circumferential and radial temperature non-uniformities were created by introducing cold gas

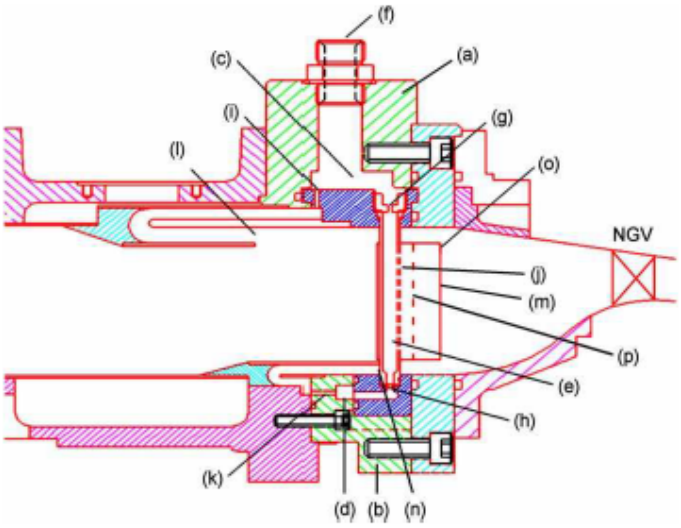

Figure 2.22: Sketch of the EOTDF generator [35]

into the heated mainstream through 32 baffled radial rods and annular slots respectively, as depicted in Fig. 2.22.

The results showed negligible differences in the NGV aerodynamic behaviour due to the introduction of the temperature distortions [84]. On the other hand, the heat transfer, in the form of the measured Nusselt numbers, was much more non-uniform than in the case without EOTDF, mainly due to the changes induced in the gas driving temperature.

In addition to the evaluation of the effect of swirl and hot streaks separately, an attempt of developing a combustor simulator capable of producing a range of engine-realistic swirl and temperature distortion profiles together, with corresponding engine realistic total pressure and turbulence profiles, was carried out. Hall et al. [22] reported the design challenges that were encountered, mainly related to the evaluation of the PVC unsteady behaviour on the resulting flow field (as mentioned in Section 2.1). As stated by the authors, particular attention must be paid to the design of combustor simulators with strong swirl and temperature distortion, since unsteady phenomena that are stabilized by the combustion process in the real application, can heavily alter the achieved overall flow field; therefore it is not possible to adopt systems which are geometrically similar to those for reacting combustor flows. The

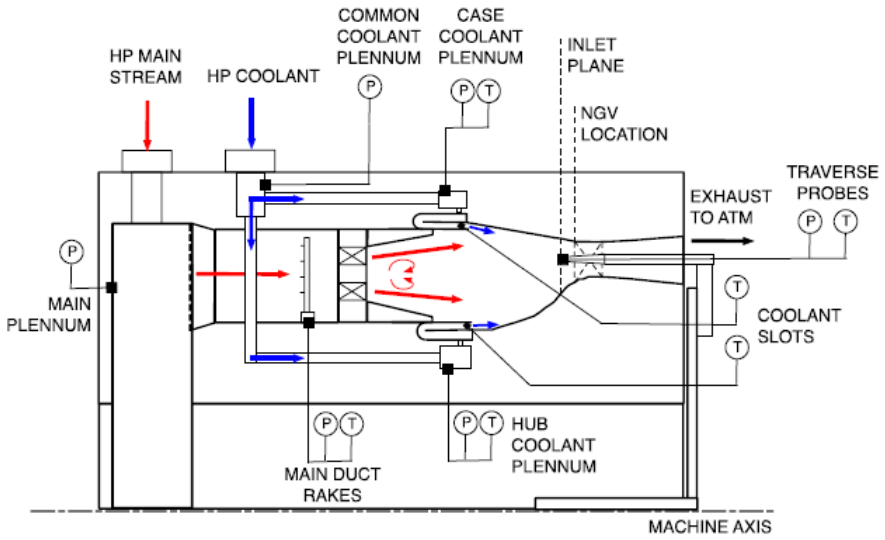

Figure 2.23: Sectional view of the combustor simulator [85]

developed combustor simulator geometry was made by axial swirlers with diffuser ducts, fed by heated mainstream, and annular slots for the coolant at nearly ambient temperature, in order to create radial temperature distortion. An axial jet on the swirler axis was adopted to damp the PVC. Fig. 2.23 shows a section of the combustor simulator.

CFD calculation on the actual combustor simulator geometry [85] showed that PVC was not properly damped, but still the overall flow field was characterized by the presence of a well-defined vortex and a predominantly radial temperature profile, with coolant concentrated close to the endwalls. The first experimental validations confirmed this conclusions. This investigation is among the firsts of its kind and constitutes a necessary step in the combustor-turbine interaction research, in the view of modern aero-engine behaviour. The developed combustor simulator was later installed in a facility for aerothermal testing [86]. In the authors' knowledge no additional literature is nowadays available regarding the experimental characterization of hot streaks migration in highly swirling flows. From a CFD standpoint, Khanal et al. [87] carried out a study to consider both the above mentioned aspects; they found that residual swirl impresses an important radial migration to the hot spot as it passes through the cascade; the direction of this displacement

strongly depended on the clocking configuration and on the sense of rotation of the swirling flow. In terms of pressure losses, qualitatively similar results to the ones obtained by Schmid et al. [78] (see Fig. 2.18) were achieved. It was also found that they are not affected by the introduction of hot streaks, as the same patterns were revealed by isothermal calculations.

2.4.4 Turbulence measurements

The evaluation of the combustor outflow turbulence intensity is another important aspect, in the view of characterizing the high pressure turbine behaviour. Its impact on the film cooling behaviour and on the hot streaks migration has been referenced in Sections 2.3.2 and 2.4.1 respectively. Several studies have been carried out in the past to highlight other effects related to the turbulence intensity at turbine inlet; in most of them high turbulence levels were generated by means of grids [88]. Among others, Nasir et al. [89] showed that the large scale free-stream turbulence promotes a slightly earlier boundary layer transition on the suction surface; an enhancement in heat transfer, on both suction and pressure sides, was found as well [89, 90].

Therefore, the knowledge of the turbulence intensity and of the unsteady characteristics at combustor-turbine interface is crucial to an adequate nozzle guide vanes design and, at the same time, achieving relevant turbulence levels is necessary in the development of non-reactive combustor simulators. The estimation of the turbulence decay across the NGV is also useful in the view of extending the analysis to the rotor cascade.

Some studies have been carried out on real combustor hardware operated in isothermal conditions [91] or with turbulence generators that resembled combustor liners [92, 93]. These studies showed turbulence intensities at combustor exit between 7 and 30 % [89]. Cha et al. [94] measured the turbulence intensity at the exit of a RQL combustor, operated in isothermal conditions: results showed values up to 35 %, generated by unstable collisions of the opposed, highly penetrating dilution jet flows, as it is possible to note from Fig. 2.24, that reports the measured turbulence intensity contour plot.

Concerning lean combustors the treatment becomes more complicated, due to the issues related to the simulation of swirling flows, that have been

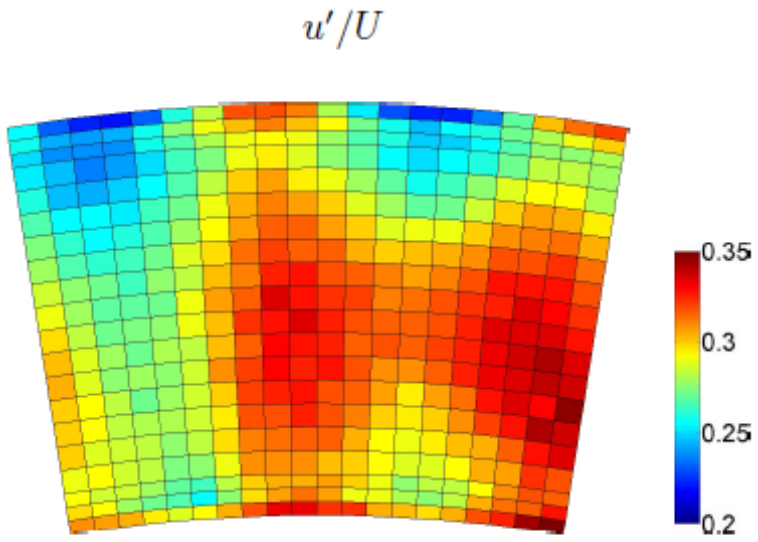

Figure 2.24: Turbulunce intensity measured at the exit of a RQL combustor [94]

detailed in the previous sections. In this kind of combustors, due to the absence of dilution holes, the peak turbulence level is promoted by the highly swirling structure generated by the injector and its maximum should be expected in the core [22]. Due to the highly three-dimensional nature of the flow field, the turbulence intensity measurement in this kind of configurations is very challenging and results can be affected by the adopted measurement technique. Moreover, particular attention must be paid in the view of extending results gathered in non-reactive conditions, to real engine applications. In particular, the combustion process determines a flow acceleration towards the chamber exit and the consequent swirl degree is reduced, with respect to a case without combustion [78]. Therefore, a non-reactive combustor simulator design process must pay attention to account for this effect, not to incur in a relevant overestimation of the swirl degree and, therefore, of the turbulence intensity. Lubbock and Oldfield [95] presented a summary of experimental activities aimed at evaluating the turbulence intensity, in reactive conditions; the review, mainly focus on lean premixed can or can-annular combustors for land based gas turbines, showed that values between 10 and

20% were mostly measured. Concerning aero-engine lean burn combustors, higher degree of swirl are normally expected, due to shorter axial dimension of the combustion chamber. The available literature data is very poor, both for experiments in reactive and non-reactive environments. Hall et al. [22] expected turbulence intensities up to about 25%, from URANS calculation, at the exit of the combustor simulator described at the end of the previous section, similarly to the values measured by Fossen and Bunker [91], for a industrial lean combustor, using a X-wire anemometry probe. Higher levels, up to 45%, were measured by Werschnik et al. [80] (Section 2.4.3), that, though, made use of a single wire probe.

2.5 INSIDE and FACTOR project overview

As stated above, there is currently very little experimental data regarding a turbine operated with realistic lean burn combustor outflow conditions. Therefore, in order to bridge for the lack of data and industrial experience, different research projects have been promoted. Within two of these projects, that are described in the following, the present research was developed.

INSIDE project (*aerothermal INvestigation of cooled Stage turbIne: Design optimization and Experimental analysis*) is a National Interest Project, promoted by the Italian Ministry of Education, Universities and Research ($MIUR$); it is mainly aimed at the investigation of the effects of non uniform outflow conditions from the combustor on the aerodynamic and cooling performance of the turbine high pressure stages. The aerodynamic and thermal characterization of the outflow from the combustor, by means of a detailed analysis of the interactions between the main and coolant flows, is among the most important investigated phenomena. The characterization of the air flow within a high pressure turbine stage for the study of stator-rotor interactions relatively to the propagation of hot and cold spots generated inside the combustor plays a big role as well. The research is part of the wider international, European in particular, research and development

project framework in which the various units are already collaborating or being proposed to participate in the next future. The opportunities offered by INSIDE project cover a strategic part guaranteeing the development of essential infrastructures and knowledge to play a constructive role at a European and international level.

Within this same project framework, the European project *FACTOR* [1] (Full Aerothermal Combustor-Turbine interactiOn Research) has been promoted. A new experimental facility has been developed, within the project, at DLR (*Deutsches Zentrum fur Luft- und Raumfahrt* - Gottingen, Germany). The research center hosts a modern aero-engine combustor simulator and a 1.5 high pressure turbine stage (one stage plus a strut module), operating at realistic Reynolds and Mach numbers. A sketch of it is reported in Fig. 2.25.

The main objective of the project is to carry out measurements, by means of the most advanced techniques, on this infrastructure, in order to create a wide database to set up boundary conditions and make comparisons with

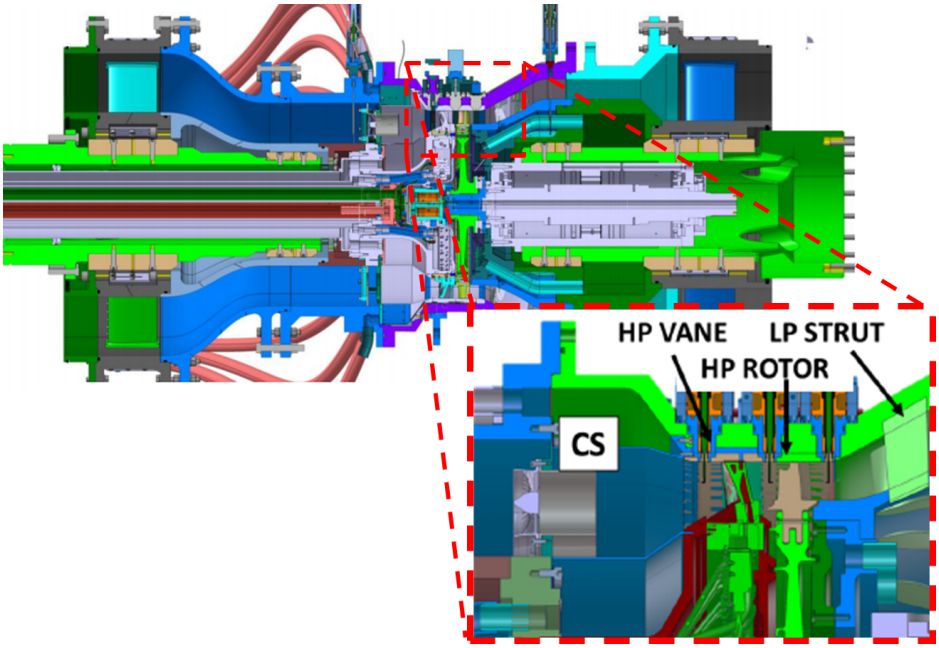

Figure 2.25: Sectional view of the FACTOR full annular rig

[1] http://www.factor-fp7.eu/

conventional and advanced CFD techniques dedicated to the modeling of this interface area, similarly to what is pursued by INSIDE project. A large test campaign has been scheduled in order to provide for a deep improvement in the knowledge of this complex system, through a massive investigation. Probe traversing will be carried out to measure velocity, pressure and temperature at several axial positions, as well as Raman spectrography, for the measurement of gas temperature, and IR thermography, to evaluate surface temperatures, adiabatic effectiveness and heat transfer coefficient on vanes, blades and on the strut. An initial planning of the experimental campaign can be found in the summary of Battisti et al. [96], even if it has been subjected to some change over the course of the project due to challenges related to instrumentation integration and time constraints. The experimental campaign is scheduled to be completed by the end of 2017.

2.5.1 Thesis outline and motivation

Within the described framework, the research carried out within this Ph.D. course was aimed at providing experimental data to deepen the knowledge of the combustor-turbine interface behaviour in modern aero-enignes. A three-sector combustor simulator was installed at the *THT Lab* of the University of Florence; it was designed in order to be able to replicate the most important flow structures and mixing phenomena that occur inside a modern lean burn combustor and, therefore, achieve an engine representative combustor outflow. In particular, the capability to simulate both the presence of enhanced temperature distortions and an aggressive swirl field was pursued, in the view of investigating their combined effects on the high pressure turbine and covering an aspect where a lack of literature data exists.

In a previous Ph.D. course [97], the overall aerothermal field at combustor exit had been measured, by means of a five hole probe campaign, for different geometries of the injectors module, in order to validate the test rig design and make some preliminary choices about its configuration. In the first part of the present activity, then, PIV measurements were exploited to characterize the flow field inside the chamber, which was made possible by the rig three-sector configuration, and to assess its effective capabilities

of meeting the mentioned requirements and flow features. In the second part of the work, the test rig was upgraded, in order to make it capable to host a film-cooled NGV module. The aerothermal field characterization was repeated at combustor exit, to double check the previous results; the same measurements were also taken at NGV exit in order to evaluate the hot streaks migration and the pressure losses through the cascade. Turbulence measurements at NGV inlet and exit planes were also carried out to characterize the turbulence decay across the vanes. Furthermore, adiabatic effectiveness measurements were performed on the vanes surface, in order to assess the impact of an aggressive inlet degree of swirl on the film cooling behaviour. Due to constraints related to the experimental techniques, adiabatic effectiveness and turbulence measurements had to be carried out in isothermal cold conditions, so the effect of temperature distortion could not be taken into account. Details of the test matrix and of the operating conditions will be provided in the following.

Summarizing, this work of thesis has been divided into three main tasks:

- Characterization of the flow field inside the combustor simulator
- Design of the upgraded test rig with the NGV module
- Characterization of the NGV module: this last task can be additionally divided in the repetition of measurements at combustor exit and the measurements at NGV exit and on the cascade airfoils

The first task and the first part of the last one provide the present research with an accurate characterization of all the boundary conditions required for the pursued investigation. All the results coming from the investigation of the combustor simulator and of its exit plane will be described in Chapter 6, either they were collected in the presence of the NGV cascade (i.e. five hole probe and hot wire measurements) or before the test rig upgrade (i.e. PIV measurements). Chapter 7 will be dedicated to the description of the results collected on the NGV exit plane and on the airfoils.

The present research is aimed at contributing to the field of combustor-turbine interaction investigation for modern aero-engines, as it tries to help

filling some voids that are currently present in the literature and in the industrial knowledge. Firstly, it provides some insights of the effects of a highly swirling combustor outflow on the high-pressure nozzle guide vane aerodynamics, integrating some existing researches with particular attention to the film-cooling behaviour. Moreover it reports a characterization of the turbulence intensity, promoted by this kind of flow fields, at the high-pressure turbine inlet and its decay through the nozzle guide vane to the rotor inlet plane; a very reduced number of works with this goal have been carried out in recent years and an important uncertainty still exists. Finally, this work constitutes one of the first attempts to characterize the combustor-turbine interface in the presence of both enhanced temperature distortions and high degree of swirl, as typical features of modern lean burn aero-engine combustors. In this way, indications to be used for the design of the first stage nozzle guide vane are provided. Information regarding the flow features approaching the rotor can be also found.

A substantial difference from the present treatment and most of the previous works, reported in literature, must be also highlighted here: most of them were focused on the evaluation of the differences induced by a particular aspect, such as enhanced swirl or temperature distortions, with respect to a traditional case with uniform turbine inflow; an investigation of both configurations and a direct comparison are generally exploited to improve the design criteria. On the other hand, the intention here is to consider most of these aspects together and describe the outcoming behaviour of a NGV cascade designed for this specific inflow: since traditional design criteria make use of tangential-wise averaged quantities, as inlet boundary conditions, local inaccuracies can be expected where highly non-uniform flow fields are considered. Flow features and phenomena will be described, in order to highlight where relevant issues can arise and where further effort must be paid in the design process. Nevertheless some comparison with the common behaviour expected for a traditional uniform-inflow case will be sometimes provided, in order to highlight where the outcome is particularly different.

Thanks to a wide experimental campaign, addressing all these mentioned aspects, this work tries to provide useful data to help in the process of an

integrated design of the combustor and of the high pressure turbine module. The campaign also provides experimental data in a CFD-friendly domain that numerical codes can be compared against, in order to understand the characteristics that these kinds of unsteady flow fields necessitate in terms of numerical modelling.

Chapter 3

Experimental Apparatus and Operating Conditions

Contents

3.1 Test rig overview

According to what was described in the lat section of the previous chapter and to the goals of this Ph.D. work, two test rig configurations were exploited. In the first part of the work, a test rig representing a three-sector combustor simulator was experimentally characterized; a big effort was later put in upgrading the test rig, in order to add a NGV module at its exit, in order to investigate the effects of the measured combustor outflow on the NGV performance and its modification through the cascade. Fig. 3.1 reports

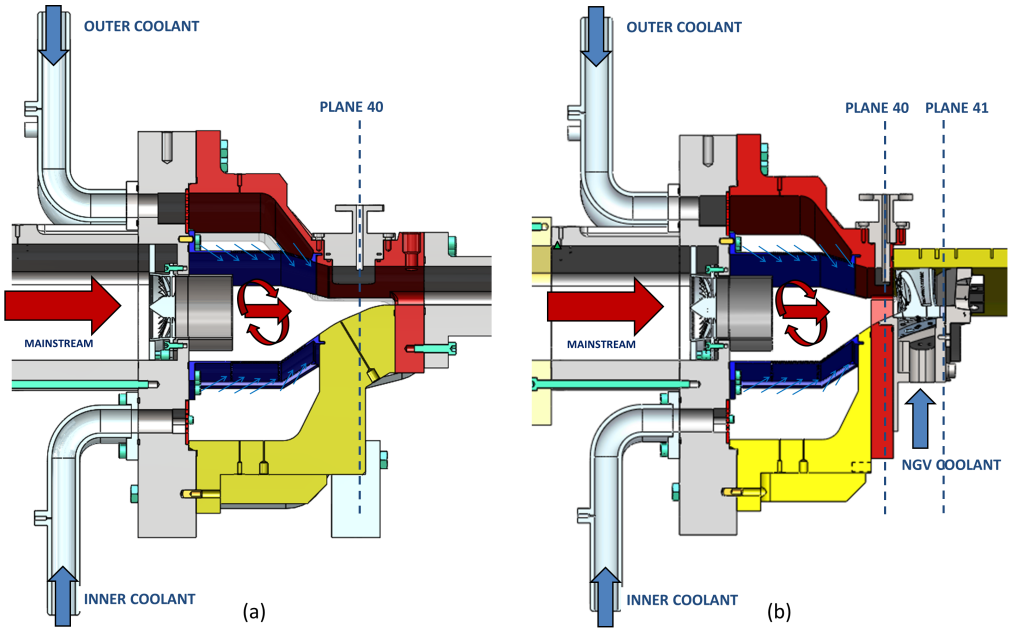

Figure 3.1: Sectional view of the first (a) and second (b) condifurations of the test apparatus

sectional views of the two test rig configurations.

Focusing on the first configuration, a heated mainstream flow reaches a plenum chamber, that has the goal to slow down the flow and damp possible non-uniformities, before getting in the combustion chamber though three axial swirlers. Two separate coolant flows, at ambient temperature, on the other hand, reach two annular (inner and outer) coolant cavities, through three pipes each; from these cavities, that plays the part of plenum chambers, the cooling flows feed the inner and the outer laser-drilled multi-perforated liners, reaching the combustion chamber. The combination between the hot swirling mainstream and the cold liner coolant allows to achieve the desired aerothermal field at combustor exit, after an important annulus contraction, with a consequent flow acceleration towards the virtual NGV position is encountered. Red arrows, in the figure, shows the path of the heated mainstream, while blue ones represent the liner cooling flows. After the combustor exit plane, the test rig is provided with an axial exit duct that leads the exhaust flow to the stack.

Figure 3.2: Picture of the test rigs installed in the test cell: first (left) and second (right) configurations

In the second configuration (Fig. 3.1b), the combustor simulator geometry was left unaltered, despite the inner and the outer casing components (yellow and red components in both pictures) were substituted to create space for the NGV module: the grey component in the figure is used to host the NGV airfoils; it is also provided with a plenum chamber, to feed the film-cooling flow to the cooled NGVs, as indicated by the blue arrow. The yellow component, on the other hand, constitutes the outer casing and hosts the instrumentation accesses for probes traversing, on the NGV exit plane. The outlet component, an annular, right-turning duct, was designed in order to follow the NGV exit flow direction and comes out of the sectional plane reported in the figure; its shape can be appreciated in Fig. 3.2, where pictures of both test rig configurations, installed in the test cell, are reported. As it is clear from the pictures, the main difference in their layout stays in the geometry of the exit ducts. Figs. 3.1 also show the positions of the measurement planes at combustor exit and at NGV exit, Plane 40 and 41 respectively. Their exact position in terms of distance from NGV leading edge and trailing edge will be provided in Section 3.3.

The main characteristics of both the components investigated in this

Ph.D. course (i.e. the combustor simulator and the NGV airfoils) have been developed within the European Project FACTOR. Each module of the rig was designed following the trend of development for modern aero-engines, in terms of liner coolant-mainstream air flow split in the combustion chamber, aggressive swirl and distorted temperature profiles at combustor exit and engine representative film cooling system on the vanes. As anticipated in the final part of the previous chapter, the work carried out within this Ph.D. course has been divided into three main parts: the first of them is completely focused on the combustor simulator, while for the final, the attention is shifted to the NGV module. According to this division, in this chapter a thorough description of the two modules will be provided separately. In the next section, the main characteristics and particular features of the combustor simulator module will be accurately described; some additional details of the first configuration of the test rig will be provided as well. In the same way, in the later section, an accurate description of the NGV profile and of its cooling system will be reported.

The whole next chapter (Chapter 4) will be dedicated to a detailed description of the work aimed at upgrading the combustor simulator test rig, in order to integrate the two modules together, since it was one of the main part of this work: an exhaustive account of the design process and of the choices made to get the desired rig layout and instrumentation accesses will be provided. Moreover a whole view of the final test rig configuration, which was the object of most of the measurements carried out within this Ph.D. course, will be found.

3.1.1 Combustor simulator

Starting from the specifications of the full annular combustor simulator of the FACTOR project DLR rig, the three sector one, installed at THT lab, was designed; its design was carried out by *Turbomeca* [1] and *Avio Aero* [2], as industrial pertners of the project, in order to precisely mimic a recent lean burn engine configuration, to capture all physical scales at the combustor-

[1] http://www.turbomeca.com/

[2] http://www.avioaero.com

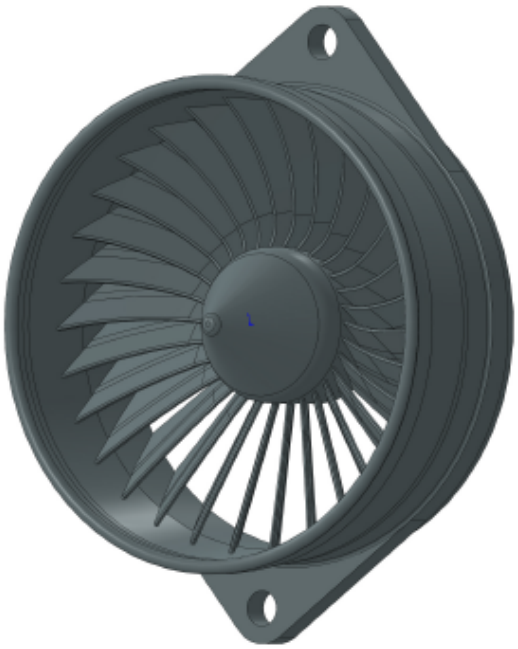

Figure 3.3: CAD model of the axial swirler

turbine interface. To ease the operability and to allow the use of different measurement techniques, no combustion is enforced in the chamber and the temperature profile is obtained only by mixing hot and cold air streams. As anticipated, a targeted temperature profile is pursued by mixing two different air flows: cold air is issued at ambient temperature, to feed the effusion cooled inner and outer liners while the mainstream, that passes thourgh the swirlers, is previously heated up to 531K. The axial swirlers, depicted in Fig. 3.3, contain 30 flat vanes disposed around a central hub, They were designed by Aero Avio in order to create a representative flow field in the chamber, without the effect of combustion and reach the target flow field and temperature patterns at combustor exit; a swirl number of 0.7 (definition of Beer and N.A.Chigier [20], see Section 2.1) is pursued according to design goals. They were manufactured with a Direct Metal Laser Sintering ($DMLS$) Rapid Manufacturing process.

The inner and outer liners are multiperforated with different patterns of effusion holes, aligned with the streamwise direction (no compound angle) in

a staggered configuration; the nominal characteristics of each patch, two for each liner, are summarized in Table 3.1. The geometry of the chamber is not scaled with respect to a real engine (1:1 scale).

Table 3.1: Main features of the different patches of effusion cooling

Patch	**d [mm]**	**L/d [-]**	α **[deg]**	S_x/d **[-]**	S_y/d **[-]**	**Porosity [%]**
MP Ext1	0.5	3.5	30	3.8	2.0	6.69
MP Ext2	0.5	2.0	60	4.0	2.0	5.74
MP Int1	0.5	3.5	30	4.8	2.0	8.31
MP Int2	0.5	2.0	60	3.2	2.0	5.20

Combustor simulator key features are representative of a lean burn technology:

- a flow split with 65% of air mass flow going through the swirlers and 35% used for liner cooling;
- liners are provided with an effusion cooling system, and no dilution holes are inserted;
- the inner liner is strongly convergent towards the final part of the chamber, with an angle of 35° (with respect to the horizontal axis)

The three sector configuration was chosen in order to make the central sector flow field, target of all the measurements, less sensitive to the presence of the rig lateral walls. The same configuration has been used in several works such as the ones carried out by Andreini et al. [98], Wurm et al. [99] and Meier et al. [100]. The results of preliminary CFD evaluations to verify this assumption can be found in the work of Koupper et al. [101].
Fig. 3.4 reports a scheme of one sector of the combustion chamber; the nomenclature used for the multperforated liners patches is the same used in Table 3.1. It also indicates the position of *Plane 40*, that represents the nominal chamber exit plane and it's the main focus of the combustor simulator experimental chracterization.

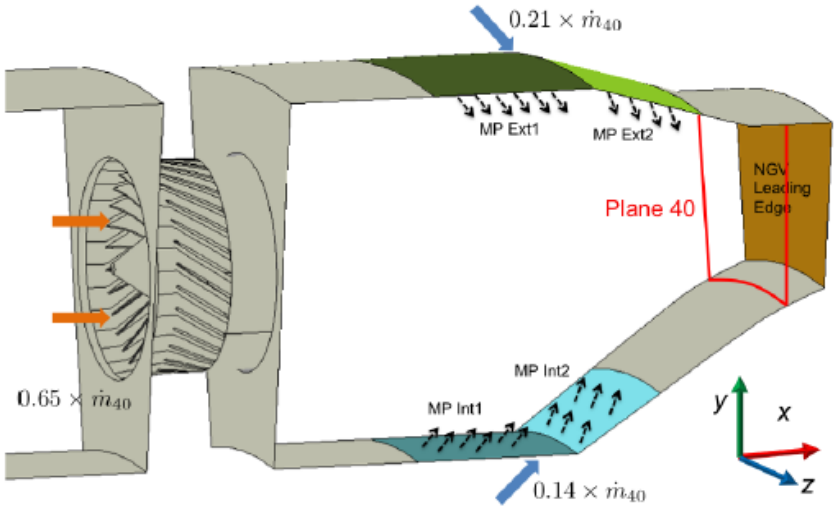

Figure 3.4: Sketch of the combustor simulator chamber

Fig. 3.5 shows a CAD model of the three-sector combustor simulator: different colours indicate the different components that are assembled in the rig, like the outer (red) and inner (yellow) casings, provided with the coolant feeding pipes (light grey), the inner and outer shaped liners, provided with

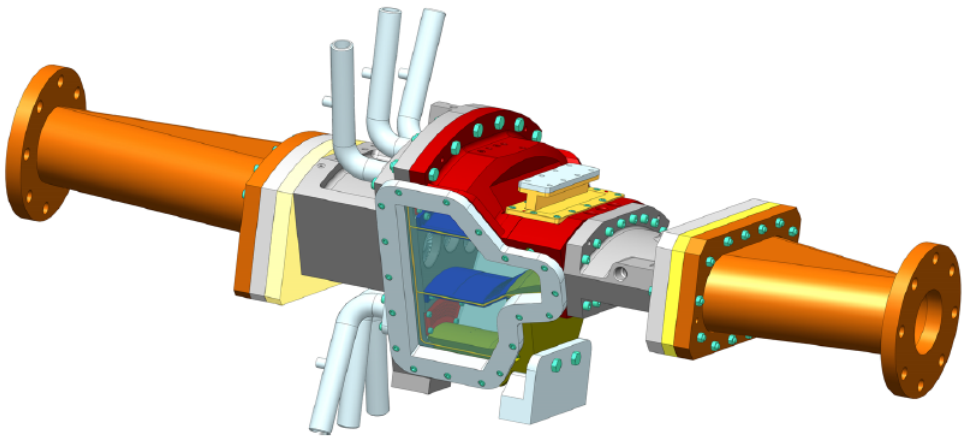

Figure 3.5: CAD model of the test rig

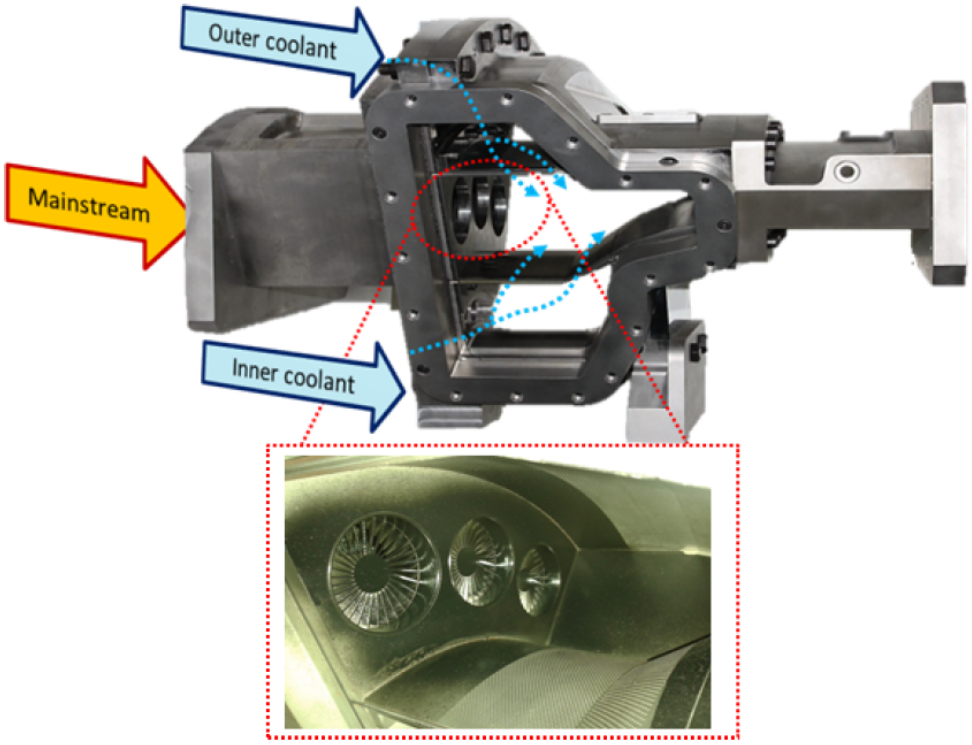

Figure 3.6: Picture of the combustor simulator

laser-drilled effusion holes (blue), and the inlet and outlet ducts (orange) that connect the annular sector to the cylindrical pipes coming from the compressors and going towards to the stack. An adaptive flange is located on Plane 40, to install the automatic traverse system, that was used for the probes handling. In order to perform optical measurements, such as Particle Image Velocimetry (PIV), the test rig includes two wide lateral pyrex windows, located at sides of the combustor simulator, that can be substituted with metal ones, as shown in Fig. 3.5. Fig. 3.6 shows a picture of the combustor simulator, together with a scheme of the different flows at its inlet and a focus on the swirlers and on the inner effusion cooled liner. In order to match the main goal of the combustor simulator, to generate a rapresentative flow field on Plane 40, ducts of 35, 45 or 55mm length (about 22, 29 and 35% of the total chamber axial extension) can be installed on the

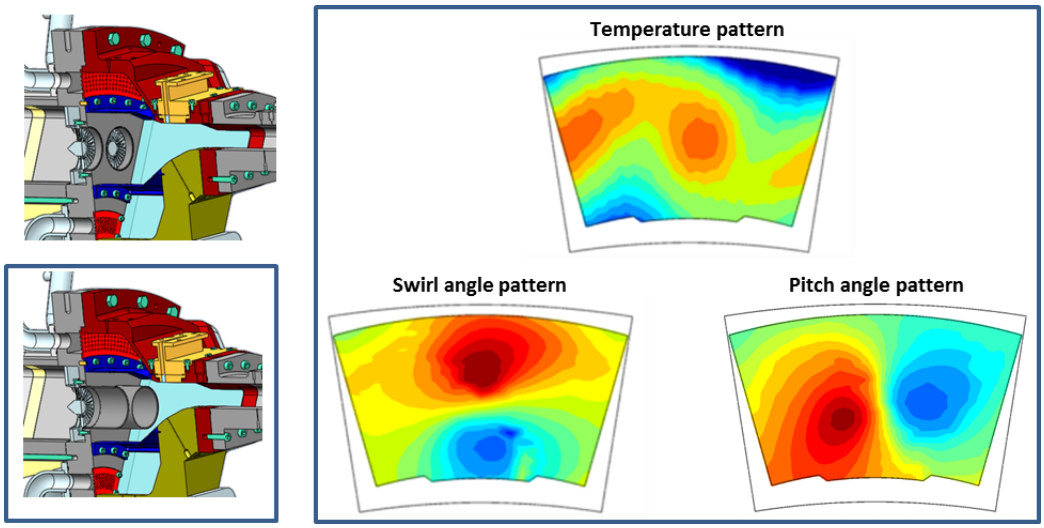

Figure 3.7: Temperature pattern and flow angles measured on Plane 40 [102]

swirlers, Doing so, the heated swirling mainflow is preserved from interaction with the cooling flows, Moreover the swirler structure opening, that occurs as the mainflow enters the combustion chamber, with consequent loss of tangential momentum, is delayed, with an effect that is comparable to the one of a shorter combustion chamber. The left pictures in Fig. 3.7 show the difference from non-ducted (top) and ducted (bottom) configurations. At the end of the preliminary experimental validation, carried out by means of five hole probe measurements on Plane 40, whose results can be found in the works of Caciolli [97] and Bacci et al. [102], the configuration with the 55mm ducts was chosen. It allowed to achieve a representative flow field at combustor exit, as it is reported in Fig. 3.7, in terms of temperature pattern and flow angles contours. Flow angles beyond $\pm 50°$, where achieved in a well-defined rotating structure. Details on the combustor exit flow, from the measurements that have been carried out within the present work after the upgrade of the test rig with the NGV cascade, will be provided in Chapter 6.

3.1.2 Nozzle Guide Vane module

The aerodynamic design of the investigated nozzle guide vane and its cooling scheme definition was carried out by Rolls Royce [3] as industrial partner of FACTOR project. The results coming from the preliminary Plane 40 investigation [97, 102] were used as input. A CAD model of the NGV airfoil is reported in Fig. 3.8: the tip is at a constant radius of 280mm, while the first part of the inner endwall has an increasing radius, to match with the converging shape of the inner liner, up to a 240 mm constant value in the final part. As it will be detailed in Chapter 4, a NGV-to-swirler count ratio of 2 was used, in order to provide a CFD-friendly domain; one NGV has its leading edge aligned with the swirler axis, while the adjacent one is clocked halfway between two swirlers. An aspect ratio (H/C_{ax}) of 1.04 and a pitch-chord ratio (S/C_{ax}) of 1.06 are achieved, considering the constant-height part of the NGV. According to preliminary evaluations and CFD calculations, carried out for the design of the test rig (Chapter 4), an exit Mach number of about 0.75, in the case without film cooling flow, is expected; the NGV exit flow angle is about 74°, even it is not completely constant through the airfoil height.

Fig. 3.9 shows the film cooling scheme characteristics of the NGV: it is made by 8 rows of cylindrical film cooling holes; four of them (SS1-3 and PS1 in the figure) are shower head rows, close to the leading edge position. The remaining four rows (PS2-5) are positioned on the pressure side, while no holes are present on the suction side far from the leading edge. The holes positioning and inclination was defined in order to adapt to the expected flow field at NGV inlet and, therefore, to the expected stagnation line position, reported in the figure. The tangentially averaged flow field at combustor exit was used for the design process, so relevant differences can be expected in the film cooling behaviour between the airfoils aligned with the swirlers and the adjacent ones. Table 3.2 summarize the geometric characteristics and the expected blowing ratios and momentum ratios of the different rows, in the nominal case of a 7.5% coolant-to-mainstream mass flow ratio. The NGV is

[3] www.rolls-royce.com

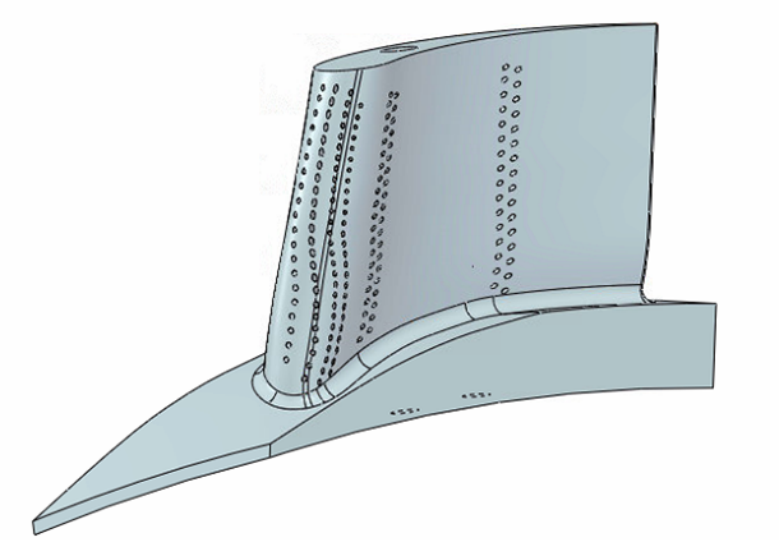

Figure 3.8: NGV 3D model

provided with a total of 171 holes. The values of BR of rows PS1 and SS1 should not be taken into account because these regions are expected to be characterized by very low velocities and therefore very high BR; the remaining rows are characterized by BR below or equal to 2. Moreover the values of velocity ratios and the penetration regime VR threshold values, according to L'Ecuyer and Soechting [54] (i.e. flat plate configuration), is reported (evaluated with Eq. 2.8, depending on the angle of injection). Despite VR is generally higher than the evaluated threshold, these values have been considered low enough to guarantee that the cooling flow would remain attached to the NGV surface. All the film cooling rows are fed by two cavities, inside the airfoils, large enough to act as plenum chambers (no significant cross flow velocity); rows SS1-3 and PS1-3 are fed by the LE plenum, while rows PS4-5 are fed by the TE plenum, as reported in Fig. 3.9. Both chambers are fed by a common plenum chamber in order to guarantee the same inlet total pressure.

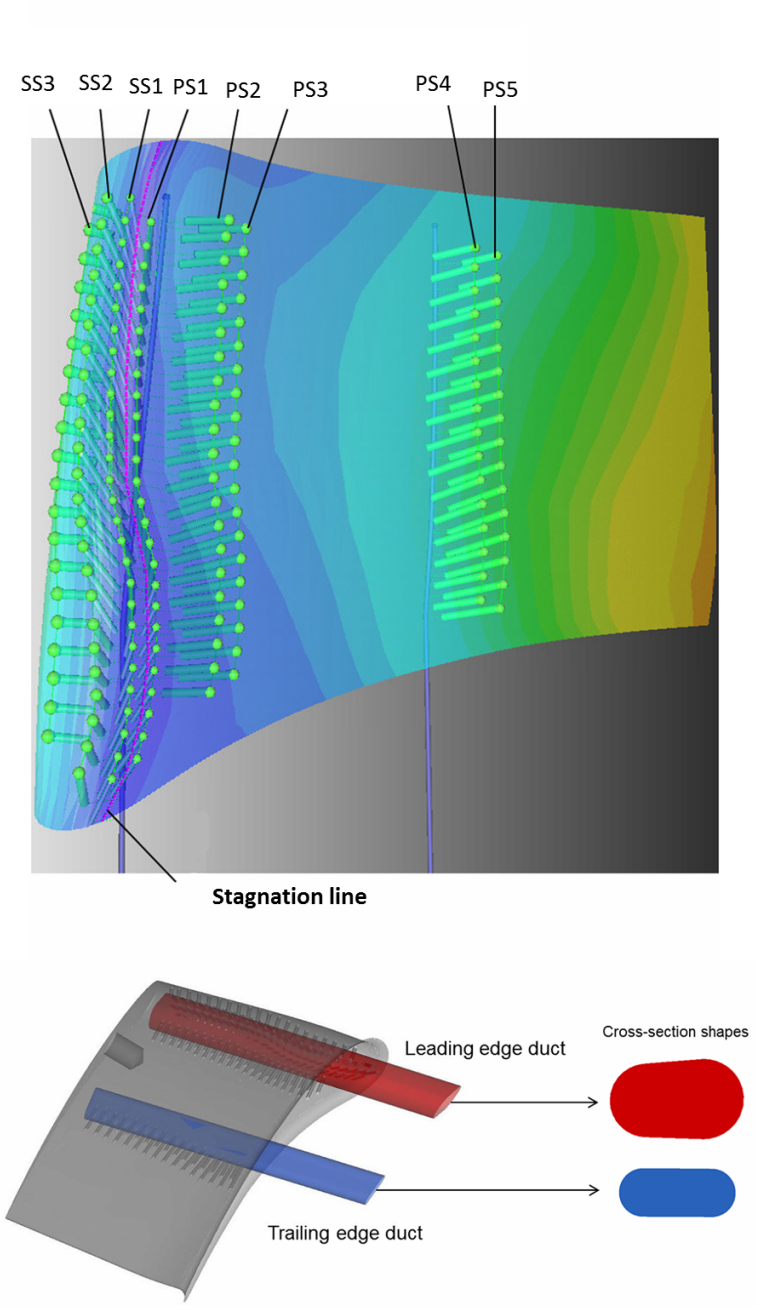

Figure 3.9: NGV film cooling scheme

3.1.3 Test rig environment and instrumentation

The combustor simulator is installed in the warm test cell of the University of Florence *THT Lab*, dedicated to long-duration, steady-state warm tests. The facility layout, adopted for the test campaign without NGV module, is reported in Fig. 3.10a: compressed air, discharged by two screw compressors, crosses an air dryer used to cool down the flow to room temperature and to remove the humidity. The mass flow rates of the three lines, one for the mainflow and two for the coolant cavities, can be independently set by regulating three automatic globe valves (1,2,3); a further Vee-Ball^{TM} valve at the test section exit (4) allows to control the combustion chamber pressure (i.e. Mach number). During the tests, valves are automatically driven through a PID control system to keep constant operating conditions, in terms of mass flow rates and pressure drops across swirlers and effusion perforation. The screw compressors are equipped with an automatic modulating valve to keep constant the air delivery pressure close to 7 bar. Along the line a $2m^3$ vessel damps pressure fluctuations. The mainstream mass flow passes through a 600 kW electric heater, which increases its temperature to the target value: a dedicated switch board with control system regulates the electric power in order to set a constant temperature at the inlet of the test rig. Coolant is delivered to the rig through two separated lines, as mentioned above: each line discharges air in a plenum, which is connected with the test article annular cavities through three pipes (see Fig. 3.5).

	SS1	**SS2**	**SS3**	**PS1**	**PS2**	**PS3**	**PS4**	**PS5**
Number of films	28.0	24.0	20.0	26.0	21.0	20.0	16.0	16.0
Diameter [mm]	0.5	0.7	0.8	0.5	0.7	0.7	0.7	0.7
Mean length [mm]	3.8	3.8	2.3	3.1	3.6	4.2	4.1	4.7
L/d [-]	7.5	5.4	2.8	6.2	5.2	5.9	5.9	6.7
Surface angle [deg]	86.0	80.0	70.0	86.0	45.0	45.0	42.0	37.0
Radial angle [deg]	50.0	50.0	5.0	50.0	10.0	10.0	15.0	15.0
Blowing ratio [-]	6.3	2.0	1.2	7.9	2.0	1.9	0.9	0.9
Momentum ratio [-]	33.7	2.8	1.0	51.9	2.8	2.4	0.5	0.5
Velocity ratio [-]	5.17	1.38	0.81	6.33	1.34	1.25	0.60	0.61
Penetration regime VR treshold [-]	0.46	0.47	0.49	0.46	0.65	0.65	0.70	0.78

Table 3.2: Film cooling parameters estimated at nominal conditions

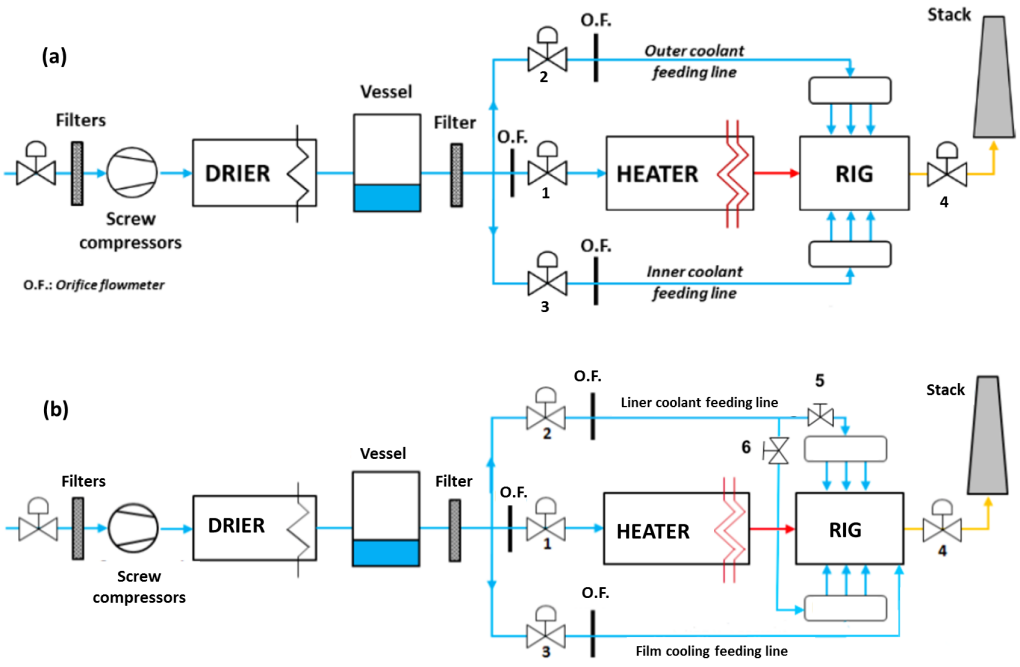

Figure 3.10: Scheme of the experimental facility for the two test rig configurations

For the second test campaign, on the upgraded test rig, the test facility configuration has been slightly changed, in order to provide a coolant line for the NGV cooling system: the new layout is reported in Fig. 3.10b. One of the coolant lines feeds both inner and liner cooling flows: the correct flow split is achieved by means of two manual valves (5 and 6 in the figure) and monitoring the pressure level in the coolant cavities. The remaining line directly feeds the NGV coolant cavity.

The test rig was equipped with several static pressure taps and thermocouples. In the following, the monitoring instrumentation of the second test rig configuration will be described; anyway, as no change in the combustion chamber instrumentation were enforced, between the two configurations, it can be also used to describe the first one, as long as the only combustor simulator module is considered. A custom-tailored *Labview*®-based application, in-house developeded, provided accurate monitoring and recording of the conventional data from measurement data scanners. A pressure scanner

NetScannerTM System 9116 with temperature compensated piezoresistive relative pressure sensors is employed to measure static pressure in different locations inside the rig; the maximum uncertainty is ±52 Pa with a level of confidence of 95%. A $HP/Agilent^{®}$ 34972A data acquisition/switch unit is used to monitor the flow temperature measured by means of several T-type thermocouples (±0.5 K uncertainty, 95%level of confidence). In addition, two thermocouples are welded on each liner and further three of them are located inside the metal, close to the location of Plane 40. Metal temperatures are also used to assess when the thermal steady state conditions are reached. Mass flow rates were measured by means of calibrated orifices; they are affected by an error of 2-3% according to the standard ANSI/ASME PTC 19.1 [103] based on the Kline and McClintock method [104]. Fig. 3.11 shows the positions of the monitoring probes inside the test rig, as also summarized in Table 3.3. Subscripts ctr, dx and sx indicates azimuthal positions of 0° and ±18° respectively. Pressure taps P_{out1}, P_{out2} and P_{out3}, placed in the outlet duct, downstream the NGV cascade, and used to check the pressure ratio across the cascade, are not reported in the figure.

3.2 Operative conditions

The test rig nominal operating point has been established in order to match the most important non-dimensional parameters, that control the behaviour of mainstream and cooling flows, at engine representative values. For the sake of clarity, it must be underlined that, throughout all the treatment, the word *mainstream* will refer to the mass flow passing through the swirlers, when the focus is the investigation of the combustion chamber, while it refers to the total mass flow at combustor exit (i.e. swirler mass flow and liner cooling flows), when the focus is shifted to the NGV cascade.

The parameters chosen to describe the physics of the flow in the combustor simulator are mainstream and liner cooling flows Reynolds numbers (Re_M, Re_1 and Re_2) and mainstream Mach number at swirler exit (M_M); Mainstream values are calculated on the swirler section, using its diameter as characteristic length. Moreover, the multiperforated plates can be

Table 3.3: Test rig monitoring probes

Pressure tap ID	**Position**
P_{Mctr}, P_{Mdx}, P_{Msx}	Mainstream, upstream swirlers
P_{COPctr}, P_{COPdx}, P_{COPsx}	Outer coolant feeding pipes
P_{CIPctr}, P_{CIPdx}, P_{CIPsx}	Inner coolant feeding pipes
P_{COctr}, P_{COdx}	Outer coolant cavity
P_{CIctr}, P_{CIdx}	Inner coolant cavity
P_{cool}	NGV coolant plenum
P_{40}	Plane 40
P_{out1}, P_{out2}, P_{out3}	Outlet duct, downstream NGV
Thermocouple ID	**Position**
T_{Mctr}, T_{Mdx}, T_{Msx}	Mainstream, upstream swirlers
T_{COctr}	Outer coolant cavity
$T_{O,lin}$	Outer liner, metal temperature
$T_{I,lin}$	Inner liner, metal temperature
T_{CIctr}	Outer coolant cavity
$T_{cool,dx}$, $T_{cool,sx}$	NGV coolant plenum
T_{40}	Plane 40, metal temperature

characterized by the blowing ratios $BR_i = (\rho_i V_i)/(\rho_M V_M)$ and by momentum flux ratios $I_i = (\rho_i V_i^2)/(\rho_M V_M^2)$. Pressure drops across swirlers and liners (defined as $(P_{0,upstream} - P_{s,downstream})/P_{0,upstream}$) are equal to ≈3.5 and ≈5% respectively, in design point conditions. A main-to-coolant temperature ratio of 1.77 is achieved by heating the mainflow up to 531 K and keeping the liner coolant at ambient temperature. Concerning the NGV investigation, Reynolds and Mach number on Plane 40, Re_{40} M_{40}, must be considered among the parameters of interest and, consequently, the Mach number at NGV exit, M_{41}. Plane 40 quantities are averaged values, evaluated by through-flow calculation, knowing the annulus passage area, the mass flow rate and static pressure and temperature. During the tests, conditions are set in terms of mass flow rates and temperatures of the three flows, and combustion chamber pressure, regulated by acting on the back-pressure

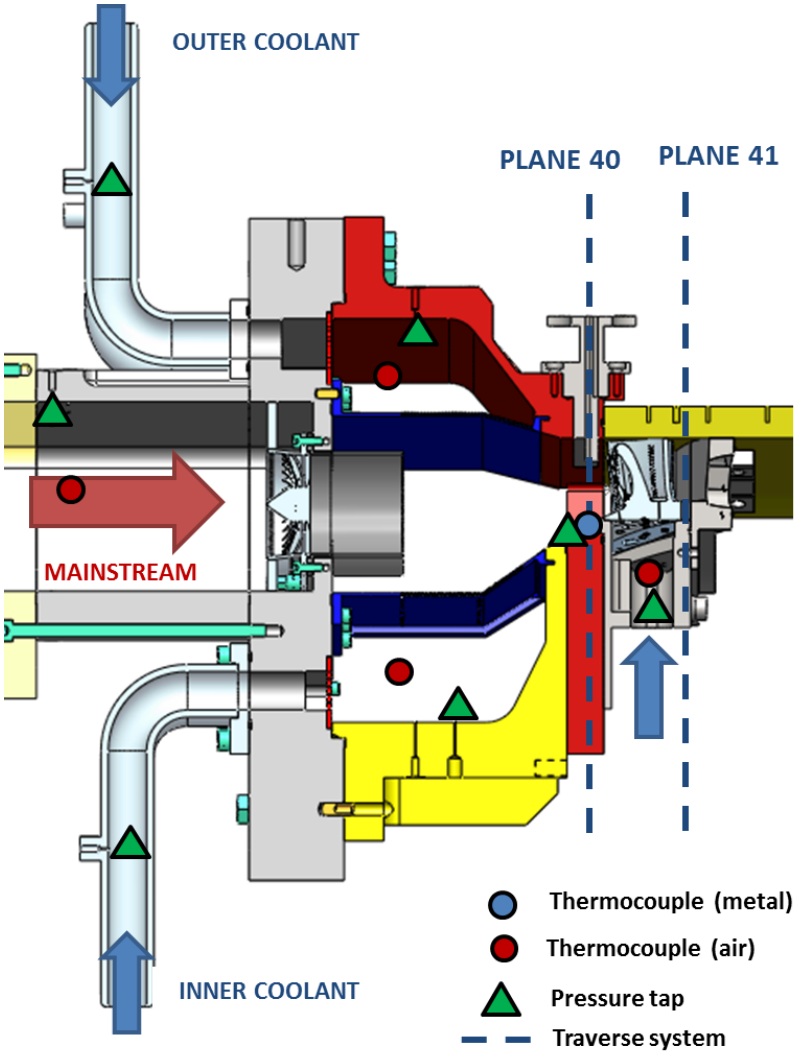

Figure 3.11: Monitoring probes positions

valve and monitored through the Plane 40 pressure tap (Table 3.3). Plane 41 Mach number was evaluated, through preliminary CFD evaluations (see Chapter 4), as average value. The average temperature ratio (i.e. coolant-to-mainstream density ratio) for the NGV film cooling system is about 1.5, since the average temperature on Plane 40 is 450 K; its local value is variable depending on the temperature gradients achieved in the combustor outflow. For the nominal operating point the NGV coolant mass flow rate is 7.5%

Total chamber mass flow (per sector)	0.24 kg/s
Flow split: swirlers	65%
Flow split: liners	35%
W (film cooling mass flow / mainstream mass flow)	7.5%
Chamber pressure	148 kPa
Swirlers inlet temperature	531 K
Liner coolant temperature	300 K
NGV coolant temperature	300 K
Swirler Reynolds number	111000
Swirler Mach number	0.112
Plane 40 Mach number	0.104
Plane 41 Mach number (without NGV coolant)	0.75

Table 3.4: Design Point operating conditions

of the total mainstream mass flow rate at NGV inlet ($W = \frac{\dot{m}_{fc}}{\dot{m}_M} = 0.075$). Depending on the measurements that have been performed, different sweeps of film cooling mass flow rate have been carried out, in order to provide a deeper evaluation of its effect on the measured phenomena (see Section 3.3). The NGV film cooling conditions in terms of local blowing ratio have already been discussed in Section 3.1.2. Table 3.4 summarizes the design point conditions both in terms of dimensional variable, to be imposed during the tests, and resulting non-dimensional parameters.

Beside the nominal operating point, an isothermal point (i.e. all the flows at ambient temperature) had to be defined, since some of the adopted measurement techniques have to be operated at ambient temperature. In the view of the combustor simulator characterization, a thorough description of the process to define the isothermal operating point (IOP) can be found in the works of Koupper et al. [101] and Caciolli [97]: with the goal of finding a good trade-off between the necessities of matching Mach and Reynolds numbers, a chamber pressure of 115 kPa was selected, compared to the 148 kPa of the design point (DP). In order to preserve the values of liners effusion cooling system blowing ratios, mass flow rates have been left unchanged, leading to relevant differences in the momentum ratios between DP and IOP (77%); however, an overall estimate based on early numerical calculations [101] in-

dicates values of velocity ratio within the range $VR \approx 2.5 - 3$. Therefore, since the effusion holes work within the penetration regime ($VR > 0.8$) [54], it was assumed that the modification in the behaviour of the cooling jets due to this changes on VR does not alter significantly the mixing process in the chamber and the resulting flow field at the outlet section.

Concerning the NGV test campaign, one consideration must be premised: the definition of the operating points for the combustion chamber investigation had been defined without the view of the NGV investigation, since this part of the work was promoted in a second moment. In the THT Lab open loop facility operation, lower limits in the NGV exit pressure exist. Despite this is not a problem for the DP conditions, since they can be easily matched also in the presence of the NGV cascade, for the isothermal point, early evaluations revealed that the combustion chamber pressure had to be increased. The first commissioning tests of the upgraded rig showed that a chamber pressure of 127 kPa was necessary, leading to an increase of Plane 40 Mach number of about 5% with respect to DP. Due to the expansion through the cascade, even higher differences were expected at NGV exit. In theory, the combustion chamber pressure could have been regulated in order to adapt the hot operating point Mach number to the new isothermal one; nevertheless, since the investigation in DP conditions plays the most important role, within this research, it was decided not to change it and keep the values of the non-dimensional parameters to the initial desired values. The impact of this differences on the achieved results, depending on the measured quantities, will be explained in the next section (Section 3.3.1). Table 3.5 summarizes the values of the main parameters for both the original isothermal point (IOP) and the new one (IOP_2), compared to the DP conditions.

3.3 Test matrix

Four different experimental techniques were exploited for the characterization of the combustor simulator and the high pressure NGV module. At the beginning, the focus was placed to the evaluation of the flow field and of the mixing phenomena inside the combustor simulator by means of particle

image velocimetry (PIV). Standard bi-dimensional PIV was employed to investigate three different planes: the first one (referred as 1 in Fig. 3.12) is the combustion chamber symmetry plane (0° azimuthal coordinate), that cuts in two halves the central swirler; the second and the third, called *Plane CC1* (2) and *Plane CC1* (3) are axial planes (i.e. defined by a normal vector with axial direction) placed 65 and 85 mm downstream the chamber inlet (i.e. 10 and 30 mm downstream the duct exit) respectively. The initial goal was to carry out PIV measurements both for IOP and DP conditions: during the test conduction it was found that the wide lateral pyrex windows could not live up to the target temperature and the mainstream temperature had to be limited to $\approx 450K$. The combustion chamber pressure was regulated in order to maintain Mach and Reynolds numbers, together with swirler/liners pressure drops, as close as possible to the DP case, as previously done for the IOP definition; mass flow rates were left unchanged in order not to change the blowing ratios of the effusion cooling systems: this new operating point will be referred to as *WOP* (warm operating point).

	DP	*IOP*	IOP_2
Normalized total mass flow	1	1	1
Flow split: swirlers	65%	65%	65%
Flow split: liners	35%	35%	35%
W (film cooling mass flow / mainstream mass flow)	7.5%	7.5%	7.5%
Chamber pressure	148 kPa	115 kPa	127 kPa
Swirlers inlet temperature	531 K	300 K	300 K
Liner coolant temperature	300 K	300 K	300 K
NGV coolant temperature	300 K	300 K	300 K
Swirler Reynolds number	111000	168500	168500
Swirler Mach number	0.112	0.108	0.098
Plane 40 Mach number	0.104	0.109	0.099
Normalized Plane 40 Mach number	1	1.05	0.95
Combustion chamber main-coolant temperature ratio	1.77	1	1
NGV main-coolant temperature ratio	1.5	1	1
Normalized effusion blowing ratio	1	1	1
Normalized effusion momentum ratio	1	1.77	1.77

Table 3.5: Isothermal operating points conditions

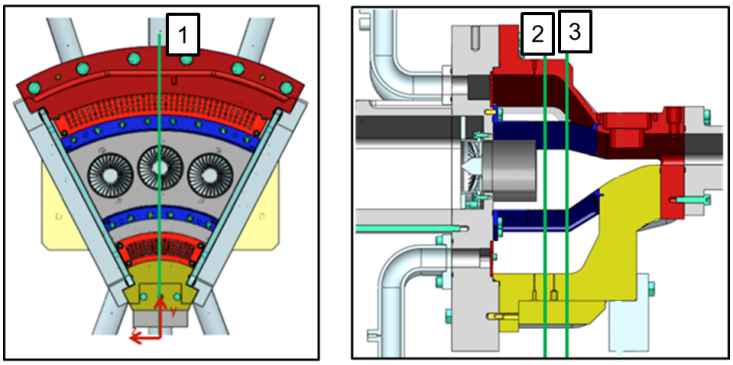

Figure 3.12: PIV measurement positions

After the test rig upgrade with the NGV module, the evaluation of the overall aerothermal field at combustor exit, by means of five hole probe traversing, was carried out; Plane 40 is the nominal combustor exit plane and it is located about half an axial chord ($\approx 20mm$) upstream the NGV leading edge position and about 156 mm downstream the swirlers (101 mm downstream the duct exit). As stated before, a preliminary activity was carried out, on the combustor simulator without NGV, within a previous Ph.D. course, in order to validate the combustion chamber design and verify the flow field at combustor exit. Five hole probe tests at combustor exit has been repeated, after the rig was provided with the NGV module, in order to verify the repeatability of the measurements after the NGV cascade installation. Due to the presence of the cascade, the investigation plane at combustor exit had to be moved upstream by $\approx 5.8mm$, as reported in Fig. 3.13; this new investigation plane, located about 0.65 axial chords upstream the LE position, was referred to as *Plane* 40_2. The comparison between the results of the two different campaigns showed a satisfactory matching and the little differences that were found were all coherent with the change of measurement plane. Five hole probe measurements on Plane 40_2 have been conducted both in DP and isothermal (IOP_2) conditions to evaluate the differences in the aerodynamic field and understand if the validity of the results obtained by the measurements techniques that require isothermal conditions can be extended to the DP investigation.

The combustor simulator characterization was completed with the evaluation of turbulence intensity and unsteady structures at combustor exit in IOP_2 conditions. Hot wire probe traversing was employed; due to the configuration of the hot wire probe, with the sensor element in-axis with its support (see Section 5.3) it was possible to carry out the measurements on the exact Plane 40.

Afterwards, the investigation of the overall flow field at NGV exit was conducted: it was carried out by five hole probe traversing on Plane 41, an axial plane placed about 9 mm ($\approx$ 0.24 axial chords) downstream of the NGV trailing edge ($\approx 67.5mm$ downstream Plane 40); as for Plane 40_2, tests were carried out both in DP and IOP_2 conditions. The same measurement plane was also investigated by means of hot wire anemometry traversing, in IOP_2 conditions. For both the measurement techniques, on Plane 41, three film cooling mass flow rate conditions were evaluated: the nominal one

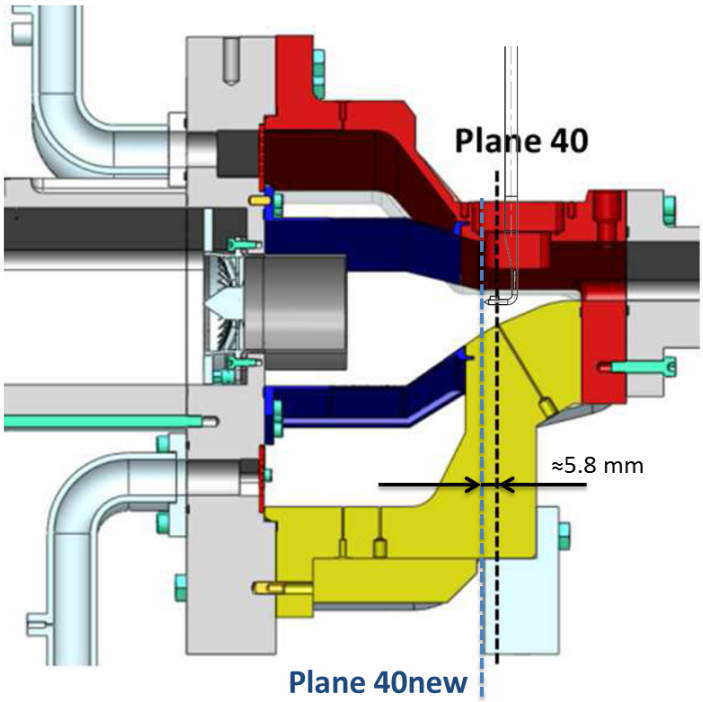

Figure 3.13: Five hole probe measurement positions at combustor exit

			PIV	5HP	HWA	PSP
Combustion Chamber	**Sym Plane**	IOP	o			
		WARM	v			
	Plane CC1	IOP	v			
		WARM	v			
	Plane CC2	IOP	v			
		WARM	v			
Combustor Exit	**Plane 40**	IOP		o		
		IOP_2			v	
		DP		o		
	Plane 40_2	IOP_2		v		
		DP		v		
NGV Module	**Plane 41**	IOP_2		v	v	
		DP		v		
	NGV Profiles	IOP_2				v

Table 3.6: Experimental campaign test matrix

(see Section 3.1.2), with $\dot{m}_{cool} = 27g/s$ ($W = 7.5\%$), the configuration without film cooling ($W = 0\%$) and an intermediate one, with $\dot{m}_{cool} = 13.5g/s$ ($W = 3.75\%$).

In the final part of the work, adiabatic effectiveness measurements on the NGV airfoils were performed, in order to understand the effect of the highly swirling combustor outflow on the film cooling performance. As for the hot wire test, the adopted PSP technique requires tests to be run in cold (IOP_2) conditions. The same two cooled configurations ($W = 7.5\%$ and $W = 3.75\%$) were investigated and a third one with $\dot{m}_{cool} = 20g/s$ ($W = 5.5\%$) was added, in order to deepen the investigation of the effect of coolant mass flow on the achieved adiabatic effectiveness, on the different positions of the airfoil.

The full experimental test matrix is summarized in Table 3.6: symbols 'o' indicate tests carried out in the previous Ph.D. course [97], while symbols 'v' indicate tests carried out within the present work.

3.3.1 Final considerations on operating conditions comparison

As stated above, the nominal operating condition for the present experimental campaign makes use of heated mainstream, in order to account for the presence of temperature gradients at combustor exit. On the other hand some experimental techniques require tests to be run with all the flows at ambient temperature, resulting in an isothermal configuration. It is useful to provide here a short description of the expected impact of these differences in the outcomes, in order to understand if and how the applicability of the isothermal results can be extended to complement the nominal condition ones. In addition to the absence of temperature gradients, the expected differences in the NGV exit Mach number, due to the differences in Plane 40 Mach number between DP and IOP_2, must be considered.

Regarding the hot wire measurements, the turbulence pattern at the exit of a lean combustor representative flow field is mostly generated by the highly swirling flow and a strong turbulence spot should be expected in the center of the rotating structure; once the correct swirl profiles are achieved, the gross turbulence intensity profile should follow [22]. Therefore if a very similar flow angles pattern at combustor exit is achieved, between isothermal and nominal point, similar turbulence profiles should be found as well. Koupper et al. [101] carried out preliminary CFD calculation to verify this analogy, in terms of both flow pattern and turbulence intensity, at combustor exit. The limited differences in Plane 40 Mach number ($\approx 5\%$) should not affect the results, due to its very low value, well below the compressibility threshold. The similarity between the flow field at combustor exit for DP and IOP_2 condition will be discussed in Section 6.2.2. Regarding the turbulence measurements on Plane 41, it has been demonstrated in the past that the presence of temperature gradients should not affect the flow field evolution within the cascade from an aerodynamic point of view [72, 84]. Even if this assumption has never been experimentally demonstrated for the case of highly swirling flows, as in the present study, and does not take into account the film cooling contribution, it is fair to expect limited differences in the

aero field on Plane 41 between DP and IOP_2. The slight variation of the exit Mach number should not significantly affect the flow development as well, as long as the operating point stays far from transonic conditions [105]. The verification of this assumption will be presented in Section 7.2.1. The expected differences in the exit Mach number can play a bigger role than on Plane 40, due to the fairly high values: a lower turbulence is generally associated to a higher acceleration (i.e. higher exit Mach number). Anyway, since in both conditions the NGV cascade stays far from sonic conditions, only slight quantitative differences can be expected, with very similar outcomes in terms of turbulence pattern.

Concerning the adiabatic effectiveness, the biggest difference between IOP_2 conditions, used for PSP measurements, and DP ones stays in the local coolant-to-mainstream density ratio. Even if carbon dioxide was chosen as foreign gas (Section 5.4.4), in order to match the average density ratio of the DP case, the effects of the temperature gradients in the mainflow can't be replicated and some differences must be locally expected. Moreover the different Mach number at NGV exit between IOP_2 and DP conditions (i.e. different pressure ratio through the cascade) could lead to different coolant mass flow rate repartition between the LE plenum chamber and the TE one, resulting in different local blowing ratios, even if the mass flow rates are conserved. As it will be explained in Section 4.1.1, these differences are expected to be very small, since the gross of the coolant mass flow rate is injected close to the LE and on the pressure side, where the differences are limited; consequently, even if the values of blowing ratios and momentum ratios reported in Section 3.1.2 can't be exactly matched, very similar and, thus, realistic values, are expected. In addition, concerning Mach number, it has been documented that it can affect the film cooling thermal performance, since an increase in the mainstream Mach number can keep the cooling jets closer to the wall, resulting in lower mixing and higher protection [64]; anyway, due to the very limited differences in terms of Mach number, especially in the position of the investigated row of holes, this effect should not be considered as a source of inconsistency between the operating conditions. Even if, due to issues related to the density ratio, only a qualitative extension of

the adiabatic effectiveness results gathered in cold conditions to the nominal conditions should be made, they completely fulfil their goal: the description of the behaviour of a NGV film cooling system under a highly swirling inflow and the effect of a coolant mass flow rate variation on the resulting effectiveness.

Different considerations must be made regarding PIV measurements, since both IOP and $WARM$ conditions, adopted for these measurements, are different from the other conditions (IOP_2 and DP) adopted throughout the rest of the campaign. The dimensional results evaluated here cannot be considered valid for the other investigations. The goal of these measurements is, on the other hand, to highlight the typical flow structures and mixing phenomena that characterize the flow field evolution in the combustion chamber and to relate them to the flow field behaviour at combustor exit. Moreover they have been useful to put in evidence the reasons of the differences between the isothermal case and the nominal one. Once the results are properly scaled, they strict this goal, despite the quantitative differences.

As a short summary of the considerations taken in this paragraph, the following statements can be used: (1) despite limited differences between the nominal conditions and the isothermal ones, a very similar behaviour should be expected for all the investigated aspects; (2) the goal of the measurements performed throughout this work is (a) to evaluate the effect of a highly swirling and highly turbulent inflow on the adiabatic effectiveness of a film cooled NGV, as well as on the resulting flow field, secondary flows and turbulence pattern at its exit and (b) to investigate the hot streaks migration through the cascade, their interactions with film cooling cold streaks and their effects on the secondary flows, once engine representative temperature gradients are introduced in the mainstream. The description of the results in Chapter 7 will follow this angle.

Chapter 4

Instrumentation Design and Integration

Contents

One of the most important activities, that were carried out within this work, was the development of a new test rig, made by both the combustor simulator and the NGV module. While the design of the two separated modules was not part of this work of thesis, as it was done by industrial partners (see Section 3.1), their integration into a single test rig had to be addressed. Moreover, in order to carry out probe traversing on the measurement planes, an automatic traverse system had to be developed. In this chapter both activities will be described. Particular attention will be given to the first one, due to its importance in the work final outcome; details of the experimental commissioning tests, carried out to verify the design procedure, will be also provided here.

4.1 Details of test rig upgrade design procedure

The upgraded test rig design has been divided in two main parts. In the first one the focus was put in integrating the two modules together from a mechanical point of view: in this stage the work was mainly made by CAD activity, aimed at installing the cascade at the exit of the combustion chamber, without modifying its geometry. Afterwards the focus shifted to the design of the module that had to host the NGV profiles and of its outlet section. In general, when it comes to designing sector cascade rigs, lot of attention must be paid in trying to achieve the correct mass flow distribution among the vanes and, hence, periodic conditions in the vane passages that have to be investigated. A CFD activity was carried out for the goal: even if CFD calculations were not directly carried out within the work of this Ph.D., this activity was closely followed, in terms of defining guidelines and evaluating results. The first part has been already briefly detailed in Section 3.1, where sectional views of the previous and of the upgraded test rig configurations have been showed and described (see Fig. 3.1). Therefore, in this section, the focus will be placed on the description of the second part.

The integration of the NGV module in the test rig had to face a number of different constraints and necessities; the most important are summarized below:

- reach the correct mass flow distribution among the vanes (i.e. re-create periodic conditions in the two central-sector passages)
- allow the correct coolant distribution among the NGV profiles
- achieve a sufficient dynamic pressure recovery (i.e. limit the total pressure losses) in the outlet section, in order to reach the design point conditions in terms of mass flow rate and exit Mach number, in the open loop facility

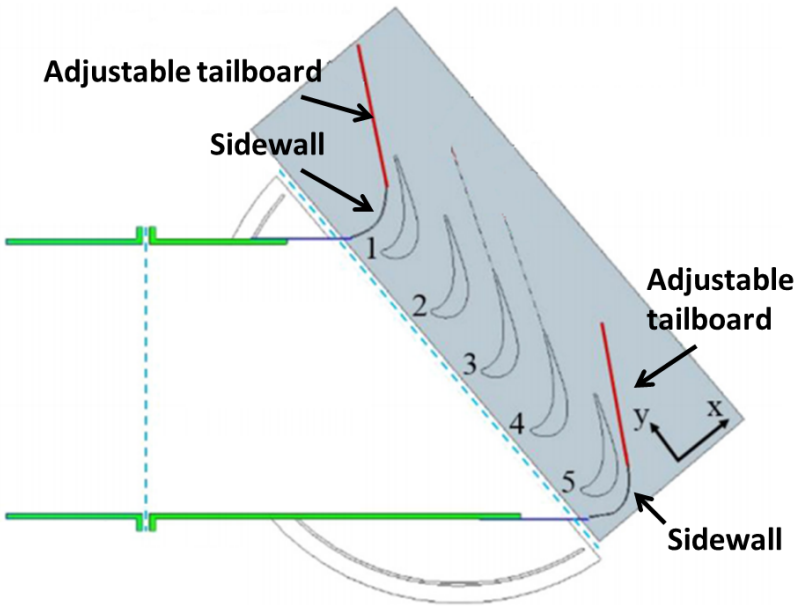

Figure 4.1: Sketch of a linear cascade rig: focus on sidewalls and tailboards (modified from [106]

- provide accesses for probe traversing at the NGV exit plane and an optical access for PSP measurements

The first two aspects are unanimously considered critical points in sector rigs design: in this kind of applications, the work must be aimed at evaluating the correct shapes of the NGV module lateral sidewalls (i.e. the walls at the sides of the NGV profiles) and of the tailboards, the rig walls in the outlet section; Fig. 4.1 provides a sketch of a linear cascade rig where these surfaces are highlighted [106].

Concerning the first geometry, it is common to adopt the shape of either the pressure or suction side of the NGV profiles, at least in the application, as the present one, where a whole passage stays between the lateral profiles and the sidewalls. The calculation of the tailboard geometry, on the other hand, is more complicated, especially in the case of annular cascades. For linear ones, in fact, it is common use to adopt flat plated tailboard, hinged at the outlet of the cascade: depending on the setting angle (i.e. their inclination with respect to the axial direction), tailboards can induce local flow

diffusion and thus affect the backpressure locally downstream of the cascade, which per se can be used for controlling the velocity distribution in the flow passages [107]. In addition it is also common to make use of movable tailboard, whose inclination can be varied, during the rig commissioning phase, to match the desired conditions, in order to make up for possible design inaccuracies [106, 108].

Concerning annular cascades, the procedure become more complex, due to two main reasons: first of all, due to the annular nature, it is not possible to adopt movable tailboards, since a rotation of this surfaces would lead to interference with inner and outer walls; applications with semi-flexible sidewalls, made of plastic materials, have been engineered to solve this problem [107], but their applicability is limited to low TRL applications. In addition, some means have to be employed to set the radial pressure distribution, that establishes in the annular cascade, at its exit. A detailed survey of guidelines for annular sector cascade rigs was provided by Povey et al. [109], as they highlighted four possibilities to strict this goal; they are sketched in Fig. 4.2.

The solution reported in Fig. 4.2b consists in increasing the mean radius of the flow path, in order to reduce the flow tangential velocity by conservation

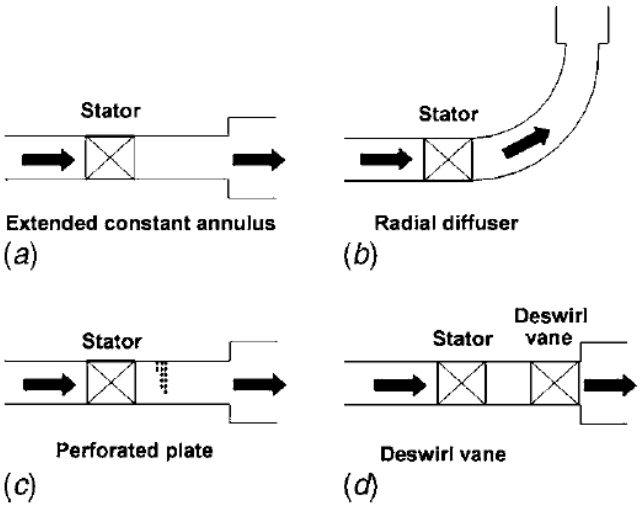

Figure 4.2: Methods of setting annular cascade exit conditions: (a) extended constant annulus, (b) radial diffuser, (c) perforated plate, and (d) deswirl vane [109]

of fluid angular momentum. This reduces the pressure difference between the hub and case so that the flow can be exhausted to a constant pressure plenum. Particular attention, though, must be paid to the design in order to avoid separation in the diffusive flow along the duct; therefore this solution is scarcely adopted. The solution in Fig. 4.2c, on the other hand, consists in using a grid with variable porosity, depending on the annulus height, so that a radial pressure gradient can be set upstream the grid, while achieving an approximately constant pressure distribution downstream of it. Such a solution was adopted by El-Gabry et al. [110]. The drawback of this solution is that it introduces an additional total pressure loss in the flow. The solution in Fig. 4.2d is the one adopted by Povey et al. [109] and consists in making use of a deswirl vane to set the radial pressure gradient at the vanes exit; while it is considered the most reliable solution, it increases the design complexity, as it introduces an additional cascade to the rig. Finally the solution in Fig. 4.2a is only based on allowing the exit flow to develop through an extended annulus of constant radius, before exhausting to a plenum at constant pressure. According to Povey et al. [109], it is usually the case that the vane exit static pressure at midspan is close to the pressure of the downstream plenum. For this reason, the hub endwall flow is subject to an adverse pressure gradient towards the exit of the annulus: this can lead to flow separation that can influence the upstream flow development. Nevertheless, this solution is often adopted [107], especially in the case where the operating point does not reach transonic conditions (i.e. where the radial pressure gradient is less enhanced). Regardless of the adopted solution, the design of an annular sector cascade rig requires a detailed design process; for this reason reduced experimental data gathered on this kind of test rigs is available. Nevertheless they are a promising solution, that allows, once its design is satisfactorily carried out, to re-create secondary flows, pressure losses and swirl angles that are representative of engine applications at reduced costs with respect to full annular facilities.

In the present case, given the advantages and the drawbacks of the different solutions and since the expected Mach number at NGV exit stays quite far from transonic conditions, it was decided to pursue the last mentioned

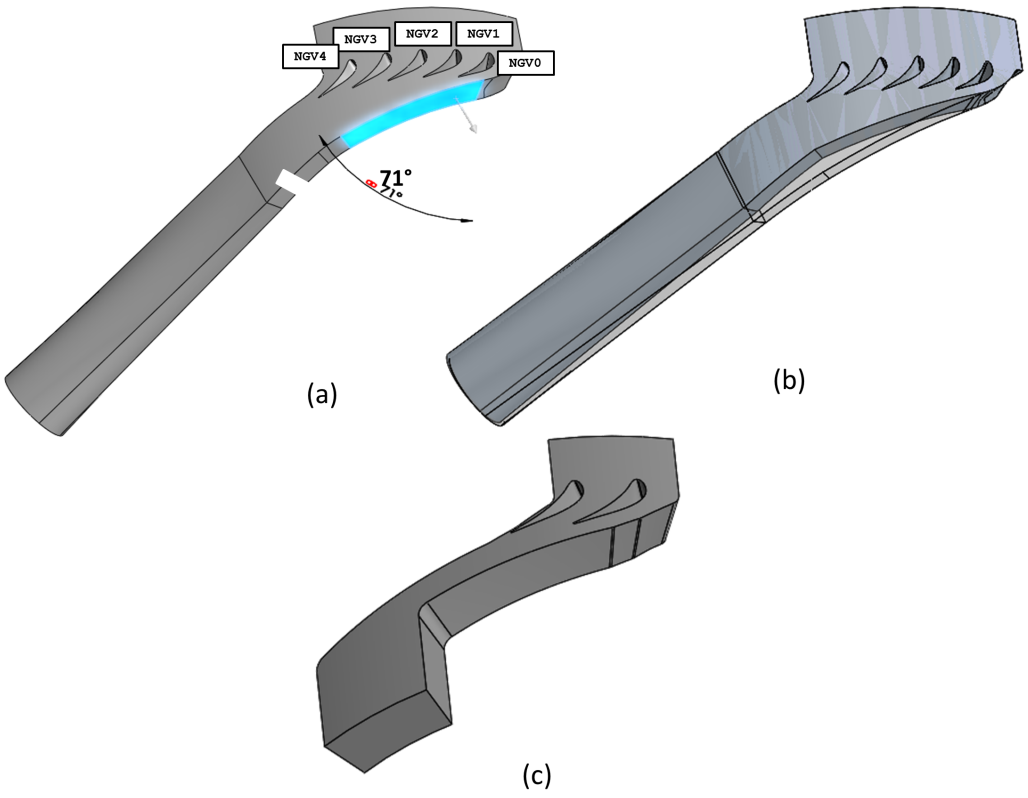

Figure 4.3: Parametric CAD (a) and reference case (b) geometries

solution. In fact, it would allow to limit the pressure losses in the cascade exit duct, that constitutes an important constraint in the THT Lab open loop facility. Concerning the shape of the tailboard walls, Povey et al. [109] highlighted the necessity to employ 3D shaped surfaces in order to adapt to the flow streamlines; nevertheless, since in the current application the variation on the NGV exit angle with the annulus height is quite limited, it was chosen to make use of flat walls. This choice allowed to provide the external wall with an optical access to be exploited for PSP measurements, as it will be detailed in the following. Finally a divergent section was adopted instead of a plenum chamber in order to achieve a more effective dynamic pressure recovery, allowing to bring the NGV outlet static pressure below ambient conditions.

An optimization procedure, similar to the one described by Shaukat [111]

was set up in *ANSYS Workbench* to minimize the discrepancy between a calculation on the rig geometry and a reference case, represented by a single sector with periodicity conditions. A parametric CAD was coupled with a meshing module and *ANSYS CFX*, giving the possibility to generate geometry and mesh of the investigated configurations, as well as perform a RANS simulation and postprocessing. The design purpose was to determine the values of opening angle of the external tailboard capable of avoiding any effect on the flow field of the central sector; a set of tailboard opening angle was automatically investigated in order to find the configuration that led to the minimum differences with the reference case, in terms of pressure distribution on the three central profiles (NGV1-3, according to the nomenclature reported in the figure). Figs. 4.3a and 4.3b report sketches of the CAD parametric model; the latter shows two models with different tailboard angles, in order to make the differences more understandable. Fig. 4.3c shows the geometry of the single sector periodic run used as a reference case.

Concerning the definition of the boundary conditions, to be used for the calculations, one issue had to be faced: while results from preliminary five hole probe measurements, carried out on the combustor simulator rig without NGVs [102, 97] were available, they only covered the central sector of the rig; therefore they could have been used for the reference run, but not for the three-sector rig geometry configuration. Since the lateral walls were expected to have a strong influence on the local flow field approaching the NGV cascade, it was decided not to simply extend the preliminary measurements results to the adjacent sectors, but to follow a different way. Results coming from a SAS calculation, carried out on the whole three-sector combustion chamber domain [112], were used, as they provided a very good matching with the preliminary five hole probe results: for the rig geometry run, the whole three-sector dataset was used, while for the reference one, only the central sector results were employed. In order to make the design procedure more reliable, an additional case, with uniform axial inlet flow and with the same mean total pressure and temperature of the SAS results, was run, both in the periodic case and in the rig configuration one. In the following the calculation with SAS boundary condition will be referred to as “swirl”

calculation, while the other will be labeled as "uniform".

Fig. 4.4 reports the comparison of the numerical results, in terms of Mach number distribution on the NGV exit plane (Plane 41). The contour plots present a very good matching between the reference case and the rig case, both for the swirl and the uniform runs. Therefore the CFD analysis demonstrated that the optimized test rig geometry was capable of reproducing the flow field that would be achieved in an ideal periodic configuration (i.e. full-annular configuration). As a further verification, Fig. 4.5 reports the pressure distributions on the NGV profiles; only the swirl runs are reported here. According to Fig. 4.3, NGV2 refers to the airfoil with the leading edge aligned with the central swirler, while NGV1 and 3 are the lateral ones that bound the rig central sector; for the reference run, only one lateral airfoil is included in the domain, due to the periodicity conditions. Results show a satisfactory agreement, confirming the conclusion taken above. In addition, it was

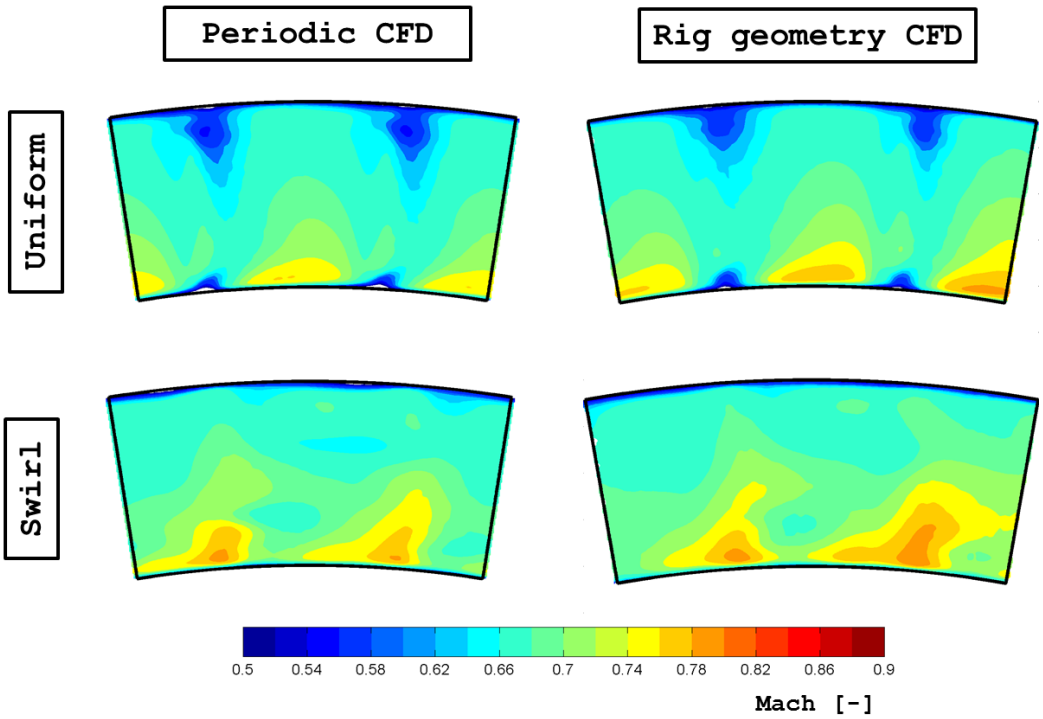

Figure 4.4: Mach number distribution on Plane 41 calculated from reference (periodic) and rig configurations

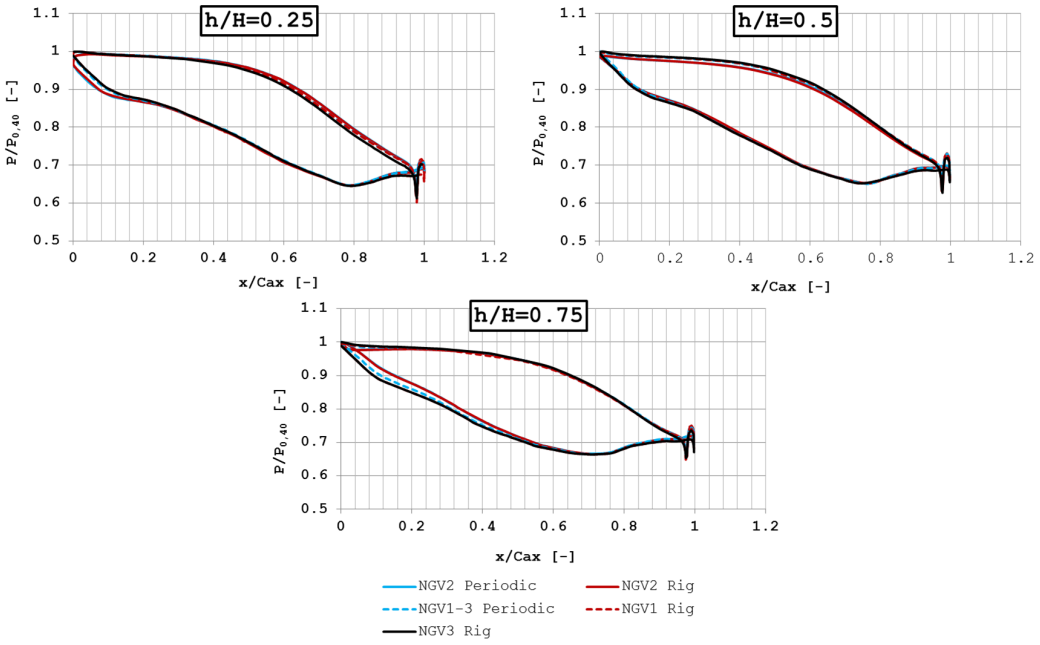

Figure 4.5: NGV pressure distribution calculated from reference (periodic) and rig configurations

found that all the profiles show a very similar pressure distribution, regardless of their clocking position, despite the different flow field characteristics approaching them: this aspect will be detailed in Chapter 6, where the flow field on Plane 40 will be described.

According to these results, the optimized rig geometry, defined with the guidelines described above, was considered adapt to the goal of creating the same flow field that would be generated in a full annular configuration where each sector is characterized by the same flow field that is achieved in the central sector of the combustion chamber exit plane of the present test rig. The final configuration is reported in Fig. 4.6, where both a CAD model of the rig (Fig. 4.6a) and a sectional view, that allows to correctly visualize the paths of the different flows (Fig. 4.6b), are shown. As stated in Section 3.1, the combustion chamber inner and outer casing had to be remanufactured, in order to reduce their axial extension and leave space for the NGV module; no changes in the combustion chamber geometry, though, were enforced. The multiperforated liners, on the other hand, were left unaltered.

A component (1) was used to host the NGV profiles and two others (2-3) to reproduce the sidewalls geometry; in this way the tested NGV profiles can be changed without having to substitute the whole NGV module. In component 1, a plenum chamber for NGV coolant is achieved, where total pressure and temperature of the cooling flow are measured. The NGV outlet duct (4), on the other hand is specifically designed for a certain NGV geometry; at its exit the flow enters a divergent section (not reported in the figure), where a part of the dynamic pressure is recovered, before passing through the back-pressure valve and going to the stack. The yellow component in Fig 4.6b (5), constitutes the outer endwall of the NGV annulus; an instrumentation access was achieved on such a component in order to allow probe traversing on Plane 41: different kind of adapting flanges, for traverse system installation, like the one that is shown on Plane 40 in the figure, can be mounted on it, in order to investigate the plane with different kind of probe geometries. The lateral combustion chamber windows had to be modified with respect to the previous configuration, in order to cope with the reduced length of the combustion chamber inner and outer casing components. They are provided with a small window, that can be exploited for optical measurements on the NGV profiles: for these kind of tests PMMA windows are used, while for probe traversing tests, where no optical access is required, they can be substituted with metal dummies. An additional window was realized in the exit duct, as stated above. The optical and the probe accesses are also reported in the figures. The figure also shows that only the three central airfoils are cooled, while the lateral ones (NGV 0 and 4) are dummies; this choice was made in order to ensure that the film-cooling mass flow rate is correctly distributed among the airfoils. In fact, since the feeding pressure is the same, as all the airfoils are fed by the same plenum chamber, as described in Section 3.1.2, and the same pressure distribution is expected on the central profiles, a uniform coolant mass flow distribution should be expected as well. On the other hand, if also the lateral profiles were cooled, relevant imbalance in the coolant mass flow split could arise, due to the different mainstream pressure distribution on these profiles.

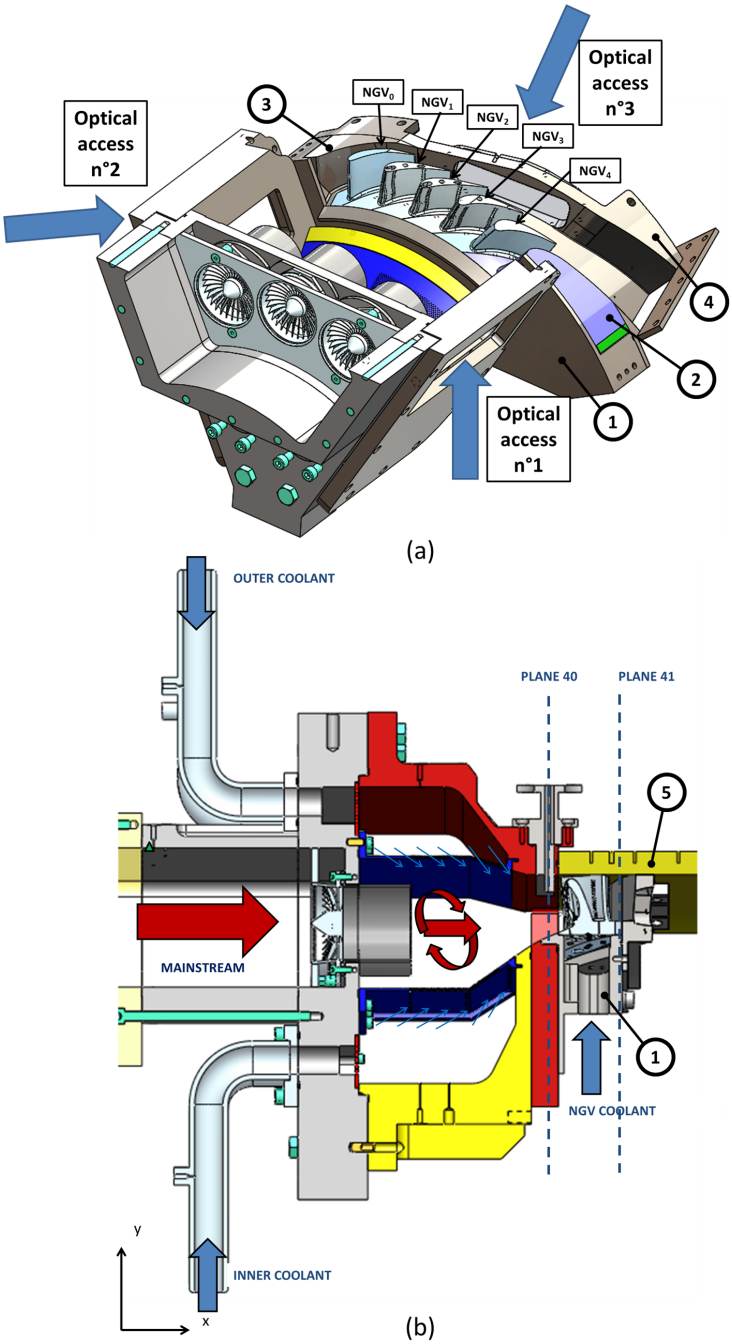

Figure 4.6: Optimized rig layout: 3D CAD model (a) and sectional view (b)

4.1.1 Upgraded test rig commissioning

It is useful here to provide some experimental results, in order to verify that the conclusions taken from the CFD optimization also stand in the manufactured hardware. In this kind of applications it is common to experimentally verify the pressure distribution on the NGV profiles, by means of dummy airfoils provided with pressure taps. In the current application, it was decided to follow a slightly different path, since such a verification was not considered enough for the pursued goals. First of all, it was also necessary to verify the flow field distribution downstream of the cascade, where measurements had to be carried out; the only verification of the NGV pressure distribution was not sufficient for the assessment of the test rig behaviour. Moreover, it was useful to understand how the coolant injection altered this pressure distribution: in fact, this would not have been feasible with dummy airfoils, as it is hard to provide them with both pressure taps and a cooling system. It was, then, decided to exploit some of the results, coming from the test matrix described in Section 3.3, to strict this goal. These results are reported in this section, since they must be directly compared with CFD findings, even if the working principle of these measurement techniques has not been described yet; it will be done in Chapter 5, before analyzing the actual results of this Ph.D. course.

In particular five hole probe results on Plane 41, have been exploited to compare the Mach number level on the NGV exit plane, to the one calculated by the periodic "swirl" CFD run; the goal of this verification was (1) to compare the Mach number level, in order to check that the foreseen pressure ratio is achieved in the rig, and (2) to check its distribution among the central NGV passages, as an unbalanced mass flow rate split among the vanes, due to the rig not working correctly, would lead to a different pressure ratio (i.e. a different Mach number) in the two central passages. It must be reminded that CFD inlet conditions are not taken from experimental data, but from a SAS calculation; the differences between this data and the actual flow field approaching the NGV cascade is, anyway, expected to be very limited.

One dimensional profiles, at three different annulus heights, were extracted from both data sets, and compared in Fig. 4.7; only the two central

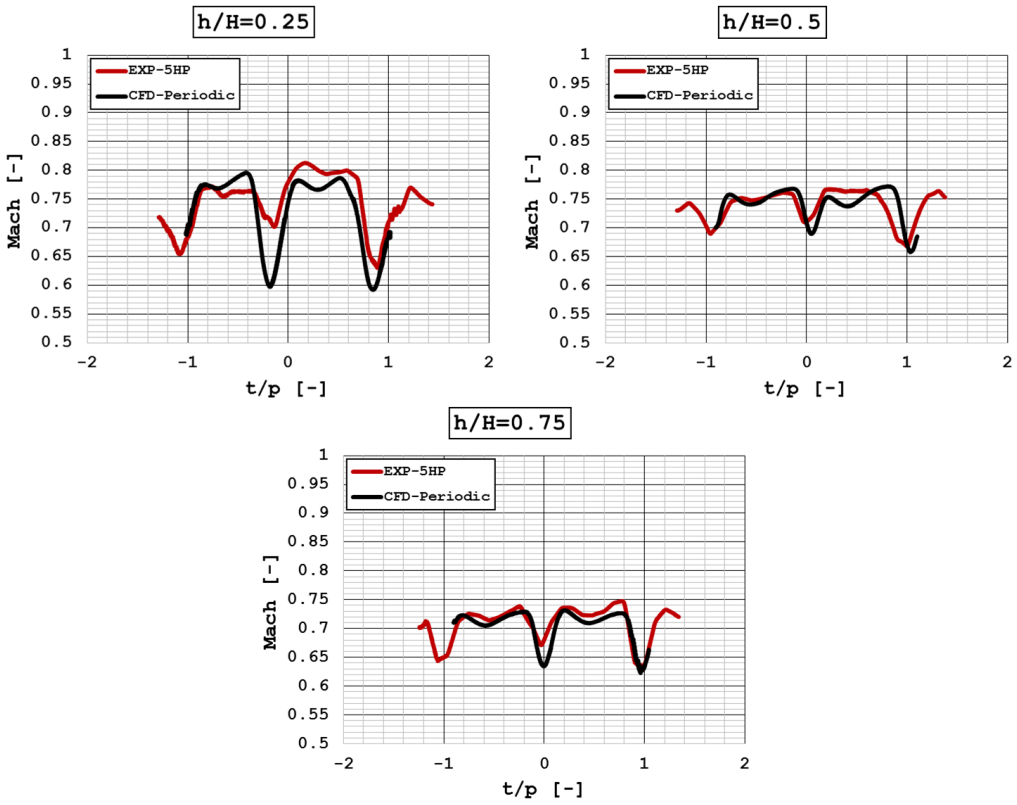

Figure 4.7: Mach number profiles at NGV exit: comparison between experimental results and CFD prediction

passages are covered from the data shown in the plots: the central sector covers the span between $t/p = -1$ and $t/p = 1$; in particular $0 < t/p < 1$ corresponds to the right passage (between NGV_2 and NGV_3 according to Fig. 4.6) exit area, while $-1 < t/p < 0$ corresponds to the left one (between NGV_1 and NGV_2). A good matching was achieved, both in terms of Mach number values and distribution, at h/H=0.5 and 0.75. At h/H=0.25, a higher Mach number was measured in the right passage, while similar values, between the two passages were expected from CFD results. A possible explanation of this behaviour will be provided in Section 7.2. Despite this aspect, limited issues related to the mass flow rate split should be found and the achieved pressure ratio across the cascade is in line with what was expected.

The verification of the pressure distribution on the NGV profiles, on the other hand, was carried out by exploiting PSP, that, as it will be detailed in

the next chapter, can be used as pressure detectors. Two considerations must be premised here. First of all, when PSP technique is adopted to measure a pressure distribution, a low measurement sensitivity is generally achieved, especially when the measured pressures are close to the ambient conditions; therefore "noisy" results will be achieved, that, nevertheless, allow to correctly understand the pressure distribution on the airfoils. Furthermore, PSP tests had to be run in IOP_2 conditions, so, as anticipated in Section 3.2 a lower pressure ratio than in DP conditions (i.e. than in CFD results) was achieved. Nevertheless the goal of this verification was not to check the actual pressure ratio, that was already accomplished with Mach numbers plots, but to compare the shape of the pressure profiles; since the differences in the pressure ratio between IOP_2 and DP conditions are limited, this shape is not expected to present important variations. Results are reported in Fig. 4.8: CFD results, from the reference periodic run, are shown on the left, while the profiles extracted from PSP results are reported on the right; for the latter, NGV 2 and 3 are only reported, since a reduced portion of NGV1 can be framed (as it will be explained in Section 5.4.4); moreover both results from tests with and without NGV coolant are shown, so that its effect on the pressure distribution can be assessed.

Even if PSP measurements do not cover the whole NGV profile, they allow to verify that very similar pressure distribution to the CFD predicted ones are measured. The only relevant difference between CFD and PSP profiles for the case without coolant (red and yellow plots) stays in the different pressure ratio, that, anyway, has already been addressed above and is only a consequence of the operating condition. In addition PSP results for the case with coolant show that the two investigated airfoils still show a very similar pressure distribution, with an increased pressure ratio, as an enhanced mass flow rate expands through the passages due to the coolant injection. This finding suggests that a correct cooling flow distribution is achieved, with no relevant unbalance. Even if this result was expected, since the different airfoils showed a very similar pressure distribution and they also have a very similar effective area (as measured from preliminary tests in a dedicated test rig with ambient discharge conditions), this evaluation works as a useful ver-

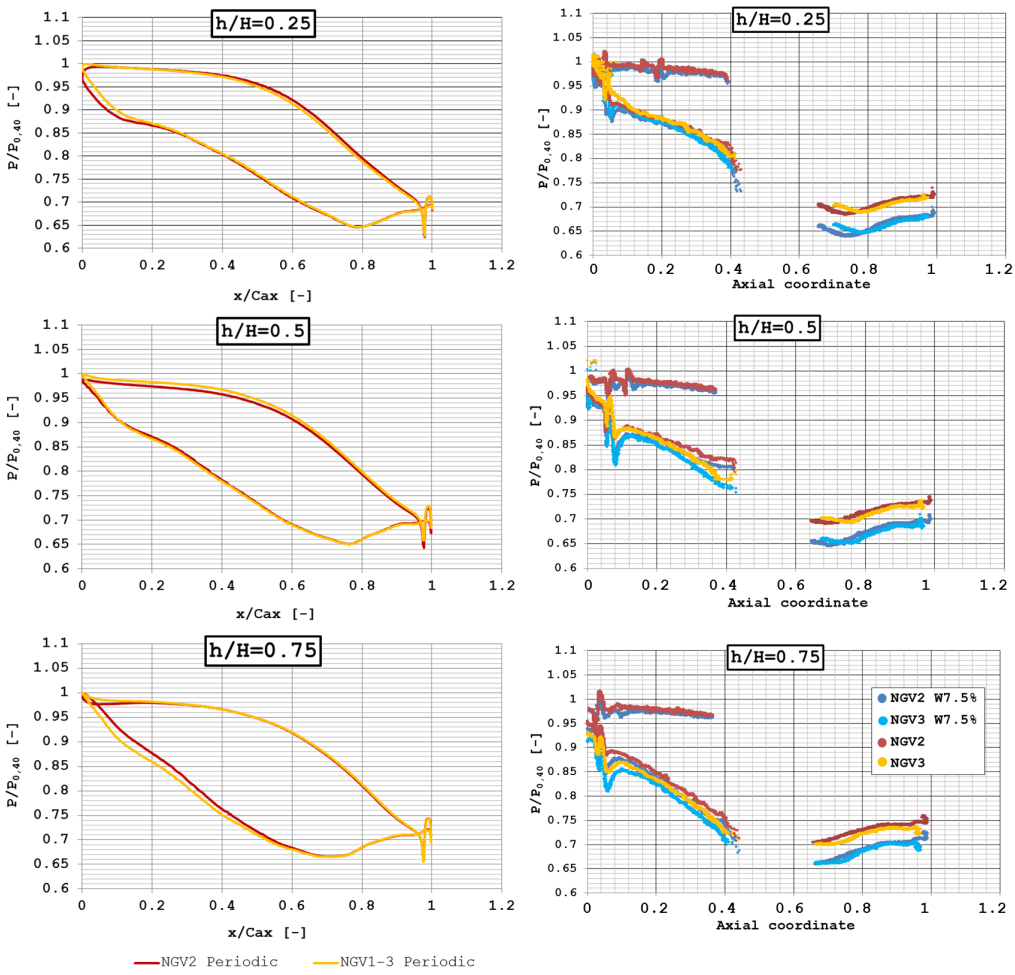

Figure 4.8: Pressure distribution on NGV profiles: comparison between experimental results and CFD prediction

ification.

A further verification of it was pursued by directly analyzing the performance of the NGV cooling system. Differently form the previous results, this can be considered as an actual commissioning test, since it was carried out only to verify the rig behaviour and not to find any general result. The two feeding cavities of each airfoil (see Section 3.1.2) were, in turn, blocked, by using a dedicated sealant material, in order to run three different tests: in the first one all the three airfoils were fed (*Test NGV123*); in the second only the central airfoil was fed (*Test NGV2*); in the last, only the lateral ones

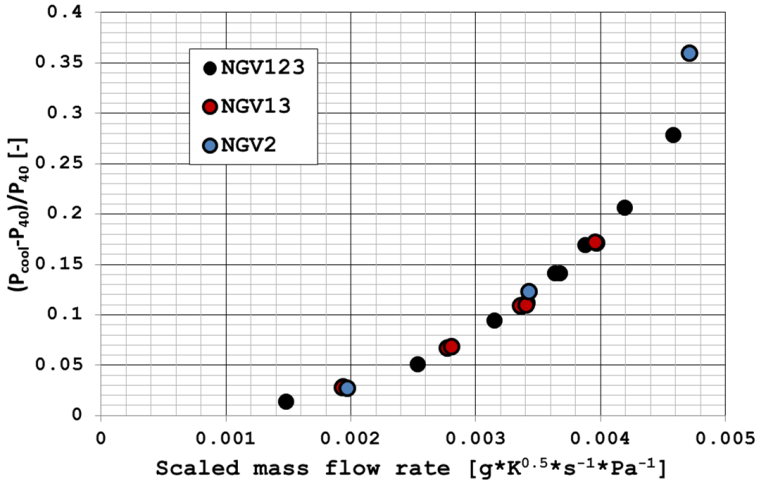

Figure 4.9: Results of selective cooling system flow checks

were fed (*Test NGV13*). For each test a sweep of coolant mass flow rates was investigated, while the mainstream was set at the nominal conditions, in order to built a characteristic curve of the system. A pressure ratio, calculated as $(P_{cool} - P_{40})/P_{40}$ was related to a scaled coolant mass flow rate; P_{cool} and P_{40} are measured in the coolant plenum chamber and by the Plane 40 pressure tap respectively. Since the Plane 40 pressure, which is constant for all the investigated airfoils, was used as the discharge pressure, an eventual unbalance in coolant mass flow among the airfoils would result in different characteristic curves. To directly compare the results of the three runs, the measured coolant mass flow rate was multiplied by three for Test NGV2 and by 1.5 for Test NGV13. Results, reported in Fig. 4.9, show that the curves of all the three tests overlap with each other in all the investigated range of mass flow rates. The mass flow rates evaluated from the runs, differed from each other by less than 2%. Therefore an additional verification that the achieved coolant mass flow split follows the expected distribution was achieved.

A final commissioning test was carried out in order to verify a different assumption; as it was detailed in the previous chapter, the different pressure ratio between DP and IOP_2 conditions could lead to a different coolant mass flow split among the different film-cooling rows, between the two cases. This

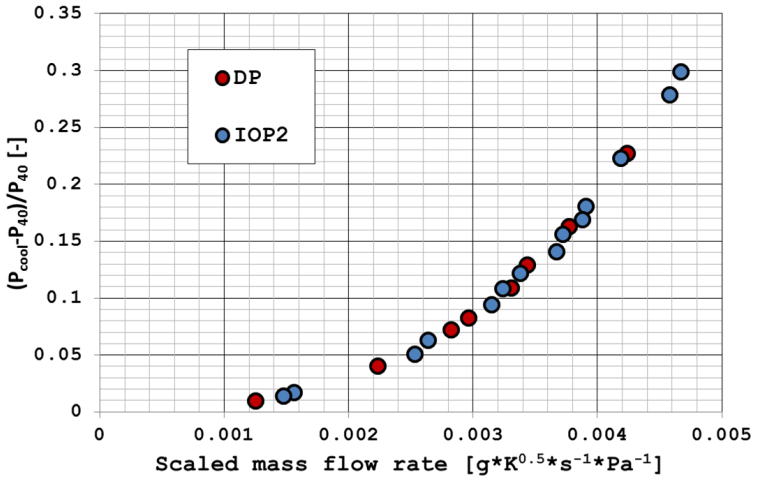

Figure 4.10: Results of cooling system flow checks in DP and IOP_2 conditions

would cause PSP tests, for adiabatic effectiveness calculation, not to be able to correctly predict the behaviour in nominal conditions; nevertheless, due to the limited differences it was stated that very reduced deviations are expected. This hypothesis was verified by comparing the characteristic curves, built with all the three airfoils fed, calculated in DP and IOP_2 mainstream conditions. As stated above, since the pressure ratio is calculated using Plane 40 pressure, instead of the actual holes discharge pressure, a different coolant distribution among the rows would lead to a calculation of different curves. Results, reported in Fig. 4.10 demonstrate that a very similar behaviour was found. In the point of nominal coolant mass flow rate, the effective areas measured for the two conditions, differ for less than 1.5%, well within the measurement uncertainty.

Summarizing, the test rig design process has been carried out by a thorough CFD activity in order to find an optimized configuration. The pursued configuration was such that the flow field evolving through the two central passages, bounded by NGVs 1 and 3, showed minimal differences with respect to a reference configuration; this ideal configuration is given by the case where the flow field approaching the NGV module in the central sector of the rig would pass through a periodic (i.e. full annular) cascade. CFD calculations were able to find a rig geometry where the evaluated differences

between actual and reference cases where very limited, in terms of pressure distribution on the NGV profiles and at the cascade exit. Moreover, some experimental results, together with additional commissioning tests, were exploited to demonstrate that the rig works as it was predicted by the calculations, regarding the above mentioned aspects. The NGV cooling system behaviour was also evaluated, in order to check that it didn't create unbalance in the coolant mass flow distribution and consequent alterations in the pressure profiles. All the results pointed out that the rig functioning was in line with what expected and, therefore, that the measurements carried out on it can be correctly exploited to pursue the goal of this work.

4.2 Development of an automatic Traverse System for probes handling

Before moving the focus to the description of the adopted measurement techniques and to the results of this treatment, which will be the focus of the next three chapters, it is useful to complete this small account of the instrumentation design process by providing a quick description of the traverse system. As stated previously, it was used to automatically traverse both five hole probe and hot wire probes on Plane 40 and 41, in order to explore the central sector domain through fine meshes. Even if its design constituted an important part of this Ph.D. activity, the description of all the evaluations related to its mechanical design go beyond the goal of this treatment. Nevertheless, a quick description of it will be provided, as it allow to have a better understanding of the probe traversing tests execution as well as of the accuracy in the probes positioning.

The traverse system was designed in order to allow three kind of probe motions, as sketched in Fig. 4.11: horizontal displacement, vertical displacement and rotation along its axis.

To fulfill these requirement, the developed traverse system is made by two main parts: the first one is a structure that allows the horizontal dis-

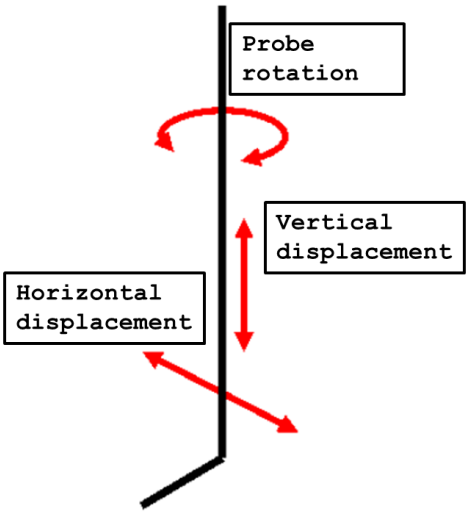

Figure 4.11: Traverse system concept

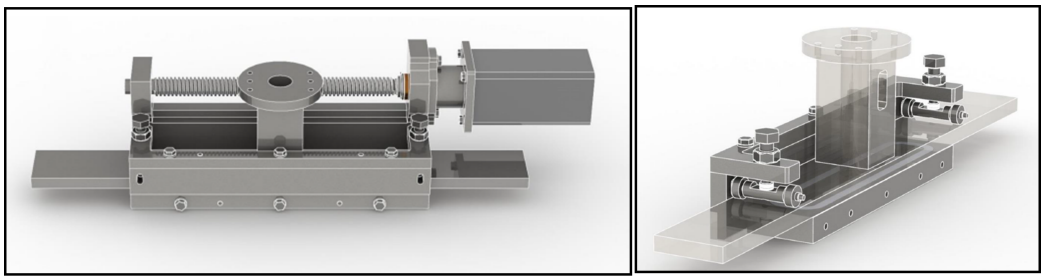

Figure 4.12: Structure for horizontal displacement: CAD model (a) and focus on the horizontal sled (b)

placement; it also has the goals of allowing to install the traverse system on the test rig without creating any leakages. A second structure, where the probe is fixed, can be mounted on the first one; it stricts the needs of vertical displacement and rotation of the probe.

Concerning the first structure, whose CAD model is reported in Fig. 4.12a, its main component is an horizontal sled, reported in transparency in Fig. 4.12b, that can be displaced by means of a nut screw system actuated by a stepper motor. The layout of the second structure, responsible for the vertical displacement, is reported in Fig. 4.13a; a flange allows to install it on the horizontal sled. The vertical displacement is achieved through a nut screw

system, similar to the one that moves the horizontal sled (vertical screw in the figure). Concerning the probe rotation, it is obtained thanks to a worm screw that acts on a gear wheel; the probe is fixed to the latter, as it is sketched in Fig. 4.13b. Both displacements are actuated thanks to two stepper motors, as it can be seen in the figure. Combining the gear ratios of the three actuating systems and the stepper motors angular resolution, positioning accuracies of $\approx 0.1mm$, for horizontal and vertical displacements, and $0.2°$, for the probe rotation, are achieved. Fig. 4.14, finally reports a CAD model of the whole traverse system, with the five hole probe installed on it. Concerning the control system, its development was carried out by an external company, following the provided guidelines. The control framework is made by a fanless PC that commands the stepper motors via Modbus connection; it is also able to acquire data from THT Lab instrumentation, as *National Instruments*® boards and pressure scanners, via ethernet connection. A National Instruments 9212 board is integrated in the framework, to acquire two J-type and two K-type thermocouples. A schematics of the

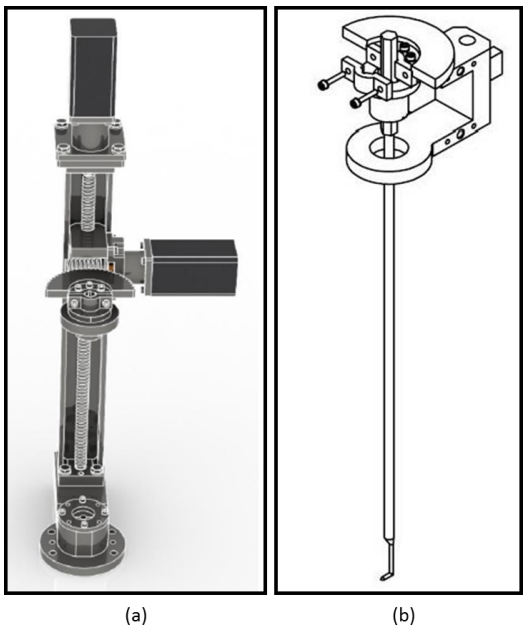

Figure 4.13: Structure for vertical displacement and probe rotation: CAD model (a) and focus on the probe fixing system (b)

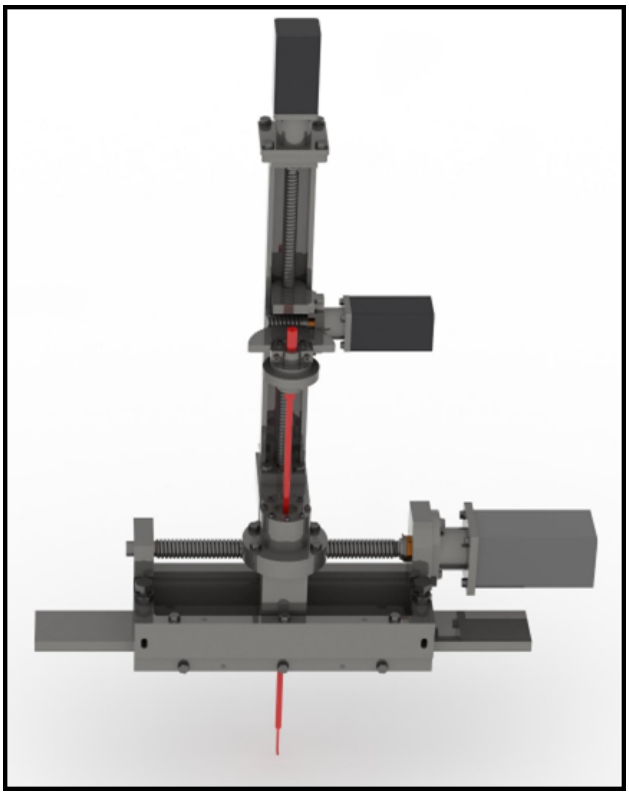

Figure 4.14: CAD model of the traverse system with five hole probe installed

control framework is reported in Fig. 4.15. A pendant can be used, to command the stepper motors, for manual probe motion, instead of the software control. The control software has been developed in *Labview*®; it allows to select the instrumentation to be used and to enable or disable each stepper motor. Measurement meshes can be selected from text files, as a list of positions where the probe has to be sequentially driven and readings have to be recorded . Parameters like acquisition frequency and duration can be independently set. Moreover a *waiting time* can be selected, so that, after the probe has reached the desired position, a certain number of seconds is put before the starting of the acquisition; in this way, hysteresis issues, for probes with reduced frequency response can be avoided. For each mesh point, an output file with the instantaneous acquisitions of all the selected instruments, is generated; moreover an additional file, where the average quantities of all the measurement points are summarized, is provided.

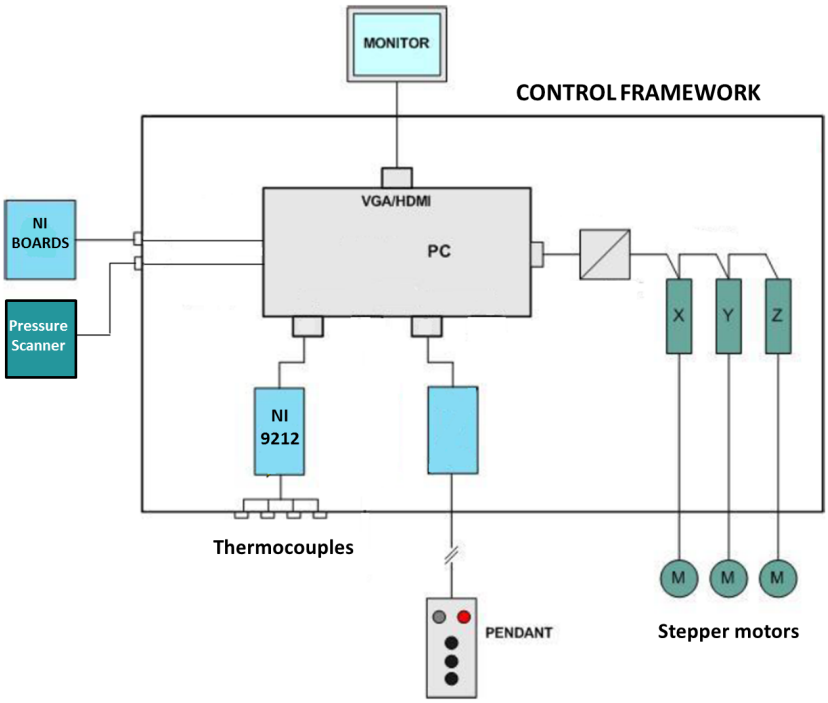

Figure 4.15: Schematics of the traverse system control framework

In the next section, where five hole probe and hot wire anemometry tests will be described, details of the employed acquisition parameters, instrumentation and measurement mesh will be provided, separately for each measurement technique.

Chapter 5

Experimental Techniques and Data Reduction

Four different experimental techniques have been exploited to carry out the characterization of the test rig. In this chapter all of them will be described. For each technique, the focus will be initially placed on its basic theory, before moving to the description of how it was applied in the present campaign.

5.1 PIV measurements

In the very first part of the research carried out within this Ph.D. course, flow field measurements of the combustion chamber were carried out; standard 2D Particle Image Velocimetry (PIV) was exploited for the goal.

PIV technique is based on the insertion of seeding particles inside the flow, in order to track the mean flow field. The particles are illuminated through a laser sheet and their positions are recorded by a CCD (Charge-Coupled Device) camera in two different instants, setting the desired time delay between two laser pulses. In order to evaluate the particle movements, the images acquired by the camera are divided in small interrogation areas and an homogeneous movement of particles within each area is assumed. A statistic approach based on 2D cross correlation methods is exploited to compute a vector associated to the particle movement. Moreover, the velocity

vector on the laser plane is directly computed by the displacement vector, knowing the time delay between the pair of images and the *magnification factor* (ratio between CCD and "real space" distances). A generic setup for PIV measurements is reported in Fig. 5.1 where it is possible to observe the main components necessary to perform the tests. The laser system,able to generate monochromatic light with high density of energy, is used to illuminate the seeding particles. A set of optic lenses are used to generate a thin light sheet while a mirror can be used to deviate it. The seeding particles must be constituted by inert substance and must have a small diameter in order to follow the streamlines of the flow field. A dimensionless number able to describe the capability of particles to follow the mean flow field is the Stokes number:

$$St = \frac{\tau.U}{l} \tag{5.1}$$

where U is the fluid velocity of the flow well away from the obstacle, l is the characteristic dimension of the obstacle and τ is the relaxation time of the particle (i.e. the time constant in the exponential decay of the particle velocity due to drag). In the case of Stokes flow, which is when the particle (or droplet) Reynolds number is less than unity, then the particle drag coefficient is inversely proportional to the Reynolds number itself and the characteristic time of the particle can be defined as:

$$\tau = d_p^2 \frac{\rho_p}{18\mu} \tag{5.2}$$

If the fluid acceleration is not constant or Stokes drag does not apply (e.g. at higher flow velocities), the equations of the particle motion become more difficult to solve. Nevertheless, τ remains a convenient measure for the tendency of particles to attain velocity equilibrium with the fluid [113]. To follow the streamlines, the particles must have a St number as low as possible. For $St > 1$, particles will detach from a flow especially where the flow

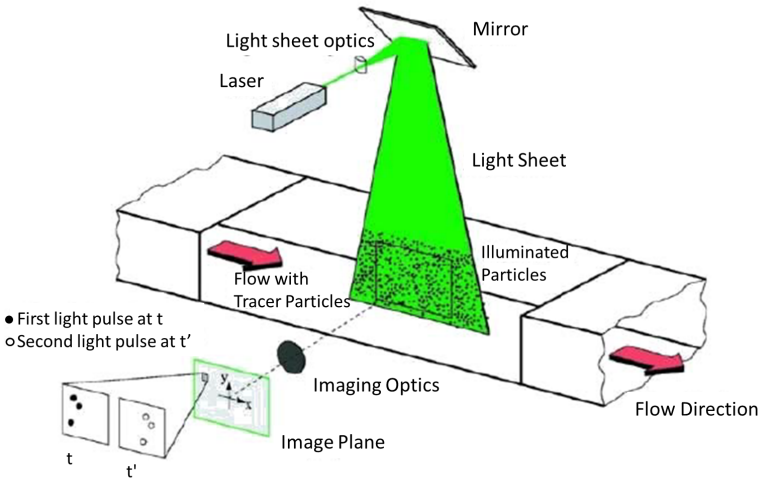

Figure 5.1: PIV measurements general layout

decelerates abruptly. For $St << 1$, particles follow fluid streamlines closely and if $St << 0.1$, tracing accuracy errors should stay below 1% [114]. In addition to the previous characteristic, the particles must have good properties in terms of Mie scattering in order to maximize the scattered light and the measurement sensitivity. In general either solid, liquid or gaseous seedings can be used. For tests at low temperature, one of most reliable substance that can be used as seeding is the mineral oil.

5.1.1 Details on endoscopic PIV

PIV is widely used in turbomachinery applications since it is a non-intrusive technique and allows a 2D flow field measurement, instead of punctual ones. On the other hand, one of the drawback is that it requires adequate optical accesses, as wide as possible, in order to carry out accurate measurements. Flow field investigations using PIV are typically performed using transparent test samples or mirrors to acquire images and insert laser sheets inside the test article [115, 116]; however the requirement of performing tests higher TRLs and in complex geometries (i.e. combustor simulators), where it is not possible to provide dedicated optical windows, demands the use of dif-

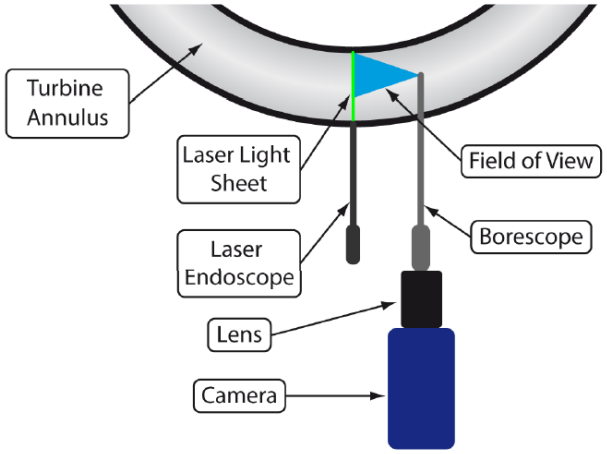

Figure 5.2: Example of endoscopic PIV layout [117]

ferent experimental approaches. The most common approach is to carry out measurements using endoscopic PIV, by using boroscopes for laser sheet insertion and/or for acquiring images. Fig. 5.2 shows an example of endoscopic PIV application setup [117]: both laser sheet insertion and image acquisition are carried out by means of boroscopes; in particular a 90° viewing direction boroscope is used to frame the measurement plane. Using this approach the required access can be reduced to the boroscope dimensions (typically 8-10mm holes). On the other hand several drawbacks must be ascribed to this technique. First of all, the measurement becomes intrusive, even if the boroscopes are not placed exactly in the measuring plane. The small aperture of the camera boroscope damps the light sensitivity and, in order to achieve relevant signal-to-noise ratios and particle image size, it is necessary to reduce the distance from the target plane [117] and increase the power of the light source, which can generally lead to issues of reflections. Moreover the boroscope optics present very low focal lengths (i.e. large viewing angles), creating very important distortions in the acquired image [118]. Even if such a distortion can be corrected, together with other effects like inaccurate optical alignment and refraction by optical windows [119], another related issue arises when carrying out 2D PIV using only one camera in complex 3D flow fields, which is a typical approach in test rigs for turbomachinery appli-

cations with several constraints in terms of optical accesses. In particular, using boroscopes with large viewing angle, the seeding particle displacements orthogonal to the measurement plane are seen as apparent radial displacements caused by the imaging in convergent light [120]. Despite the effect can be corrected in stereo-PIV application, this is not possible in 2D PIV cases. Fig. 5.3 shows the flow field measured through endoscopic PIV by Xiong and Merzkirch [121] in a fully developed flow where the velocity should be completely axial (i.e. orthogonal to the measurement plane); apparent radial components, increasing with the distance from the image center (i.e. with increasing viewing angles), are visible. As a consequence only the central part of the image is reliable, leading to very small investigated areas. Xiong and Merzkirch [121] tried to analytically correct this effect but their method requires the knowledge of the whole velocity field orthogonal to measurement plane.

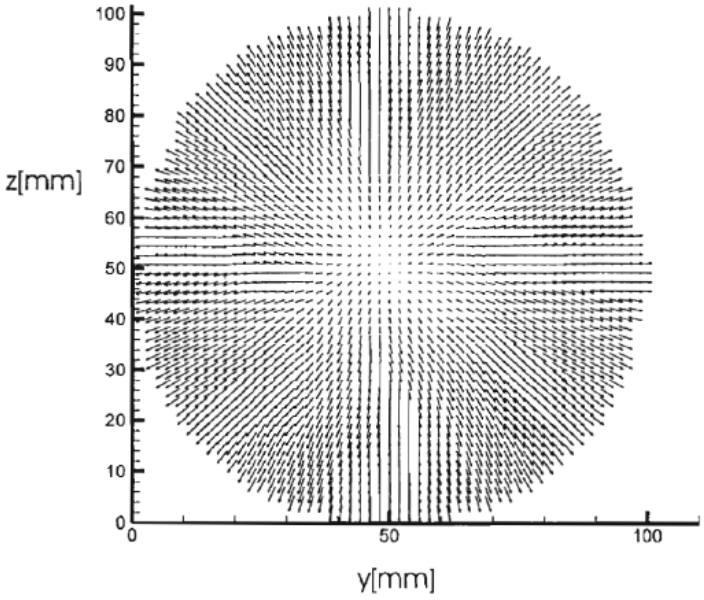

Figure 5.3: Apparent displacement measured by Xiong and Merzkirch [121]

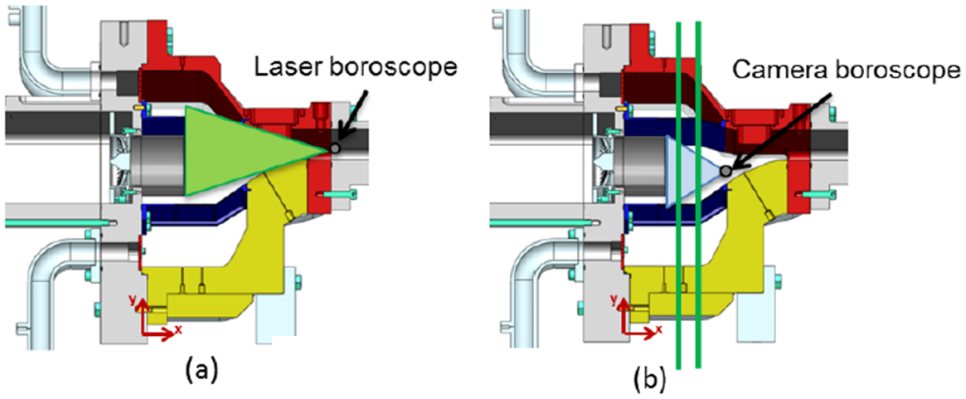

Figure 5.4: PIV measurements setup for symmetry plane (a) and for Plane CC1/CC2 (b)

5.1.2 PIV measurements setup

PIV measurements have been performed using a *Dantec Dynamics* PIV system, consisting of a 120mJ *New Wave Solo* Nd:YAG pulsed laser, operating with a wavelength of 532nm, and a *SpeedSense* 4Mpixel camera operated at a frame rate of 10Hz in double frame mode. All devices are controlled via the commercial software *Dantec Dynamic Studio*, that allows system syncronization and images postprocessing. Different experimental setups have been adopted to carry out PIV on the different planes (see Section 3.3 and Fig. 3.12), as sketched in Fig. 5.4.

For the symmetry plane, a 8mm Dantec Dynamics laser boroscope, inserted in the rig through dedicated holes in the metal lateral window and in the outlet section, is used to create a laser sheet on the target plane. The laser sheet has an opening angle of about 17° and a thickness of about 1 mm in order to limit the measurement noise due to out-of-plane drop-out particles [122]. A 12mm diameter air-cooled jacket is used to protect the boroscope; the cooling air is discharged into the ambient through an aperture in the jacket, in order to limit the boroscope temperature and to keep it clean from seeding particle deposition. A thermocouple on the tip of the air jacket is used to monitor the boroscope temperature and hence to set

the appropriate cooling flow. Images are acquired by the camera through the pyrex lateral window. In order to map a sufficient part of the symmetry plane it has been necessary to repeat the measurement for different laser position (i.e. inserting the boroscope in different holes on the metal lateral window) and inclination (i.e. rotating the boroscope so that the laser sheet enlightens different chamber positions without changing the insertion hole). The camera has been positioned at a distance from the target that results in a magnification factor close to 0.12 and in a particle image size of about 2 pixel, to minimize the measurement uncertainty [122]. Images had to be acquired in different camera positions, to map the desired portion of the measurement plane. For each camera/laser configuration 1000 image pairs have been acquired, in order to guarantee statistical convergence of the results. Each set of image pairs has been post processed, after subtracting the mean pixel intensity and the velocity field has been calculated using an adaptive cross-correlation iterative method with interrogation area shift between two image of the same pair, in order to limit the in-plane drop-out particles and to increase the signal strength [113]. Interrogation area refinement starts from a 164x164 pixel initial windows size to a final size of 32x32, with 50% overlap. Vector validation has been carried out through the universal outlier detection method [123] and the outliers have been substituted by linear interpolation with neighbour vectors. The obtained vector maps, resulting from different camera/laser configurations, have then been combined using a in-house developed Matlab-based code, to get a single vector field covering the whole measurement plane.

For planes CC1 and CC2, the laser sheet was placed on the target plane, through one of the lateral pyrex wall, without using the boroscope. On the other side of the rig the metal window was installed, in order to insert a 8mm *Olympus* camera boroscope (view angle of 25°), through one of the holes realized on it. The holes positions had been chosen in terms of trade-off between investigated area and resolution. The camera boroscope was protected by an air jacket as described earlier for the laser one. Boroscope-to-target distances were 60 and 80 mm resulting in magnification factors between 0.11 and 0.125. 1000 image pairs are acquired for each camera/laser positions. In order to

get rid of the apparent radial displacement due to the boroscope viewing angle, the obvious choice would be to cut out the areas far from the image center, and consider only the very central part of the image. This approach would require to acquire several image, in different boroscope position, in order to map a sufficient part of the investigated plane. However, due to the limited optical accesses, it is possible only to acquire images in different horizontal positions of the boroscope (i.e. regulating its insertion depth) while it is not possible to regulate the boroscope vertical position. In this way the final image would consist in a thin strip covering a wide horizontal range but a very low vertical (i.e. radial) one. In order to mitigate this issue, it has been decided to evaluate the results by only considering V_{tg}, the velocity component that is tangential to the boroscope center (i.e. the image center), since it is not affected by the radial apparent displacement. By positioning the image center as close as possible to the center of the rotating structure generated by the central swirler, this velocity component can be exploited for the evaluation of the tangential momentum which is important to characterize the strength of the swirling flow. Obviously, this choice makes it impossible to acquire images in different positions and then combine them into a single vector field, since the overlapping areas of images taken in different boroscope position would not return the same velocities, due to the different points which the tangential component is referred to (i.e. different image centers). However, the mapped area is wide enough to capture a sufficient portion of the central sector in single boroscope position.

For all the configurations, before running the tests, calibration images with a dedicated dot pattern have been acquired, so that the software can calculate a dewarping model to get rid of optical distortions. A third order polynomial mapping function was used. Concerning the seeding, silicon oil particles have been used, with an evaporating temperature around $300°C$, so that the mainstrem could be heated up to the desired temperature. The particles, with a mean diameter of about $1\mu m$, have been generated by means of a Laskin nozzle and introduced upstream the swirler, while coolant flows were not seeded. In order to damp the laser reflections inside the chamber and keep the signal-to-noise-ratio (SNR) to acceptable values, black paint

has been applied to the chamber walls. Some areas could not be painted and stronger reflections had to be accepted; for example it was not possible to black paint the multiperforated liners to avoid clogging of the effusion cooling holes. In a few of these particular zones reflections were high enough to bring the SNRs close to 1 and to prevent from distinguishing the seeding particle from the background, leading to erroneous calculated vectors. In presenting the results these zones will be masked or specified in the description.

According to Westerweel [122], the uncertainty on the particle displacement should be in the range of 0.1 pixels thanks to sub-pixel interpolation. With particle displacements varying from 3 and 10 pixels (depending on the local velocity and on the chosen time delay between to laser pulses) uncertainty between 1 and 3% are expected. Beside this source of error, another one arises from out-of-plane displacement and consequent apparent displacement generated on the 2D measurement domain. Regarding PIV results on the symmetry plane, obtained without the use of the boroscope, uncertainty around 3% on velocity magnitude, calculated knowing the values of camera optics viewing angle and out-of-plane velocity, are expected. It is worth to notice that these uncertainty values are located in the areas where the viewing angle and the out-of-plane velocity are both the highest; apparent displacement is very close to zero for all the other positions where either of the two factors decreases. Uncertainty contributions due to the seeding particles not exactly following the flow motion have been neglected since the reduced particles dimensions keep Stokes number values below 10^{-3}. Thermal expansion of the test rig, that could affect measurement positioning and calibration, have been calculated to be very limited (below 0.2 mm) and, therefore, have not been considered.

5.2 Five hole probe measurements

5.2.1 Basics on directional pressure probes

Directional pressure probes allow to evaluate static and total pressure and, together with the knowledge of the flow density, the flow velocity in a

point of the flow field. Their working principle is based on the fact that the pressure measured by a static pressure tap, for fixed total pressure of the flow, varies with the relative position between the flow direction and the tap itself. In other words, the dynamic pressure component felt by the tap varies with the flow direction. Simplifying the treatment, it is possible to state that the measured pressure varies between total, if the tap axis is parallel to the flow direction, and the static pressure, if the axis is perpendicular to the flow direction. While it is not so complex to measure the flow total pressure, a real static pressure measurement is more difficult and the tap require other characteristics in addition to be perpendicular to the flow direction; for example the tap diameter must be small with respect to the diameter of the duct in which the pressure is measured, in order to prevent the creation of a stagnation zone, that would lead to an overestimation of the read value.

However it is possible to use the fact that the measured pressure changes with the skewness of the flow, in order to evaluate its direction, beyond static and total pressure. An application of this type is based on a two-taps probe, shown in Fig. 5.5. As long as the two taps are symmetric with respect to the flow direction, they measure the same pressure value; as the flow direction changes the measured values start to deviate one from the other. It is possible to understand the flow direction, simply by rotating the probe until the values match again; hence, this is a 2D directional probe that allows to

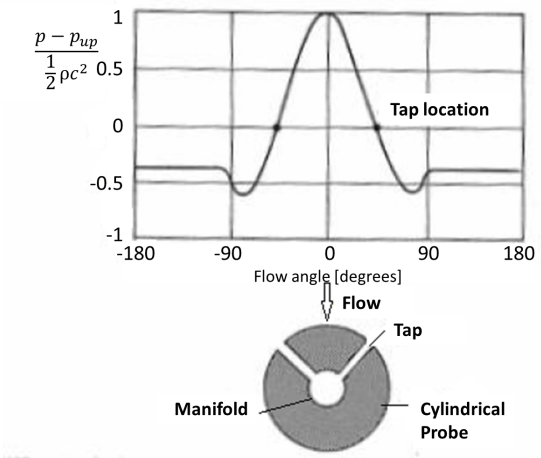

Figure 5.5: Directional probe with two pressure taps

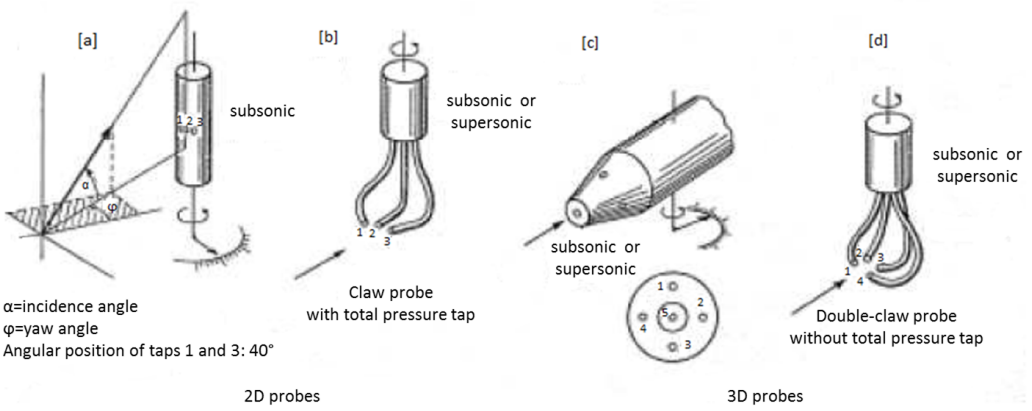

Figure 5.6: 2D and 3D directional probes examples

measure the velocity direction in the plane that contains the taps (and the velocity module if the density is known).

The probes used for turbomachinery applications are usually characterized by a central hole and two lateral ones, for the 2D configuration, or four/five in the 3D one, as indicated in Fig. 5.6; in most of the situations they are cylindrical probes of very reduced dimensions, to limit the potential effects induced on the measured flow field by the presence of the probe itself, like in the (c) case of the figure.

For their correct utilization it is necessary to establish a relationship between the pressure values, measured in the different holes, and static/total pressure and the flow direction; the latter can be identified through two angles on two orthogonal planes, referred to as pitch (α) and yaw(γ) angle, as shown in Fig. 5.7.

It would be useful to obtain such relationship from an analytical procedure; due to the nature of the equations that regulate the flow motion, though, this would be possible only for simplified geometries (like spherical probes). Beside that, such procedure would make the found relationship inaccurate due to the probe manufacturing imperfections and it is never used, even when it is, in theory, possible [124]. In order to use these instruments,

therefore, it is necessary to perform a calibration, to find the above mentioned relationship. To make it independent from the flow velocity, this relationship is not related to the values of pressure read in the holes but to non-dimensional parameters derived from them [125]. For 2D probes three parameters are used:

- $C_b = \frac{P_r - P_l}{P_c - \frac{P_l + P_r}{2}}$
- $C_{pt} = \frac{P_c - P_t}{P_t - P_s}$
- $C_{ps} = \frac{P_c - \frac{P_l + P_r}{2}}{P_t - P_s}$

where P_r, P_l and P_c are the pressures measured respectively in the right, left and central hole and P_t and P_s are total and static pressure of the flow. Therefore, the calibration consists in inserting the probe in a wind tunnel that allows to control the flow total pressure and velocity and in recording the pressure values measured in the holes, in order to evaluate the three coefficient values, for different probe inclinations. These coefficients are used for a direct procedure, since, during the probe utilization, it is possible to evaluate the first coefficient, and so the flow angle from the calibration curve, directly from the pressure values read in the holes; from the flow angle, the other two coefficients can be evaluated and so static and total pressure. An iterative procedure can be used as well, based on three different parameters, in which pressures and angle evaluation is achieved by a process that starts

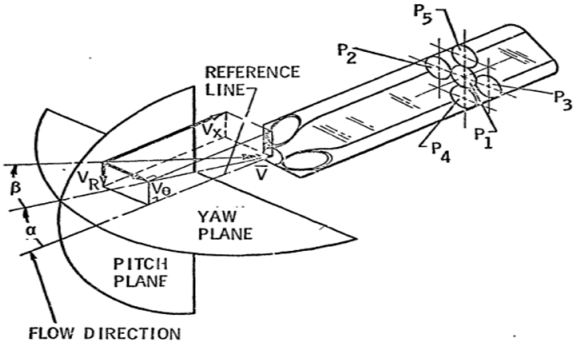

Figure 5.7: Flow angles used to characterize the flow direction in space [124]

with an hypothesis on the flow static and total pressure [125].

The same considerations can be extended to three dimensional probes with five holes, that allow to find, beyond static and total pressure, pitch and yaw angles. The difference stays in the fact that four coefficients are used; the calibration process, that is much more time consuming in this case, requires to evaluate these coefficients for each couple of flow angles, obtaining four surfaces, instead of curves, that describe each coefficient trend for varying angles. The four coefficients that are generally used in the direct procedure have been defined by Treaster and Yocum [124]:

- $C_\alpha = \frac{P_u - P_d}{P_c - \bar{P}}$
- $C_\beta = \frac{P_r - P_l}{P_c - \bar{P}}$
- $C_{total} = \frac{P_c - P_t}{P_c - \bar{P}}$
- $C_{static} = \frac{\bar{P} - P_s}{P_c - \bar{P}}$

where P_u and P_d are the pressure values in the upper on lower holes, while $\bar{P} = \frac{P_u + P_d + P_l + P_r}{4}$ is the mean value among the measured pressures in lateral holes. Fig. 5.8 reports a typical results of this kind of calibration process [124].

The typical range of application to five hole probe, with this kind of procedure stays within ± 40° at most. Beyond these values an important separation generally occurs on the hole that results positioned in the downstream side and the read value shows very small changes for further flow angles increases. Therefore, the calibration is no more valid beyond certain values. A number of novel methods have been developed in the years to extend the typical five hole probe application range [126, 127, 128]. Even if some of them have shown promising results, the classic, above described, calibration results to be the most used one, being more simple and more reliable for different typologies of probes.

Even if the non-dimensional coefficients allow to scale the effect of the velocity magnitude, making the calibration valid for different values of it, it is not possible to scale other effects like Reynolds and Mach number ones,

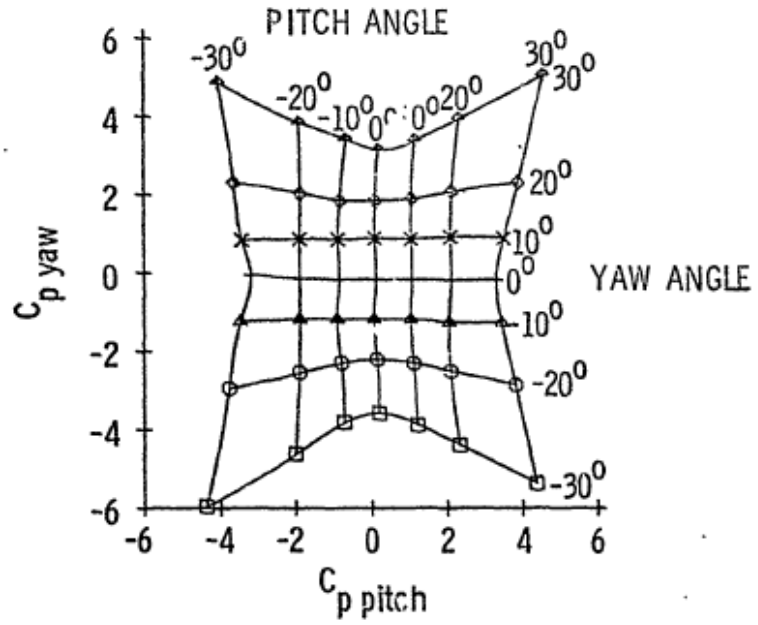

Figure 5.8: Result of a five hole probe calibration process [124]

that influence the flow behaviour around the probe and, thus, the read pressure values. Concerning Reynolds number, it alters both the characteristics of the separation, that occur on the back side hole and the deceleration of the fluid that invests the central hole. Typically these effects are important only at low Reynolds numbers; for very high numbers, on the other hand, the behaviour results quite insensitive to Reynolds variations [129]. Mach number influences the flow compressibility and, for fixed flow skewness, pressure differences among holes are altered. As a consequence, a certain calibration is valid only within certain limits of Mach number. Therefore it is common practice to carry out calibrations at different Mach numbers.

5.2.2 Five hole probe calibration and application

The five hole probe used in this work is a *Vectoflow* cobra probe, with a 3D-printed 3mm diameter head, reported in Fig. 5.9. It is provided with a J-thermocouple installed on the top part of the probe head, which is protected by a shroud, as for a Kiel probe, in order to make the thermocouple recov-

ery factor more insensitive to high flow angles and reduce the measurement uncertainty.

A thorough calibration process had to be carried out. Before going into the details of the probe calibration and application, the flow angles nomenclature must be pointed out. In general it is common to refer to flow angles as pitch and either yaw or swirl angle: the first one is the angle in the plane that contains the probe stem axis; the latter is the angle in the perpendicular plane. This was already pointed out in Fig. 5.7. Concerning the dual possible nomenclature of the second angle, most of the works that focus on probes calibrations refer to the "yaw" term, while, when the focus is placed on the evaluation of turbomachinery flow angles, it is more common to refer to "swirl". In this treatment the same approach will be adopted: the "yaw" term will be employed when referring to the calibration procedure; the term "swirl", on the other hand, will be adopted when talking about the results, either in terms of angle "felt" by the probe (i.e. in a probe reference system), or in terms of final results in the test rig cylindrical coordinate system. In fact they do not generally correspond due to the probe cartesian displacement within the rig and to probe preswirl, as it will be detailed in the following.

At combustor exit, very high flow angles, exceeding $\pm 50°$ are expected, at limited Mach numbers; on the other hand, at NGV exit, slightly lower flow angles should be encountered, at significantly higher Mach number. For these reasons, six different sets of calibration were carried out, at Mach num-

Figure 5.9: Picture of the five hole probe with the thermocouple shroud

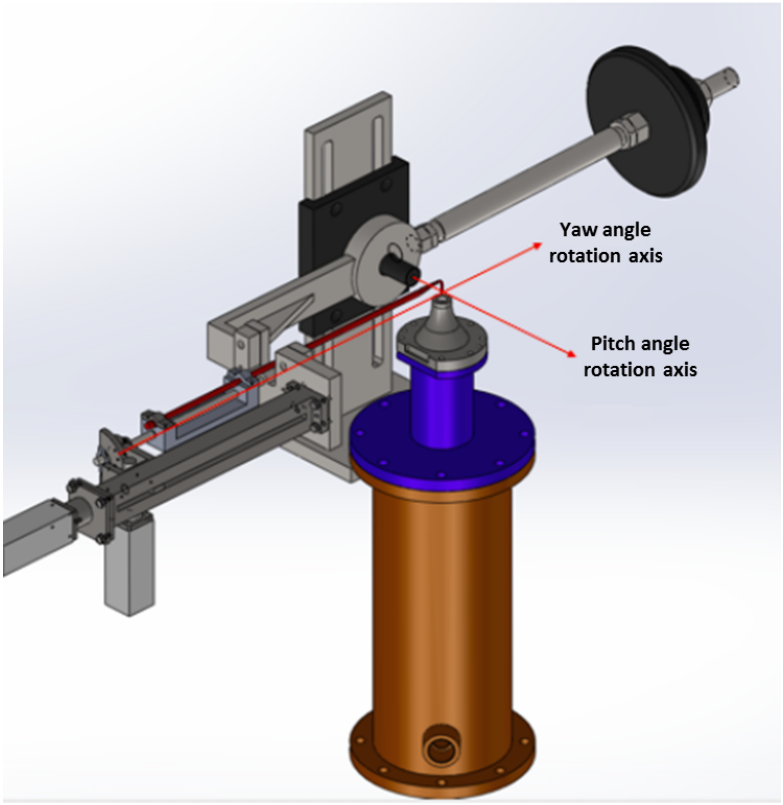

Figure 5.10: CAD model of the calibration apparatus

bers of 0.1, 0.3, 0.5, 0.7, 0.8 and 0.9. A calibration apparatus, reported in Fig. 5.10 was developed, in order to explore yaw angles up to ±75° and pitch angles up to +75°/-60°. A 150mm diameter tube (orange component in the figure) is used as a plenum chamber; its diameter was chosen in order to achieve close-to-zero velocity for all the investigated Mach number levels. A second tube, the blue component, is installed on it; its smaller dimensions were chosen in order to reach a wider pitch angle calibration range without incurring in a collision between the probe stem and the tube. A 10mm nozzle is used to create the calibration jet: its shape was designed in order to minimize the pressure losses and to achieve a jet velocity corresponding to the isentropic one for most of the jet width. The probe is handled with the same component used on the traverse system, which also allows to automatically set the yaw angle; the pitch angle, on the other hand, must be manually regulated acting on the barbell, clearly visible in Fig. 5.10.

Pressure and temperature are measured inside the plenum chamber, and the velocity at nozzle exit can be calculated simply by using isentropic Mach relationships, knowing the discharge (ambient) pressure. A set of valves and pressure regulators allow to set the desired pressure level inside the chamber (i.e. the desired nozzle velocity). Pressure was measured in both the plenum chambers and the measured differences stayed well below the measurement uncertainty for all the investigated conditions, meaning that negligible pressure losses and flow acceleration occurred during the passage of the flow in the second, smaller plenum chamber. Measurements with a Pitot tube showed that the achieved nozzle exit velocity corresponded to the value calculated through the above mentioned procedure over a span of 9mm.

Concerning the five hole probe acquisitions post-processing, the method proposed by Paul et al. [128] was employed in order to maximize the probe angular range. This method consists in a calibration sectoring, modifying the calibration coefficients defined by Treaster and Yocum [124] depending on which port is measuring the higher pressure (i.e. on the flow skewness); in this way the value measured by the port that is in a separated flow region can be bypassed. Several methods were tried, with this one providing the best results. A *Matlab*®-based code was developed for the data post-processing; it is an iterative process which continuously switch on a different Mach number calibration set, according to the calculated Mach value at the previous iteration. The process stops as the calculated Mach number falls in the range covered by the adopted calibration set at that iteration. To evaluate the quality of the results and the limits of the probe, the calibration data was re-postprocessed with the developed tool; additional points, not coinciding with calibration ones, were acquired, in order to have a more in deep evaluation. Fig. 5.11 summarizes the results: green dots represents points that have been recalculated with a deviation lower than 2° from the imposed values, for both flow angles; red dots represents points recalculated with an error higher than this threshold, for either of the two angles. Both plots of the figure show only the points acquired at M=0.85. The points acquired at the other Mach numbers showed an analogous behaviour.

It is possible to note that, despite the adopted method, relevant error

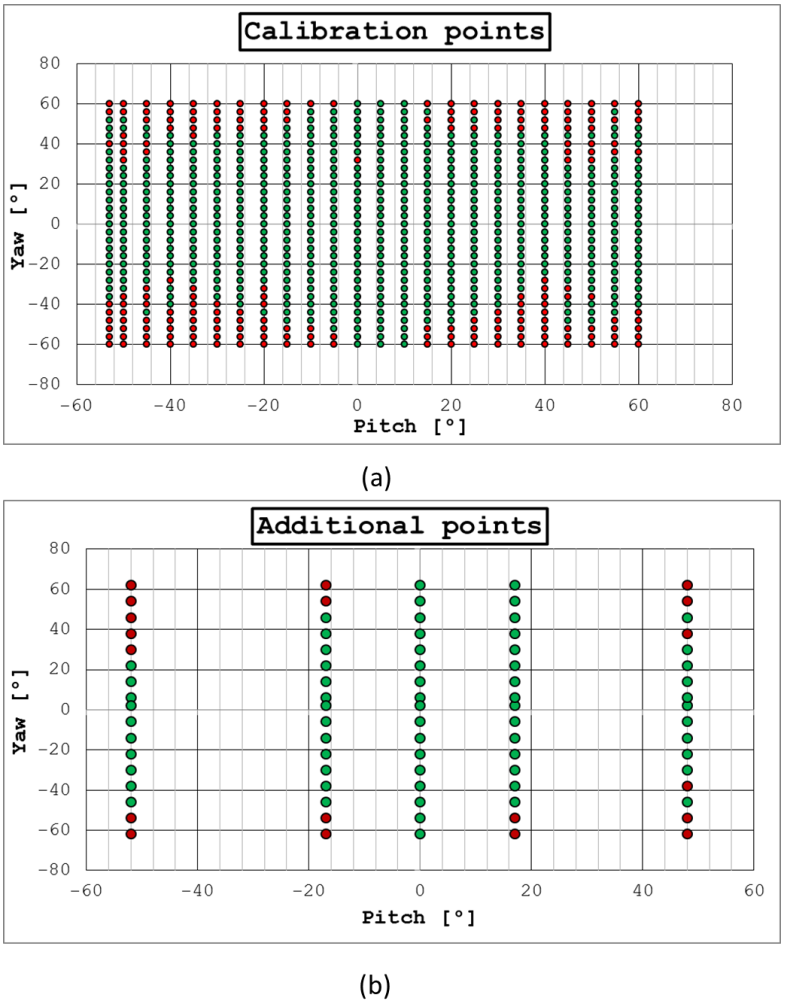

Figure 5.11: Results of five hole probe angular uncertainty evaluation at M=0.85: calibration (a) and additional points (b)

arise when both yaw and pitch angles are high. This is due to the calibration coefficients collapsing to very similar values for different angles. On the other hand, if the yaw angle is limited within ±30°, also the highest pitch angles can be measured with good accuracy. The post-processing tools was, then, modified in order to erase the points where the calibration coefficients fall in a range of singularity. In order to overcome the probe angular limitation, it was decided, for the measurements at combustor exit, to impose a preswirl of either +28° or -28° to the probe. In this way all the measured points

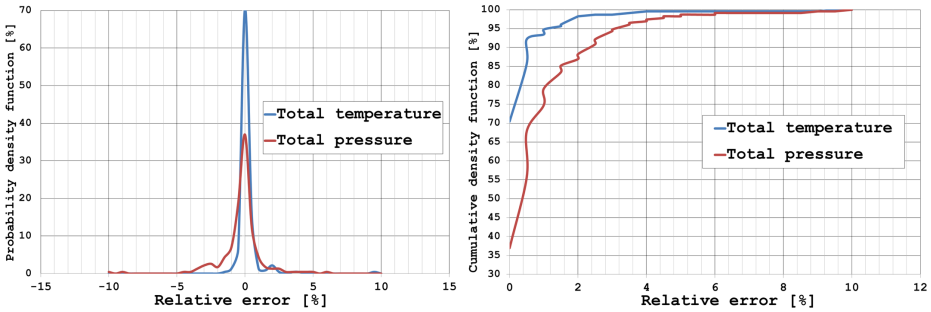

Figure 5.12: Uncertainty evaluation for total pressure and temperature

stay within the probe angular range, without incurring in singularity; results obtained by Caciolli [97] were exploited to define the correct preswirl value for each mesh point, without needing a more time consuming trial-error process. Concerning Plane 41, a preswirl of 62° was given to the probe, so that very limited yaw angles had to be measured, being the flow field much more aligned with the NGV exit angle. According to this evaluation, an uncertainty of 2° was admitted for flow angles measurements. The same method was used to evaluate the uncertainties on total pressure and temperature; Fig. 5.12 shows the results of the additional points re-calculation; since the reliability of the temperature response is poorly affected by the flow angles, results are reported for all the acquired points (about 230) and not only for the ones that fall in the accepted angular range. Results clearly show a reduced dispersion with errors that stay within 3% and 2% for total pressure and temperature respectively, for 95% of the acquired points. Values of 3% and 2%, with a 95% confidence level, were, then, considered as nominal relative uncertainties on total pressure and temperature. It must be also stated that, if only the points that fall in the accepted angular range (according to the results of Fig. 5.11), the uncertainty on total pressure can be further reduced. Additional details of five hole probe calibration and post-processing method can be found in Appendix 1.

Five hole probe tests have been carried out using the traverse system described in Section 4.2, in order to automatically move the probe in different positions within the investigated plane. A 800 points mesh was adopted on Plane 40_2, in order to achieve a resolution of about 2 mm in radial direction

and about 0.85° in the azimuthal one; in the central part of the domain, where severe gradients in the flow angle pattern are expected, the resolution has been doubled, to obtain an azimuthal resolution of 0.42°. The whole investigated area covers $t = \pm 10°$ against a central sector extent of 18°. Due to the convergent shape of the inner liner it was not possible to explore the inner part of the annulus, about 10mm, in order to prevent the five hole probe elbow from colliding with the inner wall, downstream of the measurement plane, as it could be seen from Fig. 3.13. Similarly a 5 mm span close to the outer wall could not be investigated due to the presence of the thermocouple shroud. The post-processed results, in the discrete position of the measurement mesh, were then interpolated into a finer grid, to produce 2D contour plots. Regarding Plane 41, due to the three sector nature of the rig, the measurement could not be carried out across $t = 0°$; the azimuthal position to be investigated was calculated knowing the distance between the NGV trailing edge and the measurement plane and the expected NGV exit angle. For the sake of a clearer view, results were then rotated to make the

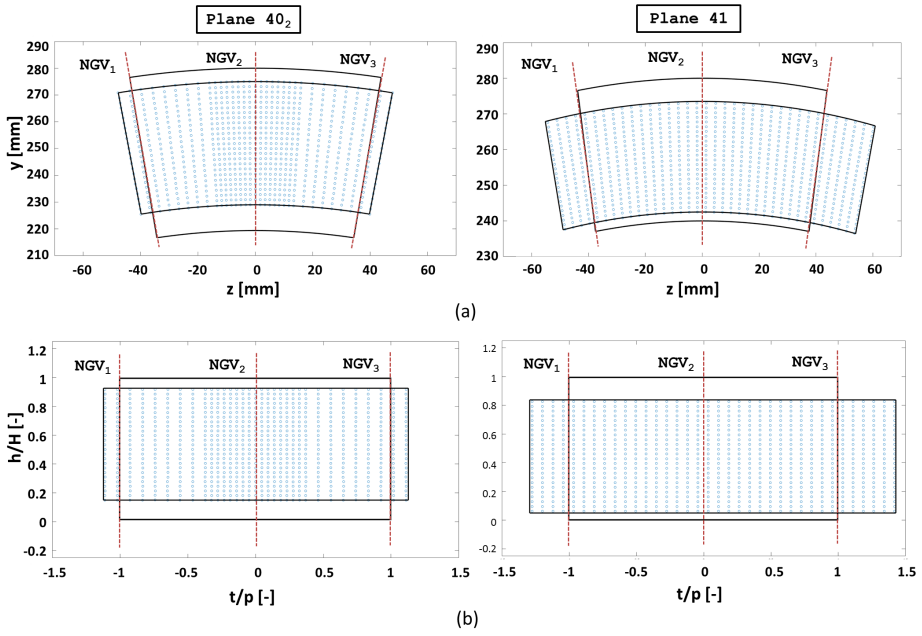

Figure 5.13: Five hole probe measurement mesh on Plane 40_2 and 41: annular (a) and linearized (b) representation

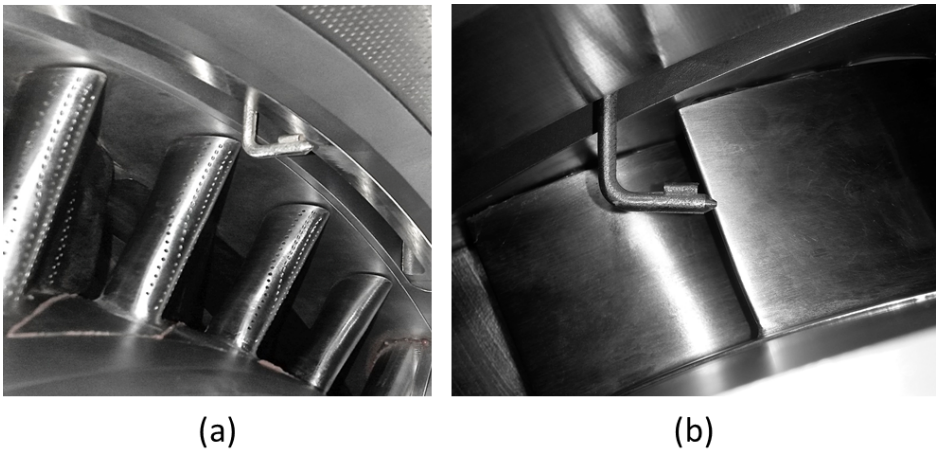

Figure 5.14: Five hole probe on Plane 40_2 (a) and 41 (b)

wake of the central NGV coincide with $t = 0°$. An 850 points mesh was used to obtain a resolution of 1.3 mm in radial direction and 0.7° in the azimuthal one. Thirteen angular positions per NGV pitch were achieved. No mesh refinements in correspondence of the profiles trailing edges was used: due to the highly swirling inflow, in fact, important flow angle gradients were expected also within the NGV passage, so the same importance, in terms of spatial resolution, was given to all the positions of the annulus. A preliminary test with a doubled angular resolution showed that no sensitive further improvements could be achieved, at least with the present instrumentation (i.e. probe size). An azimuthal extent of 24° was investigated. The investigated areas are shown in Fig. 5.13a, together with the boundaries of the central sector and the position of the NGV profiles, according to the nomenclature reported in Fig. 4.6. In order to allow for a better interpretation, in Chapters 6 and 7, results are, then, linearized and reported in terms of non-dimensional height (h/H, y-axis) and non-dimensional tangential position (i.e. tangential coordinate t [°], made non-dimensional by the 9° NGV pitch p). The linearized representation is reported in Fig. 5.13b. The central sector covers the tangential span between -1 and 1, due to the 1:2 swirler-to-vane ratio. Fig. 5.14 shows the five hole probe inserted in the test rig on Plane 40_2 and 41.

Concerning Plane 41 investigation, some additional considerations, re-

garding the impact of the probe dimensions can be made. Flow investigations in turbomachines with probes always bear the risk of measuring failures and misinterpretations. Due to the size of the probe in many cases the spatial resolution (i.e. pressure ports not located at the same position) cannot be neglected. Furthermore, interactions between the flow and the probe itself can occur [130]. The problem can be significant when the investigation is focused on cascade exits, due to flow compressibility, the proximity of the vanes trailing edges and the pressure gradients. In general different methods for spatial resolution and pressure gradients corrections have been developed [131]. In the present configuration, the probe size is not negligible with respect to the test case dimensions. In particular the ratio between the TE-probe tip axial distance and the probe diameter ($\Delta x/d$) is about 3; the probe diameter is also three times bigger than the minimum trailing edge thickness. Therefore some degree of interaction must be expected. The correction method proposed by Hoenen et al. [130] was adopted, in order to account for the spatial resolution issue. The differences between the corrected and non-corrected results were found to be negligible, showing up for a good results reliability. A remaining issue of local streamline alteration, in the very proximity of the vanes trailing edges, must be, anyway expected. According to Hoenen et al. [130], for similar values of Mach number and $\Delta x/d$, this errors should not overcome 2°. Therefore, even if this value is strongly case-dependent, it is not expected to have a large entity. More importantly, it is limited to the trailing edge azimuthal position and does not prevent from fulfilling the main goal of these measurements, in the evaluation of the global flow field and of the effects of the residual swirl. During the description of the results (Chapter 7), the positions where the outcomes are expected to be partly affected by this issue will be highlighted.

Concerning the acquisition parameters, data was acquired and averaged over two seconds; due to the low frequency response of the instrument, after the probe reached the measurement point, a stand-by interval of two additional seconds was imposed, before starting the acquisition, in order to prevent from hysteresis issues. Pressure signals were acquired by mean of a *NetScannerTM System 9116* pressure scanner, interfacing with the tra-

verse system control PC; temperature data, on the other hand, was acquired through the NI9212 board integrated in the traverse system control framework (see Section 4.2).

5.3 Hot wire anemometry measurements

5.3.1 Hot wire measurements in three-dimensional flows

Hot-wire anemometry is a velocity measurement technique based on forced convective heat transfer from a thin heated wire, immersed in a fluid flow [132]. The wire is made of a material with temperature dependent resistivity. When an electric current is passed through the wire, it heats the element above the fluid temperature and the heat transfer from the wire depends on the flow rate it is exposed to. Hence if the temperature of the wire varies, so does also its resistance and consequently the Joule heating [133]. If the hot-wire is operated in constant temperature anemometry (CTA) mode, the resistance of the wire, and hence the wire temperature, is kept constant by a feedback loop. The forced convective heat transfer from the wire will then be balanced by the Joule heating [134]:

$$\frac{E^2}{R_w} = h_{conv} A_w (T_w - T_{air}) \tag{5.3}$$

where R_w, A_w and T_w are the resistance, the projected area and the temperature of the wire respectively, T_a is the ambient fluid temperature, h_{conv} is the convective heat transfer coefficient and finally, E is the voltage across the wire. Equation 5.3 can be expressed in terms of the Nusselt number as:

$$\frac{E^2}{R_w} = kNu\frac{A_w}{d}(T_w - T_a) \tag{5.4}$$

where k is the thermal conductivity of the fluid and d a characteristic length (here the diameter of the wire). Due to the dependence of the Nusselt

number on the Reynolds number and, hence, on the flow velocity, hot wire measurements allow for accurate flow field velocity measurements. For the simplified case of low velocity flow (negligible compressibility effects) perpendicular to a sensor wire operating in CTA mode, the relation between the output sensor voltage and the velocity (u) to be measured can be usually expressed through the so called King's law [135]:

$$E^2 = A + Bu^n \tag{5.5}$$

with A, B and n, coefficients to be found through a calibration process. On the other hand, in general, a lot of different geometric and fluid dynamics parameters must be considered. In particular, the contribution of velocity components that are not perpendicular to the sensor wire constitutes an important challenge in hot wire anemometry operation. This technique is widely used in turbomachinery application, where it is common to face complex three-dimensional flow fields, due to its capability of evaluating the flow velocity in a certain position with a very high frequency response, therefore allowing for turbulence intensity evaluations.

A lot of different methods have been developed in the years, to evaluate three different velocity components by means of hot wire anemometry. The only way to achieve an instantaneous solution of a 3D velocity field is to make use of a three-wire probe; since each velocity component has a different effect on each sensor wire response, depending on their relative orientation, it is common to make use of a parameter called *effective cooling velocity* (U_{eff}), defined as the velocity magnitude that would determine the measured output voltage on a given sensor wire, if it was directed perpendicularly to the wire itself. The typical calibration procedures for three wire probe [136, 137] are therefore aimed at defining sensitivity parameters to assess the impact of each velocity component on the global U_{eff}, for each sensor wire. The procedure is made complex by the fact that these coefficients can show variations with both the flow velocity and the flow angles [138]. Moreover this kind of probes have relatively low acceptance angles (about $\pm$ 30°), meaning

that their response become insensitive to further flow angles variations; to overcome this issue four wire probes [139] can be adopted, that are usually in-house developed and present larger dimensions. Other methods make use of two-wire probes (typically X-wire probes): carrying out two tests with different probe orientations, it is possible to reconstruct the three-dimensional velocity distribution, provided that a way to correlate in time the two different acquisitions is available [140].

Another diffused method focuses on the calculation of average and rms magnitudes of the three velocity components, rather than on their instantaneous value. Carrying out different tests with a X-probe in different orientation [141] or with a rotating slanted single wire probe [142, 143, 144], allow to build a linear system to be solved in terms of mean velocity components and Reynolds stress tensor components. All these methods are usually adopted for low turbulence flow fields, since higher order terms of velocity fluctuation has to be neglected to contain the number of test points (i.e. number of probe orientation) to be acquired and the order of the system of equation; particular attention must also be placed to chose the probe positions in order to produce a well-conditioned problem. It must be also reminded that proper accesses must be available to insert and rotate the probe along a certain axis inside the test rig, which is not always possible for high technology readiness level measurements.

5.3.2 Hot wire measurements setup

The HWA measurement technique selected within this application is somehow similar to the one described by Huu and Beguier [141], who used an X-wire probe with two different orientations, to resolve the three-dimensional flow field. In this work *Dantec Dynamics* split fiber probes were used due to their wider angular acceptance (up to $\pm 90°$ according to the vendor), required for the very high flow angles expected on Plane 40. On the other hand, techniques like the rotating slanted single wire could not be adopted because the expected turbulence intensities were too high to allow for higher order terms neglecting.

Dual sensor split fibers look similar to a single wire probe, but, instead

of a thin sensor wire, a 3 mm long quartz cylinder, with a 200 μm diameter, is placed between the prongs; two identical nickel film sensors, with 1.25 mm active length, are deposited on the quartz cylinder. A cross section of this kind of probe is reported in Fig. 5.15. These probes have been developed to investigate 2D flow fields with no velocity components parallel to the quartz cylinder: in this case they allow to evaluate both the velocity component in the plane perpendicular to the cylinder, which is proportional to the sum of the output voltages from the two sensors, and the flow angle within this plane (φ in the figure), proportional to their difference [145, 146]. Nevertheless, relevant errors can arise in this procedure when a third velocity component is added; moreover, the sensor is not exactly a cylindrical wire and the large amount of literature developed to take into account for velocity components parallel to wire sensors can't be straightforwardly extended to split fibers. For these reasons, in the author's knowledge, no attempts of using split fiber probes in highly three-dimensional flows are reported in literature; only a few application in 2D flows can be found [147, 148]. In order to pursue this goal two different tests had to be performed, for each test point, with two different probes: probe 55R56 was used with the primary goal of evaluating

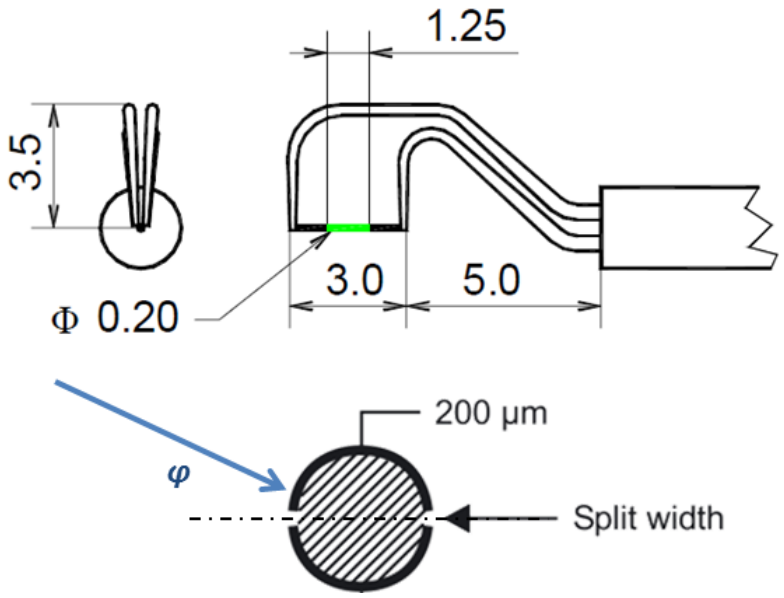

Figure 5.15: Split fiber probes configuration and cross-section

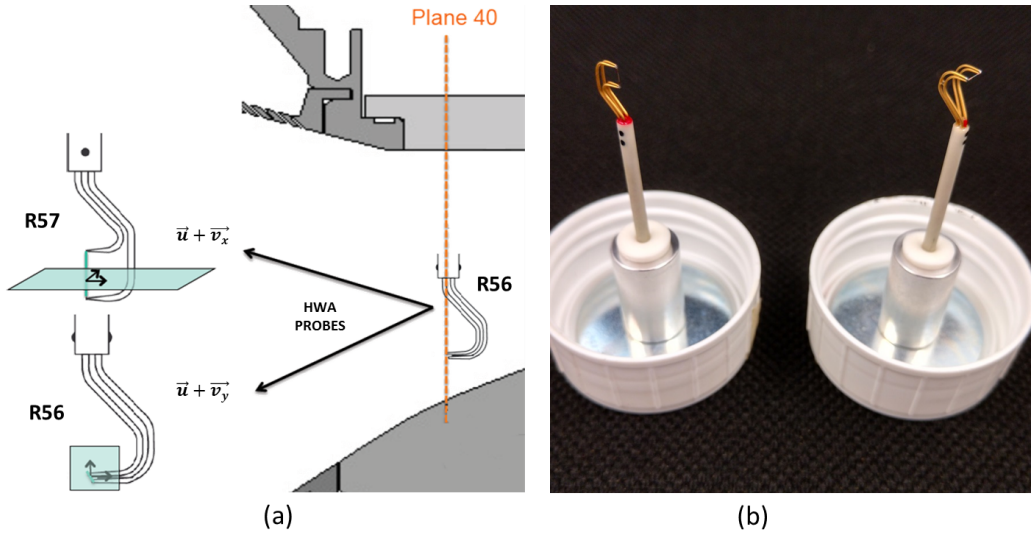

Figure 5.16: Split fiber measurement concept (a) and picture of the probes (b)

the velocity field on plane x-y (see Fig. 5.4 for axis notation), while probe $55R57$ was employed for plane x-z; as just stated, anyway, each probe feels the effect of all the three velocity components. Fig. 5.16a summarizes the probe configurations and the investigated plane, while Fig. 5.16b reports a picture of the two probes ($55R57$ on the left and $55R56$ on the right).

A thorough calibration process had to be carried out with the same calibration apparatus described in Section 5.2.2. The main challenges of the calibration and data-reduction procedures were related to the necessity to account for the flow compressibility, for measurements on Plane 41, and for the velocity component that is parallel to each probe wire.

Concerning the calibration procedure, as stated above, it is common, for this kind of probes, to relate the flow velocity, on the plane normal to the probe wire, to the sum of the sensors voltages [145, 146]; a $Nu-Re$ approach, instead of the classical relation between output voltage and flow velocity, was adopted, in order to account for the effects of flow density and temperature. For the development of the calibration curve the following steps have been followed. First of all the Nusselt number has been calculated from the acquired voltages; Eq. 5.4 was used for the goal. Since the system works in CTA mode, the sensors resistances don't change during the calibration nor during

the tests; together with the geometric parameters, they reduce to constants that do not affect the results. Eq. 5.4, therefore, reduces to:

$$Nu = \frac{E_1^2 + E_2^2}{k(T_w - T_f)} \tag{5.6}$$

In order to evaluate the sensors temperature (T_w), the procedure described by Cukurel et al. [149] was followed; concerning the fluid temperature (T_f), it was found that the parameter that led to the better scaling of the results was the total flow temperature, once it was scaled with the recovery factor, leading to:

$$Nu = \frac{E_1^2 + E_2^2}{k(T_w - \eta_r T_0)} \tag{5.7}$$

The same value of fluid temperature was used for the calculation of the fluid properties (thermal conductivity k, viscosity μ for Reynolds calculation). The total temperature (T_0) was measured inside the plenum chamber of the calibration apparatus. The recovery factor (η_r) was evaluated through the values of the Mach number and Knudsen number ($Kn = \frac{1.587e^{-8}}{\rho d_w}$). The adopted relations can be found in Appendix 2. The *effective Reynolds number* (using the two velocity components that lay in the plane orthogonal to the probe wire) was calculated as well, knowing total and static temperatures and pressures of the calibration airflow. Calibration points were acquired, for each probe, at different flow velocity and air temperature (T_0), in order to provide independent variations of both Mach and Reynolds numbers and assess their influence on the results. Once the $Nu - Re$ approach was used, the results were found to collapse on a single curve, reported in Fig. 5.17a; the traditional voltage-velocity approach on the other hand would lead to a spreading of the results, mainly due to the variation of the total flow temperature (T_0) and of the Mach number (i.e. of the recovery factor) , as shown in Fig. 5.17b. Cukurel et al. [149] proposed a correction on the Nusselt number, with a coefficient that depends on Reynolds and Mach numbers: this scaling was adopted to consider the effect of the flow compressibility on the heat transfer,

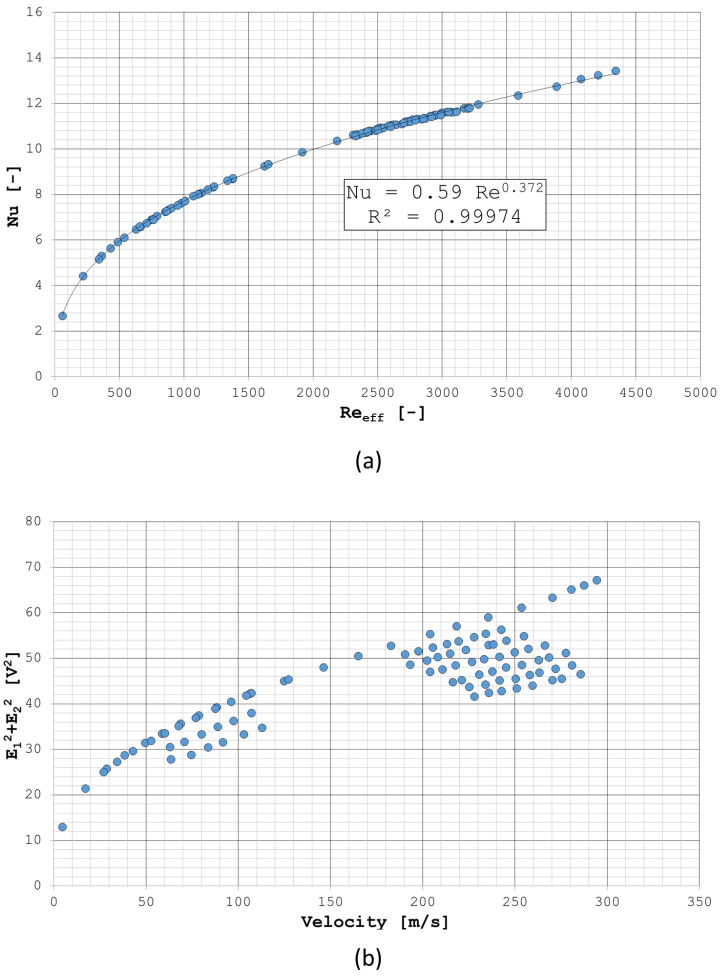

Figure 5.17: Example of mass-flux calibration in the case of Nu-Re (a) and voltage-velocity (b) scaling

rather than only on the convection temperature. Such a correction was not found to be suitable to the present data, as it resulted in a worse fit of the calibration points on a $Nu - Re$ curve.

This $Nu - Re$ curve constitutes the "mass-flux calibration". The "angular calibration", on the other hand, was carried out by relating the flow angle in the plane orthogonal to the probe wire to Re_i/Re_{eff}. The parameter Re_i was calculated from Nu_i, adopting the same relations developed from the mass-flux calibration and using either E_1 or E_2 for the evaluation of Nu_i, through Eq. 5.7. Since, as expected, both calibrations suffer from the effect

of the velocity component parallel to the cylinder (i.e. the second flow angle) and are strongly modified by it, several curves have been developed for different "out-of-plane" angles.

The test execution and data post-processing procedure, summarized in Fig. 5.18, is based on aligning, point by point, the $55R56$ probe with the expected time-average swirl angle (i.e. flow angle on the x-z plane), so that the second flow angle effect could be neglected in its post-process; the calibration curves at $yaw = 0°$ are, therefore selected. The alignment was made possible thanks to the use of the automatic traverse system. For the calculation of the Nusselt number through Eq. 5.7, the total flow temperature (T_0) was acquired by a thermocouple placed in the plenum chamber upstream the swirlers: since all the flows are at ambient temperature, it is not expected to change between the different mesh points, except for a limited drift in the ambient conditions, that is corrected through the thermocouple reading. The Mach number and the flow pressure, for the calculation of Knudsen number and recovery factor, were taken, for each mesh point, from five hole probe results, on time averaged basis. For the pre-swirl definition, data was taken from five hole probe results as well. The calculated time-average pitch angle and Reynolds number are then used for the evaluation of probe $55R57$ results, in order to select the correct calibration curve, as reported in the figure, and evaluate the actual swirl angle. Additional details on the hot wire probes calibration and data post-processing can be found in Appendix 2.

Two considerations are worth to be highlighted here: first, only a time-average information on the flow angle is transferred from one probe to the other, to integrate the post-process, and used for all the istantaneous acquisitions. A post-process procedure where istantaneous values were passed through the probes for each acquisition was also tried. The procedure had to be made iterative since the measured swirl angles from the test with probe $55R57$ were passed back to the first probe in order to further correct the results; significant deviations could, in fact, occur between the time-averaged pre-swirl value and the instantaneous swirl evaluation. Results, anyway, were found to lead to negligible variation, with respect to the original procedure.

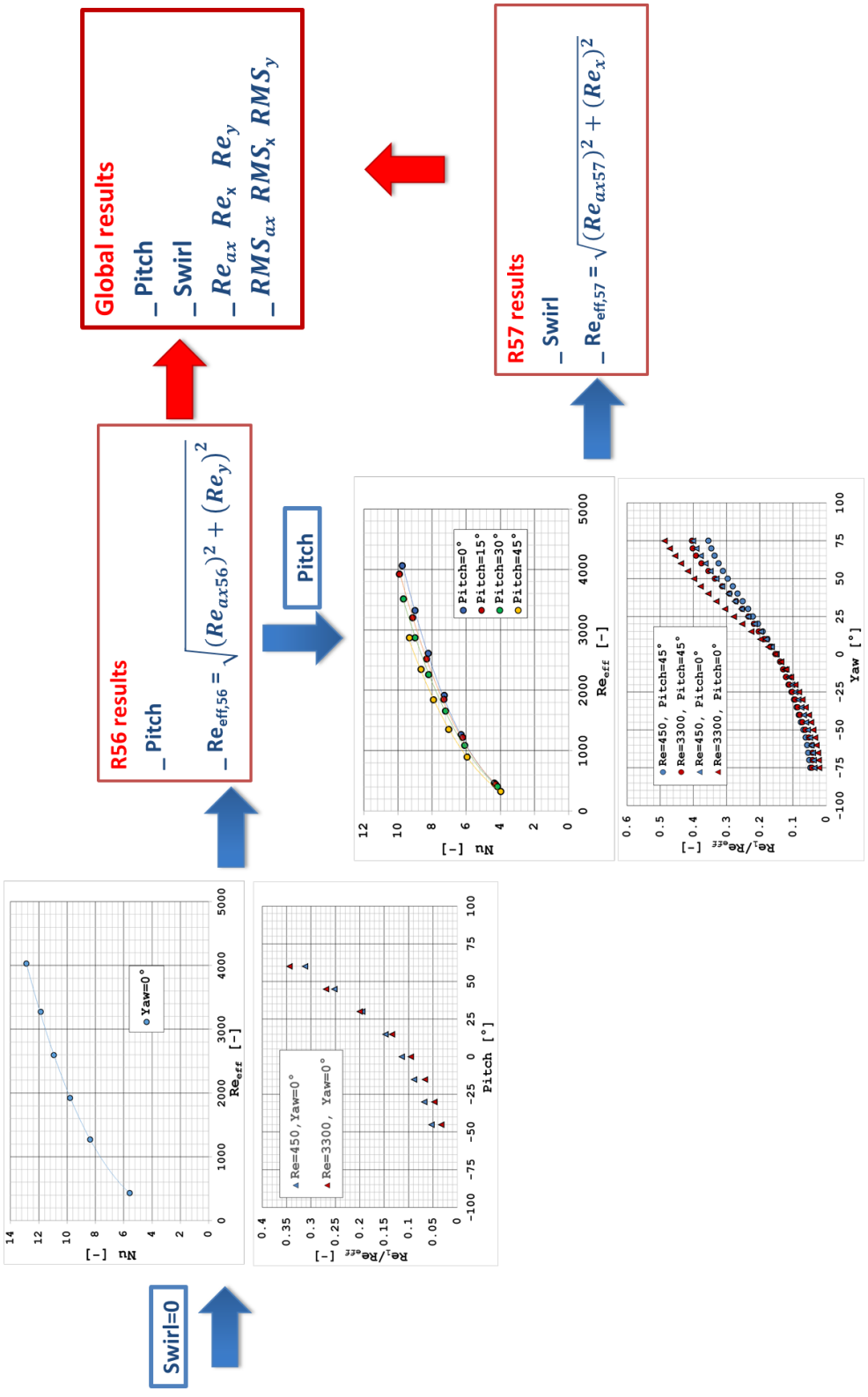

Figure 5.18: HWA measurements post-process conceptual map

An evaluation of this result is reported in Appendix 2. Moreover, results are not obtained in the rig cylindrical coordinates, but in the "probe coordinates"; they differ from each other both because the probe is moved by a cartesian traverse system and because the "probe coordinates" depend on the imposed pre-swirl, meaning that axial, horizontal and vertical direction can be different for all the points of the measurement mesh. As a result of the second point, it is not possible to obtain the time-evolution of the velocity components in the "relevant" directions; it is possible, anyway, to collect both average and statistical results and combine them. Concerning the turbulence intensity, for example, the following equation was used:

$$Tu = \frac{\sqrt{\frac{1}{3}((\rho u_{ax})^2_{rms} + (\rho u_x)^2_{rms} + (\rho u_y)^2_{rms})}}{\sqrt{((\overline{\rho u}_{ax})^2 + (\overline{\rho u}_x)^2 + (\overline{\rho u}_y)^2)}} \tag{5.8}$$

where subscripts ax, x and y refer to probe coordinates, point by point different from each other. It must be noted that this procedure, by its own, does not allow to divide the density and velocity contributions, to get the velocity value from the mass-flux (ρu). In general, different approaches have been developed in order to carry out this step. Most of them are based on the experimental evaluation of sensitivity coefficients, that describe how the output voltage fluctuation is influenced by temperature, pressure and velocity fluctuations respectively, in order to find their values. This approach is rarely followed due to the complexity in the experimental evaluation of the coefficients. Cukurel et al. [149] described a procedure based on identifying their values, by repeating tests with different over-heat ratios (i.e. different sensor wire temperatures). An alternative approach is based on neglecting the temperature fluctuations and utilizing simplified analytical correlations, that are mostly valid for supersonic and transonic flows, to discern between density and velocity effects [150]. Nevertheless it is also common to consider a mean density [151], so that Eq. 5.8 corresponds to the classical definition of turbulence intensity. The last approach will be, therefore, used in this treatment; in Appendix 2 it will be shown that the analytical approach, anyway,

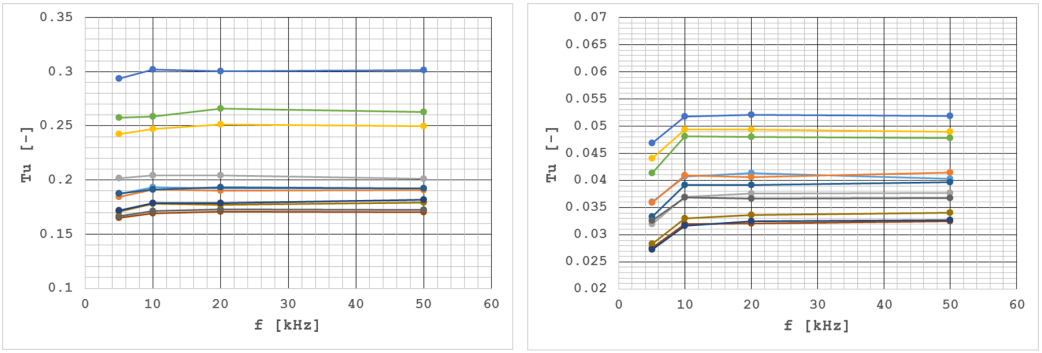

Figure 5.19: Sensitivity to acquisition frequency on Plane 40 (a) and 41 (b)

leads to limited variations.

The same calibration and post-processing procedure was used for both Plane 40 and 41 measurements, even in the first one no effects of compressibility arise, due to the low Mach number; nevertheless this does not introduce inaccuracies, since the procedure applies both to compressible and incompressible cases.

In order to provide an evaluation of the measurements uncertainty, a similar approach to the one of the five hole probe setup was adopted. Several points, at different velocities and flow angles, were acquired on the calibration apparatus for both the probes, and the developed post-processing procedure was applied to re-calculate the mass-flux (ρu) values. Errors within 5% were found, in the flow angle range that was expected during the tests. Applying the method developed by Kline and McClintock [104] to Eq. 5.8, an uncertainty up to 7% can be expected on the turbulence intensity measurements. It must be considered that the method has been adopted in a conservative way, as the same uncertainty has been related to both the mean velocity and to its rms: in case of systematic errors that lead to a constant bias in the velocity measurements, this component would not affect the rms readings.

Concerning acquisition setup, measurement meshes of the same type of the ones reported in the previous section were adopted, with very similar spatial resolutions; despite the smaller dimensions of the HWA probes with respect to the five hole probe, which would allow to explore areas closer to

Figure 5.20: Probe $55R57$ on Plane 40

the rig walls, the measurement domain was not extended beyond the five hole probe one, since results from the pressure probe are necessary for a complete HWA data post-processing. An acquisition time of three seconds was set, in order to get statistical convergence of the results; the assessment of the required acquisition frequency was carried out by acquiring a reduced number of mesh points at different frequencies, up to 50 kHz, the maximum allowed by the acquisition chain. Results, for both Plane 40 and Plane 41 are summarized in Fig. 5.19; since, beyond $f_{acq} = 10kHz$, the evaluated turbulence intensity doesn't show any further variations, this value was chosen as acquisition frequency for the tests. For each point a stand-by interval of one second was set before the starting of the acquisition. A *National Instruments 9234* board was used for the acquisition of the probe voltages, by means of the traverse system control PC. Together with the sensors voltages, the air temperature at the rig inlet was acquired, point by point, to get the flow total temperature value needed for Nusselt numbers calculation, by means of the the NI9212 board integrated in the traverse system control framework (see Section 4.2).

Fig. 5.20, finally shows a picture of probe $55R57$ inside the test rig for the investigation of Plane 40.

5.4 PSP measurements

Pressure sensitive paint (PSP) is an organic substance, composed by oxygen sensitive molecules embedded in the paint solution using a polymer binder permeable to oxygen. Through the exploitation of the luminescence behaviour of these molecules, PSP can be used to measure the oxygen concentration of the atmosphere surrounding the paints, which in turn can be linked to the partial pressure of air. The oxygen sensitive molecules are excited by the absorption of a photon, to higher energy levels by an incidence light of a certain frequency (UV light). From the excited state the molecule has several competing relaxation paths. The path of interest for PSP involves a forbidden transition to an excited triplet state from which the molecule may simply emit a photon. However, if oxygen is present, the molecule may interact with it, transmitting its energy into a vibrational mode of the oxygen. This radiationless deactivation at lower frequency results in a system where the luminescent intensity from the molecule is a function of the partial pressure of oxygen to which the molecule is exposed; the intensity of the light increases as the oxygen concentration in the ambient around the sensitive molecules is decreased. This well known phenomenon is called *oxygen quenching* [152]. PSP is sprayed on the surface of the test article where the oxygen concentration has to be measured.

5.4.1 Measurement theory

Since the PSP is a sensor of the oxygen concentration, this paint is suitable for gas concentration technique based on the heat and mass transfer analogy [153], with the ultimate goal of evaluating the adiabatic effectiveness.

Starting from a simple 2D film configuration reported in Fig. 5.21a, the governing equation for the heat transfer into a turbulent boundary layer is:

$$G_x \frac{\partial T}{\partial x} + G_z \frac{\partial T}{\partial z} = \rho(\epsilon_T + \alpha) \frac{\partial^2 T}{\partial^2 x} \tag{5.9}$$

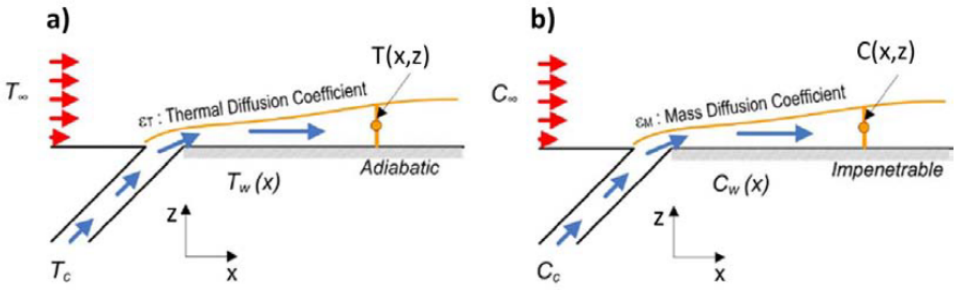

Figure 5.21: Heat and mass transfer analogy for film cooling situations: thermal (a) and mass transfer (b) boundary conditions [59]

where G is the mass flux per unit of area, ϵ_T and α are respectively the turbulent and laminar diffusivity. In the case of adiabatic wall, the boundary conditions are the following:

$$T(z=0) = T_{ad} \tag{5.10a}$$

$$\frac{\partial T}{\partial z}(z=0) = 0 \tag{5.10b}$$

$$T(z > \delta_f) = T_\infty \tag{5.10c}$$

$$T(x=0) = T_c \tag{5.10d}$$

For the analogous case for mass transfer situation, where the hot mainstream has a tracer element concentration of C_∞ and the coolant has a tracer concentration of C_c (Fig. 5.21b), the governing equation of tracer gas diffusivity inside the boundary layer are:

$$G_x \frac{\partial C}{\partial x} + G_z \frac{\partial C}{\partial z} = \rho(\epsilon_C + D)\frac{\partial^2 C}{\partial^2 x} \tag{5.11}$$

with ϵ_C representing the turbulent mass diffusivity. An impenetrable wall

situation yelds to the following boundary conditions:

$$C(z=0) = C_w \tag{5.12a}$$

$$\frac{\partial C}{\partial z}(z=0) = 0 \tag{5.12b}$$

$$C(z > \delta_f) = C_\infty \tag{5.12c}$$

$$C(x=0) = C_c \tag{5.12d}$$

Hence the set of equations for heat and mass transfer situations have same modelling expression [154]. Moreover, if the boundary conditions of the two analogous problems are the same and if the molecular and turbulent Schmidt number Sc_T are identical to molecular and turbulent Prandtl number Pr_T respectively (i.e. turbulent Lewis number Le_T equal to one), the solutions of the heat and mass transfer phenomena are identical.

$$Le_T = \frac{Pr_T}{Sc_T} = \frac{\epsilon_T + \alpha}{\epsilon_C + D} \approx 1 \tag{5.13}$$

In turbulent flows, experimental results suggest that the coefficients of turbulent transport diffusivity, represented by the Sc_T and Pr_T numbers, have similar magnitudes [155]. Concerning the applicability of the heat and mass transfer analogy to film cooling situations with moderate Mach number, turbulent main flow and high blowing rate, the mixing process of interested generally occurs far from the wall, where turbulence effects are dominant, and therefore the analogy is generally satisfied. Even if the hypothesis of turbulent Lewis number is met ($Le_T = 1$), the similarity of molecular diffusion may not be satisfied and thus Lewis number may deviate from one: in this case, the difference between Pr and Sc influences the heat/mass transfer rate near the wall boundary layer in the thin viscous sub-layer [154]. However, only a small influence of molecular parameters is expected as a consequence of the zero temperature/concentration gradient at the adiabatic/impenetrable wall of the test plate.

Assuming the heat-mass transfer analogy valid, if a tracer gas without free oxygen is used as coolant in a film cooling system, it is straightforward to replace the temperature definition of film cooling effectiveness by mass fractions of oxygen [153]:

$$\eta_{ad} = \frac{T_{main} - T_{ad}}{T_{main} - T_{cool}} = \frac{C_{main} - C_w}{C_{main}} \tag{5.14}$$

where C_{main} is the oxygen concentration of main free stream and C_w is the oxygen concentration in proximity of the wall. In order to express Eq. 5.14 in terms of partial pressure of oxygen, as measured with PSP, the expression of adiabatic effectiveness is elaborated using the molecular weights [156]:

$$\eta_{ad} = \frac{C_{main} - C_w}{C_{main}} = 1 - \frac{1}{(1 + (\frac{P_{O_2;air}/P_{O_2;ref}}{P_{O_2;fg}/P_{O_2;ref}} - 1)\frac{W_{fg}}{W_{air}})} \tag{5.15}$$

Subscripts fg and air stand for a case with foreign gas (without free oxygen) and air injection trough cooling system respectively; moreover ref is used to identify a reference case. Therefore, in order to evaluate the adiabatic effectiveness distribution using PSP technique, four types of images are needed for each tested flow condition; the experimental apparatus must be equipped with the same illumination system and camera used for calibration test:

1. The first image (Dark Image) is acquired with the UV illumination system switched off and it is necessary to correct the background noise of the camera CCD (I_{dark}).

2. Using a tracer gas for the cooling line and air for the mainstream, a second image (*Tracer Image*) is acquired setting the desired flow conditions.

3. The third image (*Air image*) is acquired imposing the same conditions of the previous one, but using air as coolant instead of tracer gas.

4. The last type of image (*Ref Image*) is captured with no flow condition and it represents the reference intensity field of the measurements (I_{ref}).

From the ratio of the reference (I_{ref}) and tests 2 intensity images, both corrected with the dark field (test 1), the calibration curve can be used to estimate pixel by pixel the normalized partial pressure of oxygen in case of tracer gas injection through holes array ($P_{O_2;fg}/P_{O_2;ref}$). In the same way the intensity image acquired with the third test (air injection) is elaborated in order to achieve the ratio $P_{O_2;air}/P_{O_2;ref}$. Finally both the distributions of partial pressure of oxygen can be combined, as suggested by Eq. 5.15, to estimate the bidimensional map of adiabatic effectiveness.

An important aspect of the PSP technique is that it allows to perform tests which can be considered really adiabatic. In the case of a thermal technique such as IR, TLC or TSP thermography the adiabaticity is guaranteed when there are no thermal gradients across the test plate; this requirement can be only partially satisfied using a low-conductivity material; even in these cases, thermal conduction corrections, that can be detrimental to the measurement accuracy, must be employed. Caciolli et al. [157] carried out a comparison between PSP and TLC measurements in order to highlight pros and cons of both.

5.4.2 PSP calibration

Before their use on a test model as a oxygen partial pressure measurement device, PSP must be accurately calibrated in a dedicated hardware. The calibration apparatus, depicted in Fig. 5.22, is constituted by a vacuum/pressure chamber, housing an aluminium test plate with Pressure Sensitive Paint, where both pressure and temperature of the test plate can be

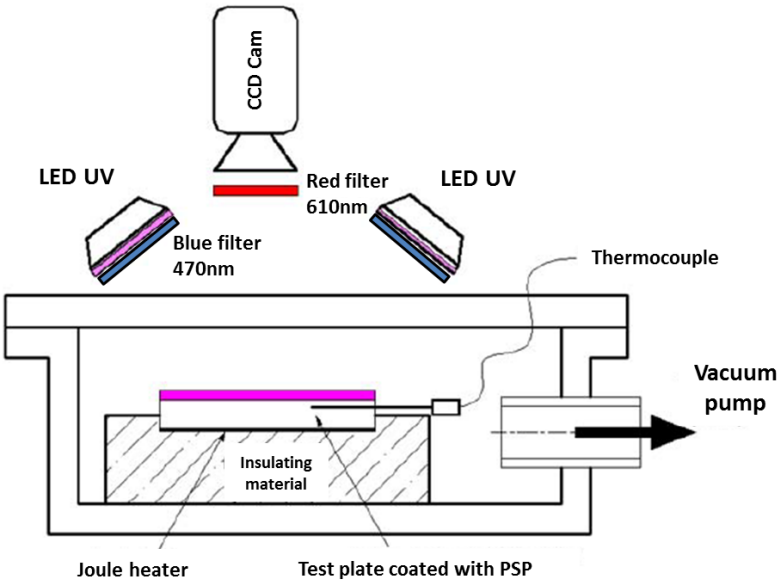

Figure 5.22: PSP calibration apparatus [158]

controlled. The calibration environment can be either put in vacuum or pressure conditions, by means of a vacuum pump or a compressed air system; the first configuration is reported in Fig. 5.22. Additional details on the calibration setup can be found in the work of Picchi [158].

PSP used in the present work is supplied by *Innovative Scientific Solutions, Inc* and is made by a blend of Fluoro Isopropyl Butyl polymer (FIB) and Platinum tetra porphine ($PtTFPP$). As shown in Fig. 5.22, an UV 400nm Led system provides the adequate light source for paint excitation. A blue filter is employed to filter out the emission components above 470nm. A 1600x1200 resolution 14-bit CCD camera ($PCO1600$) with a 610nm red filter records the intensity emitted by PSP. These filters are necessary to ensure that the exciting light is not captured by the scientific grade camera. A typical emission spectra of PSP paint based on PtTFPP luminophore is reported in Fig. 5.23.

Since the PSP emission depends on both the oxygen partial pressure and the surface temperature, attention must be paid to scale the latter effect. It was found by Han and Rallabandi [160] that if the if the reference (no flow)

image is acquired at the same surface temperature of the correspondent flow image ($Air/Tracer\ gas$) this effect can be scaled. Fig. 5.24 shows these results: in Fig. 5.24a different calibration curve with test image acquired at different temperatures and reference image acquired at constant temperature are shown; it is possible to note relevant differences between the curves. In Fig. 5.24b the case with reference image acquired at the same temperature as the test image is depicted; curves collapse to very similar values, once they are reported in terms of $(I_{ref} - I_{dark})/(I - I_{dark})$ vs P/P_{ref}. This behaviour was also verified with the instrumentation and PSP used within the present work; the description of the procedure and the results can be found in the work of Picchi [158].

Since, for PSP tests, a combustion chamber static pressure of 127kPa had to be imposed (Section 3.2), the maximum expected pressure on the airfoils surface is slightly higher than this value. Therefore, the PSP calibration was pushed up to $P/P_{ref} \approx 1.3$. An in-situ calibration was also carried out, to double-check the calibration data above ambient pressure, pressurizing the test rig by closing inlet and outlet automatic valves (1,2,3 and 4 in Fig. 3.10). The emission of the PSP on the painted airfoils was acquired and related to

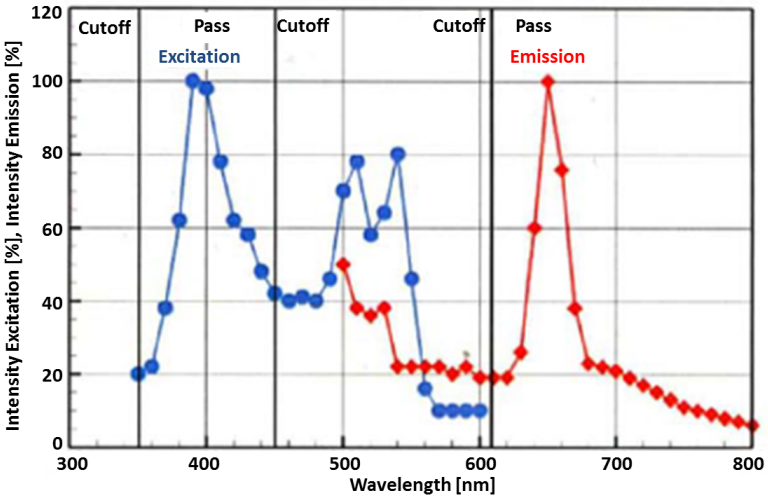

Figure 5.23: PSP with PtTFPP luminophore: typical emission spectra [159]

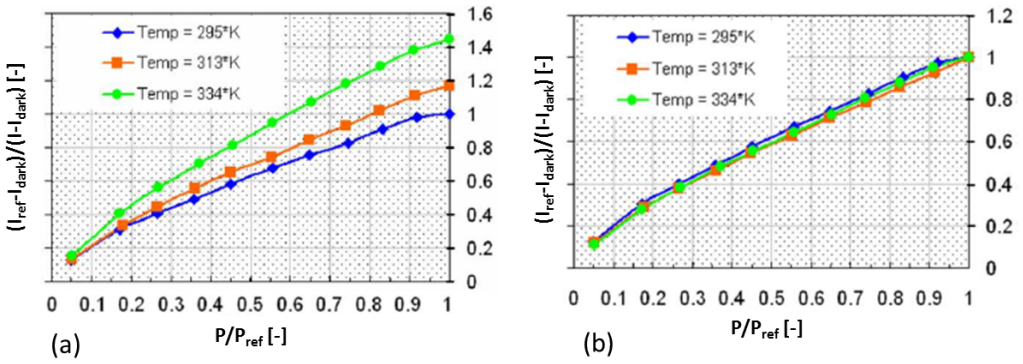

Figure 5.24: Han and Rallabandi [160] calibration results with (a) $T_r = 295K$ and (b) T_r maintained at test temperature

the measured pressure in the chamber, that could be considered uniform due to no flow conditions. Different pressurization levels were explored in order to compare to the existing calibration curve. This procedure was made possible by the fact that, once the results are properly scaled with a reference images, they are not sensitive to changes in viewing angle. Beside, the camera shows a very good linearity in its response, within most of its operation range, meaning that its intensity output increases linearly with the collected light; therefore, if the camera is operated in the linear range, far from CCD saturation, results don't depend on the intensity of the UV light used for PSP excitation, as long as it remains the same for test image and reference image and its spectral content doesn't change (i.e. same illumination system). Fig. 5.25 shows the calibration results. A very good matching was achieved between the initial and the in-situ calibrations; moreover the calibration curve shows a good similarity with the calibration curve provided by the PSP vendor. A third order polynomial was used to define a relation between the camera response $((I_{ref} - I_{dark})/(I - I_{dark}))$ and the measured oxygen partial pressure (P/P_{ref}).

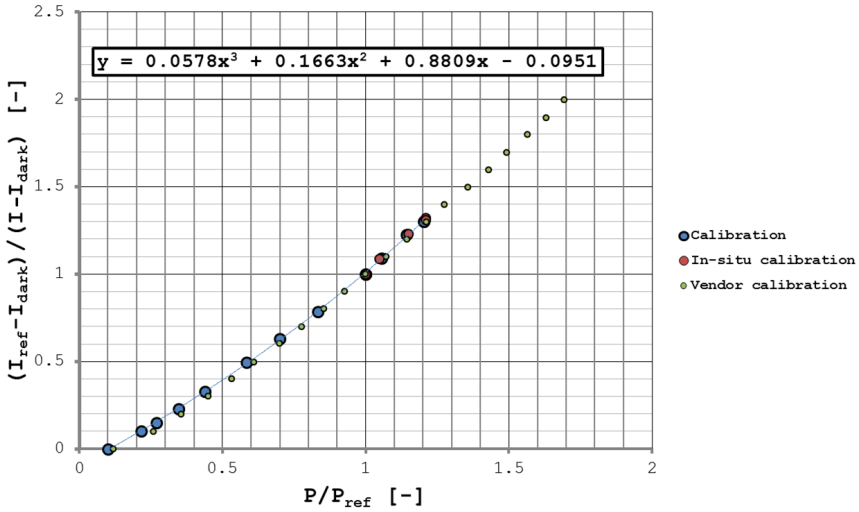

Figure 5.25: PSP calibration curve

5.4.3 PSP uncertainty evaluation

PSP uncertainty evaluation is a complicated task due to the number of parameters that can affect the measurement and to the complexity of the relationships that link one to another, that makes their combination not straightforward. The contribution to the uncertainty considered within this treatment are the following:

- noise of the camera acquisition
- calibration pressure transducer uncertainty
- temperature differences between test image and reference one
- residual effect of surface temperature

The first contribution was evaluated through a characterization of the camera output for constant pressure and illumination: the response standard deviation I_{var} was evaluated (2σ, 95 % level of confidence). The pressure transducer used for the calibration is of the same type described in Section 3.1.3, with an uncertainty of ± 52 Pa. Regarding temperature effect, even if attention is paid during the tests, to acquire test and reference image

at the same temperature, by checking that mainstream and coolant are at the same temperature of the surrounding ambient and acquiring one image right after the other, some differences can exists due to heating effects of the surface by the illumination system and to flow/no flow conditions switch. Moreover even if both images are acquired at the same exact temperature, still some deviation is introduced if such test temperature is not exactly the same as calibration, as it can be seen by Fig. 5.24b, with the different curves not perfectly collapsing; even if this effect is very reduced it was taken into account in the procedure. A statistical procedure, considering a mean temperature variation of 2.5 K between tests and calibration and no temperature differences between test and reference image was carried out; the test result was simulated for 1000 runs, imposing a standard variation of 3K on both the above mentioned temperature differences, in order to find the deviation from the "ideal" result with no temperature differences, in terms of measured pressure. All these four contribution were then combined through the Kline and McClintock method [104], exploiting Equation 5.15, to find the adiabatic effectiveness measurement uncertainty for various effectiveness and air pressure (i.e. NGV surface pressure) levels. The results, reported in Fig. 5.26a, show that the relative uncertainty decreases with increasing effectiveness levels and it is slightly increased for higher air pressures, since the PSP emission is reduced. 1D plots have been extracted in Fig. 5.26b, for different air pressures (P/P_{ref}), typical of this application: while the uncertainty is very low for high measured adiabatic effectiveness, it can reach 40 % for $\eta = 0.1$; nevertheless the absolute uncertainty is very limited, resulting in reliable results.

5.4.4 PSP tests execution

In order to map a sufficient portion of the three cooled NGVs invested by the central sector combustor outflow, three different camera positions were necessary, as sketched in Fig. 5.27a. Frame 1 and 2 were acquired through the lateral optical accesses realized in the combustion chamber; PMMA windows were manufactured for the goal and substituted to the lateral metal walls. In particular, frame 1 was acquired through the right window (look-

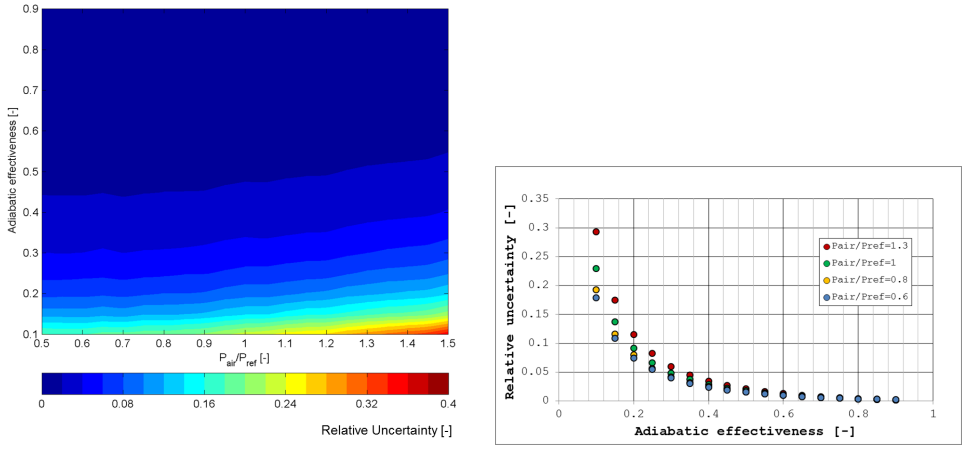

(a) (b)

Figure 5.26: Adiabatic effectiveness measurement uncertainty map (a) and extracted 1D profiles for fixed air pressure level (b)

ing downstream), allowing to investigate the LE zone and the early part of the pressure side of NGV 1 and 2, according to the enumeration reported in Fig. 5.27b. Frame 2 was acquired through the left window, focusing on the LE and the early suction side of NGV 2 and 3. Moreover a third frame was acquired through the optical access placed downstream, in the outer duct, allowing to investigate the final part of the suction side of NGV 2 and 3. This optical setup allowed to investigate the four surfaces, two PS and two SS, placed in the rig central sector: NGV1 suction side and NGV3 pressure side were not explored since they are outside of this region. Even within the central sector, the final part of each pressure side could not be investigated due to optical access issues: in particular the film cooling behaviour of rows PS4 and PS5 (see Section 3.1.2) could not be assessed, even if some interesting conclusion could be made from the analysis of the three acquired frames. Fig. 5.27b also reports two sketches of the NGVs CAD model that allow to visualize the portions of airfoil that have been investigated through frame 1 (red), frame 2 (blue) and frame 3 (green).

For all the camera positions, the target NGVs were illuminated through the same optical accesses used for image acquisition. 20 images were acquired for each test point and averaged in order to limit the camera noise, before

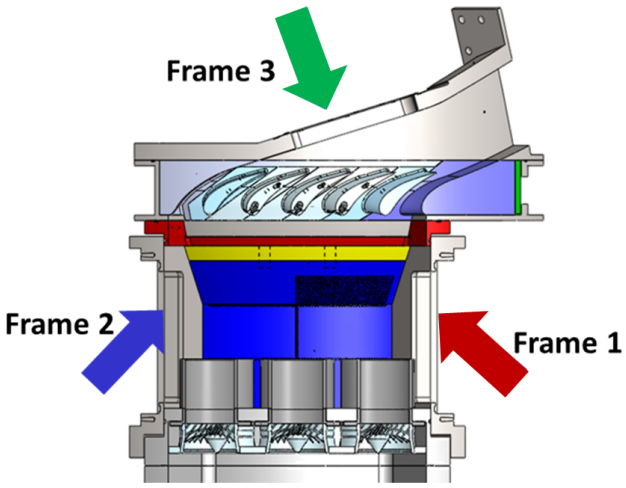

(a)

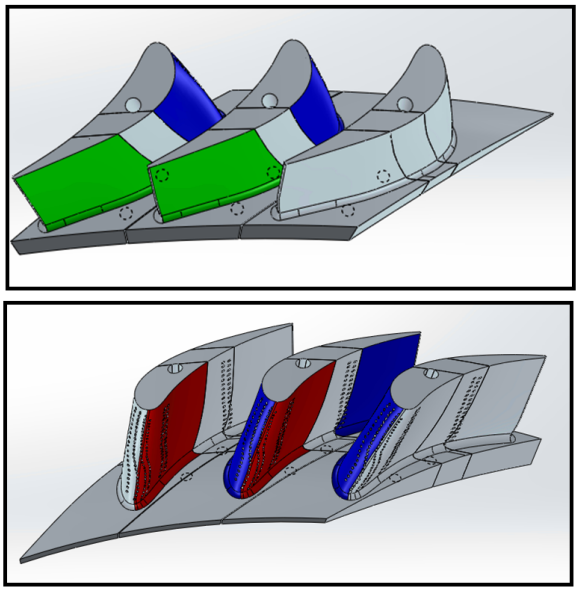

(b)

Figure 5.27: Optical accesses used for PSP measurements (a) and investigated areas (b)

being postprocessed using equation reported in Section 5.4.1 pixel by pixel. At the end of the process, the resulting images were masked in order to white-

out the areas that were not object of the measurement and get the results in the form reported in Section 7.1.3. Since the image acquired from the camera are directly elaborated to estimate a 2D film cooling distribution, it is not straightforward in the present test case to associate a space coordinate to each camera pixel due to the curvature of the vane airfoils and perspective effects. Nevertheless, the knowledge of a vane surface coordinate for each camera pixel is essential to perform proper data comparisons without map distortion and perspective effects. For this reason, each 2D effectiveness map is elaborated using an in-house 3D mapping procedure. The first step of the procedure is based on the reconstruction of the acquired camera frame, modelling the field of view of the camera using the 3D model of the rig: knowing the spatial position of the camera and optical parameters, this step is used to reconstruct a first rough set of pixel coordinates. Finally in a second step, the set of pixel spatial coordinate is improved using a de-warping procedure based on polynomial interpolation of several marker points with well-known space position.

CO_2 was used as foreign gas in order to match the same coolant-mainstream density ratio of 1.5 of the DP conditions, on average basis (see Section 3.2).

Chapter 6

Experimental Characterization of the Combustor Simulator

Contents

The first part of the experimental work was focused on the investigation of the combustion chamber; results coming from this part will be reported and described in this chapter. The final goal of this stage was, initially, to highlight the flow structures that occur and evolve inside the combustor simulator; afterwards the focus moved to combustor exit, in order to characterize the turbine inlet conditions. Both these aspects are useful to assess the capability of the test rig to replicate the behaviour of a modern lean burn aero-engine combustor, in terms of highly swirling and turbulent flow field and distorted temperature patterns, in the view of the NGV investigation, reported in the next chapter. Comparisons between design and isothermal conditions were also pursued in order to justify the possibility to carry out some measurements in the latter operating point (see Section 3.3.1).

Among the results that will be shown in this chapter, only PIV ones

have been collected on the test rig without the NGV cascade. All the probe traversing tests have been performed in the upgraded rig configuration. As stated in Section 2.5.1, five hole probe measurements upstream of the cascade had already been carried out in the previous rig configuration. The comparison, though, will not be reported here, as the investigated planes slightly differ between the two campaigns (see Section 3.3). The results, anyway, showed limited differences, coherent with what should be expected by the change of the investigated position. Therefore no relevant potential effects of the NGV cascade should be expected on the flow field in the measurement axial position (≈0.65 axial chords upstream of the LE).

6.1 Flow field inside the combustor simulator

The flow field measurements carried out by means of boroscopic 2D PIV will be reported in this section. Among the three investigated positions (Section 5.1.2), the symmetry plane allow for a global view of the whole combustion chamber and will be described first; afterwards, planes CC1 and CC2 will be described, in order to catch some details on the evolution of the structure generated by the swirlers and to provide some clues about the combustor simulator outflow. Fig. 6.1 shows the 2D velocity magnitude, made by axial and radial components, measured by PIV on the symmetry plane. As explained in Section 3.3, the maximum mainstream temperature had to be kept to 180°, to limit the thermal stress induced in the windows. Therefore, the isothermal and the warm operating points have been investigated on such a plane and for the whole PIV campaign in combustion chamber. Since, as a result of the mainstream temperature increase, a higher flow field velocity is achieved, in order to effectively compare the results from different operating points, the velocity fields have been scaled using the following parameter:

$$V_{nd} = \frac{V_{PIV}}{U_{ref}} \tag{6.1}$$

where U_{ref} is the mean axial velocity on the swirler section, calculated

as a macro-parameter by the knowledge of the mass flow rate, of the flow temperature and pressure and of the swirler section area; it increases with the mainstream temperature due to the density reduction and its values are respectively 37.5 m/s and 47.1 m/s for isothermal (IOP) and warm (WOP) conditions. Velocity vectors have been overlapped to the maps in order to provide a better understanding of the flow field evolution; for the same reason, the combustion chamber boundaries, as well as the central duct shape, have been sketched in black. As anticipated (see Table 3.6), isothermal measurements on this plane were carried out in an earlier stage of this survey and a single camera position was used; for the warm conditions, a higher number of camera positions were adopted in order to map a wide portion of the measurement plane, at the expense of an increase in experimental time and complexity. Nevertheless, the investigated portion of the combustor camera in IOP conditions allows to evaluate the most important phenomena and to conduct an in depth comparison between the two different conditions.

Typical flow structures of modern swirl-stabilized combustors can be found; the central swirler creates a high velocity region, visible on the measurement plane as an inner and an outer jet. Due to the axial configuration of the swirlers a limited radial inclination is impressed to the jets and no strong impingement phenomena of the jets on the effusion cooled liners can be recognized. Also, effusion cooling flows don't seem to affect the coherence of the swirler jets in a relevant way, as it is suggested by the vectors. The high tangential momentum of the flow structure generates a central recirculation zone, due to vortex break-down, and typical corner vortex structures, while, downstream, the flow accelerates towards the chamber exit. Regarding the corner vortex a particular behaviour can be observed in Fig. 6.2, where a focus on the corner structures is reported for the WOP case; the same behaviour was found for IOP conditions.

While the classical behaviour of the corner vortex is generated by a break-down of the swirler jet [98] and would create, in this configuration, a clockwise rotating structure, in the investigated case the effect of the coolant alters the phenomenon. The flow coming from the first rows of effusion cooling holes (which starts at about x = 45 mm) is bled towards the swirler jet by the

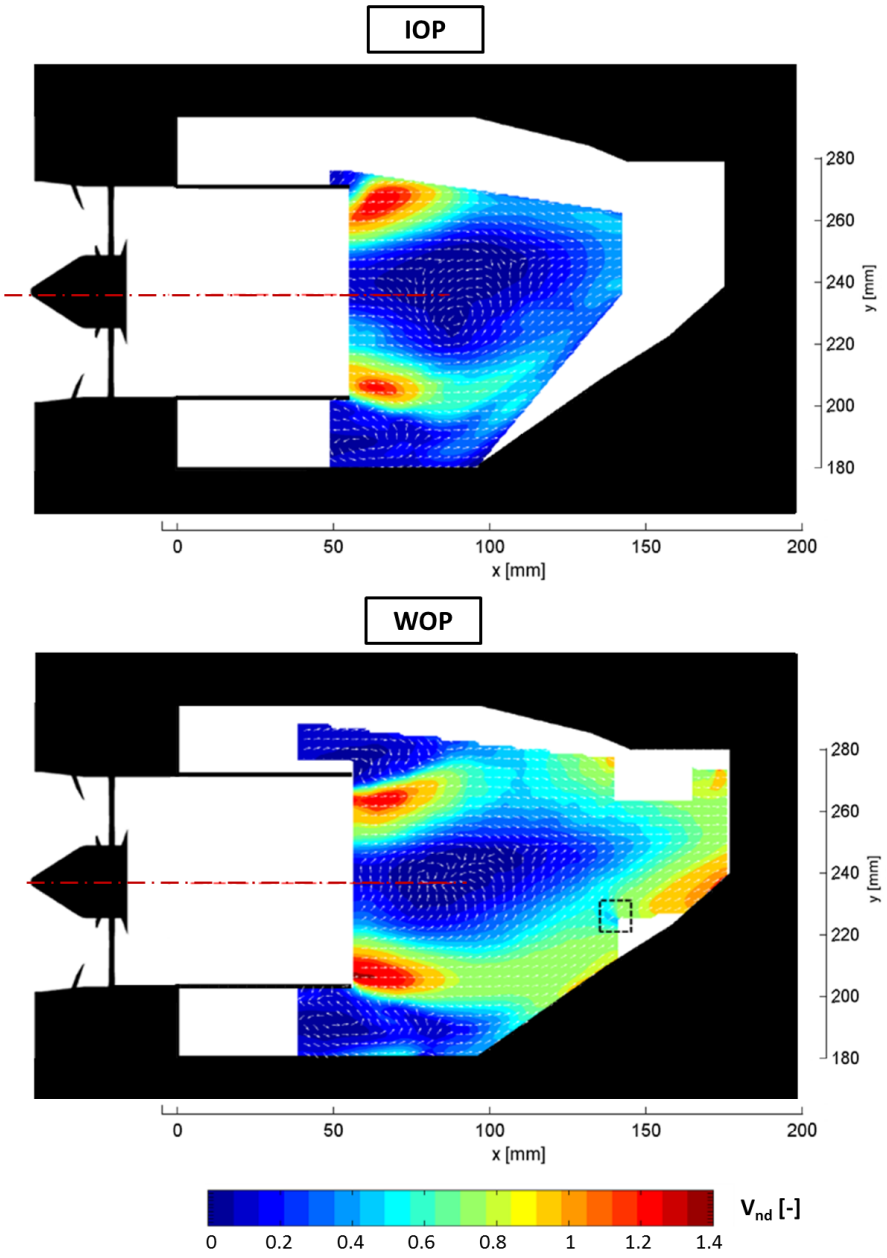

Figure 6.1: PIV results on symmetry plane - scaled velocity

low pressure zones generated by the swirling jet itself; therefore a counter-clockwise structure is created. A strong influence of the liner cooling flows on the corner vortex structures had been documented also by Andreini et al. [24]; while in their work a clockwise rotating structure, generated by the

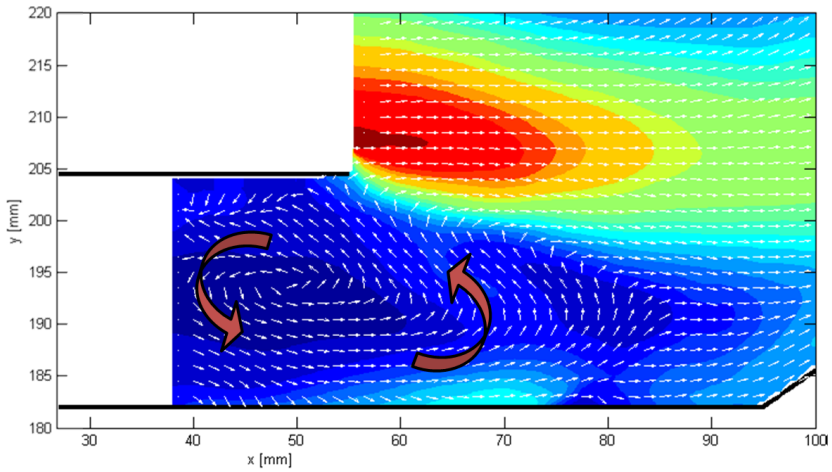

Figure 6.2: PIV results on symmetry plane - corner vortex

swirler jet break-down, was still recognizable, next to the counter-clockwise one due to the effusion coolant recirculation, in the present investigation the first one has completely disappeared; the reason is probably due to the axial nature of the swirler, compared to the radial one in the referenced work, that impress a higher axial momentum to the mainflow jet.

Regarding measurement quality, the warm velocity map is affected by two issues. The first one is a non-physical deceleration near the image top right corner generated by a bright glare on the upper edge of the outer liner: despite the black paint that was applied on the surface, it was not possible to reduce this effect. The boroscope insertion position is very close to the liner edge and the local laser energy is very high. For this reason, results in this area have been whited-out to avoid misunderstandings. A further deceleration can be found in the bottom right part of the investigated area (marked region at x=140mm; y=230mm); this effect is due to the presence of the boroscope that locally slows down the flow field. As anticipated in Section 5.1.1, this is one of the main drawbacks of boroscopic PIV; however the blockage effect is limited to a very reduced part of a wider investigation area. Finally, the white zone below this position is due to the impossibility of covering the entire test section with the laser sheet.

Regarding the comparison between the two different operating conditions,

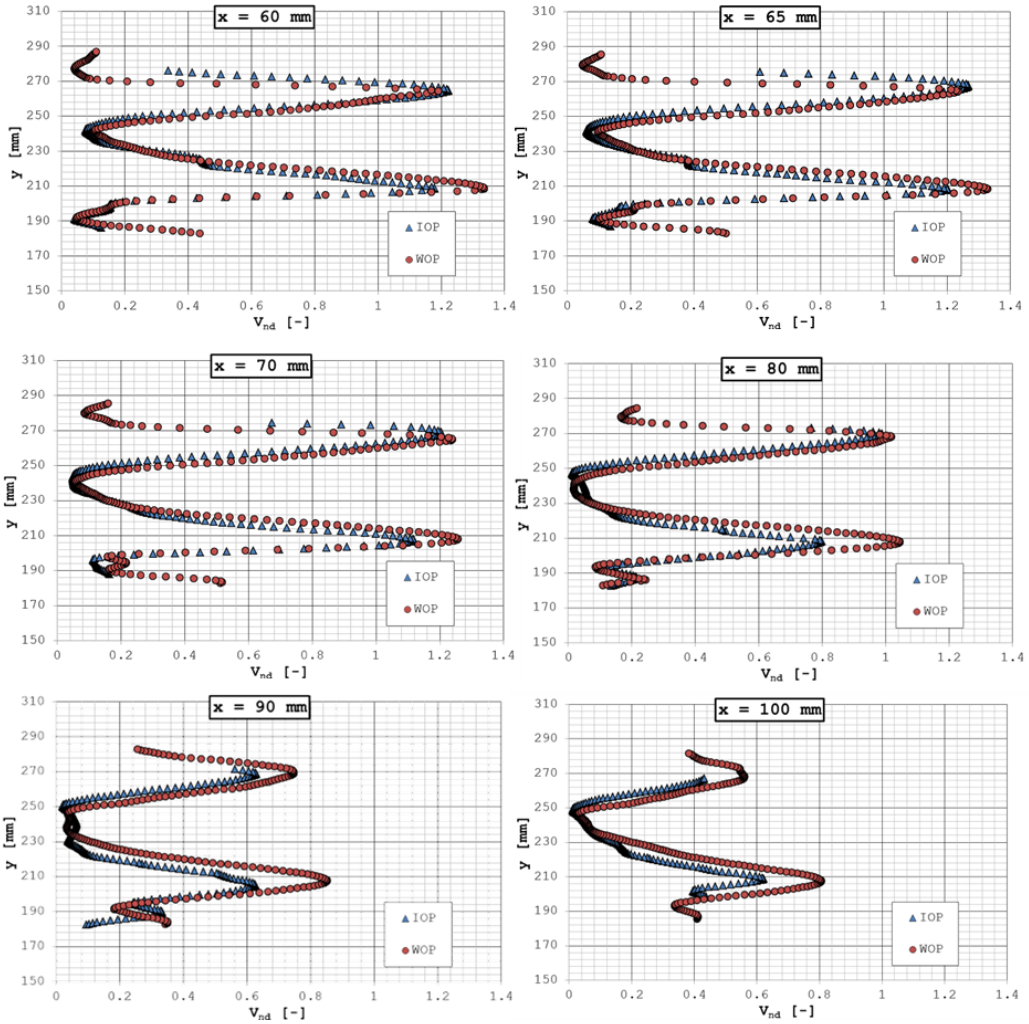

Figure 6.3: PIV results on symmetry plane - 1D profiles

the two flow fields look very similar, in terms of flow morphology and scaled velocity values. However, significant differences can be found in correspondence of the inner swirling jet close to the converging part of the liner; even if the investigated domain is limited for the IOP case, it is evident that, for WOP conditions the jet presents high axial velocities, while in isothermal conditions it looks slowed down by the convergent inner liner. A more in depth comparison can be carried out through the evaluation of the 1D velocity profiles at different axial positions, as reported in Fig. 6.3. One of the most interesting result that comes out from the velocity profiles is the

effect of temperature ratio on the opening angle of the swirler jet. Heating up the mainstream, an axial acceleration of the mainflow occurs, reducing the jet/liner angle (i.e. "axialization" of the jets). On the other hand, the isothermal jet presents a higher radial aperture and the highest velocities are reached farther from the chamber centerline compared to the warm condition; even if the differences are limited, this behaviour is particularly recognizable from the profiles extracted at x=70mm. Considering the positions closer to the swirler (x < 90mm), the isothermal condition presents lower inner jet velocity while the outer jet is more similar. Moving downstream (i.e. approaching the combustor section contraction), these difference increases and the inner jet is lifted towards higher radial positions: this behaviour can be appreciated comparing the profiles at x = 90mm and x = 100mm. A similar behaviour can be appreciated also for the outer jet, but the entity is much lower. Consistently with this conclusions, the axialization of the mainflow jet, observed for the warm conditions, causes a slight reduction of the recirculation zone with respect to the isothermal ones, as depicted in Fig. 6.4, where recirculation zones (negative axial velocity) are highlighted in blue. Important differences can be observed, for WOP conditions, in the extent of the corner recirculation zone between inner and outer jets; for IOP conditions, the field of view is not wide enough to draw similar conclusions.

Concerning planes CC1 and CC2, as anticipated in Section 5.1.1, the apparent radial displacement created by the boroscope viewing angle, has been bypassed by considering only V_{tg}, the velocity component that is tangential

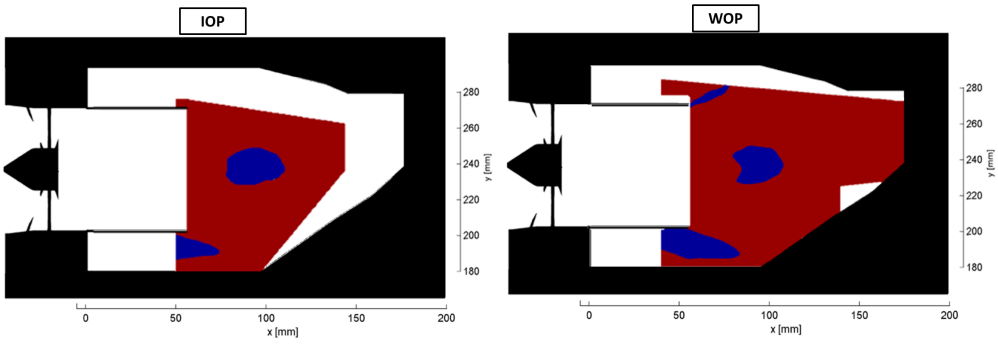

Figure 6.4: PIV results on symmetry plane - recirculation zones

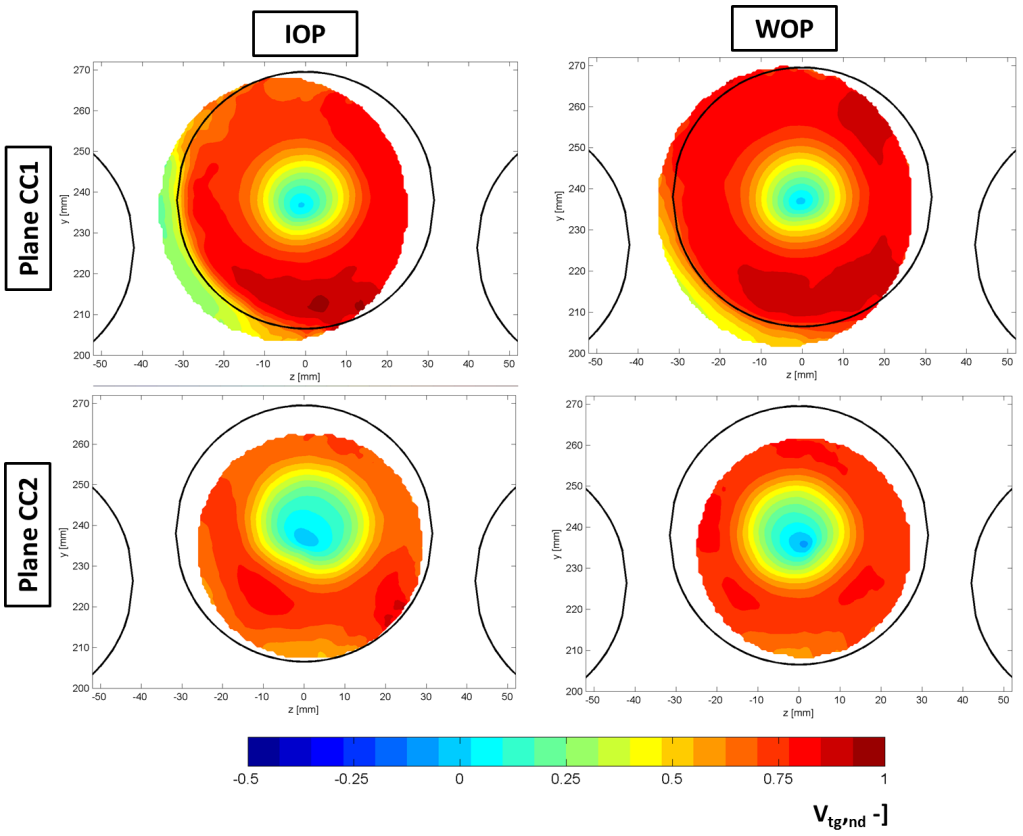

Figure 6.5: PIV results on axial planes - scaled velocity

to the boroscope center (i.e. the image center). In addition to not being affected by the apparent radial displacement, this representation allows to directly evaluate the tangential momentum of the swirling structure evolving in the chamber. Fig. 6.5 shows the 2D maps of such a velocity component normalized using U_{ref} ($V_{tg,nd} = V_{tg}/U_{ref}$); a positive value of $V_{tg,nd}$ stands for a clockwise direction for the tangential velocity, looking from upstream to downstream, as the results are reported.

In order to understand the extension and the position of the investigated areas, the shape of the three ducts has been sketched. The investigated area on plane CC1 is wider than on plane CC2 because the distance between boroscope and target is slightly smaller for the latter (see Section 5.1.2). From all the results the clockwise rotating structure promoted by the swirlers is clearly recognizable, with a central low velocity zone and a surrounding

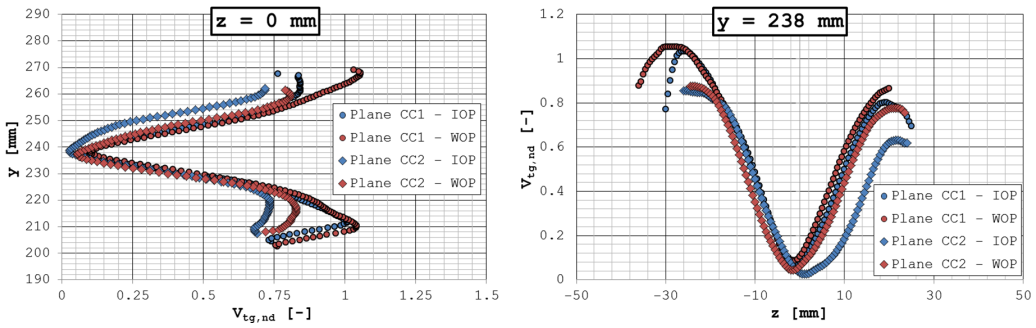

Figure 6.6: PIV results on axial planes - 1D profiles

region with high tangential momentum. A lack of uniformity can be noted in the tangential velocity pattern for both positions and operating points. The main conclusion coming from the maps is that, moving from the first plane to the second (i.e. moving downstream), the tangential velocity of the rotating structure decreases, as expected due to the progressive opening of the jets. Limited differences seem to arise between WOP and IOP, but a more quantitative comparison can be made by analyzing the one dimensional profiles extracted at z=0 and y=238 mm (swirler centerline) and reported in Fig. 6.6.

Both extracted profiles confirm the reduction in tangential velocity, going from Plane CC1 to CC2; moreover, concerning the profiles at z=0 mm, in the outer zone of Plane CC1, WOP condition shows a higher scaled velocity than IOP, while similar values, between the operating conditions, are measured in the inner part; moving to Plane CC2, the difference between IOP and WOP is reduced in the outer zone, while, in the inner one, an important reduction in the IOP velocity occurs, with respect to the other condition. Similarly, at y=238 mm, the scaled tangential velocity is globally higher on the left side, but, on Plane CC2, a strong reduction of the right side velocity occurs for IOP conditions, leading to the maximum differences between the operating conditions. Even if in both the investigated positions (x=65 mm and x=85 mm) the chamber height is still constant (i.e. not converging liners, see Fig. 6.1), both the differences highlighted by the extracted profiles are expected to be due to the converging shape of the inner liner: in fact, it (a) inhibits the flow field swirling motion in the inner part of the annulus

and (b) creates a superimposed ascending motion that enforces the rotation on the left side and reduces it on the right one; as explained before, the flow field looks more sensitive to these effects in the case of IOP conditions, due to the slightly higher aperture of the swirler jets.

Finally, a further analysis was carried out in order to evaluate the displacement of the center of the rotating structure through the two axial planes. Despite the issue related to the apparent displacement, it is reasonable to consider the 2D velocity measured by PIV on these axial planes, instead of V_{tg}, limiting the investigated areas to the very center of the images (20x25 mm). Considering the out-of-plane velocity (i.e. axial velocity) measured at z=0 on the symmetry plane, errors due to apparent radial displacements up to 5%, limited to the outer regions, can be admitted. This analysis, however, allows to achieve a good qualitative visualization of the center of the structure and of the flow field morphology. The velocity fields on the proposed portions of the measurement planes are collected in Fig. 6.7: velocity vectors and the center of the swirler (red cross) have been included for the sake of a better flow field interpretation.

On Plane CC1, the center of the structure, is at the same height of the swirler axis; despite the measure is performed only 10 mm downstream the duct exit, a slight left displacement can be noted, especially in warm condition. On Plane CC2, as already noted from Fig. 6.6a, no significant displacements in vertical direction occur, while for IOP conditions the center of the rotating structure appears to be stretched and moved towards right, as it could be also noted in Fig. 6.6b.

In order to provide a brief summary of the results described in this section, it can be said that PIV measurements have highlighted flow structures typical of swirl stabilized combustors; the swirling structure generated by the central swirler, even if its tangential momentum decreases moving downstream, is clearly recognizable in all the investigated planes and it is expected to reach the chamber exit, due to its fairly limited length and the reduced interaction with effusion cooling flows. The convergent shape of the inner liner seems to play an important role in the evolution of such a flow structure. Regarding the effect of the main-coolant temperature ratio, some

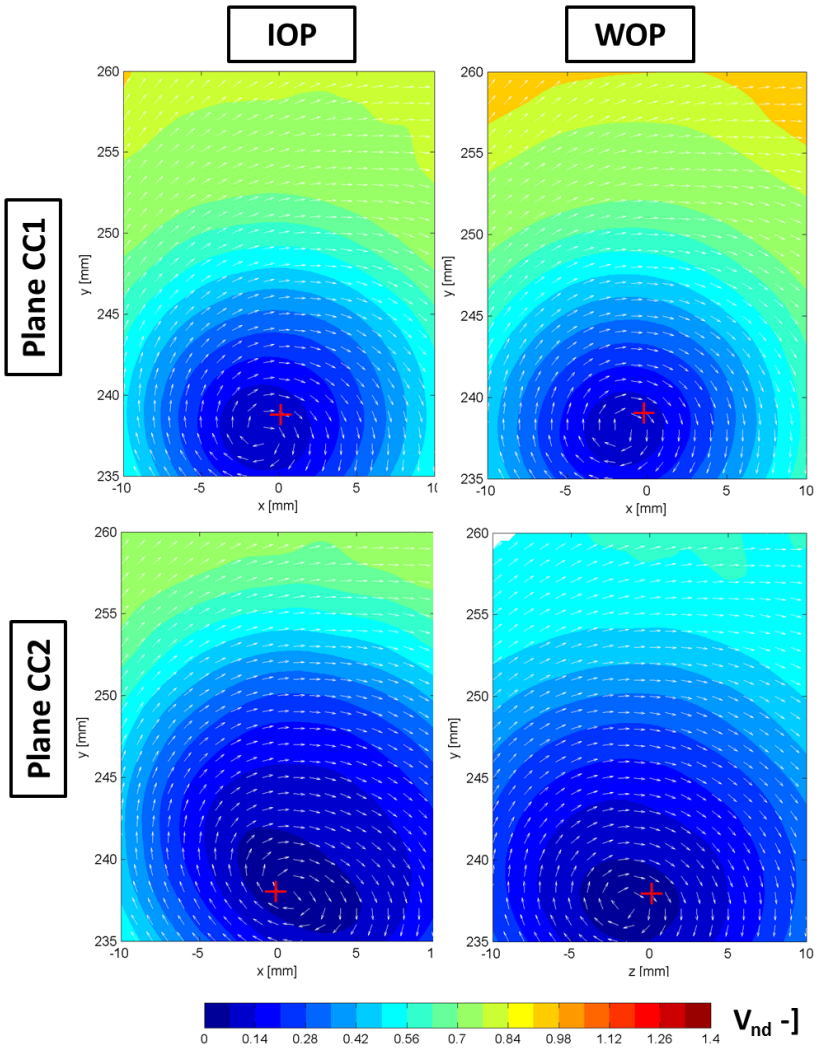

Figure 6.7: PIV results on axial planes - focus on swirling structure center

differences have been highlighted, mainly related to a slight alteration induced in the swirler behaviour and, consequently, different interactions with the inner liner; nevertheless, very similar flow fields have been measured for both the investigated conditions. Even if, in the view of the NGV cascade investigation, the findings coming from the measurements at combustor exit, which will be the focus of the next section, have a much higher relevance, PIV results are useful to fully understand and justify them.

6.2 Aerothermal field at combustor exit

In the view of the characterization of a high pressure turbine behaviour in the presence of a representative lean burn combustor outflow, the most important flow features that have to be evaluated at combustor exit are the intensity of the swirl degree, the temperature distortions and the turbulence intensity. Therefore, the description of the results in this section will follow this necessity. Moreover, as anticipated, a comparison between the aerodynamic field obtained in design point and isothermal conditions will be provided, in order to find boundary conditions for the measurements taken in the latter operating point.

6.2.1 Aerothermal field in design point conditions

Five hole probe measurements, that allow to evaluate both the overall aerodynamics and the thermal field, thanks to the thermocouple installed on the probe, have been carried out on Plane 40_2, which is located about 0.65 axial chords upstream the NGV leading edges, as reported in Section 3.3.

Fig. 6.8 shows the thermal field measured on such a plane; a non-dimensional parameter (T_{nd}) was used, which is defined as follows:

$$T_{nd} = \frac{T - T_{cool}}{T_{swirler} - T_{cool}} \tag{6.2}$$

where nominal values of $T_{swirler}$ and T_{cool} are 531 and 300 K respectively, as explained in Table 3.4; very limited alterations of these values can arise between test to test. A similar parameter was defined by Jenkins et al. [74]; according to them, it can be seen as a quantification of the strength of the hot spot in the measurement plane; a value of T_{nd} equal to 1 would be achieved at the very swirler exit. Results are reported in terms of non-dimensional height (h/H, y-axis) and non-dimensional tangential position (i.e. tangential coordinate t [°], made non-dimensional by the 9° NGV pitch p). The central sector covers the tangential span between -1 and 1, due to the 1:2 swirler-to-vane ratio, while the investigated domain slightly exceeds this area. Results

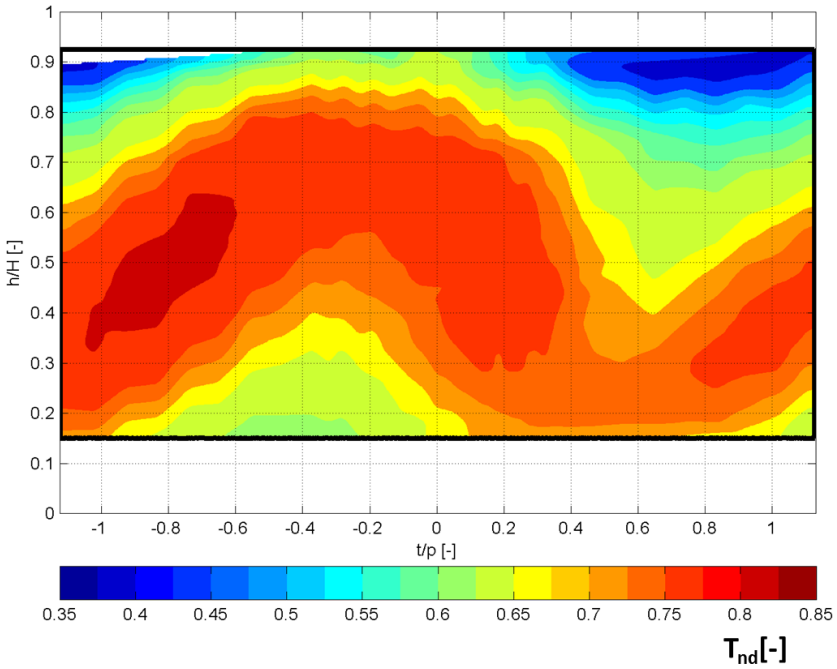

Figure 6.8: Non-dimensional temperature map measured on Plane 40_2

are reported, as for in all the rest of the treatment, as they are seen watching from upstream to downstream.

The maps show the presence of a wavy hot strip, covering the whole tangential investigated span. Even if the investigation area does not reach the inner and outer walls, the presence of "cold" coolant layers, generated by the liner cooling flows that have hardly mixed with the hot mainstream, is clearly recognizable. The hot spot is not well-bounded and axisymmetric as it is generally pursued in this kind of investigation. The wavy shape of the hot streak is due to the flow field conditions, in that the clockwise swirling flow draws cold coolant from the outer (right cold spot) and inner (left spot) coolant layers. The maximum measured values of non-dimensional temperature stay around 0.8, meaning that the hot streak strength is reduced by 20%, as it passes through the combustion chamber. The temperature distortion is still important enough for the aim of the study: a maximum-to-minimum temperature ratio of about 1.25 is achieved within the investigated domain. One dimensional radial profiles have been extracted from the T_{nd} maps, in

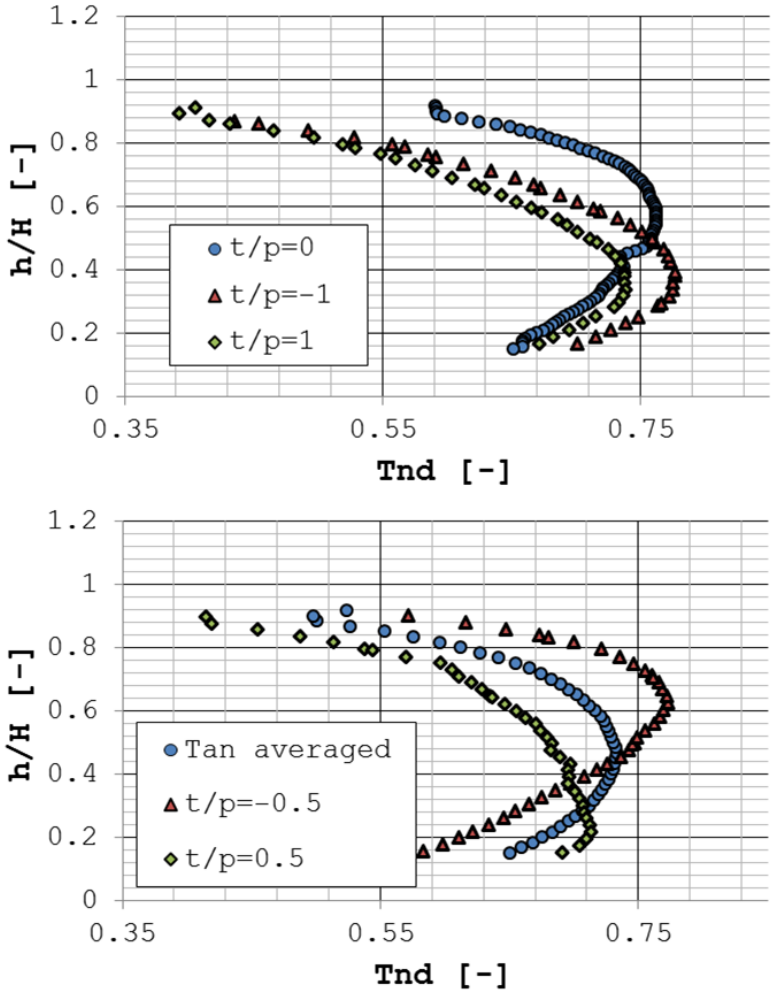

Figure 6.9: One dimensional T_{nd} profile on Plane 40_2

order to draw quantitative conclusions about the temperature gradients approaching the cascade; they are reported in fig. 6.9. Five different tangential positions have been extracted, correspondent to the central airfoil leading edge ($t/p = 0$), to the lateral ones ($t/p = \pm 1$) and to the left and right NGV passages ($t/p = \pm 0.5$). Additionally, a tangentially averaged profile is reported, in order to get an overall information of the temperature distortion, which is also the most common parameter that is normally considered during the NGV design phase.

Results highlight different temperature distributions at different tangen-

tial positions. Concerning the first plot, where only "leading edge profiles" have been collected, a clear difference in the position of the maximum temperature can be noted: while for $t/p = 0$ the maximum is achieved at $h/H \approx 0.6$, for the lateral airfoils it is reached at $h/H \approx 0.38$. The difference in the maximum temperature for the two lateral profiles is due to a not-perfect periodicity of the central sector, as it was also possible to note from the 2D contours, since they should nominally presents the same values. Concerning the second plot, similar considerations can be drawn: the "passage profiles" ($t/p = \pm 0.5$) show important differences between each other, both in terms of maximum temperature position ($h/H \approx 0.62$ for the left profile and $h/H \approx 0.2$ for the right one) and maximum temperature value. Finally the tangentially averaged profile reaches the maximum temperature at $h/H \approx 0.45$ with a maximum non-dimensional value of about 0.73, that stays in between the values achieved in correspondence of the NGV passages (≈ 0.78 and 0.71) and slightly lower than the one at $t/p = 0$ (≈ 0.76).

Concerning the aerodynamic field at combustor exit, as anticipated, the focus is mainly placed on the characterization of the flow angle pattern; Fig. 6.10 show the swirl and pitch angles 2D contour plots on Plane 40_2. The first is defined, in the rig cylindrical coordinate system, as the angle between the velocity vector and the axial direction in the $x - t$ plane; the second one, one the other hand is defined as the angle between the same elements in the $x - r$ plane. Both angles can be evaluated, knowing the three velocity components, with the following relations.

$$swirl = atan(\frac{V_{tan}}{V_{ax}}) \tag{6.3a}$$

$$pitch = atan(\frac{V_{rad}}{V_{ax}}) \tag{6.3b}$$

A sketch of these angles is also reported in Fig. 6.10 for the sake of a better understanding. From five hole probe acquisitions, the raw results, calculated by the post-process code, must be processed to get rid of the probe preswirl, in order to get the results in the cartesian traverse system coordinates; afterwards a further rotation, depending on the local tangential

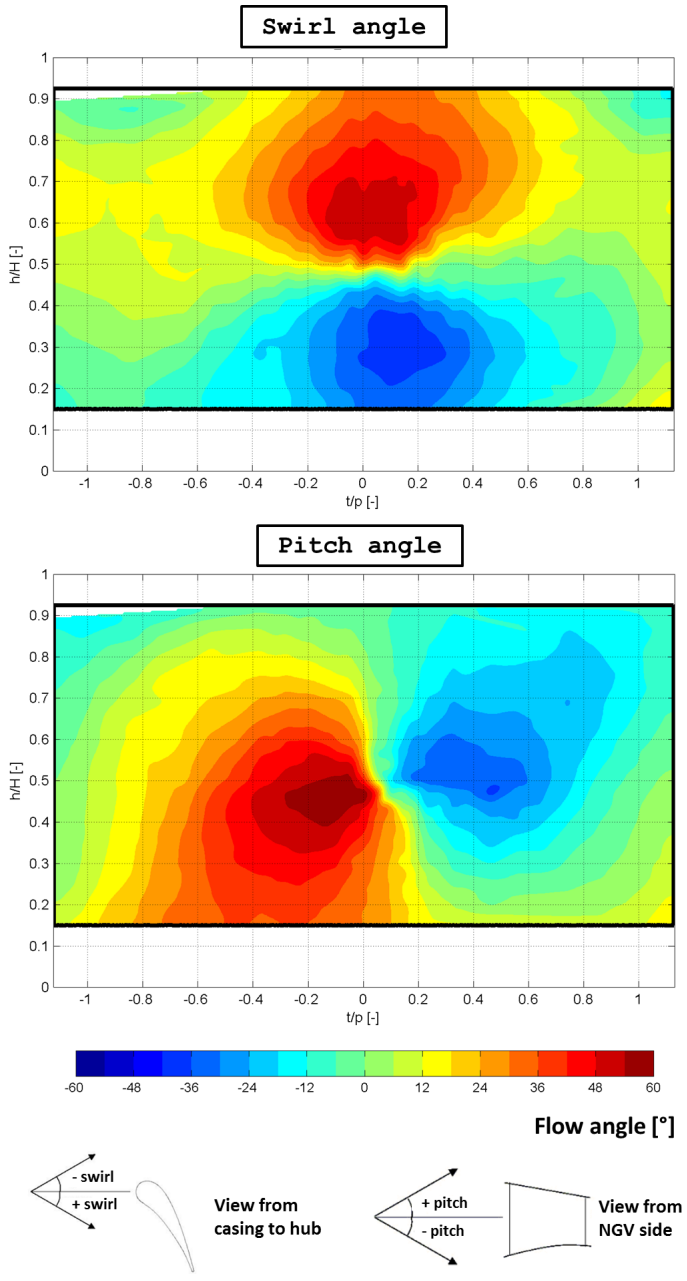

Figure 6.10: Flow angles maps measured on Plane 40_2: swirl and pitch angles

position of the considered mesh point, is applied to calculate the velocity components in the rig coordinates and calculate the flow angles through Eq. 6.3. From a "turbine" point of view, a higher swirl angle (flow motion from left to right, looking at Plane 40 from the combustor side), determines

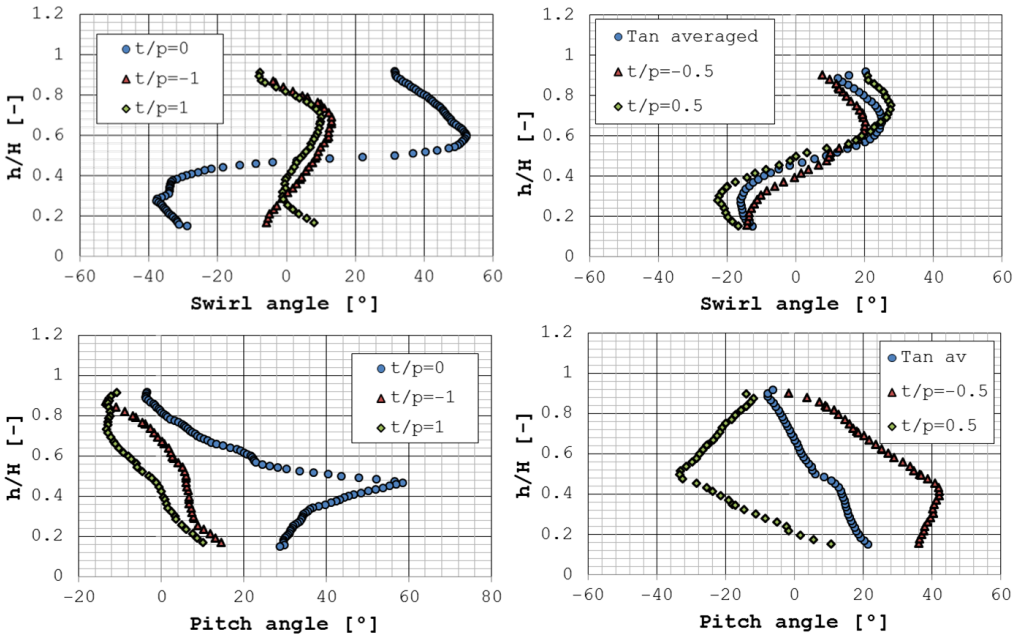

Figure 6.11: Flow angles 1D profiles

a lower incidence on the NGV profiles. The pitch angle, on the other hand, can not be represented in the blade-to-blade plane.

A highly non-uniform flow field, in that a clear rotation can be recognized, is achieved at combustor exit; the highly swirling structure promoted by the swirler and identified through PIV measurements is, therefore, found to be conserved up to Plane 40_2, despite its tangential momentum is progressively dissipated. Maximum swirl angles above 50° and pitch angles up to 60° are measured. Beyond this global qualitative view, some more detailed conclusion can be taken by evaluating the 1D profiles, reported in Fig. 6.11, extracted in the same positions as for the thermal field. First of all, it is possible to note a sensitively different behaviour between the flow field approaching the central NGV ($t/p = 0$), characterized by very high swirl angles and the lateral ones ($t/p = \pm 1$), with angles that do not exceed 15°. Therefore, even if a qualitatively similar swirl sweep approaches all the profiles, its intensity is much bigger for the central one. As a result, the central NGV must be expected to present a higher front load (higher incidence) in the hub zone, while the opposite (reduced incidence) occurs in the casing area.

CFD-predicted pressure profiles (Fig. 4.8, left images) confirmed that the central blade shows a slightly higher loading in the very frontal part than the lateral one in the hub region; an opposite behaviour can be noted in the area close to the casing, as the stagnation line moves towards the suction side for the central NGV. Concerning the pitch angle, similar considerations can be made: the centerline profile shows a "spike" up to 60 °, while the lateral ones have reduced angles, since they are at the sides of the swirling structure. Focusing the passage profiles ($t/p = \pm 0.5$), the swirl is qualitatively similar to the centerline profiles, with reduced peak values, similar to the result of the tangentially averaged profile. Pitch results, on the other hand, show very high angles, at $t/p = \pm 0.5$; in tangentially averaged terms a qualitatively different profile is found, since it only presents slightly negative angles, in the top part of the annulus, and positive ones, in the bottom part, as a result of the converging shape of both inner and outer walls. A further analysis allows to note that angles are higher in the top part of the annulus, with respect to the inner (swirl angles of $\approx 52°$ and $\approx -39°$ respectively, on the centerline) and on the left side, with respect to the right one, as it is clearly visible from the 2D map. Both these aspects should be seen as consequences of the inner liner shape: as explained in the previous section, it inhibits the rotation in the inner part of the annulus and creates a superimposed ascending motion that enforces the rotation on the left side. A further consequence of this behaviour is the shift of the swirling structure core towards right, with respect to the rig centerline, as it can be seen from the swirl map; this phenomenon also explains the spike value in the pitch angle centerline profile. This conclusion has also been verified by overlapping a vector map, which allows to point-by-point visualize the flow field direction in the measurement plane, to the Mach number contour, as reported in Fig. 6.12; a shift of the rotation center towards right (at $t/p \approx 0.15$) is clearly recognizable. The 2D contour also shows a very reduced Mach number, especially in the vortex core, with slightly higher values in the surrounding "high-momentum" zones, even if they never exceed 0.16.

Summarizing, the analysis of the overall aerothermal field at combustor exit has demonstrated that the test rig is capable of reproducing the pur-

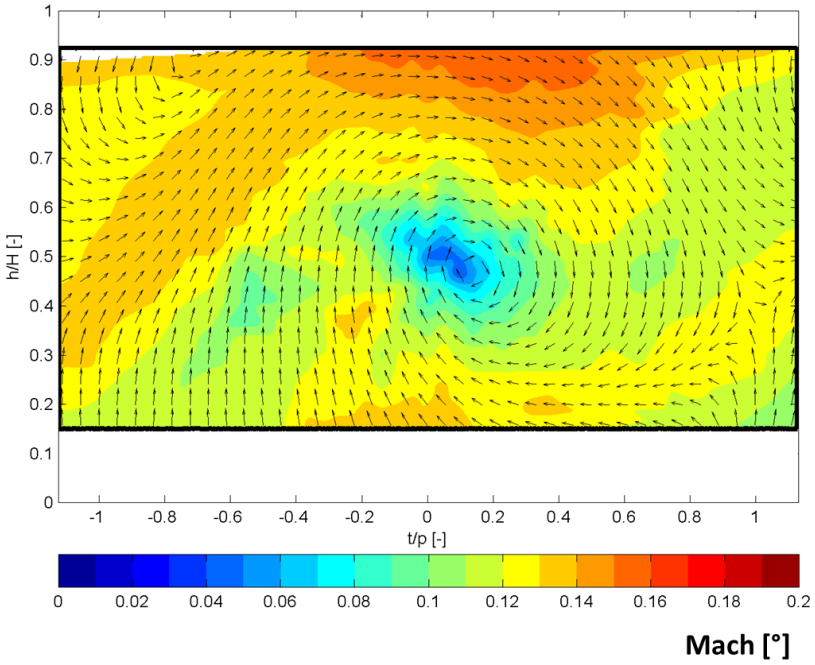

Figure 6.12: Mach number contour on Plane 40_2

sued flow features and temperature distortions, with scaled temperature and flow angles values that are comparable with what is typically pursued in experimental investigations of this kind. Moreover it has been shown that tangentially averaged temperature and flow angles profiles present important deviations from the local ones: therefore, with this kind of inflow, a NGV design procedure that considers only average parameters, which is the common procedure, results in relevant inaccuracies in the prediction of local turbine inflow conditions; the effects and entities of these inaccuracies will be detailed in Chapter 7.

6.2.2 Comparison with isothermal conditions

In this section a comparison between the five hole probe results achieved on Plane 40_2 in nominal conditions DP (i.e. with heated mainstream) and in isothermal ones IOP_2 (i.e. all the flows at ambient temperature) will be provided. The goal is to demonstrate that a very similar aero-field is achieved despite a substantially different main-coolant temperature ratio, in

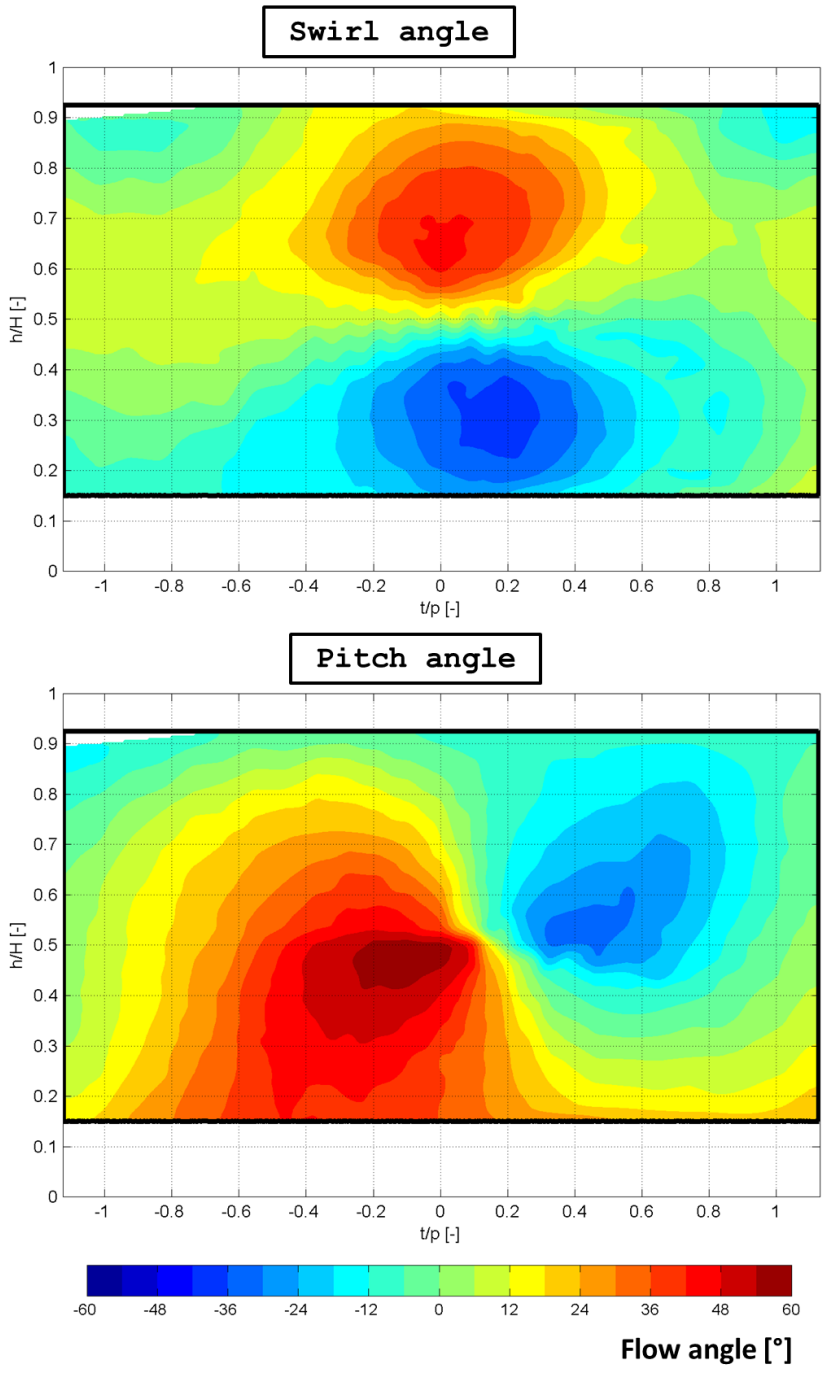

Figure 6.13: Flow angles on Plane 40_2 in isothermal conditions

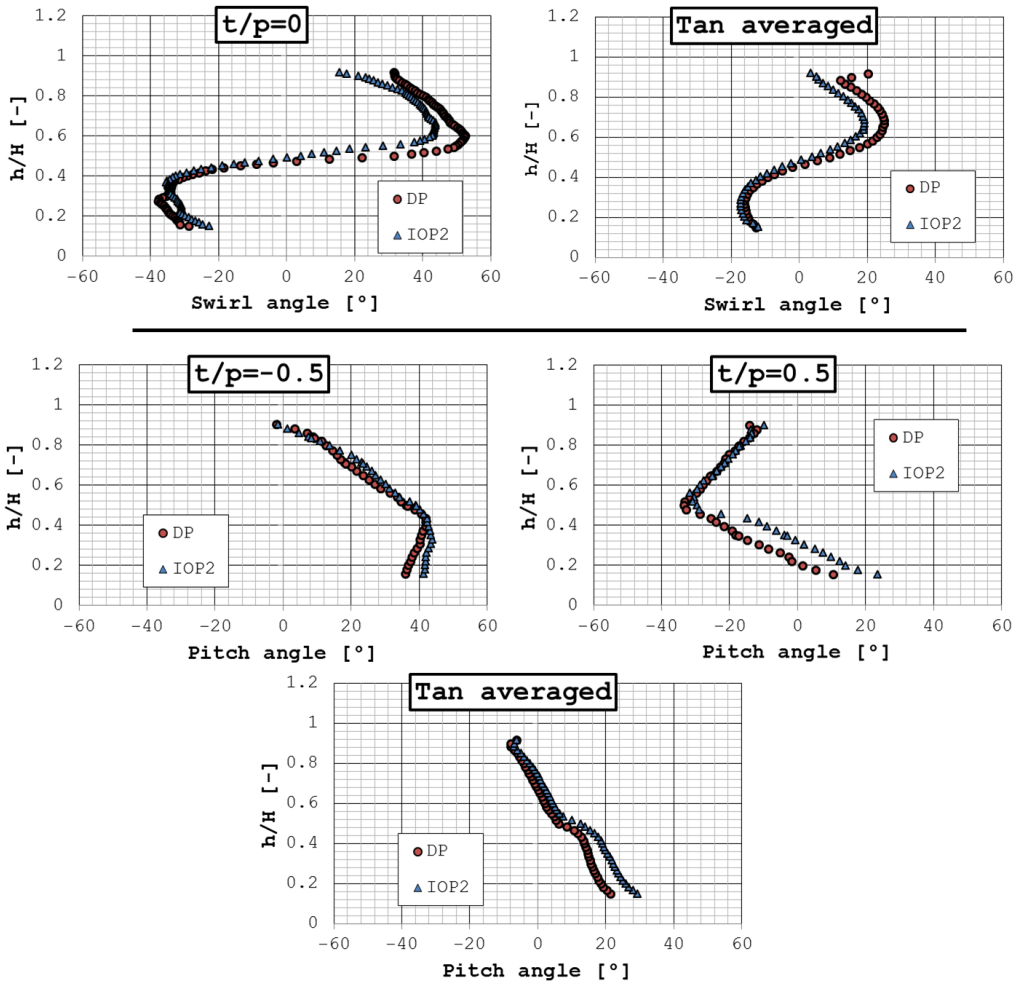

Figure 6.14: Flow angles profiles - comparison between DP and IOP_2

order to extend the results of the measurements taken in the second operating condition to the first, with the limitations described in Section 3.3.1. Preliminary CFD calculations [101] showed a very good matching in terms of flow angles; this experimental comparison was carried out as a verification. Fig. 6.13 shows the flow angles measured on Plane 40_2 in IOP_2 conditions, to be compared with Fig. 6.10.

A very similar pattern stands out, with a very good qualitative and quantitative matching; the main difference seems to be located where the maximum swirl angle is measured, since it is a little higher in DP conditions. To get a more detailed comparison, 1D profiles have been extracted and reported

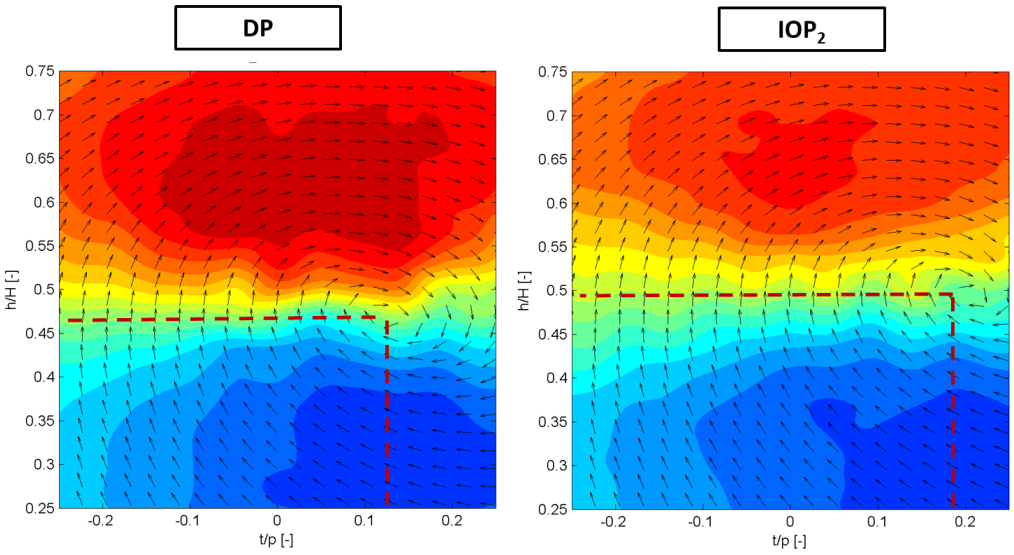

Figure 6.15: Evaluation of swirling structure center for DP and IOP_2

in Fig. 6.14; in order not to make the treatment too heavy, only tangentially averaged profiles and in the positions where the measured values are close to the highest (i.e. centerline profile for the swirl and passage profiles for the pitch) are shown. The analysis of the profiles confirms what was noted from the 2D contours: a very similar flow field, between the operating conditions, is achieved, with limited differences that are confined in the maximum swirl area (52° for DP and 45° for IOP_2) and in the inner part of the annulus for the $t/p = 0.5$ pitch profile (12° for DP and 24° for IOP_2). The tangentially averaged profiles effectively summarize these conclusions. Moreover the exact position of the swirling structure core was evaluated, since it plays an important role in the definition on the NGV airfoils incidence and, as it will be demonstrated in Chapter 7, in the evolution of the flow field through the NGV. Fig. 6.15, where vectors have been overlapped to a zoom of the swirl contour, shows that the structure core is slightly moved up and right for the isothermal case. The differences are, anyway, very limited as they stay within 2mm.

All these aspects are coherent with the differences between the results in the two operating condition highlighted by PIV measurements, even if some modifications arise moving to combustor exit. Nevertheless, a very

good matching between the two operating conditions was found despite the slight change in the scaled pressure (i.e. in the combustor exit average Mach number) that had to be introduced for the isothermal point. Thanks to this verification, it is legit to expect very similar turbulence field at combustor exit, in IOP_2 and DP conditions, making the hot wire results, which will be described in the next section, able to also describe the nominal condition. A very similar incidence on the NGV airfoils should also be expected, that is crucial in the view of the PSP campaign evaluation, that will be reported in Section 7.1.3.

6.3 Turbulence intensity at combustor exit

According to the goals of this work, in order to account for all the main aspects that characterize combustor-turbine interface area, it is also important to characterize the turbulence intensity, due to its relevant influence on the turbine aerodynamics and heat transfer. While the goal of the overall field characterization was to check if the test rig was able to reproduce high enough distortions to simulate modern lean burn combustors behaviour, in this case the problem can be seen from a slightly different angle. Since very reduced experimental data is available regarding the turbulence level in these kind of test cases, the actual value of the turbulence intensity measured at the exit of a lean burn combustor simulator can provide good information and comparisons with the data coming from traditional combustors. While it is not in the author's intention to claim that the unsteady behaviour reached in the test case is exactly the same as in a real engine, due to aspects like heat release that can't be replicated, it is known that the gross of the turbulence intensity, for these applications, should follow the swirl profiles [22, 95]. Hence, since the aerodynamic field at combustor exit, and the swirl degree in particular, was found to be good for the pursued goals of this work, the hot wire measurements provide useful data to help covering this lack of knowledge. It must be reminded that turbulence measurements have been carried out in isothermal conditions (IOP_2); the impact of this aspect on the applicability of the results have been discussed in Section 3.3.1.

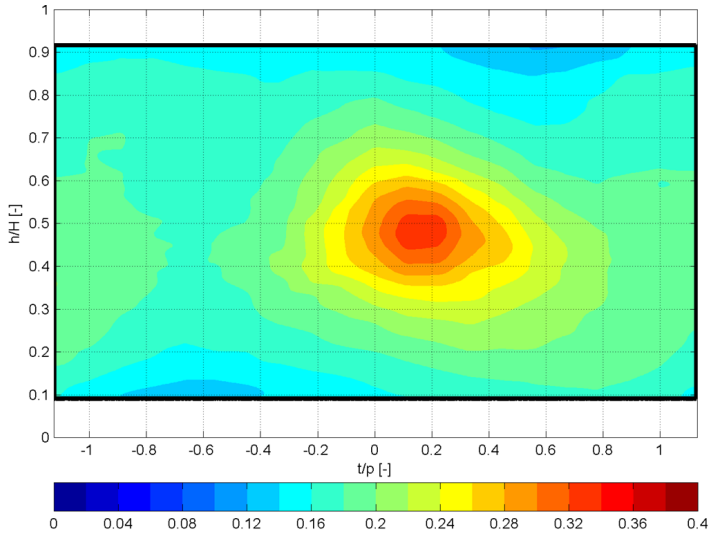

Figure 6.16: Turbulence intensity on Plane 40

Fig. 6.16 shows the turbulence intensity contour plot measured on Plane 40, in IOP_2 conditions, evaluated through Equation 5.8. As for five hole probe measurements, the results have been linearized, to have a better understanding of the investigated positions. The map shows a well-defined high-turbulence spot, where values go beyond 30 which perfectly corresponds to the position of the swirling core center. The turbulence intensity progressively decreases as the distance from this center increases. It is pretty clear, therefore, that most of the turbulence intensity contribution, as expected, is generated by the highly swirling structure promoted by the swirler that reaches the combustor exit. Even if it was not possible to extend the investigation close to inner and outer walls, the results suggest that no relevant contribution to the turbulence intensity is given by the interaction between the mainflow and the coolant layers, that occurs in the top and in the bottom parts of the annulus.

Fig. 6.17 shows the 1D radial profiles extracted from the map: the same tangential positions as for the thermal field and the flow angle pattern were investigated; a profile at $t/p = 0.17$ was also added, since it corresponds to the spot with maximum turbulence. While the latter profiles reaches 33 %

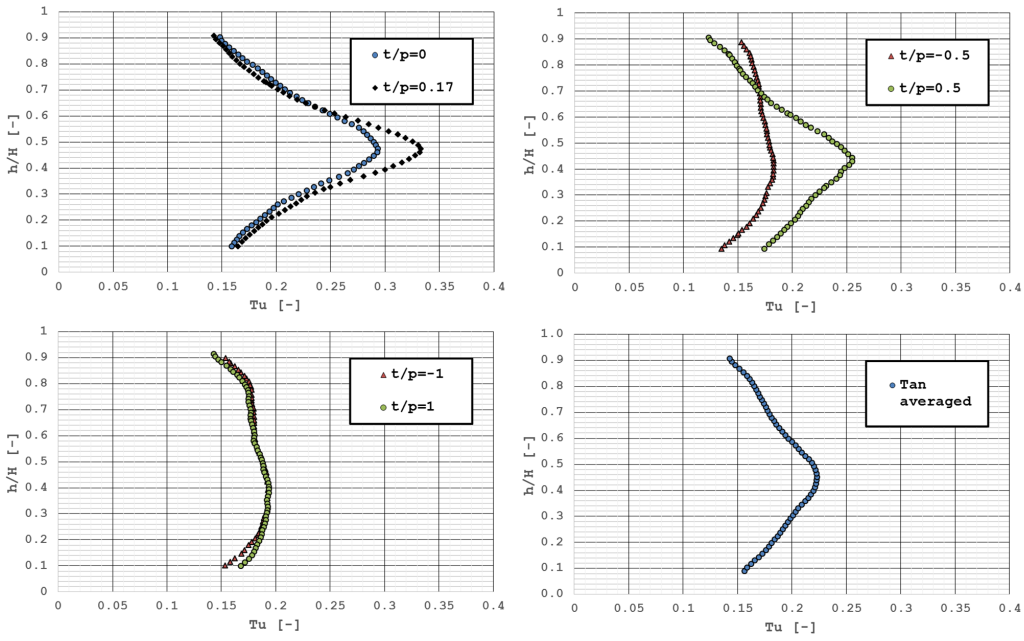

Figure 6.17: Turbulence intensity profiles on Plane 40

in the high-turbulence spot, which is the maximum measured value, and the centerline profile almost reaches 30 %, the turbulence intensity stays below 20 % in correspondence of the lateral NGVs leading edges; effects attributable to a higher turbulence level, in terms of heat transfer and mixing phenomena, should be, therefore, expected on the central NGV rather than on the lateral ones. Concerning the passage profiles, the measured turbulence is higher for the right one, as the swirling structure is shifted towards that direction. Finally, the tangentially averaged profile presents limited turbulence intensities, up to 22 % at $h/H = 0.45$, showing, as also concluded for the overall aerothermal field, relevant differences with the local profiles.

The evaluation of turbulence intensity gives an idea of the average deviation of instantaneous velocity from its mean value and, therefore, of the mean kinetic energy per unit mass associated with the turbulent flow eddies; beside that, it is also interesting to investigate how this energy is distributed among different scales. To do so the Fast Fourier Transform has been applied to the three fluctuating components of velocity, finding their frequency spectra on a discrete number of frequencies from 0 to 5000 Hz (half of the ac-

quisition frequency according to Nyquist-Shannon sampling theorem). Then the turbulence kinetic energy, for every frequency, has been calculated using the following relation:

$$K(f_i) = \frac{1}{2}(V'_{ax}(f_i)^2 + V'_x(f_i)^2 + V'_y(f_i)^2) \tag{6.4}$$

where f_i is a frequency value between 0 and 5000 Hz with a resolution of 1/3 Hz (three seconds sampling). The frequency spectra, depicted in Fig. 6.18, have been averaged on steps of 10Hz in order to have a clear view of their trend. The variable on the y-axis is the spectral density $E(f_i) = K(f_i)/df$, where df is the resolution step on the frequency axis. With such a visualization, the area under the curve between two frequencies f_1 and f_2 represents the turbulent kinetic energy (K) content of the flow field within these frequencies, that are inversely proportional to the size of the turbulent eddies in the flow (i.e. to the turbulence scales).

The turbulent spectral density is shown for five different mesh point, whose position in the measurements plane is reported in the top left contour; they correspond to the points of maximum turbulence, maximum and minimum swirl and maximum and minimum pitch respectively, going from point 1 to point 5. A lot of other mesh points have been investigated showing very similar results. From the spectra reported in the figure a typical trend that is commonly associated to turbulent flows can be recognized, with TKE progressively decreasing as the turbulent frequency is increased (i.e. as the lengthscale decreases). A curve with a $k^{-5/3}$ slope is also reported in order to compare the measured trend with the one obtained from Kolmogorov hypothesis [161]. The matching is quite good, at $f > 500Hz$, for most of the reported points; no clear evidence of a deviation from the slope can be noted, as the acquisition frequency is not high enough to appreciate the Kolmogorov scales. Only in the very last part of the curve ($f_{acq} \approx 4500Hz$) a little deviation seems to occur, suggesting that the effect of viscosity is beginning to affect the slope of the spectra. The following relations, developed for the Kolmogorov scales calculation [161], have been used to provide an

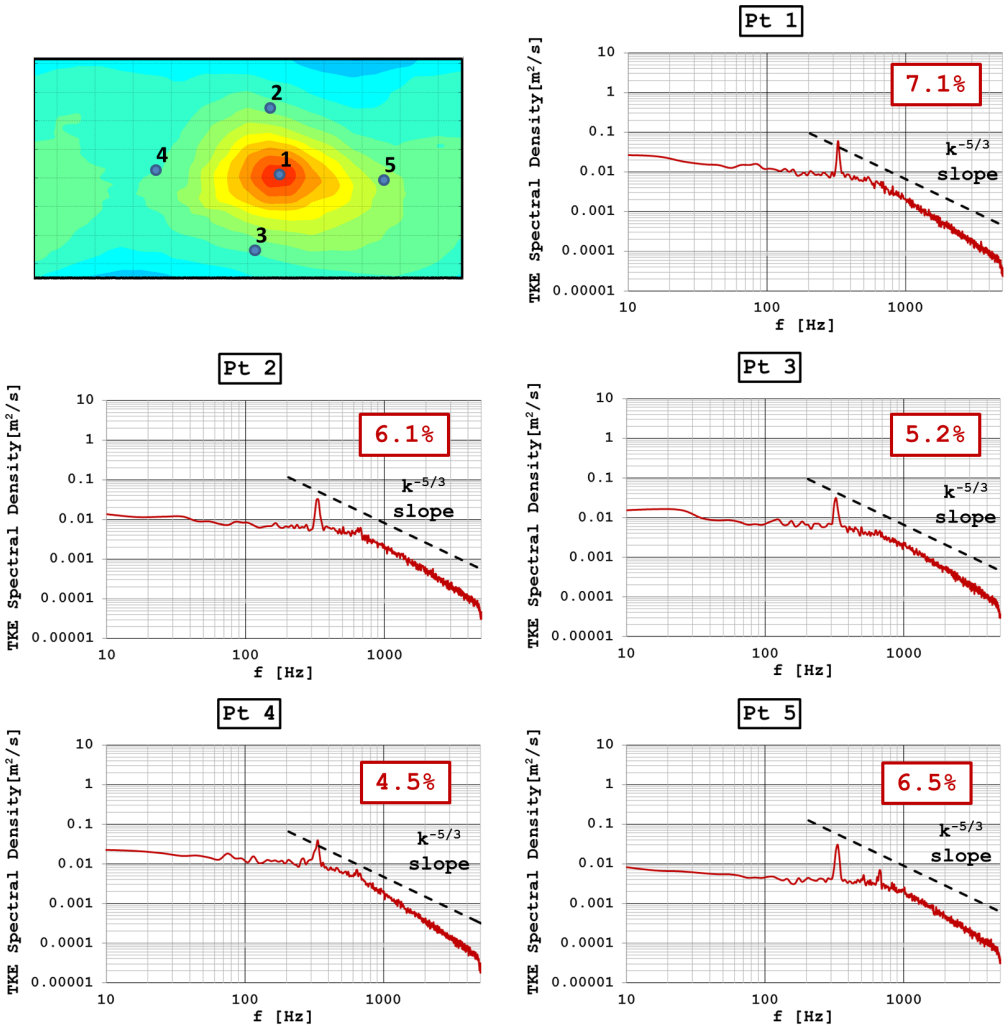

Figure 6.18: Turbulence kinetic energy spectral density for different mesh points on Plane 40

overall estimation of the frequency value where the effect of viscosity should be found:

$$l_{kolm} = lRe^{-3/4} \tag{6.5a}$$

$$U_{kolm} = URe^{-1/4} \tag{6.5b}$$

$$\tau_{kolm} = \tau Re^{-1/2} \tag{6.5c}$$

According to Pope [161], the dissipation range should begin when the scales decrease to a value that is about 60 times bigger than Kolmogorov's scales (l_{kolm}). Re and U calculation, the average Reynolds number and flow velocity, have been calculated through the knowledge of the mass flow rate, the annulus area and the average static pressure (127kPa) and temperature (300 K). The annulus equivalent diameter was adopted for l. A frequency of $\approx$ 4300 Hz was calculated as the value where the dissipation should begin to occur (i.e. where the effect of viscosity begins to affect the trend), very similar to the one calculated through the spectra. While this calculation is not aimed at finding a precise value, since the goal of this part of the treatment is not to provide a description of the smallest turbulent scales, this comes as a confirm of the coherence of the measured spectra and, thus, of the reliability of the HWA results.

Beside the common trend, a clear peak can be observed for all points, at $f = 324 - 334Hz$: since the results are averaged on 10 Hz spans, it is possible to state that all the test points show the TKE peak at the same frequency. A further analysis has allowed to understand the reason of this spectral density maximum: experimental data have been compared to the velocity components temporal evolution extracted from LES calculations carried out both internally at University of Florence [162] and by Cerfacs [163], as a partner in FACTOR project; for both CFD runs, data were taken from probes positioned at the very duct exit, in order to check if the peak experimentally detected on Plane 40 was due to an unsteady structure generated within the swirling core. Results, shown in Fig. 6.19a show that a clear peak, at a very similar Strouhal number compared to experimental data, is detected by both CFD calculations; the use of Strouhal number was made necessary to scale the results, since the calculations were run in DP conditions. In particular it was shown that this peak frequency was associated to a PVC structure. Fig. 6.19b depicts this structure, shown as isosurface of constant pressure (red), together with the central recirculation zone (blue) [162].

As it was stated in Section 2.1, PVC structures are generally damped by the heat release, in the presence of the combustion process of the engine application, and, in non-reactive conditions they can significantly alter the

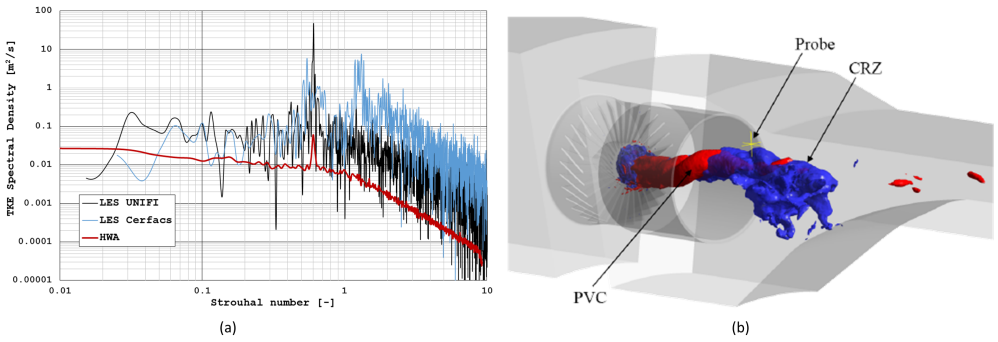

Figure 6.19: Comparison between experimental and CFD calculated spectral density (a) and visualization of PVC structure (b)

overall flow field expected at combustor exit. For this reason, the design of non-reactive lean combustor simulators is generally aimed at avoiding the generation of the PVC. Even if a residual structure is still present in the rig, it doesn't lead to substantial issues regarding the overall field at combustor exit, since, as it as just been shown, a satisfactory and coherent highly swirling flow is achieved, together with relevant temperature distortion. Concerning the PVC contribution to the total turbulence intensity, it was evaluated simply by substituting the spectral density amplitude, for the three velocity components separately, measured at the PVC frequency, with an average between the two adjacent ones, not interested by the peak (i.e. by the PVC). A new calculation of the velocity RMSs, and therefore of the TKE, showed that the PVC contribution stays within 7.1 % and reaches this maximum only in the maximum turbulence spot (i.e. in the swirling structure core); the evaluated percentages are shown in Fig. 6.18 for all the reported mesh points. Therefore the main part of the turbulence kinetic energy measured at combustor exit is not due to the unsteady structure of the PVC, but due to the swirl-induced broadband unsteadiness of the flow field.

Summarizing, the investigation of the turbulence intensity and of the unsteady aspects on Plane 40 has offered interesting insights. An important turbulence intensity, up to 33 %, was measured in a well-bounded spot, generated by the highly swirling structure promoted by the swirlers. This behaviour is completely different with what is generally expected for traditional RQL combustors, where the gross of the turbulence intensity arises

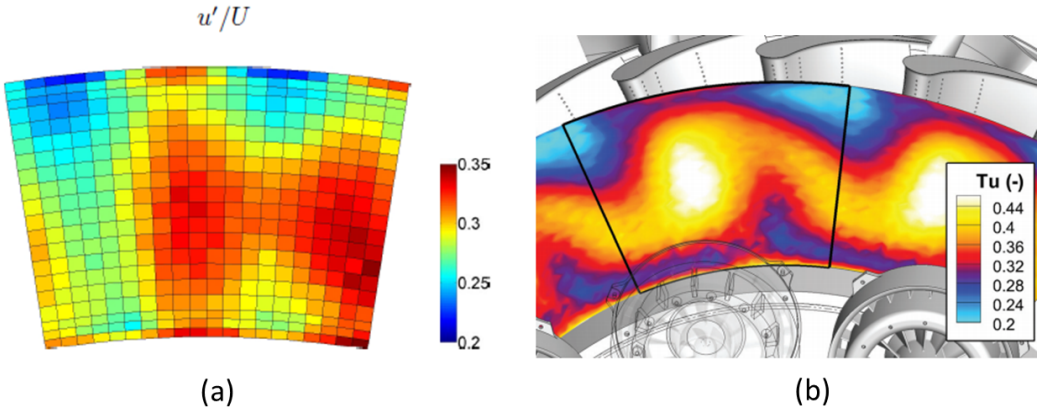

Figure 6.20: Turbulence kinetic energy measured at the exit of RQL (a) and lean (b) combustors simulators [94, 80]

from the interaction between opposite dilution holes, as it was found by Cha et al. [94] (Fig. 6.20a): this result was detailed in Section 2.4.4. Results achieved by Werschnik et al. [80] on a lean burn combustor simulator (see Section 2.4.3 and 2.4.4), on the other hand, showed a similar qualitative behaviour even if higher intensities were measured (Fig. 6.20b). The evaluation of the turbulence spectral density revealed the presence of a residual PVC. Nevertheless both its effect on the overall flow field and its contribution to the total turbulence intensity were found to be very limited and don't compromise the capability of the test rig to produce the pursued typology of combustor outflow.

Once all the main features of the combustor outflow have been described, in the next chapter, their combined effect on the NGV module performance will be detailed. Insights of the nature of the flow field approaching the rotor will be also provided.

Chapter 7

Effect of Combustor Outflow on the Turbine NGV

Contents

After the combustor outflow characteristics have been described in the previous part, their effect on different aspects of the high pressure turbine performance will be addressed in this chapter. The investigation of the NGV cascade has a double purpose: first of all it is important to evaluate how the behaviour of the NGV itself is affected by such a particular inflow. Moreover, it is also useful to investigate how these flow characteristics are convected and modified through the cascade, in order to draw considerations regarding the flow field approaching the rotor. The measurements that will be described in

the following try to address both these aspects. According to what was stated in Section 2.5.1, the final goal of the treatment is to describe the behaviour, and evidence possible issues, of a NGV cascade specifically designed for this kind of inflow, through a traditional design procedure based on tangentially averaged radial profiles as inlet boundaries. In the first part only the effect of the swirling flow will be investigated. In the final part of this chapter the evaluation of the NGV aerodynamics and of hot streaks transport in the presence of both swirl and temperature distortions will be considered.

7.1 Flow field characteristics in isothermal conditions

7.1.1 Overall aerodynamic field

The investigation of the overall aerodynamic field, in IOP_2 conditions, is mainly aimed at understanding the flow field evolution within the NGV, by highlighting flow features and secondary flows. Even if it is not possible to detail all the flow features that can be generated within the cascade, since bigger experimental scales would be required, together with the possibility to explore the very vicinity of the endwall zones, several details and a global behaviour can be effectively described. Considerations about the NGV performance can be drawn as well, thanks to the evaluation of the pressure losses. Since both this aspects, as described in Section 2.3.1, are closely connected, they help to better understand each other and to gather a clear view of the physics of the whole phenomenon. While the effect of a swirling inflow on NGV pressure losses and secondary flows has been in part detailed in past studies, this evaluation allows to draw some useful insights about the present configuration; it is also necessary to gain knowledge of the flow field evolution and allow a better understanding of the results reported in the following sections. These results will be also briefly compared with other studies aimed at analyzing similar kind of inflows. Even if three different NGV coolant mass flow rates have been investigated (see Section 3.3), due to the limited differences induced in the aero-field, only the two extreme conditions will be

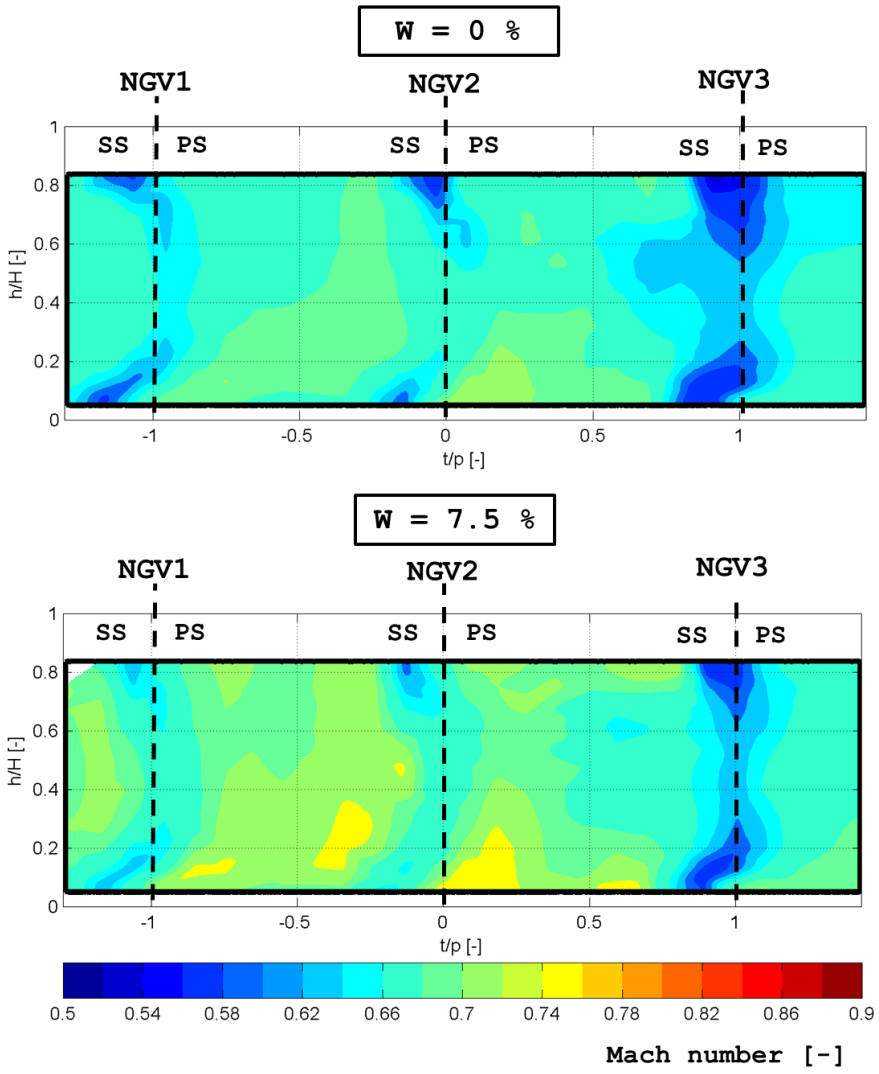

Figure 7.1: Mach number maps measured on Plane 41 in IOP_2 conditions

shown, for the sake of clarity, when no particular further indications can be obtained by the investigation of all the three configurations.

Beside the above mentioned phenomena, it is useful to begin the treatment by presenting the Mach number maps, evaluated by five hole probe traversing on Plane 41 (0.24 axial chords downstream of the NGVs trailing edges). They are reported in Fig. 7.1, for both the condition without coolant ($W = 0\%$) and the condition with nominal coolant mass flow rate ($W = 7.5\%$). Even if the Mach number distribution is not directly use-

ful to strict the just listed goals, it provides a necessary indication of the boundary conditions of the present research. A brief account of the Mach number achieved at NGV exit, in DP conditions, had already been provided in Section 4.1.1, as a part of the commissioning activity. Nevertheless, IOP_2 results are reported here because a lower Mach number is expected; a full comparison of the Mach number levels for the two operating conditions, will be, then, provided in Section 7.2. As described in Section 5.2.2, the contour plots have been rotated in order to have the central airfoil wake, at the mean radius, at $t/p = 0$ (according to the non-dimensional and linearized representation described in Section 6.2.1). The central sector, therefore, covers the span between $t/p = -1$ and $t/p = 1$; in particular $0 < t/p < 1$ corresponds to the right passage (between NGV_2 and NGV_3 according to Fig. 4.6) exit area, while $-1 < t/p < 0$ corresponds to the left one (between NGV_1 and NGV_2). The position of the three central NGVs is reported in the figure. As in all the other contour plots, the results are reported as looking the measurement plane from upstream to downstream; this can be also understood from the position of pressure and suction sides, indicated in the figure. Results show the expected pattern, in that the Mach number is higher in the inner part of the annulus, because of the radial equilibrium dominated flow pattern. The positions of the trailing edges wakes of the three airfoils can be also noted as low velocity zones. Since the inlet pressure (i.e. Plane 40 pressure) is kept at the same value (127 kPa), for the different coolant mass flow rate conditions, the case with $W = 7.5\%$ shows a higher global Mach number, than the $W = 0\%$ case, since a slightly higher mass flow rate passes through the vane passages and a higher expansion is achieved.

Fig. 7.2, that reports the average and maximum Mach numbers on the central 18° span ($-1 < t/p < 1$), summarizes this trend, with the mean value increasing from 0.68 to 0.703 and the maximum ranging from 0.736 to 0.763. Hence, it is clear that the treatment is focused on subsonic flows, where no shocks nor locally supersonic conditions, that could partially modify some of the conclusions taken throughout this chapter, occur.

Shifting the focus to the flow field non-uniformity at NGV exit, swirl angle 2D contour maps are reported in Fig. 7.3, for both W = 7.5 % and W

= 0 % cases. On Plane 41, from a "turbine" point of view, the swirl angle represents the NGV exit flow angle on the blade-to-blade plane. A higher measured swirl, therefore, results in a higher incidence on the rotor blades. Even if the flow field is clearly dominated by the deflection given by the NGV cascade, as the measured swirl angle is pretty close to the NGV exit flow angle in all the points of the annulus, a clear pattern can still be recognized and some interesting conclusions can be taken. First of all, it is possible to note high swirl angles in correspondence of the trailing edge wakes. Even if a similar qualitative behaviour, with higher swirl angles in correspondence of the vane wakes, was also evidenced by early CFD calculations, the experimental reading in these spots is expected to be slightly overestimated due due to the interaction between the airfoil trailing edges and the probe tip (see Section 5.2.2). Nevertheless, results have not been masked out in this area, since these inaccuracies do not alter the conclusions taken from the measurements, nor the qualitative pattern of the secondary flows that will be shown in the following. The measurements in correspondence of the vane passages, on the other hand, are not affected by this problem and their expected uncertainty is in line with what was evaluated during the calibration process. The most interesting conclusion can be taken by evaluating the different patterns that are measured within the two passages. The left passage

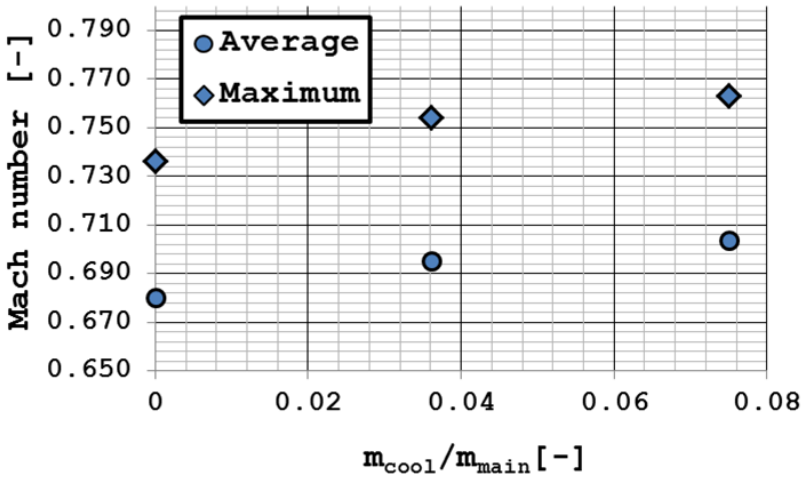

Figure 7.2: Average and maximum Mach number for different coolant mass flow rates

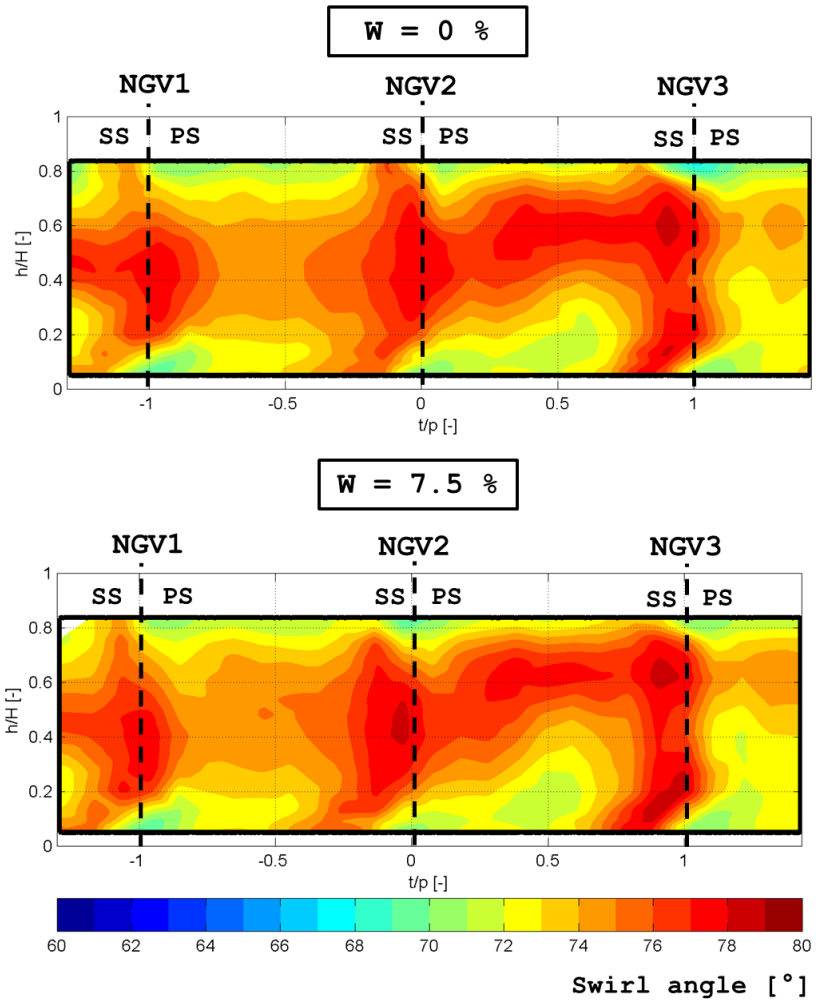

Figure 7.3: Swirl maps measured on Plane 41 in IOP_2 conditions

doesn't show relevant swirl, compared to the average exit angle, while in the right one a clear spot with swirl close to 77-78° can be appreciated.

Similar considerations arise from the analysis of the pitch angle contour plots, reported in Fig. 7.4. Important non-uniformities can be observed in the right passage, with positive pitch angles, up to 30°, in its left part, and negative ones, around -30°, in the right one; the left passage, on the other hand shows much reduced angles. Combining the observations taken from the 2D maps of both flow angles, a residual clockwise swirling structure can be recognized in the right passage, while no particular flow structure is evidenced

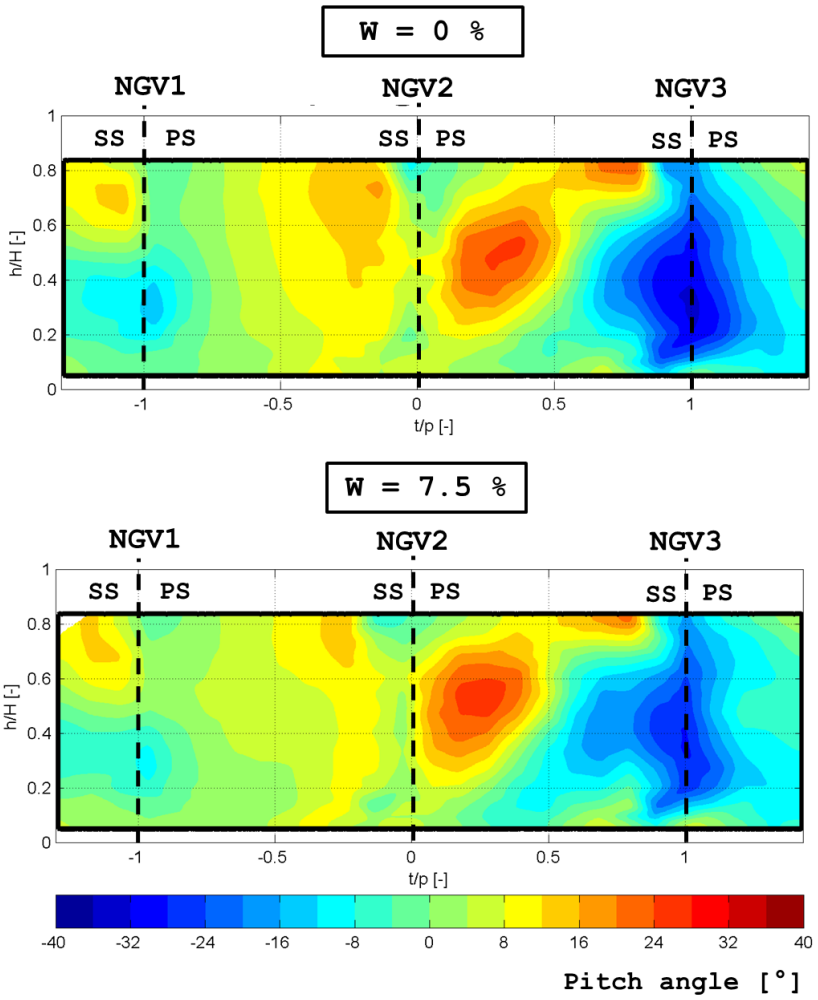

Figure 7.4: Pitch maps measured on Plane 41 in IOP_2 conditions

in the left one. Concerning the effect of coolant mass flow rate, very little differences can be noted between the two reported configurations: in the case of no coolant flows, the flow angles in the right passage, that are attributable to the residual swirl, look to be slighlty enhanced: the mixing induced by the coolant injection affects the coherent rotating structure, resulting in slightly reduced angles. The evaluation of the 1D profiles for both swirl and pitch angles provides a confirm of all the considerations taken above. Tangential profiles at 25% and 50% of the annulus height, where angles non-uniformities reach their maximum, are reported in Fig. 7.5. At $h/H = 50\%$, the swirl

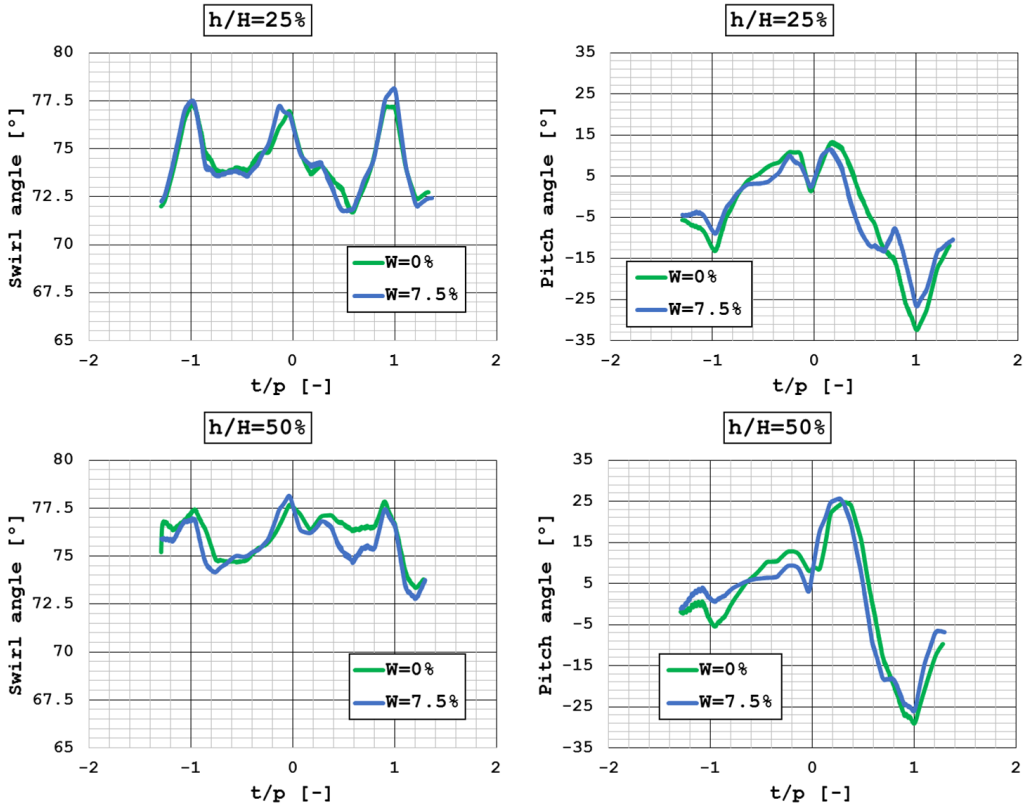

Figure 7.5: Flow angles 1D profiles on Plane 41 in IOP_2 conditions

angle is higher in the right passage than in the left one and its value is slightly higher for the case without NGV coolant; the opposite behaviour occurs at $h/H = 25\%$, as the swirl angle is slightly lower in the right passage. Moreover the pitch profile clearly shows a highly non-uniform distribution in the right passage, with positive flow angles next to negative ones: extreme values, both positive and negative ones, are always higher for the W=0% case, as it is particularly clear from the profile at $h/H = 25\%$. Even if the differences are very limited, this trend is highlighted.

A unique representation of such a flow pattern can be obtained thanks to the evaluation of the secondary flows on the investigated plane. In general, the calculation of secondary flows at the exit of a turbine cascade is not straightforward: several studies make use of the flow field measured at the annulus mean radius and evaluate the secondary flow pattern as a local

difference from the flow field in such a position [105, 164]. In the present configuration, this solution could not be adopted, due to the highly 3D flow field generated by the inlet swirl. The goal was achieved by locally subtracting the spatially averaged flow angles over the investigated domain, in order to define a new velocity field through the following relations:

$$V_{tan}^{sf} = V_{ax} \cdot tan(swirl - swirl_{mean}) \tag{7.1a}$$

$$V_{rad}^{sf} = V_{ax} \cdot tan(pitch - pitch_{mean}) \tag{7.1b}$$

where the subscript *mean* indicates a spatially average value over the central sector domain ($-1 < t/p < 1$). The defined vector field allows to assess how much the flow direction, in each point of the domain, deviates from the mean one, taking into account the local value of the axial velocity. A vector map, representing both the direction of the defined 2D velocity field and its intensity has been overlapped to pressure loss coefficient contour plots, calculated through Eq. 2.5, in Fig. 7.6. The mass-averaged total pressure, measured through the 5-hole probe tests upstream the cascade, was used for the calculation. The contribution of the coolant injection was not directly considered in the calculation. In this way the results of the cooled tests provide an overall indication of the combined effect of momentum injection and main-coolant mixing. A clearly different behaviour between the two passages is recognizable: due to the shift towards right of the swirling structure core, measured on Plane 40, most of the structure is convected in the right passage and is conserved up to the cascade exit. CFD studies carried out by Qureshi et al. [44] on a similar configuration, in terms of inflow, swirler-to-vane ratio and clocking (see Section 2.4.3), showed that the clockwise vortex was divided in two "legs" by the leading edge: the main one filled the right passage, while a smaller one, with the same sense of rotation, was convected through the left one. At the NGV exit plane, the right vortex was still clearly visible, while only a residual ascending motion, close to the airfol trailing edge position, remained in the left passage. Since a similar secondary flow pattern is found in the present study, the same phenomenon is expected to occur through the cascade. The main difference stays in the fact that, in the present results,

the swirling structure shape, identified in the right passage, has wider dimensions and extends beyond the passage boundaries ($t/p = 1$) on the right side, probably due to the same reasons that led to the shift registered on Plane 40. The rotating structure identified in the right part of the investigated domain, is more intense than the correspondent (i.e. shifted by two NGV pitches) one that can be partially noted in the extreme left of the domain ($t/p = -1$), generated by the left swirler. This result is due to the fact the flow field in the lateral sectors is affected by the presence of the walls: therefore, the flow structures generated by the lateral swirlers are characterized by a reduced degree of swirl, with respect to the central one, as they approach the cascade. Nevertheless, the behaviour is qualitatively very similar and the three-sector nature of the test rig does not prevent from taking conclusions regarding the differences between left and right passages of the central sector. The same phenomenon could be noted also from the analysis of the pitch angle maps.

In terms of Cp pattern, important contributions of profile losses, in correspondence of the airfoil wakes, and of endwall secondary losses can be appreciated. The pressure loss coefficient measured in the center of the right passage is globally higher than in the left one: beside the enhanced pressure losses generated by the residual swirling flow, this result is due to the lower total pressure at the passage inlet which collects the low-pressure core of the swirling structure.

In Fig. 7.7, the same results are considered in order to highlight the flow field behaviour in the right passage and to evaluate how it contributes to the measured pressure losses. A zoom of the same contour plots reported in Fig. 7.6 is shown and arrows are overlapped to evidence the main flow structures. The colormap scale was changed in order to allow a better visualization of the vectors. The black arrows show the direction of the passage vortexes, as they are commonly known: even if the investigation can not reach the inner and outer walls a pressure-to-suction side motion is still expected close to the endwalls. Red arrows show the main swirling structure, that fills the center of the passage and interacts with the endwall secondary flows. In the bottom-right part of the annulus, the descending flow interacts with the endwall flow structure and a local zone of high pressure loss is gen-

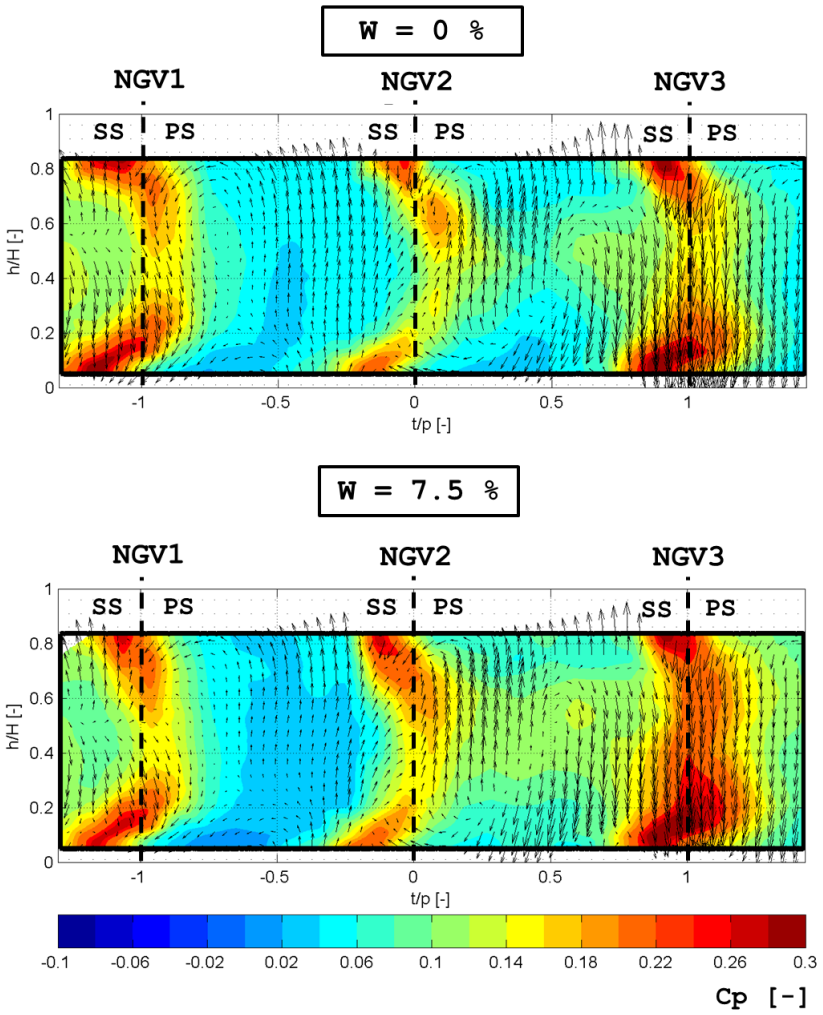

Figure 7.6: Pressure loss coefficient and secondary flows vectors

erated ($t/p \approx 0.85$, $h/H \approx 0.1$). This interaction seems to partially destroy the classic passage vortex, as the flow is pushed towards the inner endwall; still, a residual shape of the suction-to-pressure motion, that constitutes the closure of the passage vortex, can be noted (smaller black arrow). In the top part of the annulus a high degree of interaction between residual swirl and classic secondary flows exists as well. In the top-right part, while most of the swirling flow follows its clockwise path, a portion of it is drawn towards the outer band (right blue arrow); an opposite flow structure can be recognized in the top-left part (left blue arrow). As a result, high pressure

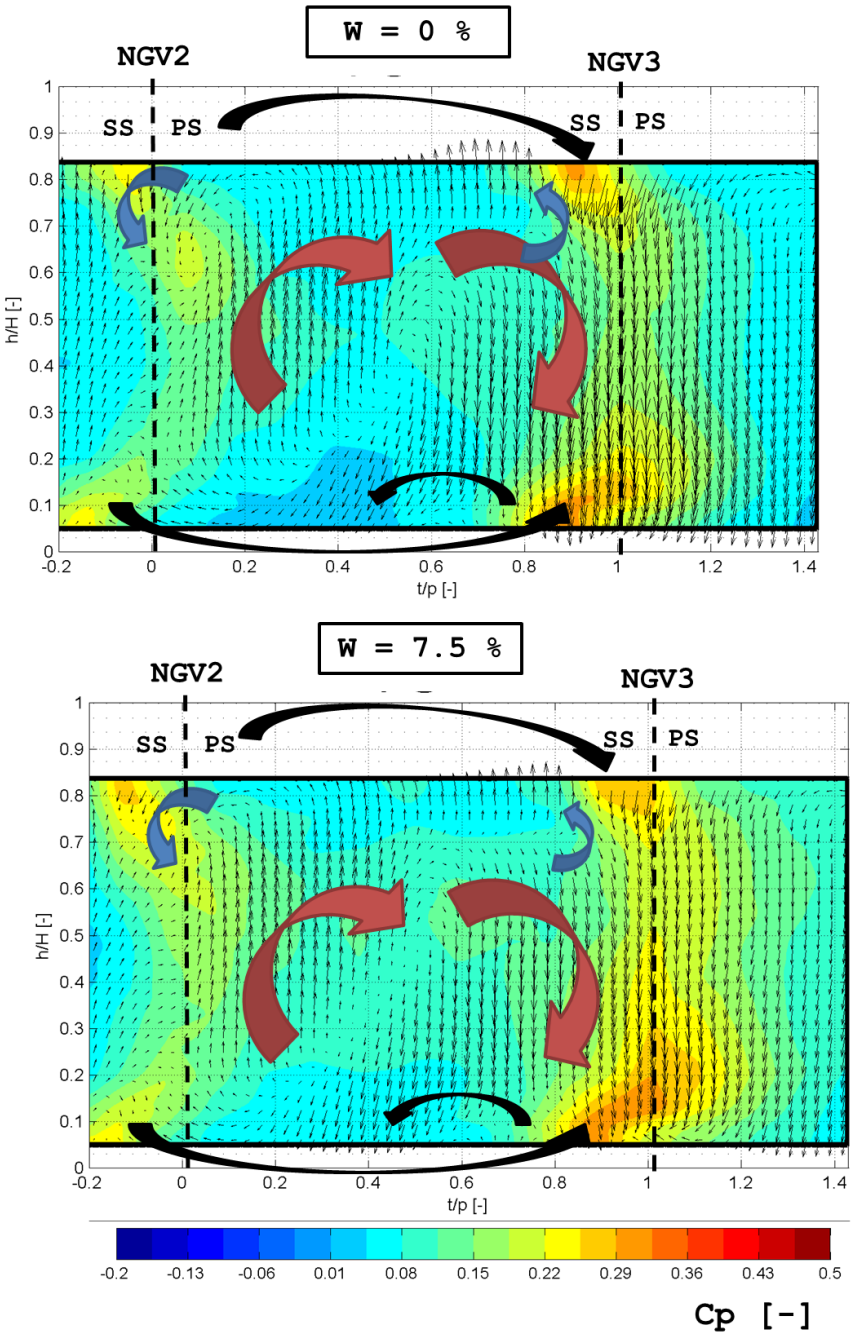

Figure 7.7: Pressure loss coefficient and secondary flows vectors - focus on right passage

loss spots are created, both in correspondence of the wake of the right airfoil ($t/p \approx -1$, $h/H \approx 0.8$), and of the central one ($t/p \approx 0$, $h/H \approx 0.8$).

Higher pressure losses are measured for the lateral NGV; the difference is particularly evident near the hub, since the residual swirl directly collides with the passage vortex and pushes it towards the hub. Comparing these findings to literature results, the measured Cp pattern looks very similar to the one that was found for a passage clocking configuration (i.e. swirling core aligned with vane passage) by Schmid et al. [78]. In their work a low pressure zone, in the center of the right passage, and a high pressure loss spot in the hub region of the lateral airfoil suction side, are found in passage clocking configuration with clockwise swirl orientation (Fig. 2.18, top-right image). This finding indicates that the displacement of the swirling structure towards right, highlighted on Plane 40, plays an important role in defining the flow field evolution through the cascade, which is, therefore, completely different between the two investigated passages.

A very similar behaviour is achieved between the two different coolant mass flow rate conditions. One dimensional profiles, extracted at different radial positions from the 2D maps, allow to deepen this aspect, by quantitatively comparing the pressure loss coefficient results. They are reported in Fig. 7.8. The peaks in the C_p distribution due to the airfoils profile losses are clearly evident: pressure losses in correspondence of the lateral airfoils are higher than for the central one both at $h/H = 12.5\%$ and $h/H = 50\%$. The reasons stay in the above described phenomena of interaction between residual swirl and both the endwall flows (limitedly to $h/H = 12.5\%$) and the NGV profile boundary layer. Closer to the outer endwall ($h/H = 75\%$), the measured pressure loss coefficient is more similar between the three airfoils: in fact, as it has been described previously, flow field structures that lead to pressure loss enhancement are present for both central and lateral NGVs. Concerning the effect of coolant injection, it globally leads to higher pressure losses especially in correspondence of the wakes and in the right passage, due to its interaction with the swirling flow; a higher degree of swirl for the case without coolant was noted from the evaluation of the flow angles, indicating a more important deviation from the average field. Therefore, film cooling tends to weaken the coherent swirling structure, convected in the passage, and to increase shear stresses and pressure losses. Nevertheless the differ-

ences are very limited, meaning that the swirling inflow, rather than the film-cooling flows, constitutes the driving force for the determination of the measured pattern. Fig. 7.9, finally, summarizes the mass-averaged pressure loss coefficients measured within the central ($-1 < t/p < 1$) sector, for all the three investigated coolant conditions: results are shown both in absolute terms (left image) and as a percentage of increase with respect to the case without film cooling flow (right image). According to what was stated above, film cooling leads to an enhancement of the average pressure loss coefficient, that reaches 21%, for $W = 3.75\%$, and 25%, for $W = 7.5\%$. The measured trend, tending to an asymptotic value, is qualitatively similar to what was found by Ligrani [37] (see Section 2.3.1). Coherent conclusions were also taken by Werschnik et al. [79]: as reported in Section 2.4.3, they found that, for axial inflows, the pressure loss pattern was dominated by the film cooling flows positions in the airfoil wake; with the introduction of inlet swirl, on the

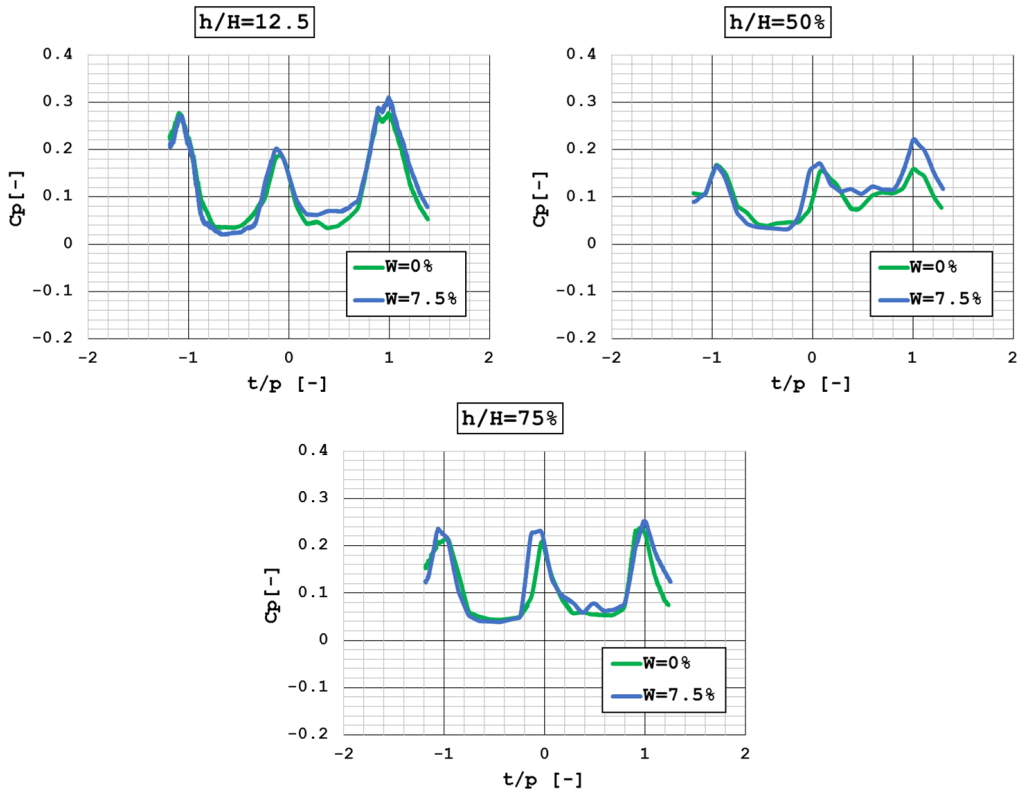

Figure 7.8: Pressure loss coefficient 1D profiles

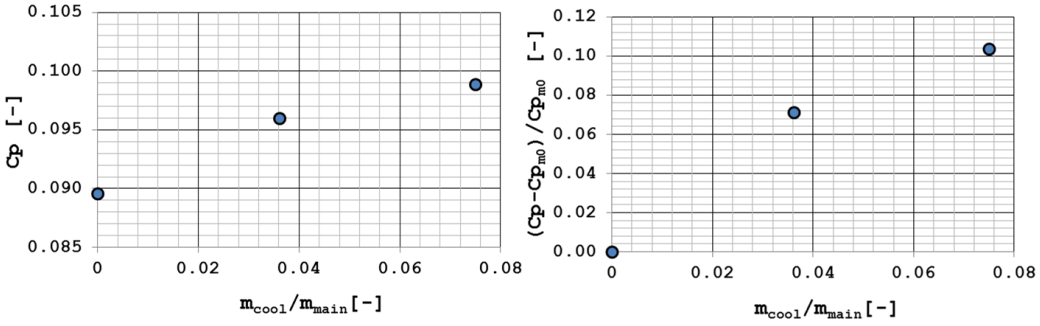

Figure 7.9: Influence of film cooling mass flow rate on pressure loss coefficient

other hand, the pressure loss pattern became smoother and less influenced by the film-cooling configuration.

7.1.2 Turbulence intensity

As anticipated in Section 2.5.1, the evaluation of the turbulence intensity across the NGV cascade is one of the main contribution that this work tries to provide. In this view, an indication of the turbulence that should be expected at turbine inlet in the presence of a highly swirling flow, representative of a modern combustor, was given in Section 6.3. In this section complementary results will be described, in order to highlight how the turbulence field is modified through the cascade and what kind of pattern can be expected at rotor inlet. Moreover, as it will be seen, the evaluation of the turbulence field will allow to make some additional considerations regarding the aerodynamic field, described in the previous section, and deepening its understanding.

Fig. 7.10 shows the turbulence intensity measured on Plane 40 and 41. For the second position, only the results from the test without film-cooling ($W = 0\%$) is reported. Plane 41 results have been rotated in the same way that was adopted for five hole probe tests. The investigated domain is slightly smaller than for five hole probe due to the different shape of the instruments: the extreme left part of the maps is missing here. This is due to the fact that the HWA doesn't have a cobra shape, which allowed, for five hole probe tests, to overcome the limits, on the left side, of the buttonhole used for the instrumentation insertion. Nevertheless, no information about the central

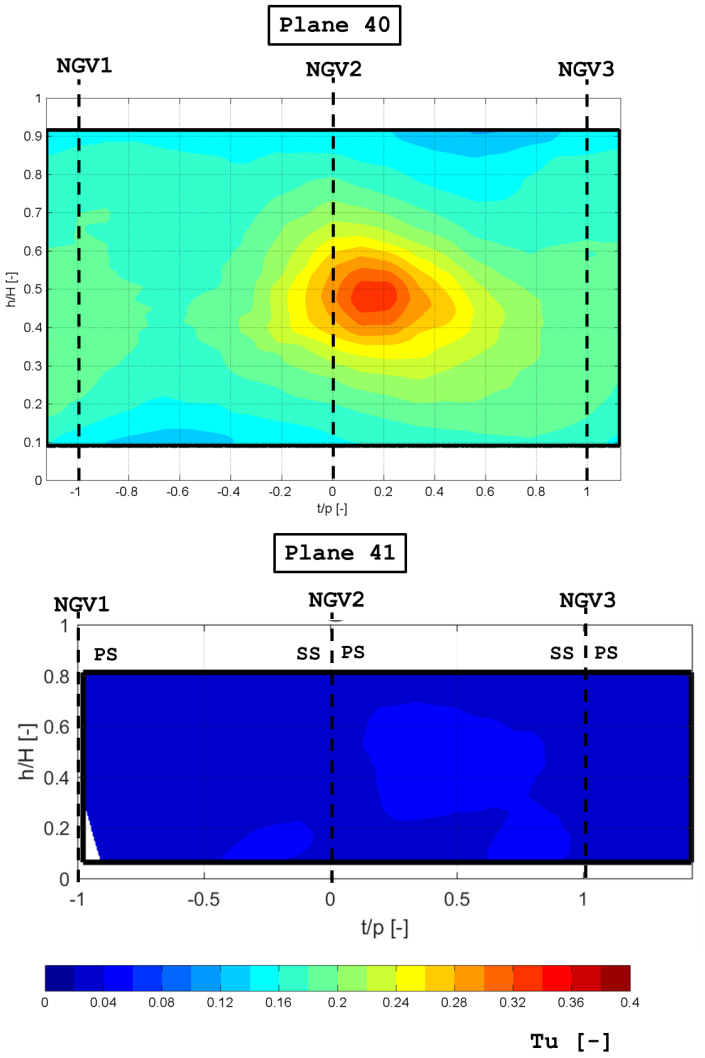

Figure 7.10: Turbulence intensity on Plane 40 and 41 ($W = 0\%$)

sector is lost. The comparison clearly shows that an important reduction in the turbulence intensity occurs, as the focus moves from Plane 40 to 41. While values above 30% were measured upstream of the cascade, they do not exceed 5% downstream of it, due to the severe acceleration of the flow field. Fig. 7.11 shows the turbulence intensity contour plots measured on Plane 41, for all the three investigated coolant mass flow rates. The colormap scale has been adapted, so that a proper analysis of the turbulence field downstream of the cascade can be conducted.

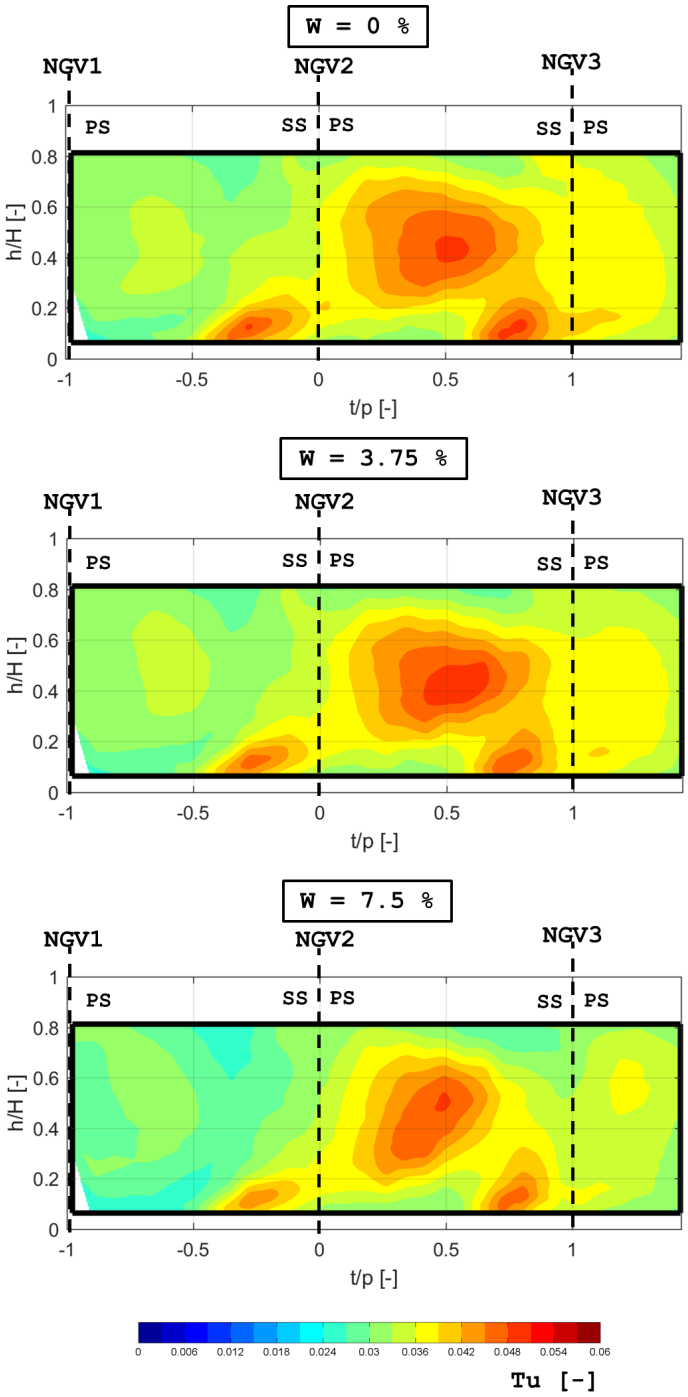

Figure 7.11: Turbulence intensity on Plane 41

Concerning the measured pattern, important differences can be noted with respect to a traditional one: a few number of works, aimed at evaluating the turbulence field at the exit of generic turbine cascades, highlighted that, in the case of axial and uniform inflow, higher turbulence intensities should be expected in the wakes of the airfoils and in correspondence of the passage vortexes, both at inner and outer endwalls, due to their mixing with the main flow [165, 166]. In the present treatment, on the other hand, a different turbulent spot can be recognized, similar to the Plane 40 one. In agreement with what was found from the five hole probe investigation, this maximum is reached in the right passage, where the residual swirling structure was detected. Other spots with relevant turbulence intensity can be found in the inner part of the annulus, in the same positions where high pressure losses due to endwall secondary flows were revealed. Even if they are evident for both the central and the lateral airfoils, a slightly higher turbulent intensity is measured for the right spot, in agreement with five hole probe findings. The extent of the investigated area doesn't allow to visualize any presence of similar structures close to the outer endwall. Beyond the spots close to the hub, no particular evidence of high turbulence intensity in the trailing edge wakes can be found. Even if this contribution strongly depends on the distance between the trailing edge and the investigated position and its value is therefore significantly case dependent, it is clear that it is not the main source of turbulence in the present configuration. Therefore, the results evidence that different phenomena, with respect to the traditional case with uniform inflow, define the turbulence pattern at NGV exit; in particular, the vortex structure, responsible for a very high turbulence intensity at combustor exit, that is mainly convected in the right passage and interacts with the endwall secondary flows, is still the main source of turbulence at the cascade exit. Steelant and Dick [167] found that, in configurations with uniform axial inflows, the turbulence reduction at the exit of a turbine cascade can be effectively related to the velocity ratio through the cascade

itself, by the following equation:

$$\frac{Tu_{exit}}{Tu_{inlet}} = (\frac{U_{inlet}}{U_{exit}})^{3/2} \tag{7.2}$$

where the 3/2 exponent was found to allow to take into account both the effects of increase of mean velocity and reduction of TKE. According to this finding, turbulence intensities between 1 and 2%, considering the average and the maximum turbulence intensities on Plane 40 respectively, should be found at the cascade exit in the investigated test case. At the same time, an average turbulent kinetic energy of about 145 m^2/s^2 is measured over the investigated domain (compared to $\approx$ 195 m^2/s^2 on Plane 40), while values around 75 m^2/s^2 would be predicted by the mentioned approach. While the developed relation (Eq. 7.2) can not be expected to precisely apply to any test case, the fact that significantly higher values have been measured comes as a confirm that different phenomena, with respect to a traditional treatment, occur and contribute to contain the TKE reduction through the cascade.

The comparison of the results obtained for different coolant mass flow rates shows very similar characteristics. Nevertheless some differences can be highlighted. While results coming from tests at $W = 0\%$ and $W = 3.75\%$ look very similar to each other, the test at at $W = 7.5\%$ shows slightly reduced turbulence intensities, in the locations where the maximum values are reached, and a different shape of the turbulent spot in the right passage. One dimensional profiles have been extracted, in the same radial positions as for five hole probe results, to help in the interpretation. As a confirm of what was seen from the analysis of the 2D contour maps, $W = 0\%$ and $W = 3.75\%$ data shows a very good agreement; some differences can only be observed for the profile at $h/H = 12.5\%$, where the profile at $W = 0\%$ reaches slightly higher values, in correspondence of the two peaks (i.e. in the two turbulent spots close to the inner endwall). On the other hand, the profile at $W = 7.5\%$ stays almost uniformly below the others; the maximum value reached in the right passage, as it can be noted from the profile at

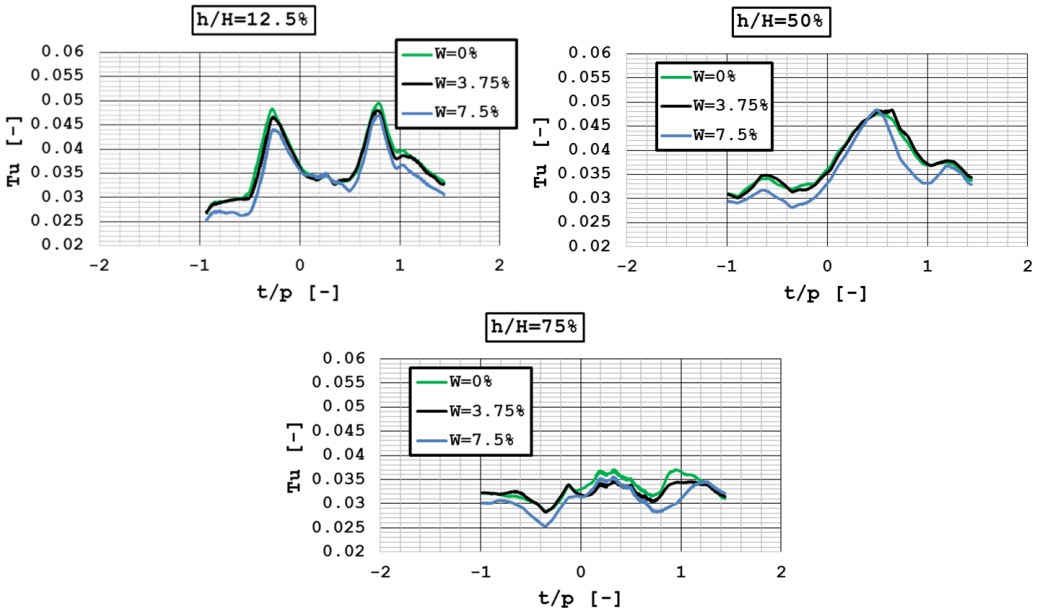

Figure 7.12: Turbulence intensity 1D profiles on Plane 41

$h/H = 50\%$, is actually very close to the other ones, but the shape of the profile (i.e. the shape of the turbulent spot) differs. These considerations suggest that coolant injection somehow alters the coherence of the residual swirling flow, hence slightly reducing its turbulence; this contribution is more important than the one coming from the enhancement of mixing and shear stresses, promoted by coolant injection, that should lead to an increase in turbulence. While this effect is not marked when the coolant mass flow stays within a certain value ($W = 3.75\%$), it becomes important with a further increase ($W = 7.5\%$). In order to summarize and quantify this phenomenon, the average turbulence intensity within the central sector has been calculated; results are summarized in Fig. 7.13.

A reduction in the average turbulence intensity up to 9% is found for the case at $W = 7.5\%$, while it hardly reaches 2% for $W = 3.75\%$. Due to the limited value of the measured turbulence the absolute differences are small, especially if the measurement uncertainty is considered; nevertheless a clear trend is highlighted.

As it was done for Plane 40, an evaluation of how the turbulence intensity is distributed among the different scales, was achieved through the calculation

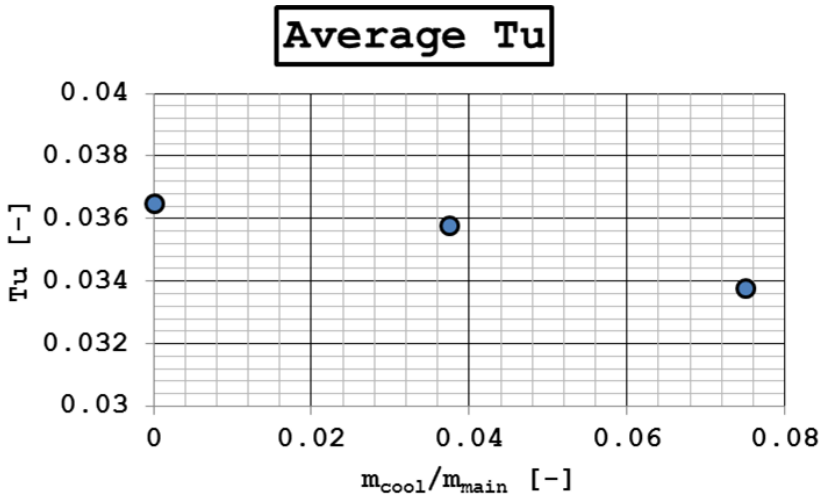

Figure 7.13: Effect of coolant mass flow rate on average turbulence intensity

of the TKE spectral density; Fig. 7.14 reports the calculated spectra in six different positions, sketched in the top map, that respectively correspond to:

1. wake of the central airfoil
2. center of left passage
3. wake of the right airfoil
4. center of right passage (turbulent spot)
5. inner endwall turbulent spot (right airfoil)
6. inner endwall turbulent spot (left airfoil)

A very similar trend to the one measured on Plane 40 is shown, with the peak frequency, that was attributed to the PVC structure, still clearly visible. This peak frequency could have been expected to increase as a result of the flow acceleration (i.e. unsteady fluctuating structure increasing its frequency and maintaining its Strouhal number); on the other hand, it was found at the same exact frequency as it was measured on Plane 40. Jacobi et al. [81] found a similar peak behaviour on both pressure and suction side of the investigated cascade, with the same frequency regradless of the position;

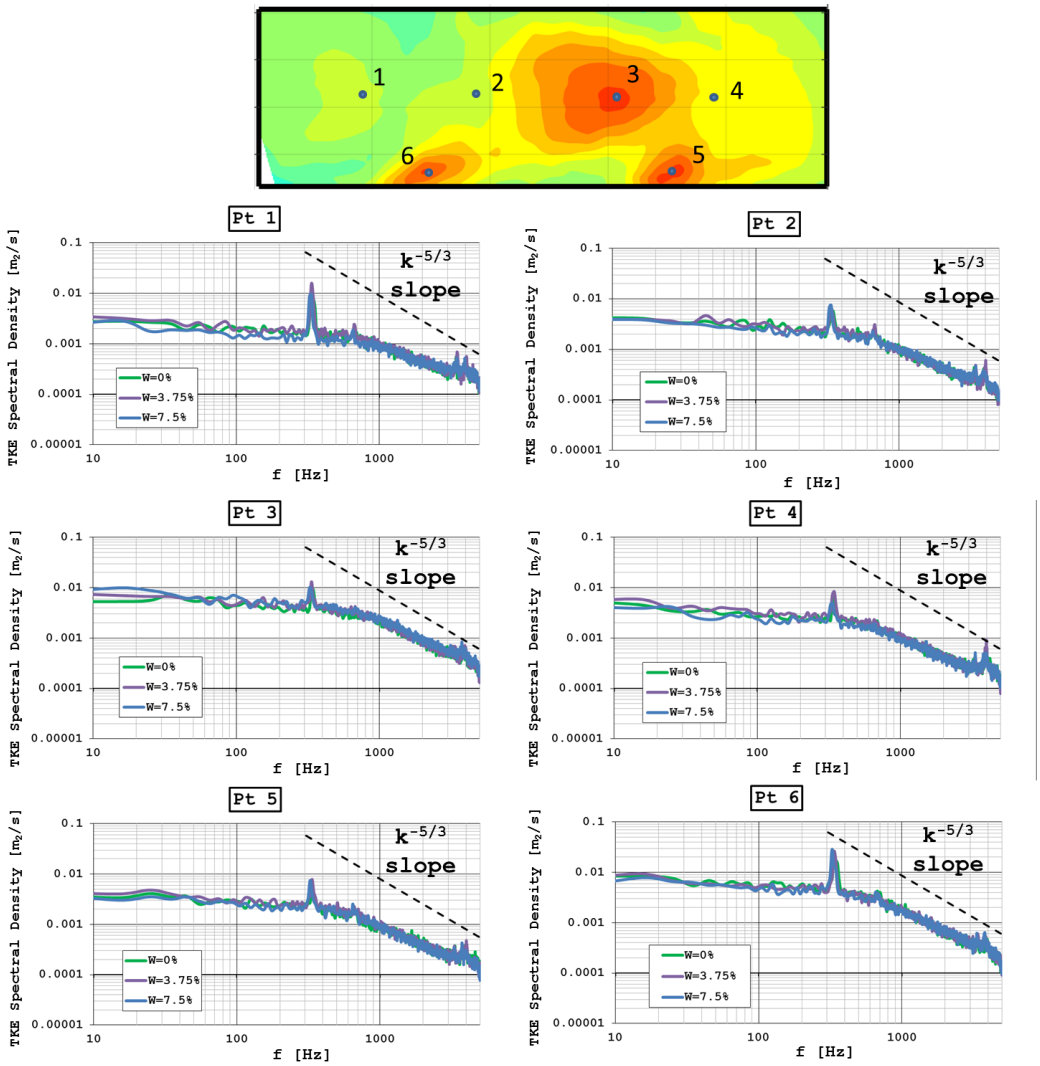

Figure 7.14: Turbulence kinetic energy spectral density for different mesh points on Plane 41

it was not present in the case without swirl. Thanks to LES calculations, they attributed the reason to the formation of small vortexes, due to the interaction between the swirl pressure distribution and the vane potential field. Even if no mentions to a PVC were made, the detachment frequency of these vortexes was expected to be determined by the swirl behaviour and, in turn, affect passage and horseshoe vortexes. Despite none of these details can be found here, since more detailed and non-experimental analysis would

be required, similar phenomena can be expected to occur, to justify the peak of TKE found at the cascade exit. No other particular peak frequencies, related to other flow structures, can be seen, except for, in some of the reported points, a second harmonic of the previous peak, at an exactly double frequency. The trend seems to show a slightly reduced slope with respect to the traditional $k^{-5/3}$ one, reported as a dotted line, and no deviation from this slope, as it was found on Plane 40, occurs within the measured range. This was actually expected due to the fact that the increased flow velocity, going from Plane 40 to Plane 41, leads to higher frequencies associated to the same turbulent scales. The investigation of all the measured points showed very similar results to the ones reported in the figure and no effect of local phenomena, as trailing edge vortex shedding, which is generally present when measurements are carried out downstream of turbine cascade, was revealed. Nevertheless, according to literature results, it generally occurs at values of Strouhal number between 0.2 and 0.3 [168]: considering the velocity measured on Plane 41 and the trailing edge thickness ($\approx 1mm$) these values translate in frequencies between 40 and 60 kHz, that are way out of the maximum measurable values; in fact, the maximum acquisition frequency of the measurement chain is 50kHz, so no frequencies higher than 25kHz can be analysed.

7.1.3 Adiabatic effectiveness

Once all the boundary conditions, in terms of swirling flow behaviour and turbulence intensity through the cascade have been set, it is possible to shift the focus to the adiabatic effectiveness. As explained in Section 2.5.1, the goal of the PSP measurement campaign is to deepen the knowledge of how a combustor representative outflow, characterized by a strong degree of swirl and significant turbulence intensity, can affect the NGV film cooling capabilities. As anticipated in Section 5.4.4, three different setups were necessary to investigate a sufficient portion of the three cooled NGVs (i.e. of the surfaces invested by the central sector flow): according to the nomenclature reported in Fig. 4.6a, pressure and suction side of the central airfoil (NGV_2), as well as the pressure side of NGV_1 and the suction side of NGV_3 have been

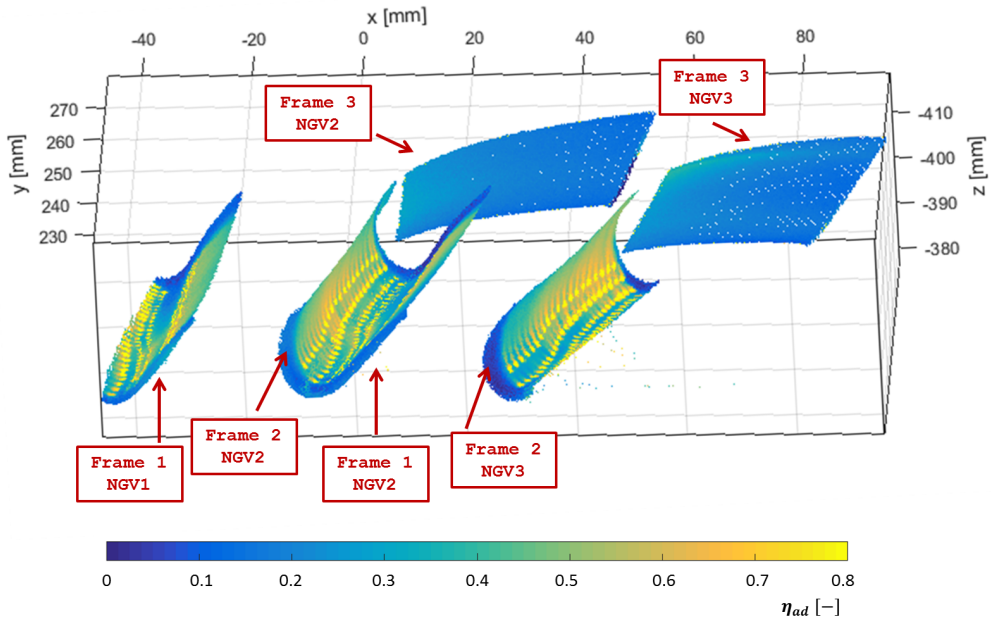

Figure 7.15: PSP results: reconstructed 3D geometry

investigated; due to the correspondent inlet flow of NGV_1 and 3, since they are one swirler pitch far from each other, the investigation can be considered aimed at describing the performance of the central airfoil, aligned with the swirler, and of a generic lateral airfoil, clocked halfway between two swirlers. The analysis of the differences between these two airfoils plays a big role in evidencing issues and design challenges of the present configuration.

An unwrapping procedure (see Section 5.4.4) was used to recalculate, from the 2D images, the 3D coordinates, for each image pixel, in order to associate the results to precise position on the NGV profiles. Combining the outcomes from all the three frames, a total results, in 3D real coordinates, like the one reported in Fig. 7.15 can be produced. It is easy to recognize the geometry of the three investigated airfoils (NGV_{1-3} according to the nomenclature of Fig. 4.6). Nevertheless, during the description of the results, it will be always referred to the 2D images, as they allow for a more direct visualization of the results and of the investigated positions.

In the first part of the description, the focus will be placed on the results of the operating point at nominal coolant mass flow rate (W=7.5%); adiabatic

effectiveness results will be shown, while pressure distributions will be used to provide a better understanding of them. In the second part the focus will be moved on how the coolant mass flow rate affect the results, by also describing the outcomes from tests at W=3.75 and 5.5%.

Before moving to the film effectiveness results, an analysis of static pressure distribution maps captured with PSP technique is reported. Fig. 7.16 shows the pressure distribution, scaled with the mass-averaged total pressure on Plane 40, measured through frame 1 (a) and frame 2 (b) close to the LE of the airfoils. The results look very similar between the two airfoils, as it was expected from CFD predictions (see Chapter 4). Nevertheless, an accurate evaluation of the contours allows to highlight some differences that will be useful to the interpretation of the adiabatic effectiveness results. In particular frame 1 shows a quite uniform pressure distribution, close to the value of the total inlet pressure, as it is expected in the early part of the pressure side; a slightly lower pressure, anyway, is measured for NGV_2, especially in the midspan area. A similar behaviour can be also detected from frame 2 results as long as the investigation is limited to the LE zone; this phenomenon is harder to be appreciated, since the pressure distribution has a wider variation over the investigated domain and the pressure rapidly decreases in the suction side. Nevertheless, looking at the midspan between rows PS1 and SS2 (see Fig. 3.9 for the cooling rows nomenclature), the normalized static pressure is equal to about 0.98 for NGV_2 and to 1.01 for NGV_3. A low pressure zone is hence present in the center of the swirling structure which is convected in the right passage towards the combustor exit due to the flow field morphology. A similar results was detected by Qureshi et al. [44]. Pressure distribution influences the quantity of coolant injected by each row of holes and this effect is particularly intense in the high pressure region of the vane where cooling holes work with a very low pressure drop: a slight variation of the discharge static pressure produces high variation of the coolant injected. This aspect, together with the knowledge of the flow field evolution, developed through the five hole probe measurements on planes 40 and 41, allows to easily evaluate the adiabatic effectiveness distributions, reported in Fig. 7.17.

The classical pattern that is commonly expected in a leading edge zone is shown: several holes are characterized by clearly visible coolant traces, while others, closer to the stagnation point position, generate film cooling in jet

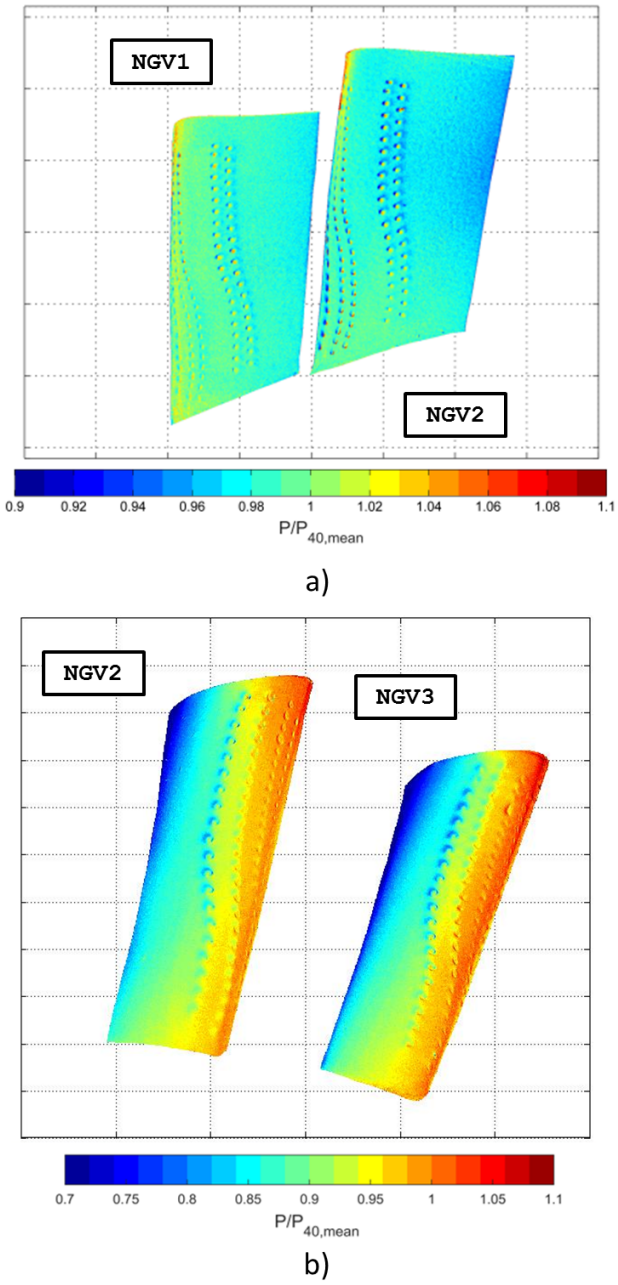

Figure 7.16: Pressure distribution close to LE: frame 1 (a) and 2(b)

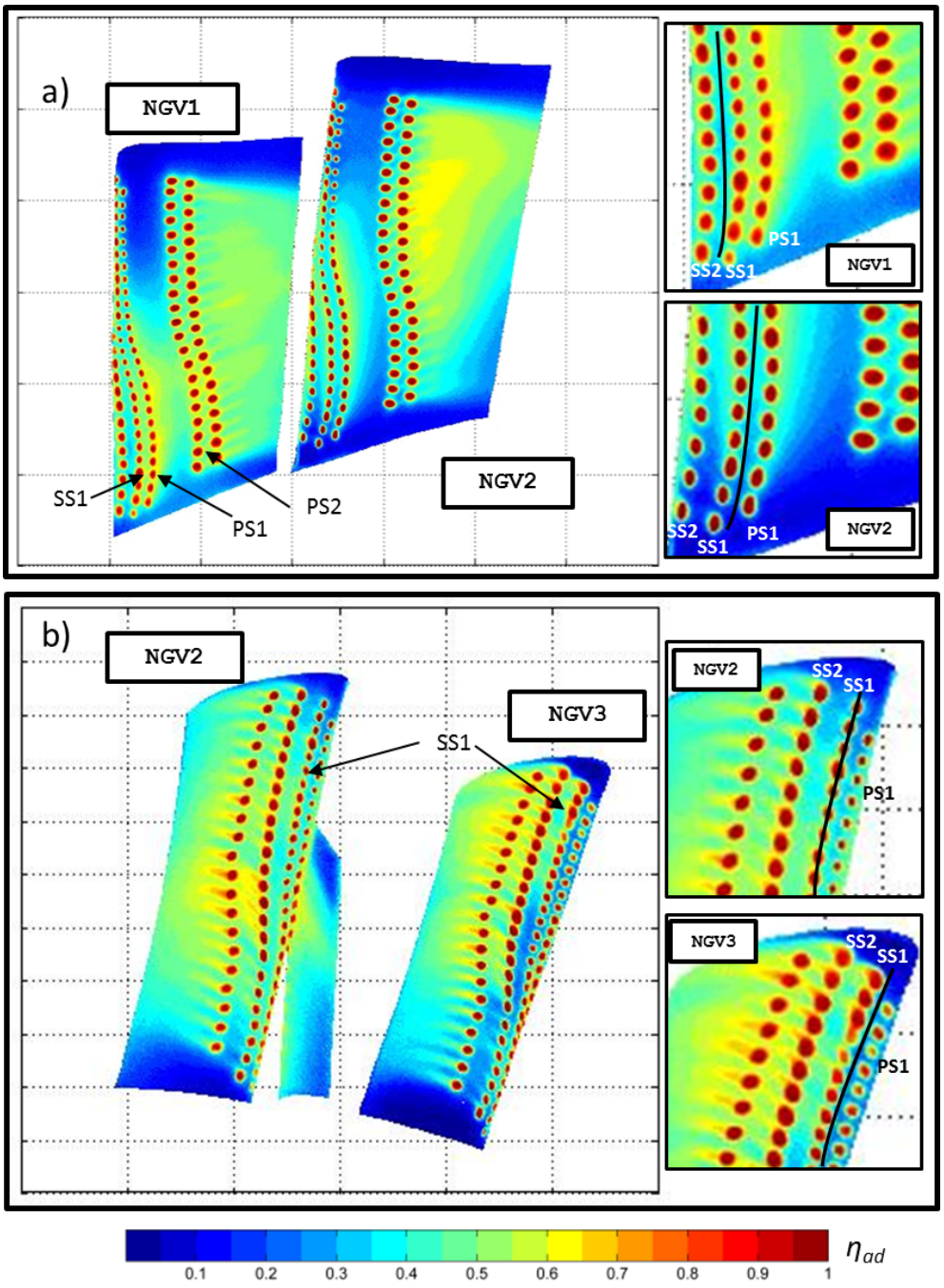

Figure 7.17: Adiabatic effectiveness distribution close to LE: frame 1 (a) and frame 2 (b)

penetration regime due to a low mainstream local velocity. Zones with very low effectiveness are revealed close to the inner and outer endwalls and in the top part of both the investigated airfoils, between rows PS1 ad PS2.
In addition to the effect of external static pressure, film cooling in the leading edge zone is affected by the stagnation line position induced by the swirling flow, highlighted in Section 6.2.1. The images on the right, that reports enlargements of the shower head zones in the inner (Fig. 7.17a) and outer (Fig. 7.17b) areas, help in this evaluation. The stagnation position is reported as a black line. In the lower part of the airfoil, close to the inner endwall, the shape of the coolant traces shows that, for NGV_2, the stagnation point is located between rows PS1 ans SS1. As a result, a low effectiveness zone can be noted between rows PS1 and PS2, since it is only covered by the contribution of PS1. On the other hand, for NGV_1, the stagnation point position moves between rows SS1 ans SS2, since the mainflow has a lower swirl angle. As a consequence both rows SS1 and PS1 contribute to cover the above mentioned area increasing the adiabatic effectiveness. A correspondent behaviour can be appreciated, from frame 2 results, in the upper part of the airfoils: for NGV_3, the stagnation line lays between rows PS1 and SS1, while for the central airfoil it is more aligned with row SS1, due to the positive swirl angle at its inlet. The lateral airfoil is, hence, characterized by well defined coolant traces towards the suction side and a lower contribution to the low-effectiveness area in the top part of the NGV pressure side between rows PS1 and PS2.
In order to clarify the effect of the pressure distribution induced by the inlet swirl, non-dimensional pressure ($P/P_{0,40}$) and adiabatic effectiveness profiles have been extracted in two positions of the pressure side (Fig. 7.18) and two on the suction side (Fig. 7.19) exploiting the 3D mapping of the surface. Since adiabatic effectiveness profiles have been extracted in positions that are quite close to the cooling holes, they have been smoothed, in the radial direction, through a moving average procedure, in order to get rid of the fluctuations due to the alternation of the coolant traces; the goal, in fact, is not to focus on the single hole trace behaviour, but to gather information about the coverage performance at different NGV span.

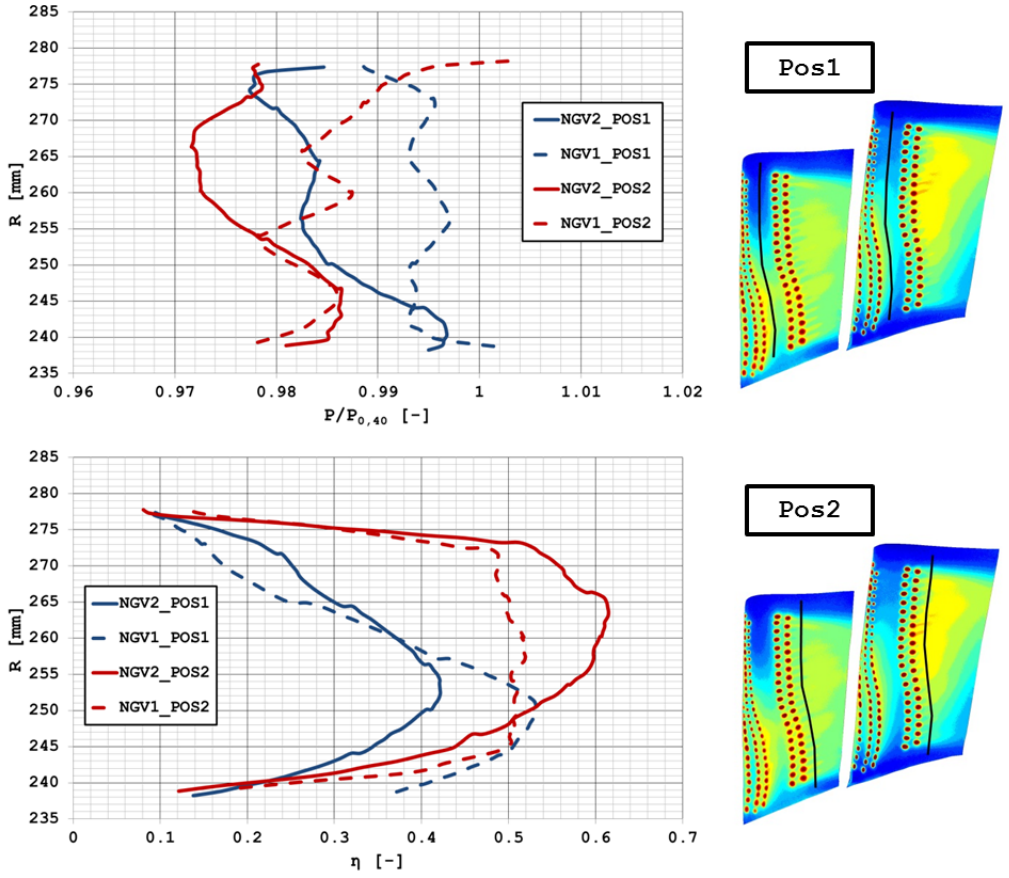

Figure 7.18: Adiabatic effectiveness and pressure profiles on the pressure side

Focusing on the pressure side, the first profile was extracted between rows PS1 and PS2, while the second is located downstream of row PS3. They confirm the lower pressure on the central NGV in both the evaluated positions; in terms of film-cooling performance, for the first position, this translates in a higher effectiveness for the central airfoil, only in its midspan and upper part. Close to the inner endwall the pressure profiles collapse on very similar values and a slightly higher effectiveness is measured for NGV_1, due to the above described effect of the stagnation point alteration. At the position of the second profile, which is not much affected by the stagnation point position, the effectiveness is globally higher for the central NGV, as it was also evident from the contour plots. Only the very last portion of the airfoil, close to the inner endwall, shows a lower adiabatic effectiveness

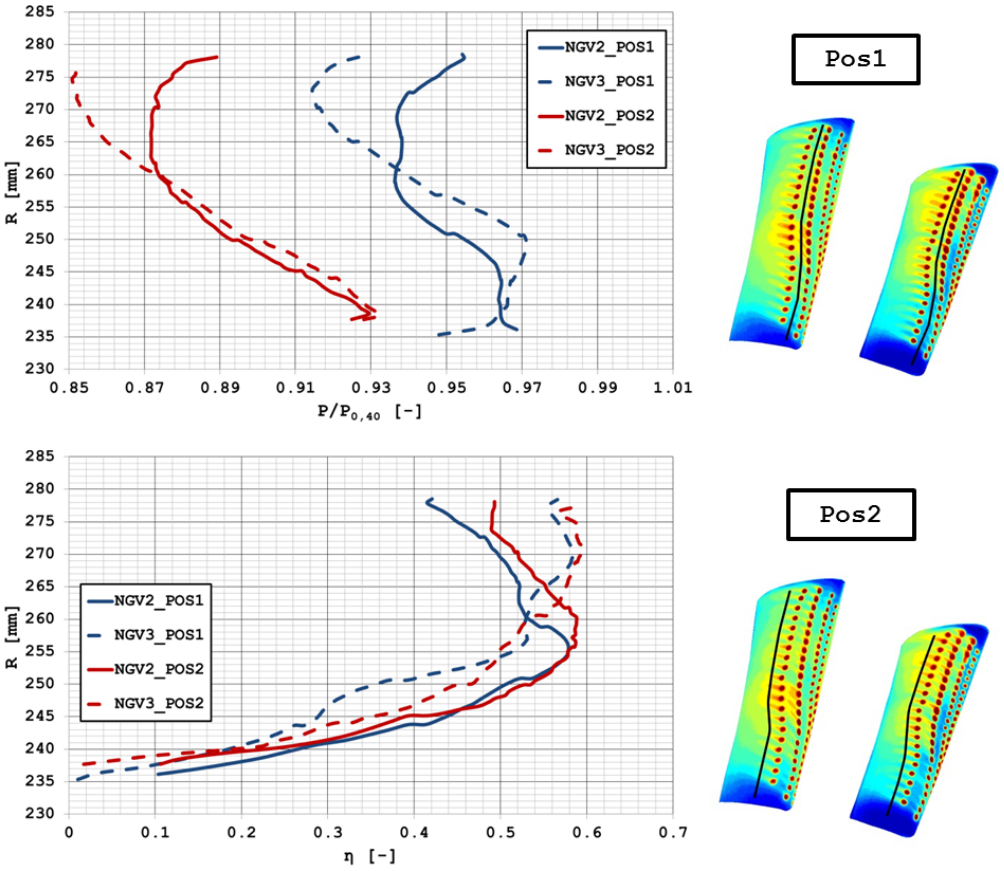

Figure 7.19: Adiabatic effectiveness and pressure profiles on the suction side

respect to the lateral profile: this result is due to the radial motion of the mainstream in this zone, caused by the swirling flow convected in the right passage (between NGV_2 and NGV_3), that determines an important coolant upwash. This constitutes a critical area of the airfoil, since all the coolant traces are lifted towards the top part of the channel and the bottom part of the profile remains almost uncovered. The contour plots of frame 2 allow to visualize this phenomenon, as the last part of the pressure side is visible between NGV_2 and NGV_3 (Fig. 7.17b). Even if the measurement setup was not optimized to investigate this area, and the measurement quality is poor due to issues related to camera focus and resolution, it was not masked-out to allow a better understanding of the mentioned phenomenon.

Concerning the suction side, the effect of pressure variation between lat-

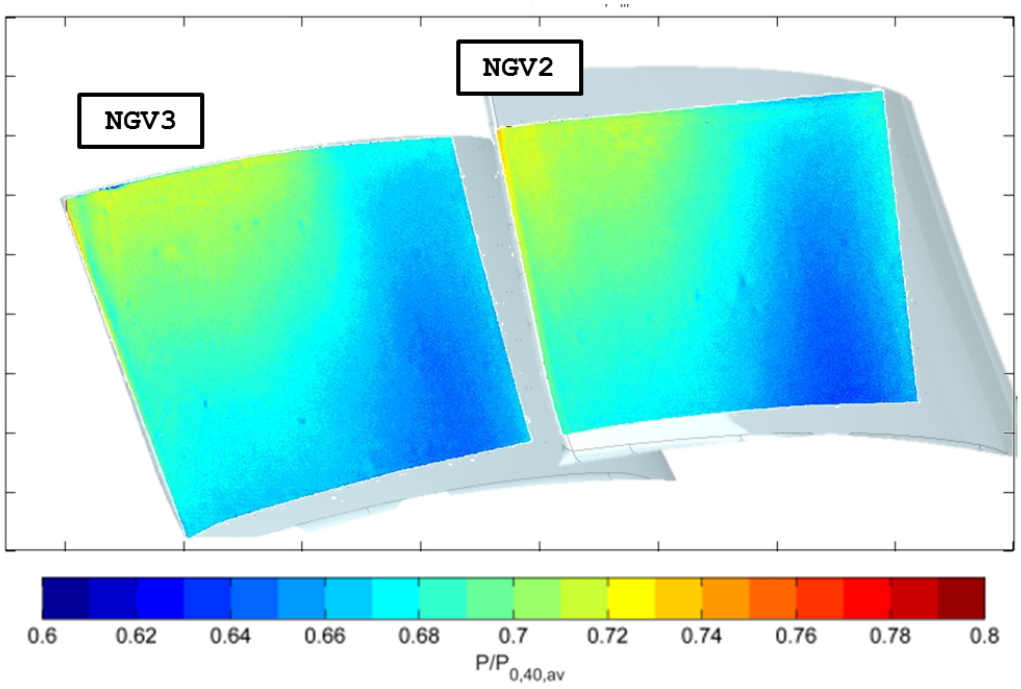

Figure 7.20: Pressure distribution in the final part of the suction side: frame 3

eral and central airfoils and its direct effect on coolant distribution is evident comparing the pressure and η_{ad} profiles reported in Fig. 7.19. Important differences in the pressure distribution can be noted for both positions in the casing area ($R > 260mm$): as already mentioned, here the stagnation line is moved towards the suction side, due to the effect of the positive swirl angles, and therefore a higher pressure is measured. At this position, the coolant traces are very short indicating an high degree of jet penetration due to the proximity of stagnation line and, hence, low mainstream velocity; therefore the adiabatic effectiveness profiles show lower values for the central airfoil. On the other hand, in the midspan area ($R \approx 250mm$) the lateral vane NGV_3 has a higher pressure respect to the central one, resulting in lower film protection.

The conclusions drawn regarding the behaviour of the part of the cascade close to the leading edge can also be exploited to provide a better understanding of the performance of the downstream part of the vanes. In particular the final part of the suction side of NGV_2 and NGV_3 was investi-

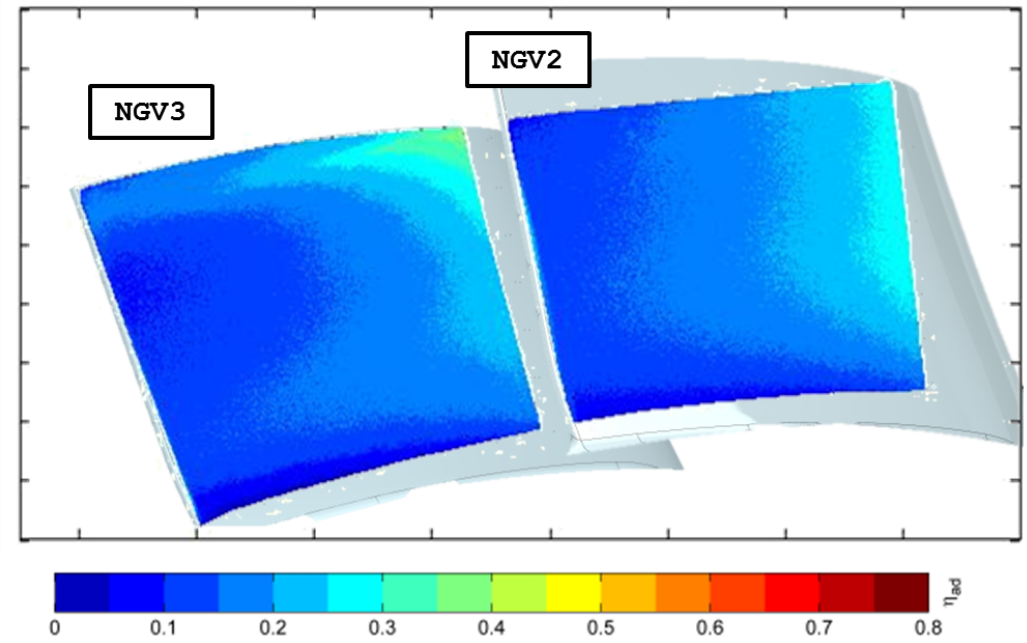

Figure 7.21: Adiabatic effectiveness distribution close to TE (Frame 3)

gated through frame 3. Fig. 7.20 reports the pressure distribution measured in these locations; the NGV suction sides are framed from downstream as it was sketched in Fig. 5.27. The shape of the vanes is sketched in transparency to allow a easier understanding of the limits of the investigated areas. A clear low-pressure zone, with values of $P/P_{0,40}$ around 0.65, can be identified, corresponding to the throat area; the minimum pressure is registered in the lower part of the airfoils, as it follows the common radial equilibrium distribution. Downstream of the throat, pressure recovery occurs, until a radially-averaged value of $P/P_{0,40}$ around 0.7. Very similar values are measured for both the airfoils. No coolant holes are present in this investigated zone, so the cooling performance are mainly a consequence of the observations made on the early part of the suction side (frame 2, Fig. 7.16b) and of the mainstream behaviour in the left and right passages. Fig. 7.21 shows the adiabatic effectiveness distribution.

Despite the global level of effectiveness is quite low, due to the absence of cooling holes, traces of residual coolant can be appreciated in the top part of the NGV_3 surface, as a consequence of the good performance of the upper

holes of rows SS2 and SS3 of this airfoil. On the other hand, slightly better results for NGV_2 can be observed close to the midspan, due to similar reasons.

The 1D profiles, extracted in the throat area and close to the trailing edge (Fig. 7.22) confirm these conclusions: the pressure profiles on the first position reveal that the central NGV still shows a higher pressure in the upper part of the surface; much more similar profiles are shown close to the trailing edge, with the lateral airfoil that presents slightly lower pressure values. Concerning adiabatic effectiveness, both positions show a very low coverage close to the inner endwall due to the well-known effects of secondary endwall flows, that drive the coolant traces towards midspan; a similar phenomenon, with reduced intensity can be also appreciated close to the outer endwall (see NGV_3 in Fig. 7.21). On the central airfoil a similar shape of the profiles can be observed, both in the throat and in the trailing edge areas, with a maximum of adiabatic effectiveness reached around R=260mm and progressively reduced towards the outer endwall. On the other hand, for the lateral airfoil, a different behaviour was found: a profile with two maxima, one close to the outer endwall and the second which moves from $R = 252mm$ at POS1 to $R = 257mm$ at TE, can be detected. The movement of peak location confirms the trend of the coolant traces to follow the radial descending motion of the swirling main flow on the suction side, in contrast with the upward flow illustrated on the pressure side. This phenomenon helps to counteract the lift off effect generated by the secondary flows of the inner endwall.

The detailed description of the performance of the film-cooling system in the case of the nominal coolant mass flow rate, was useful to evidence the positions where low film-coverage can be found and, therefore, where particular attention must be dedicated in the cooling system design process. Once all the main causes of the highlighted behaviour have been understood, an evaluation of the effect of coolant mass flow rate can be carried out; in fact, it can be useful to understand how the performance are sensitive to this parameter and to deepen the understanding of the cooling holes working regime. Results are summarized in Fig. 7.23. Despite no particular differences arise in the morphology of the adiabatic effectiveness distribution, since the results

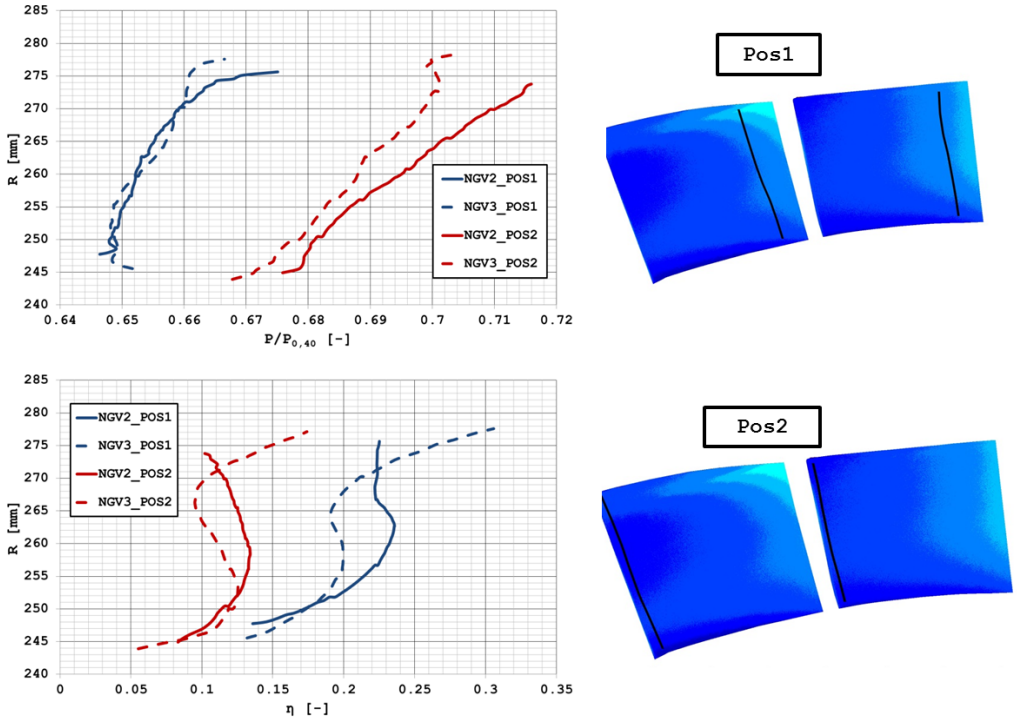

Figure 7.22: Adiabatic effectiveness and pressure profiles in the final part of the suction side

are similar from a qualitative point of view, some quantitative differences must be highlighted. Focusing on the results at $W = 7.5\%$ and $W = 5.5\%$, an opposite behaviour seems to arise between pressure and suction side. For the first one, the analysis of frame 1 results (left pictures) suggests that a reduction of coolant mass flow rate leads to slightly worse cooling performance. On the other hand, on the suction side (frame 2, central pictures), the reduction of coolant mass flow rate from $W = 7.5\%$ to $W = 5.5\%$, seems to determine an increase in the measured adiabatic effectiveness. When the focus moves to the test at $W = 3.75\%$, different conclusions must be taken, since the mass flow rate is significantly lower: even if the effectiveness level is not much different in several positions, as in the midspan area of the early suction side, some of the leading edge cooling holes are no more able to provide coolant ejection as mainstream ingestion begins to occur. In fact, the pressure in the coolant feeding plenum gets very close to the inlet total pressure. This phenomenon, anyway, allows to have a clearer view of how

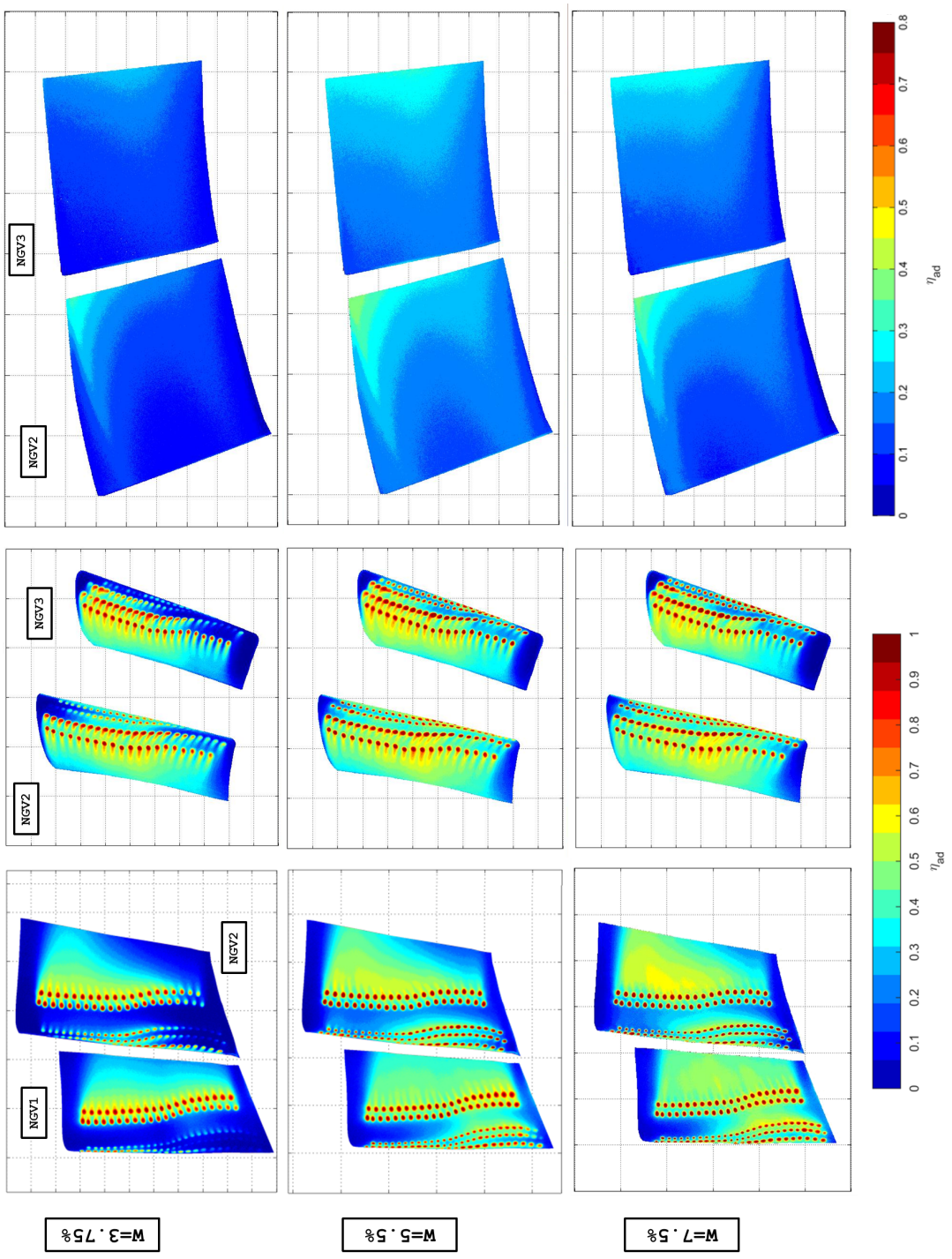

Figure 7.23: Adiabatic effectiveness results for different coolant mass flow rates

the stagnation line is positioned among the coolant rows and it confirms the conclusions taken previously: on the upper part of the airfoils the stagnation line moves towards the suction side for the central NGV, as the SS1 holes of NGV_3 are still filming towards the suction side (see frame 2 results), while the correspondent ones of NGV_2 are ingesting; on the other hand the stagnation line moves towards the pressure side in the inner part of the central airfoil, as it is evidenced by the fact that the last holes of PS1 are ingesting, while the correspondent ones on NGV_1 are still creating a weak film on the pressure side.

In order to deepen the comparison between $W = 5.5\%$ and $W = 7.5\%$, two additional profiles have been extracted for each of the first two frames. For frame 1, the first profile was extracted in the very proximity of row PS3 ($\approx$1.5 hole diameters downstream), while the second is located further (about 7 hole diameters) downstream. Similarly, for frame 2, the first and the second profiles were extracted at the same distances downstream of row SS3. The results are reported, together with the exact locations (Fig. 7.24), for all the three coolant conditions, both in the first location (solid lines) and in the second one (dashed lines). Concerning the pressure side (frame 1, Fig. 7.24a), a very similar behaviour can be observed, on NGV_2, on the first profile position, regardless of the coolant mass flow rate. Moving downstream (second position, dashed lines), the case with the nominal coolant mass flow ($W = 7.5\%$) shows the better performance, while the effectiveness progressively decreases, as the coolant mass flow is reduced. This finding results in agreement with the common behaviour expected for concave surface (see Section 2.3.2), as an increase in the coolant momentum is beneficial to the film-cooling performance downstream of the holes, where the jets tend to reattach due to the shape of the surface. The case at $W = 3.75\%$, for this reason, show the worse behaviour, especially close to the hub, where, due to the reduced coolant momentum, jets can not even slightly oppose to the upwash promoted by the mainstream . For the lateral NGV (NGV_1), results are qualitatively similar to the central one, but a worse coverage is achieved in the proximity of the cooling holes for all the cases except the one at $W = 3.75\%$. An opposite behaviour can be recognized in the downstream

region (bad coverage for the case at $W = 3.75\%$), as no significant coolant reattachment is generated due to the low amount of coolant and low momentum.

Moving the focus on the suction side (frame 1, Fig. 7.24a), results are still in line with what is commonly expected for this kind of surface shape. A decrease of coolant mass flow rate from $W = 7.5\%$ to $W = 5.5\%$ leads to a slightly enhanced coverage in both positions: the lower is the coolant momentum, the more important is the pressure gradient effect that tends to turn the jets towards the surface. Going to $W = 3.75\%$, on the other hand, is detrimental, especially in the downstream region, since the coolant amount is not enough to create long traces. The drop-off for the $W = 3.75\%$ case, in the second position, anyway, is much less marked than on the pressure side, as no reattachment phenomena arise in this surface. No additional profiles have been extracted from frame 3 results, as the conclusions are qualitatively similar to what was found in the second position of frame 2.

7.1.4 Characterization of the NGV module in isothermal conditions: concluding remarks

The investigation of the overall field and of the turbulence field on Plane 41 allowed to highlight how the main flow structures, detected on Plane 40, evolve up to the cascade exit; the understanding of the overall flow field evolution through the cascade was useful both to provide an evaluation of what kind of flow field can be expected at rotor inlet and to allow a deeper interpretation of the adiabatic effectiveness results. Despite the clocking configuration, with the swirler aligned with the leading edge of the central NGV, a strong residual swirling flow was found at the exit of the right passage. For this reason, it constitutes the driving force for the obtained flow angles, pressure losses and turbulence patterns. In particular, enhanced pressure losses were found in the suction side hub region of the lateral NGV wake, due to the action of the residual swirl that tends to push the inner passage vortex towards the endwall. The detected C_p distribution is very similar to what was found, in other literature studies, in a passage clocking configuration;

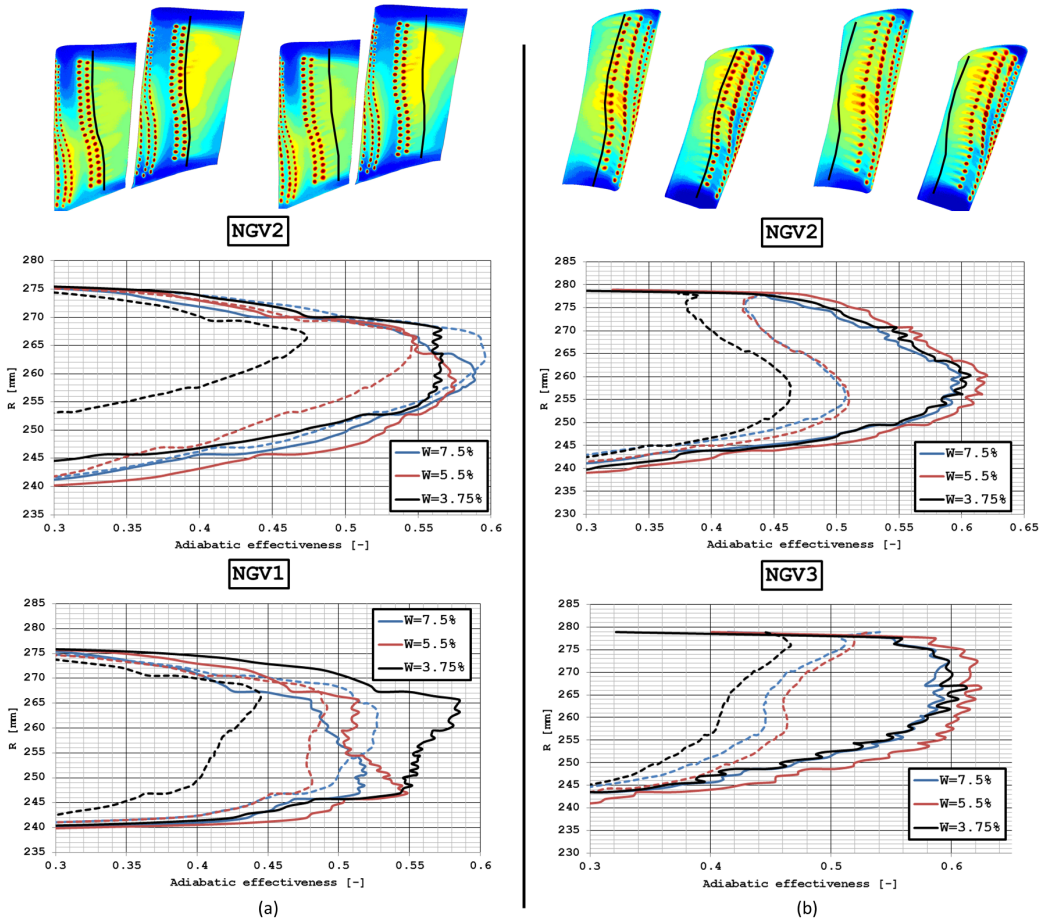

Figure 7.24: Adiabatic effectiveness 1D profiles on (a) pressure side and (b) suction sides (frame 2) for different coolant mass flow rates

the shift towards right of the swirling structure, that was measured on Plane 40, therefore, plays a crucial role in determining the outcoming flow field. Moreover a reduced turbulence decay, with respect to traditional test cases with uniform inflow, have been detected. The presence of a coherent swirling structure determines a particular turbulence pattern at the NGV exit, with spots where turbulence is higher than in the rest of the annulus, up to about about 5%; this kind of values are unconventional for NGV exit and rotor inlet positions. The results, therefore, demonstrate how the residual turbulence is an aspect that can be critical and must be taken into account during the rotor design process, as it can significantly increase the heat transfer rates

and the mixing between film-cooling and mainlflow, leading to reduced performance of the cooling system.

The effect of film-cooling injection on the aerodynamic behaviour is quite limited respect to the residual swirl one. Globally an increase in film-cooling mass flow rate leads to a slight reduction of the residual swirl degree and, therefore, to a lower turbulence intensity; pressure losses, on the other hand, are increased.

Once it was gained knowledge of the flow field conditions, the focus have shifted to the adiabatic effectiveness results; they provide indications that can be directly used to evaluate, and possibly modify, the guidelines of a design process. Since in a real engine application the swirler-to-vane ratio is rarely an integer value, the NGV profiles are subjected to local inflow conditions that are different from each other; therefore the design procedure, both of the NGV profile and of its cooling system is normally based on tangentially averaged flow conditions, as it is the case for the investigated geometry. The simplified clocking configuration allows to investigate two different airfoil conditions, with one of them that has the leading edge aligned with a swirler and the adjacent one that is clocked halfway between two swirlers; evidencing differences in their behaviour, an evaluation of the inaccuracies introduced by a traditional design procedure was provided.

In particular, important differences in the stagnation line position were found, which in turn, influence the behaviour of the early parts of the pressure and suction sides. The inlet swirl also determines a low pressure zone in the midspan area of the central NGV pressure side, drawing more coolant and improving the coverage of this zone; opposite behaviour is registered for the holes located close to the LE outer region with the consequence of a poor film protection on the suction side of the central foil.

Finally the swirling flow approaching the NGV module was found to have a large effect on the cooling performance of the final part of both pressure and suction sides, as it creates respectively strong ascending or descending mainstream motion, that can drive coolant away from large regions of the airfoils. This effect is more important as the coolant mass flow rate (coolant momentum) is reduced. In the tested configuration, the pressure side of the

central foil represents the most critical position. On the other hand, the suction side of the passage, where the core of swirling flow is convected, takes benefits from the mainstream motion since it helps to partially compensate the effect of secondary endwall flows, that are generally well-known to wipe coolant away from the inner part of the suction side.

Summarizing, it is possible to draw general conclusions regarding the behaviour of film cooling under representative swirl conditions:

- the main effects of the swirling flow, that are relevant to the film cooling performance, are: the pressure non-uniformity, the stagnation line alteration and the streamline modification on both pressure and suction sides;
- different positions of the stagnation line between central and lateral vanes are crucial to the performance of leading edge film cooling system, which in turns influences the film coverage moving downstream;
- relative clocking position between swirler and vane has a strong impact on film effectiveness distribution;
- the swirling inflow can have a significantly detrimental effect on film distribution; in this configuration the pressure side of the central NGV shows very poor coverage (coolant upwash phenomena); a detailed knowledge of the flow field characteristics at the cascade inlet and outlet is necessary in the view of optimizing the cooling system design;

From a design point of view, particular effort must be paid to take these phenomena into account in order to limit the efficiency-detrimental safety margins that would have otherwise to be adopted to prevent from engine life reductions.

7.2 Aerothermal field characteristics in the presence of temperature gradients

In the past sections, the flow field characteristics and the NGV film-cooling performance have been characterized with all the flows at the same,

ambient, temperature; according to the goal of this treatment described in Section 2.5.1, the analysis has to be completed in order to understand how the temperature distortions, measured at combustor exit in DP conditions, migrates towards the rotor inlet plane. For this sake, five hole probe measurements on Plane 41, in DP conditions, will be exploited. In addition to the thermal field results, the aerodynamic field will be described as well, in the first of the next sections.

7.2.1 Aerodynamic behaviour

Despite, as above stated, the goal of the design condition tests is to highlight the hot and cold streaks migration through the cascade, the aerodynamic field achieved in DP conditions will be described first, in order to effectively complement the temperature results and deepening their understanding. Moreover this part of the results will be also useful to compare the aerodynamic fields achieved in DP and IOP_2 conditions, in order to validate the hypothesis taken in Section 3.3.1, regarding their similarity; in this way, the possibility to carry out different measurements in cold conditions, without compromising the applicability of their results to the DP case, will be justified. As already mentioned, the only relevant difference in the combustor outflow, between DP and IOP_2, regards the Mach number, that is about 5% lower for the second condition. On Plane 41, this difference was expected to be slightly enhanced due to the expansion through the cascade and it is confirmed by the Mach number profiles reported in Fig. 7.25.

The profiles show that the Mach number pattern is similar between the two conditions, with fairly well matched trends at all the radial locations. The only notable difference stays in the inner profile (h/H=12.5%) where, in DP conditions, the Mach number in the right passage seems to be a little higher that in the left one; this feature does not occur in the IOP_2 case. Even if it is not simple to assess the reason of this result, with the available data, this could be an effect of the inlet temperature pattern, as it will be explained in detail in the following. Beside this aspect, no other differences in the Mach number pattern arise: on the other hand, a shift can be easily appreciated in its absolute value, as Mach number is clearly higher for the

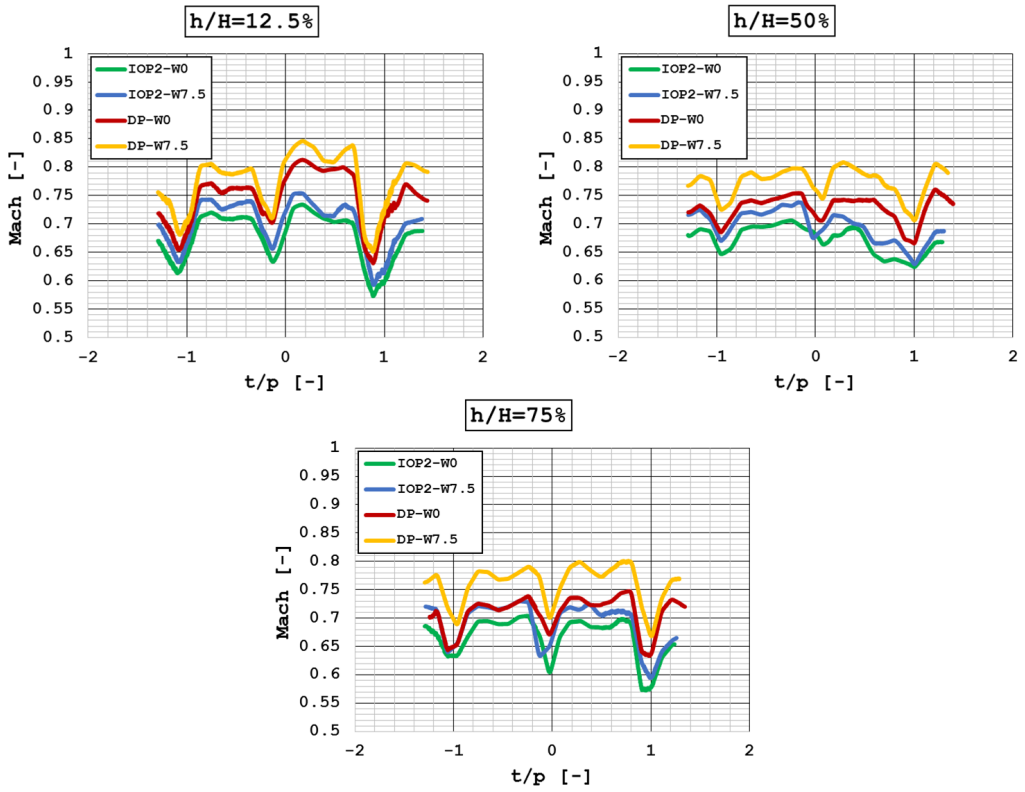

Figure 7.25: Mach number 1D profiles on Plane 41: comparison between DP and IOP_2 conditions

DP case. In order to effectively quantify this deviation, Fig. 7.26 reports the average and maximum Mach numbers, within the investigated domain, for different coolant mass flow rates and for the two conditions. A difference between 7.5 and 11% exists, for $W = 0\%$ and $W = 7.5\%$ respectively, both for the average and the maximum values.

Once this main difference has been highlighted, it is possible to extend the comparison to the flow angles pattern. On Plane 40 they showed a good match between the two operating conditions: a further comparison on Plane 41 will allow to check if and how the difference in the exit Mach number and the introduction of temperature gradients bring to significantly different flow field evolutions through the cascade (i.e. different flow angle patterns at NGV exit, between DP and IOP_2). Fig. 7.27 shows the swirl and pitch angles patterns on Plane 41, for DP conditions, which have to be compared

to the ones reported in Figs. 7.3 and 7.4, for IOP_2 conditions.

Both flow angles show exactly the same distribution that was found in isothermal conditions; very limited distortions can be found in the left passage, while higher ones, with a pattern that indicates the presence of residual clockwise swirling flow, are detected in the right one. The most important differences, can be found in the locations where the measured angles reach the highest values (i.e. in the location of the residual swirl). In particular, in the location with downward flow direction ($t/p \approx 1$) the differences in the (negative) pitch angle reach about 6°, with the maps at IOP_2 conditions showing the higher values, in absolute terms.

To have a comparison of the global behaviour in a single map, secondary flow vectors have been plotted over pressure loss coefficient 2D maps in Fig. 7.28. Results for $W = 7.5\%$, in both operating conditions, are shown next to each other in order to have a clear view of the limited difference that can be found. The focus is placed on the only right passage zone, since it is the most interesting in the view of a secondary flow pattern understanding and it is where the main differences between the operating conditions have been detected. The effect of coolant mass flow rate on the residual swirl has been found to be poor during the evaluation of the IOP_2 results (see Section 7.1.1); it was also confirmed, for the DP case, by the above described flow angles maps. Therefore, only the results at the nominal coolant mass flow are reported here. The same flow field behaviour can be observed, with all the considerations taken regarding how the swirling flow develops and interact with endwall secondary flows that are still valid; the calculated vectors have

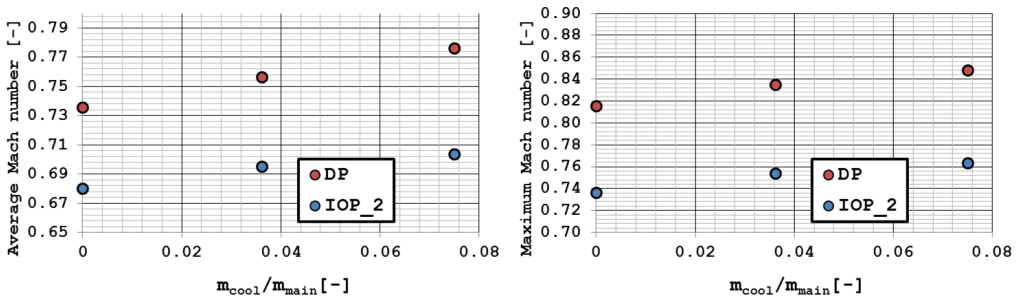

Figure 7.26: Average and maximum Mach numbers on Plane 41

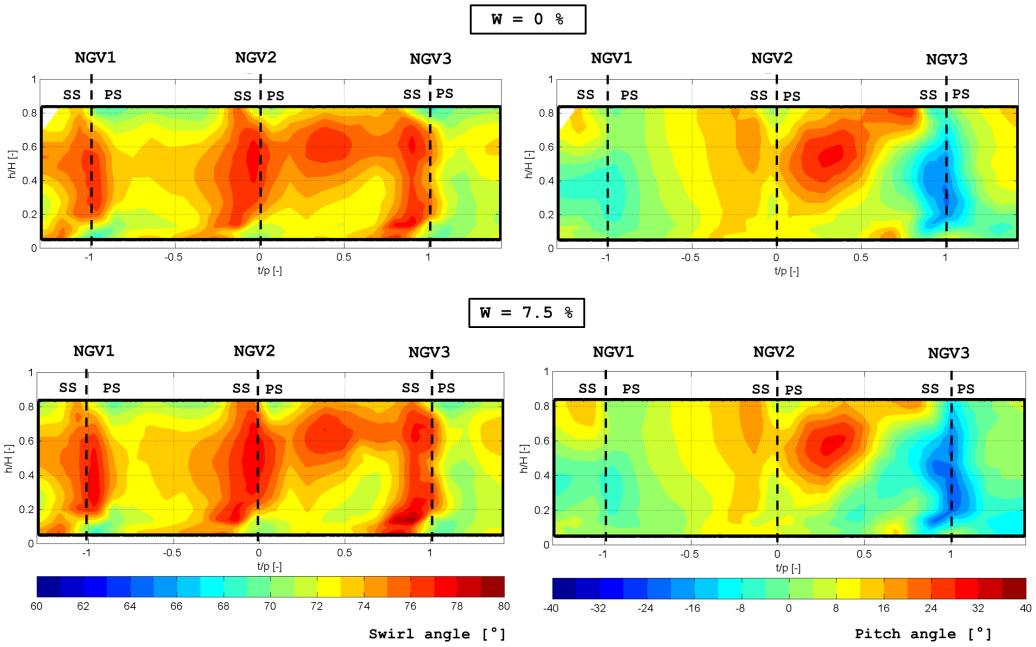

Figure 7.27: Flow angles contour plots on Plane 41: DP conditions

the same direction, between the two cases, in all the investigated positions. The only difference, in agreement with the conclusions taken from the evaluation of the flow angles patterns, is that, for the isothermal condition, the velocity vectors have a slightly bigger dimensions, especially in the location of downward flow direction; this result indicates that the measured secondary flows are stronger than in DP conditions. Accordingly, a spot with higher pressure losses was measured, in isothermal conditions, where the residual swirl interacts with the passage vortexes, especially in the hub region. The one dimensional profiles of pressure loss coefficient, extracted at four different radial positions (Fig. 7.29), confirm that very similar values of pressure losses are achieved, with limited differences located in the above mentioned spots ($t/p \approx 1$, $h/H = 25\%$) and in the swirling core ($t/p \approx 0.2 - 0.8$, $h/H = 25 - 50\%$).

Summarizing, the comparison between the aerodynamic field in DP and IOP_2 conditions showed that very little differences arise between the two cases. The main source of difference stays in the fact that the degree of the residual swirl is slightly weakened in DP conditions: anyway this effect can

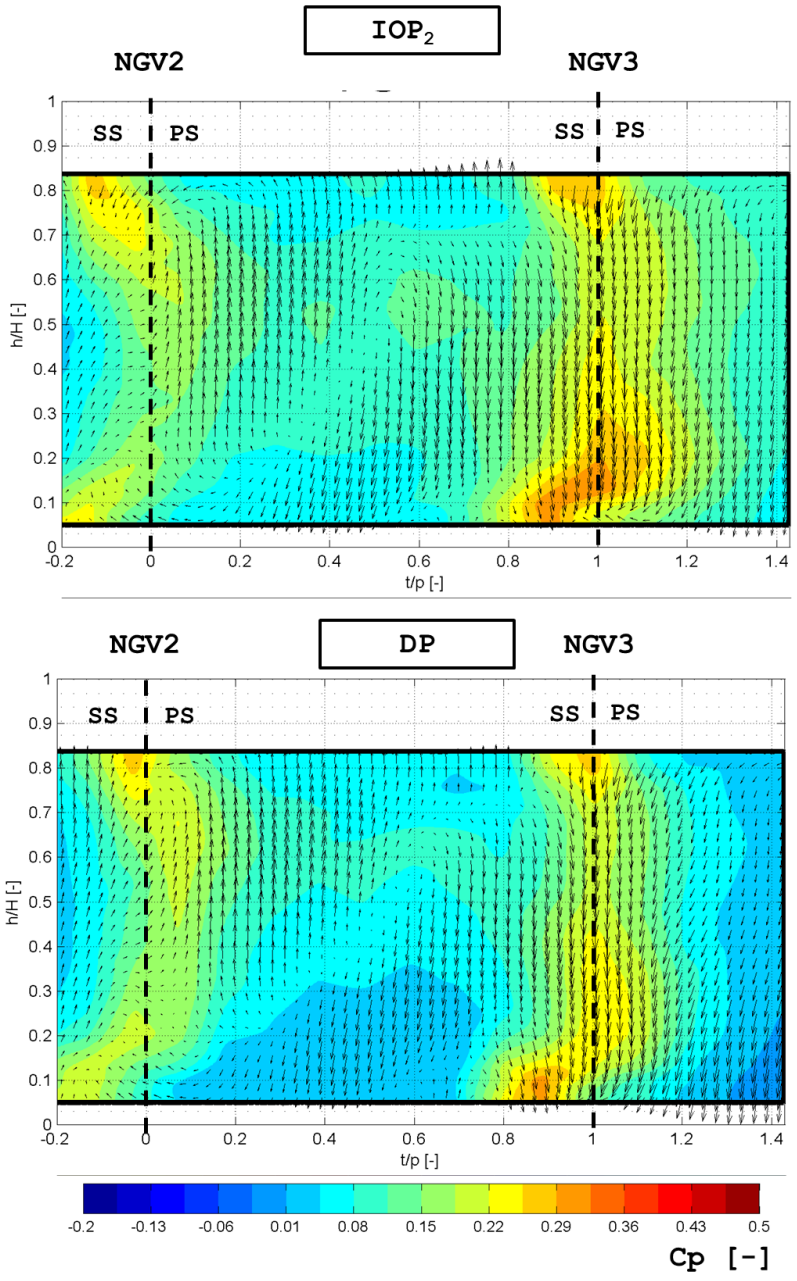

Figure 7.28: Secondary vectors at $W = 7.5\%$: comparison between DP and IOP_2

be expected to be related more to the increase in Mach number, with respect to the isothermal point, than to the presence of temperature gradients. In fact, in the case of higher acceleration , a more pronounced alignment of the

flow field to the main direction should occur, with a consequent reduction in the degree of swirl. The difference in main-coolant momentum ratio, that exist between DP and IOP_2 conditions is not expected to affect this finding, as the same differences, between the two operating points, can be found both in cooled and not cooled configurations.

Even if very limited, a similar effect of swirl degree reduction was found to be produced by the increase in coolant mass flow rate (see Section 7.1.1). Nevertheless, these two factors (i.e. injection of coolant and enhancement of inlet/exit Mach number due to shift to DP conditions) act on the rotating structure in different ways. In the case of an increased inlet/exit Mach number, the weakening of the swirl strength is caused by a more intense acceleration of the flow field in the main direction of the flow, resulting in a loss of tangential momentum. In this case, in fact, lower pressure losses occur, with respect to the case with lower exit Mach number, since a reduced interaction between this structure and endwall secondary flows is achieved; less intense shear stresses within the structure itself should be found as well. On the other hand, in the case of film-cooling injection, the reduction of the

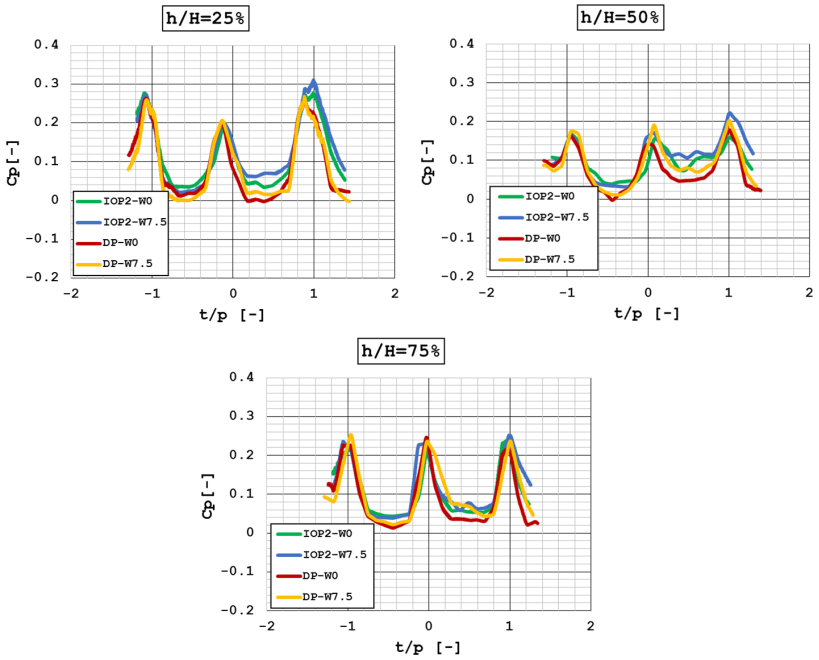

Figure 7.29: Pressure loss coefficient: 1D profiles

swirl degree is due to the interactions between the swirling structure and the coolant flow, that results in a reduction of the structure coherence and an enhancement of mixing. In fact, higher pressure losses are found, in the right passage, for the case with higher coolant mass flow rate.

The only flow feature that actually seems to be related to the introduction of temperature gradients within the cascade inflow, is the slight enhancement of the Mach number in the inner part of the right passage, with respect to the correspondent position in the left one. As it was showed in Fig. 7.25, in fact, this aspect was not present in isothermal conditions. A possible explanation of this phenomenon will be provided in the next section, after the description of the thermal field on Plane 41 will be completed.

Despite all the evidenced phenomena, the differences between the two operating conditions, in terms of Plane 41 flow field are very reduced. Hence, according to goals of this comparison, the following conclusions can be taken. The effect of temperature gradients on the achieved flow field at NGV exit is limited, in agreement with previous findings [72, 84]. The turbulence results, gathered in isothermal conditions, can provide a reliable estimation of the gross turbulence level, and a precise definition of the turbulence pattern, also for the DP case; therefore, they constitute a useful data set of boundary conditions for the investigation that will be described in the next section.

7.2.2 Hot streaks migration

Through the previous sections different results have been discussed regarding turbulence and flow field modifications through the nozzle guide vanes; they have been exploited as necessary boundary conditions to provide a better understanding of other, more specific, results, like PSP ones, that have been described in Section 7.1.3. In this section one last aspect, according to the goals of this work, summarized in Section 2.5.1, will be described, exploiting the findings of the previous results to achieve a global view of the phenomena and of the relations between each other. In particular the hot streaks migration will be addressed here, so that an assessment can be provided of how the temperature distortions, measured on Plane 40, evolve up to the cascade exit and how they interact with coolant cold streaks. In this

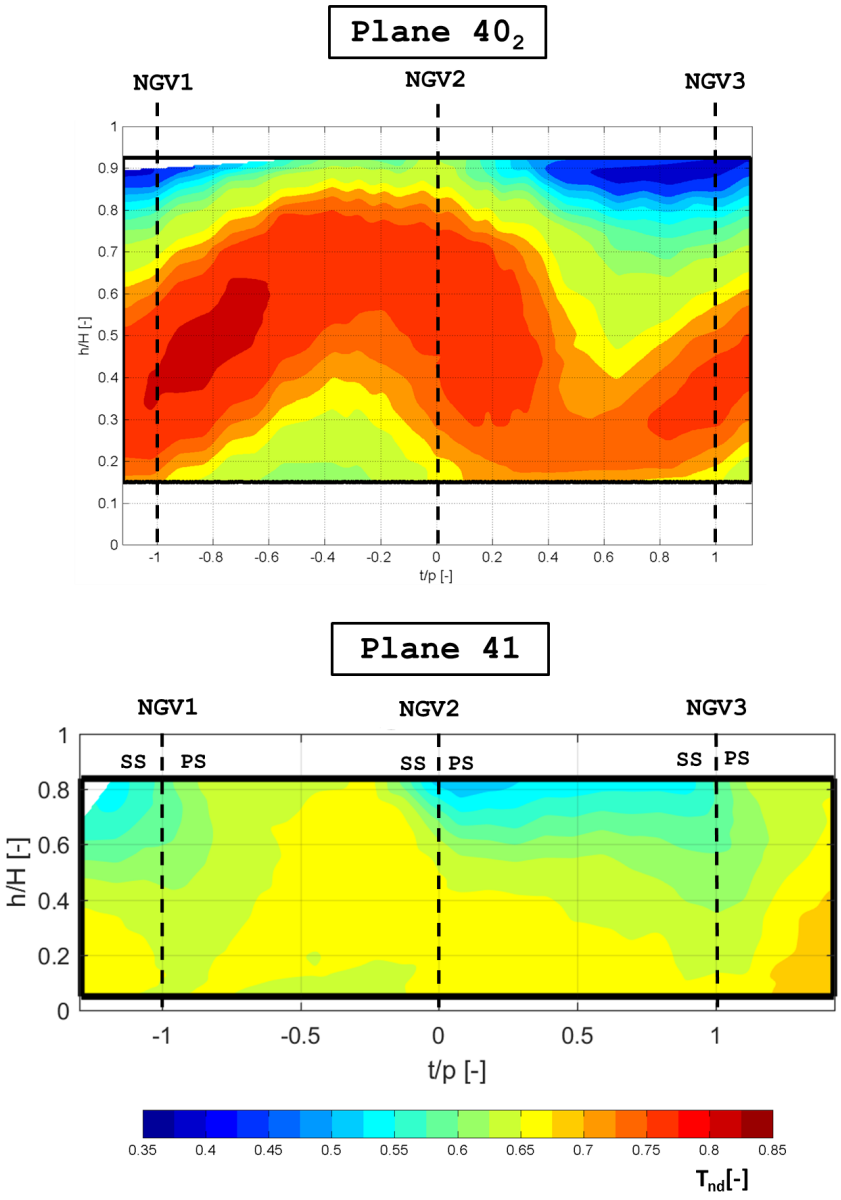

Figure 7.30: Non-dimensional temperature maps on Plane 40 and 41 ($W = 0\%$)

way a description of the temperature gradients approaching the rotor will be provided; moreover, even if no direct measurements on the NGV airfoils were carried out in these conditions, some considerations on how these distortions can affect the NGV heat transfer and its design, will be discussed.

Temperature maps on Plane 40 and 41 are reported in Fig. 7.30; only

the case at $W = 0\%$ is reported for the latter measurement plane. The same temperature scaling as in Section 6.2 is used, in order to evaluated the entity of the hot streak variation across the cascade. Beside the pattern of the thermal field it is possible to note that the maximum non-dimensional temperature is reduced from about 0.8, upstream of the cascade, to less than 0.7, downstream of it. The mass averaged temperature, evaluated by an enthalpy balance between swirler and liner coolant flows, would correspond to a value of 0.65. Therefore, an important reduction in the hot streak intensity occurs, due to the mixing promoted by the high turbulence intensity and the secondary flows. Nevertheless, important distortions can be still appreciated on Plane 41. With the goal of deepening their evaluation, Fig. 7.31 depicts the non-dimensional temperature maps on Plane 41, for all the three investigated mass flow rate conditions. The same temperature scaling is used, in order to check how the coolant mass flow influences the temperature levels in the different parts of the annulus. The colormap scale has been modified to adapt to the measured range. In general very different patterns can be appreciated between left and right passages: in the first one, the temperature level looks quite uniform, while the latter shows wider variations due to a cold spot that can be seen near the outer endwall. This contribution comes from the outer liner cooling flow, that is bled towards the mean radius by the swirling flow. According to thermal field measured on Plane 40, a similar feature could be expected in the left passage, near the inner liner; nevertheless it can't be found in the results, as in this passage no relevant swirling flow is present and the cold layer is not drawn towards the midspan. As a result, the cold layer is maintained close to the endwall and progressively mixes with the swirler hot flow, due to the convergence of the inner wall, that promotes the interaction, and the high turbulence intensity. From a design point of view, it places an important challenge, since corresponding parts of different airfoils can be subjected to different heat transfer rates; particular attention must be paid to the inner endwall design, since it is interested by an important portion of the remaining hot spot. Concerning the hot streak intensity a maximum value around 0.68 was measured, in the inner endwall zone of the right passage; the maximum value, measured in the left one is

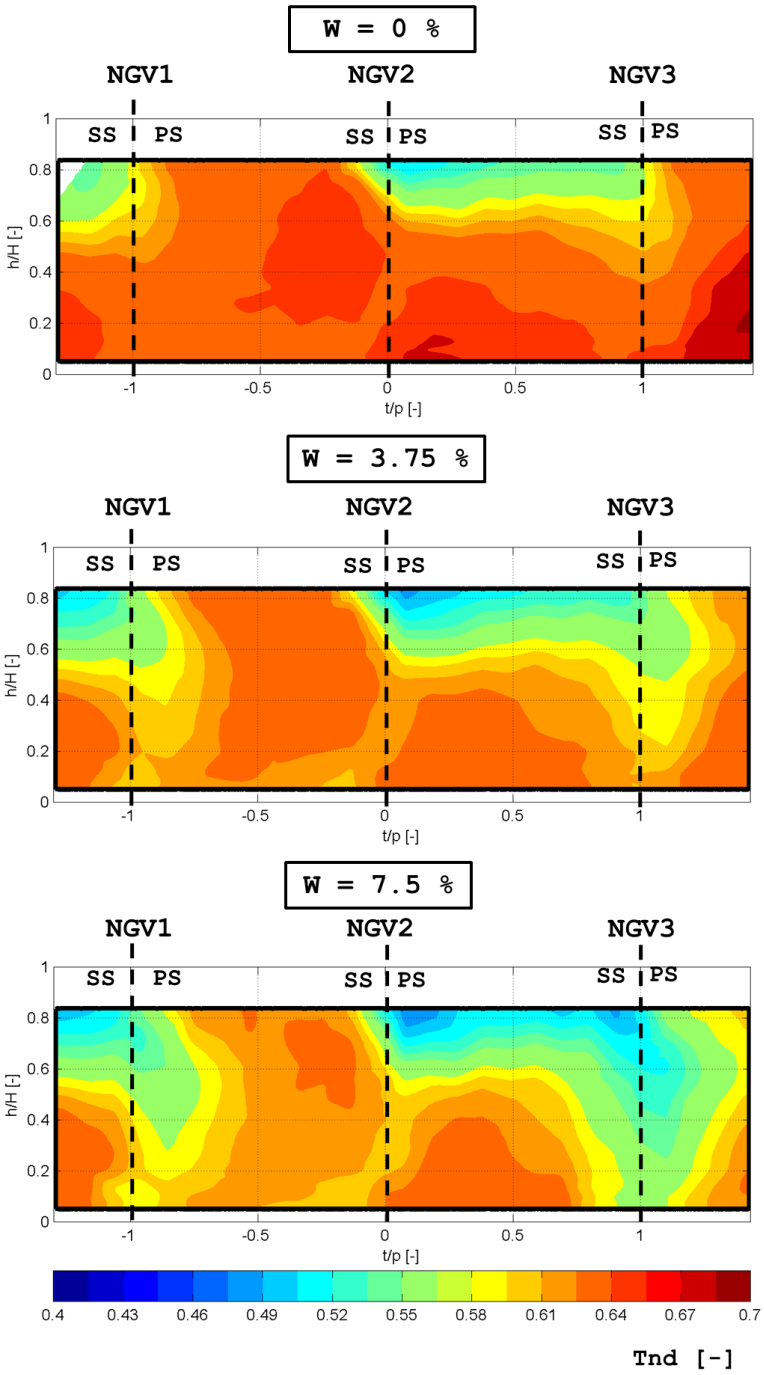

Figure 7.31: Non-dimensional temperature maps on Plane 41

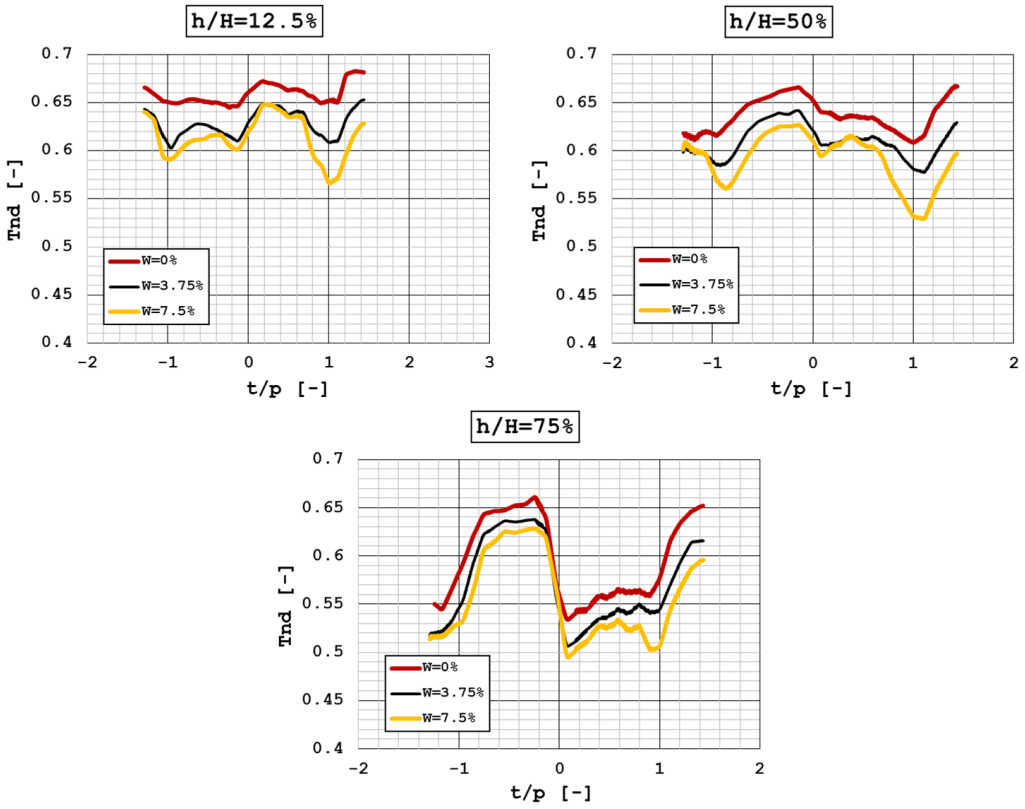

Figure 7.32: Non-dimensional temperature profiles on Plane 41

slightly lower. The fact that a high-temperature zone is detected close to the hub, in the right passage, is in line with what has been detailed in the previous section, regarding the enhanced Mach number measured in this area. In fact, a higher local temperature determines a lower density and, therefore, a higher flow velocity in this position.

The coolant NGV injection determines, as expected, a further reduction in the measured temperatures. Despite this reduction looks quite uniform over the investigated area, a deeper analysis was carried out, through the extraction of one dimensional profiles, at four different radial positions (Fig. 7.32. Even if not constant through the different axial and tangential positions, a clear difference between the three curves can be seen; such a difference is always more marked between $W = 0\%$ and $W = 3.75\%$, with the curves of the two cooled cases, falling on the same temperature levels in different posi-

tions. Moreover the differences between the two passages can be highlighted: the passage that is interested by the residual swirling motion is characterized by a very non-uniform thermal field, with non-dimensional temperatures going from ≈0.68, close to the inner endwall, to ≈0.56, close to the outer one; on the other hand the left passage temperature always stays in the 0.65-0.67 range. While the dimensional values provides information regarding the temperature levels in the different parts of the annulus, useful to gain confidence of where particular effort must be paid in a design phase, an evaluation of the temperature distortion factor (LOTDF) can be useful as well. The definition reported in Eq. 2.4 was adopted:

$$LOTDF = \frac{T - T_{mean}}{T_{mean} - T_{cool}} \tag{7.3}$$

where T_{mean} was averaged over the two central sectors ($-1 < t/p < 1$).
While the LOTDF representation does not allow to estimate the temperature level and compare it to the one at combustor exit, it provides a more detailed evaluation of the thermal pattern and of how it is affected by both hot and cold streaks (i.e. cold spot due to film cooling streaks). In fact, since the mean temperature, used for the LOTDF calculation, changes from test to test (decreases moving from $W = 0\%$ to $W = 7.5\%$), the evaluated parameter has an average value, in the range $-1 < t/p < 1$, equal to zero for every coolant condition and allows to effectively visualize the positions of the cold streaks generated by film-cooling flows. Therefore, a local lower value of LOTDF for the tests with coolant, respect to the reference test with $W = 0\%$, means that the effect of a cold streak is present at that location. On the other hand, where the film cooling flows have already mixed with the hot main flow and no defined cold streaks are detectable, the test with coolant will show a similar value to the test at $W = 0\%$, or even lower due to the reduced T_{mean}.
The contour plots indeed confirm that the calculated temperature distortion factors fall on very similar values through all the investigated domain. This is due to the fact that most of the coolant is ejected close to the leading edge and mixes with the mainstream before reaching Plane 41. Still, from a detailed

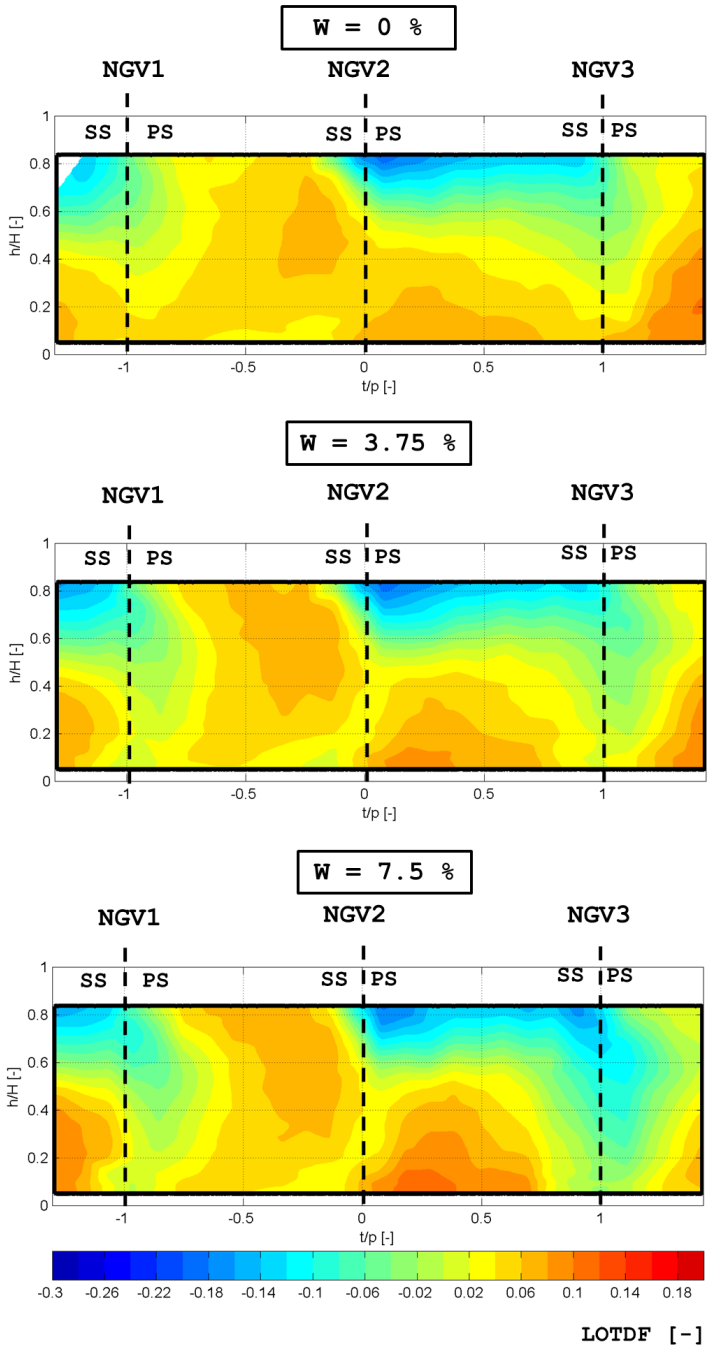

Figure 7.33: Temperature distortion factor maps on Plane 41

analysis of the results, carried out by analyzing the 1D profiles reported in Fig. 7.34, some observations can be made. First of all the profiles (Fig. 7.34)

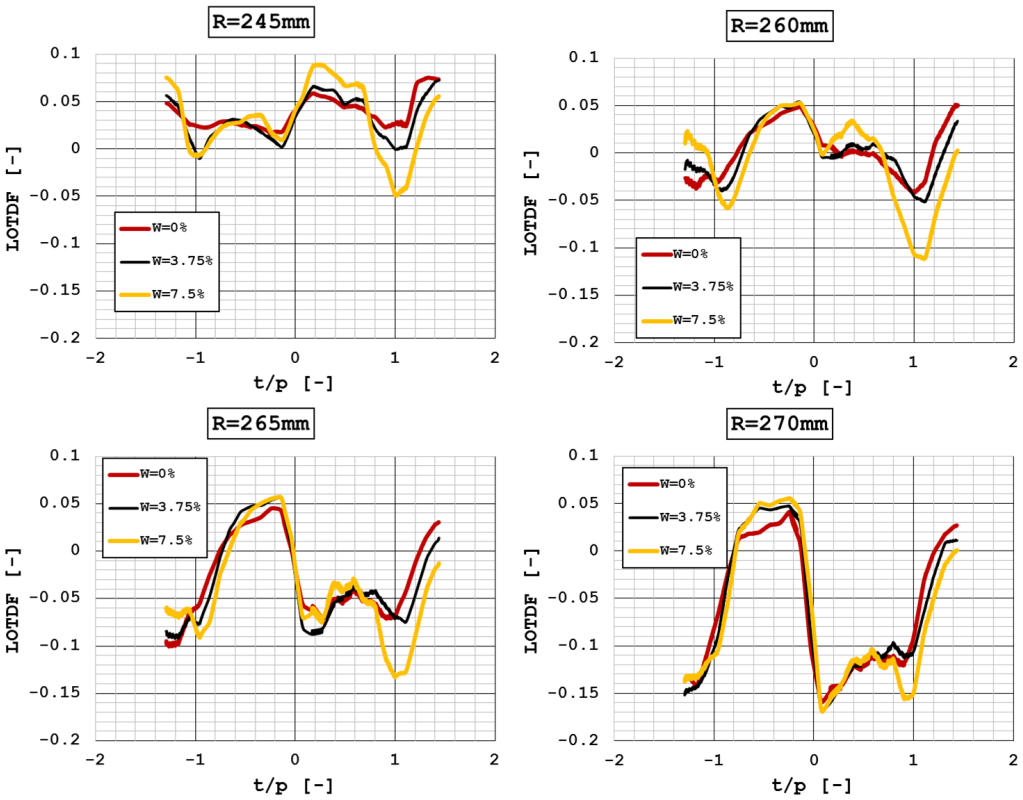

Figure 7.34: Temperature distortion factor profiles on Plane 41

confirm the enhanced temperature distortion measured at the exit of the right passage, as the LOTDF varies from ≈0.08 in the inner part (h/H=12.5%) to ≈-0.11 in the outer (h/H=75%); on the other hand, variations between 0.03 and 0.06 can be found at the exit of the left passage. The most important information, from the 1D profiles analysis, comes from the evaluation the cold streaks positions. The profiles for W = 7.5% generally show a higher value, than the ones for W = 0%, in the center of the right passage; this is especially detectable on the profiles at h/H=12.5% and h/H=50%. As explained before, it means that the effect of no actual cold streak, due to film-cooling flows, can be found in these positions. Similar considerations can be made for the very central part of the left passage, where the plots always present similar values, or slightly higher for W = 7.5%. The positions where the results of the tests with coolant stay significantly below the no-coolant test ones, are

in the proximity of the airfoil wakes; the minimum values are reached in the pressure side end of the wake (i.e. right side looking at the profile plots). This is due to the fact that some coolant is ejected in the final part of the pressure side from rows PS4 and PS5 (Fig. 3.9), while no cooling holes are present in the final part of the suction side. Hence, cold streaks due to film-cooling flows not completely mixed with the hot mainflow can be found in these positions. Noteworthy, while this phenomenon is clear in the wakes of the lateral airfoils, no evidence of cold streaks can be found behind the central one. Such a result should be ascribed to the effect of the residual swirling flow: according to the flow pattern, highlighted by five hole probe measurements, and to the film-cooling behaviour, detailed through the PSP campaign, it can be expected that the swirling mainstream wipes coolant away from the pressure side of NGV_2, and brings it towards the outer endwall and the suction side of NGV_3. Regarding this aspect, one last observation can be made: all the profiles of the test without coolant show similar LOTDF values in correspondence of the two lateral airfoils ($t/p = \pm 1$), due to a fairly good periodicity of the cascade inlet temperature field. On the other hand, for the test at W = 7.5%, lower LOTDFs can be found in the right (NGV_3) wake. This finding seems to confirm that some of the cooling flow, that is wiped away by the swirling flow from the pressure side of the central NGV, is brought towards the right lateral airfoil and locally decreases the flow temperature; no equivalent effect can be found on NGV_1, since the airfoil at its left (i.e. NGV_0) is not cooled.

To quantify the highlighted behaviour, two further analysis were carried out: first of all, it was summarized how the coolant injection affects the hot streak reduction and its overall distortion; moreover it was highlighted how such a distortion is divided within the two passages, in order to highlight the effect of the residual swirl on the global result. For the first goal, Fig. 7.35 reports three series, where different non-dimensional temperature values are reported; in particular the maximum, mean and minimum values measured on Plane 40_2 and 41 are shown. First of all, the figure confirms that an important reduction in the degree of distortion occurs moving from Plane 40_2 to Plane 41: focusing, for Plane 41, on the test without coolant, a very similar mean temperature to the one measured on Plane 40_2 can be found,

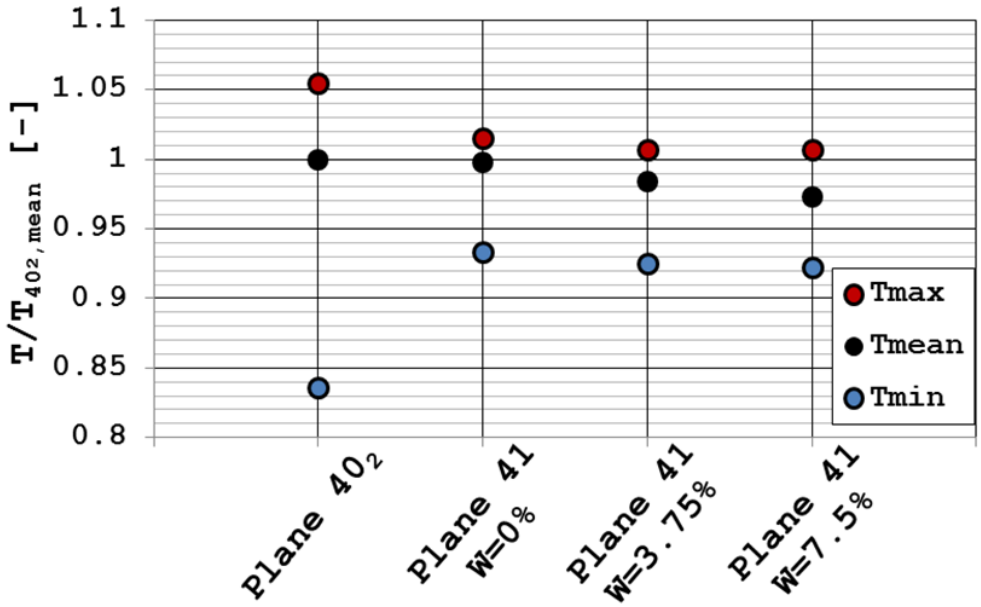

Figure 7.35: Summary of temperature distortions

meaning that negligible heat conduction losses occur through the rig walls; maximum and minimum non-dimensional temperatures goes from 0.8-0.4, upstream the cascade to 0.68-0.5, due to the mixing between the flows at different temperature, promoted by the free-stream turbulence and by the secondary flows within the cascade. Varying the film-cooling flows ejection, it can be seen that the mean temperature value keeps decreasing as the coolant mass flow rate is increased: the entity of this reduction is very close, in dimensional terms, to the one that would be calculated by an adiabatic enthalpy balance between mainstream and cooling flows. On the other hand, focusing on maximum and minimum temperatures, a particular behaviour can be noted: while for the test at W = 3.75%, a reduction in both maximum and minimum temperatures occurs, no further reduction can be found when the focus is moved to W = 7.5%. This means that some zones of the annulus are not affected by a further coolant mass flow rate increase. In more detail, this finding indicates that it is not possible to directly extend the results when sensitively different NGV coolant mass flow rates are considered, as it can occur within the engine working cycle: considering a mean

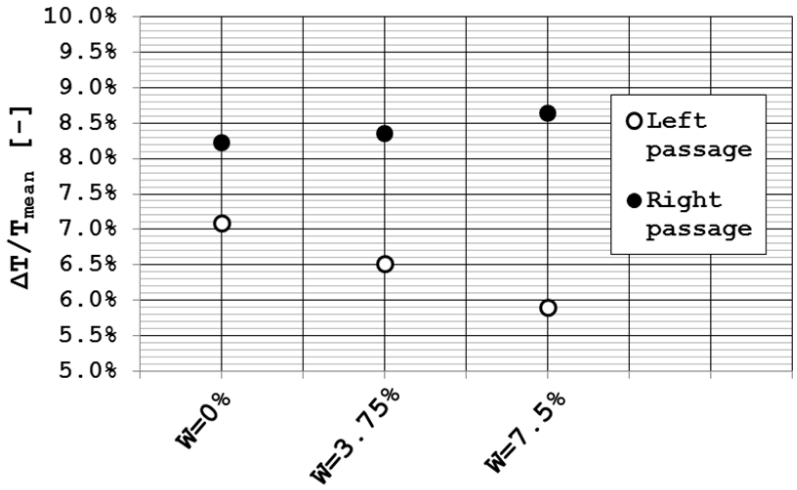

Figure 7.36: Maximum temperature difference within left and right passage

temperature calculated by enthalpy balance and a maximum temperature from the $T_{nd,max}/T_{nd,mean}$ value of the case without NGV coolant, an underestimation of the maximum temperature of about 3% would arise for the case at $W = 7.5\%$. When higher main-coolant temperature ratios are considered, which can be the case for several kind of aero-engines, this value can increase and represent an important issue in the rotor airfoil design procedure, when the focus is placed on evaluating its inlet temperature. For the second goal, Fig. 7.36 shows the maximum temperature difference, measured within the domains of the left and the right passages, as a percentage of the mean temperature on the whole domain. As anticipated, such a difference is higher at the exit of the passage where residual swirl exists; it increases with coolant injection and reaches almost 9% for the case with the maximum coolant mass flow rate. Noteworthy, in the left passage, the measured difference decreases as the coolant mass flow rate is increased, going from 7.1%, for the test at W = 0%, to 5.9% for the test at W = 7.5%.

These two overall findings allow to draw important conclusions about the impact of NGV cooling flow on temperature distortions. The residual swirl plays a big role in enhancing temperature distortions at the right passage exit: it determines a particular flow pattern in that some areas are not affected by the coolant injection, once it overcomes a certain value. A

higher maximum-to-minimum temperature is therefore reached within the domain. An opposite behaviour is achieved in the other passage, where coolant injection tends to uniformly reduce the temperature level and damp the distortions.

7.2.3 Hot streaks migration: concluding remarks

In this part of the work, the focus was placed at evaluating the hot streaks migration through a NGV cascade invested by a combustor outflow characterized by both enhanced temperature distortions, aggressive swirl field and high turbulence intensities. Aero-field results have been exploited to deepen the knowledge of the cascade flow and help in the understanding of the hot streaks evolution. The highlighted behaviour influences the hot streaks migration and its interaction with NGV coolant cold streaks. Significantly different outcomes, from the known behaviour of hot streaks within uniform flow fields, were found: strong temperature distortions have been measured at the exit of the passage where the residual swirl is convected segregating the hot spot close to the inner endwall. The effect of the swirl is such that temperature distortions are enhanced by coolant injection, despite a lower mean temperature is achieved. On the other hand, a fairly uniform temperature pattern was found in the other passage. As a result, very different heat transfer rates should be expected on the different airfoils; this can lead, in a traditional design process based on averaged inlet conditions, either to the adoption of wide safety margins, that are detrimental to the whole engine efficiency, or to dangerous underestimations of the maximum gas temperature. From a design point of view, the measured thermal field evidences the importance of including the rotor in the integrated design approach, as the knowledge of the actual temperature pattern in the definition of rotor cooling system is necessary. The applicability of these results, beside in providing a general description that can be used to evaluate current design guidelines, stays in the creation of a wide experimental database that can be used to tune numerical codes. As a big effort is nowadays put in deepening the knowledge of the behaviour of the combustor-tubine interface, the development of reliable CFD codes for its modelling plays a key role in this process; for the

assessment of the modelling strategies, that are required for these kind of flow features, a comparison against experimental data is necessary.

Conclusions

The present work collects a large part of the activities performed during the Ph.D. course, dealing with the the topic of combustor-turbine interaction for modern aero-engines. Conclusions of the present investigation are now drawn, trying to provide a brief outline of the performed study, summarizing the main achievements, as well as discussing what the impact of these results can be moving forward.

This research is part of a wide European research and development project framework focused on the study of the combustor-turbine interface area; it was aimed at evaluating different aspects of the flow field evolution across a NGV cascade in the presence of a combustor representative outflow. In detail, the focus was placed in trying to analyse the effect of the flow characteristics that are typical of modern lean burn combustors, where highly swirling and unsteady flow fields, together with enhanced temperature distortions, approach the high pressure turbine. Different works have been carried out in recent years, with the goal of deepening the knowledge of these phenomena, mostly separately one from the other, and of their impact on the turbine module performance; a direct comparison with a reference case, with uniform inflow conditions, was generally employed to highlights the effect of a certain flow phenomenon. In the present study the analysis is carried out from a slightly different angle: the adopted test case allows to simulate most of the characteristic flow features together and a thorough experimental campaign was employed to evidence their combined effect on a NGV cascade specifically designed for this kind of inflows.

In the first part of the work, the analysis has been focused on the experimental characterization of a non-reactive, three-sector combustor simulator.

Its design process had been carried out in order to mimic the precise behaviour of a modern lean burn combustor: representative temperature and swirl profiles at combustor exit are pursued through the mixing of a heated swirling mainstream, that passes through three axial swirlers, and liners effusion cooling flows at ambient temperature. Preliminary measurements had been carried out, outside of this Ph.D. course, to verify the aerothermal field at the rig exit. Within this Ph.D. course, PIV measurements have been used to detail the flow field evolution, in order to evidence the flow structure evolution and mixing phenomena that influence the achieved combustor outflow. The analysis revealed the presence of typical flow structures of swirl-stabilized annular combustors: the significant tangential momentum of the mainflow led to vortex breakdown and to the formation of a central recirculation zone. Due to the limited interaction with the cooling flows and the reduced length of the combustion chamber, the swirling structure was found to poorly dissipate its tangential momentum as it moves towards the chamber exit. The test rig was later upgraded with a NGV cascade. Its design was carried out exploiting the preliminary measurements at combustor exit data: tangentially averaged radial profiles were used, as it is common for this kind of operation. A swirler-to-vane ratio of 1:2 was chosen, in that one vane is aligned with the swirler and the adjacent one is clocked halfway between two swirlers, for a total of five vanes and six passages. The evaluation of the differences in the behaviour of the NGV profiles in different clocking positions play a big role in evidencing the limits of traditional design procedures, based on averaged quantities.

After the upgrade, measurements have been initially carried out on the combustor exit plane (Plane 40), in order to provide precise boundary conditions for the cascade investigation. In particular, five hole probe measurements were carried out, to detail the aerothermal field characteristics in terms of flow angles and temperature distortions; hot wire measurements, in isothermal conditions, were conducted as well to assess the turbulence intensity. Results globally showed the presence of the typical flow structures that were pursued. A residual swirling structure, slightly moved towards right with respect to the centerline, with flow angles beyond 50° was recognized,

together with a marked hot spot; local conditions were found to strongly differ from the tangentially averaged ones, in several positions of the annulus, leading to significant inaccuracies in the prediction of the turbine inlet conditions by the traditional design procedure. The flow field was also found to be highly unsteady, with turbulence intensities up to about 30% in the very center of the swirling structure.

The attention was then moved to the evaluation of the cascade exit conditions, by means of the same experimental techniques. The investigation was, in the first part, carried out in isothermal conditions, in order to assess the impact of the highly swirling flow on different aspects of the NGV behaviour. Five hole probe measurements were carried out on the NGV exit plane (Plane 41) to detail the flow field evolution and the effect of the inlet swirl on secondary flow development and pressure losses across the cascade; while other past studies had already focused on this aspect, this step was necessary to gain knowledge of the flow physics and set the basis for the following investigations. It was found that, despite the leading edge clocking (i.e. swirler aligned with the central vane leading edge), the residual swirl was mainly convected in the right passage (pressure side end of the central NGV); its interaction with endwall secondary flows determined the presence of local spots with enhanced pressure losses, especially close to the hub of the lateral NGV. Similar findings had already been found, in past studies, for passage clocking configurations (i.e. swirler aligned with a vane passage); the slight displacement of the flow structure towards right on Plane 40, therefore, played a crucial part in determining the flow field evolution within the cascade. This conclusion shows up for the importance of knowing the exact swirl-vane clocking in the view of the prediction of the turbine aerodynamic performance. Hot wire measurements were then carried out on the same measurement position. Spots with significant turbulence intensities, mainly located in the position of the residual swirling core and close to the hub, where such a structure interacts with endwall flows, were revealed. Values up to about 5% were found in these locations. Even with the high turbulence intensities measured at the cascade inlet, these values are significantly higher than what would be normally expected in this position with the measured

flow acceleration, as the partial preservation of the residual swirl through the cascade clearly contributes in containing the TKE reduction, with respect to a uniform configuration. Film-cooling injection was found to poorly affect the above described aspects, mainly leading to pressure losses enhancement and reduction of both residual swirl degree and turbulence intensity.

Once a proper knowledge of the flow field was gained, the focus moved to the evaluation of more specific aspects, to draw conclusions that could be directly adopted to complement or modify the current design procedures. In particular, the effect of the highlighted flow structures on the film-cooling behaviour was detailed. A PSP (*Pressure Sensitive Paint*) campaign was exploited to evaluate the adiabatic effectiveness on the NGV cascade. Such a measurement technique presents a useful means to measure this parameter, on complex test cases like the present one. Being based on heat-mass transfer analogy, in fact, it is not affected by thermal conduction within the investigated surface, that can, on the other hand, strongly affect the results coming from thermal measurement techniques with the same goal. The experimental campaign showed that the inlet swirl influenced the film-cooling performance in different ways: the effects were highlighted by comparing the results on the two investigated airfoils, subjected to a different inlet flow (i.e. different swirl-vane relative position). First of all, it determined an alteration of the position of the stagnation line, with different entity on the two airfoils; this resulted in a different behaviour of the shower head rows, that, in turn, influenced the film coverage moving downstream. Moreover, the swirling structure pressure field slightly alters the local coolant repartition: in particular, the midspan holes of the central NGV provided a better performance due to the lower pressure in the swirling core. A further effect is due to the streamline alteration, that can provide significant coolant downwash or upwash in the final part of the pressure and suction sides that bound the passage where the residual swirl is convected: in the tested configuration the pressure side of the central airfoil shows a very poor coverage, that would result in metal temperatures significantly higher than the expected. Globally, adiabatic effectiveness results demonstrated that a design procedure based on averaged inlet conditions can lead to significant inaccuracies in the pre-

diction of the film coverage in several positions of different airfoils. A step forward, based on the precise knowledge of 2D inlet conditions and of the flow field evolution, would be required, in order to limit the safety margins that would be otherwise necessary.

In the last part, five hole probe measurements in design conditions (i.e. with heated mainflow) have been described. This part of the work constitutes one of the first experimental attempts to detail the hot streaks migration through a NGV cascade within a highly swirling and highly turbulent flow, as it must be expected at the combustor-turbine interface. The results complement the existing literature data regarding hot streaks migration within uniform inflows. In particular, some interesting insights were provided. In the left passage, where no significant swirling motion is found, the thermal field is quite uniform, due to the mixing promoted by the high turbulence intensity that was measured at the cascade inlet. The residual swirl, on the other hand, is responsible for drawing liner coolant from the outer endwall in the passage where it is convected and for, at the same time, segregating the hot spot towards the hub. As a result important temperature distortions can be find at the right passage exit. Moreover, enhanced temperature distortions are achieved with coolant injection; even if the mean temperature is clearly reduced, the swirl-dominated thermal field is such that some areas of the annulus are not affected by coolant injection: higher maximum-to-mean temperature, therefore, are reached. These distortions, together with the important values of turbulence intensity, described above, must be expected to give a significant contribution in determining the heat transfer rates both within the nozzle guide vanes and on the first stage rotor; the necessity to also include the rotor in an integrated design process, based on a detailed knowledge of the actual aerothermal field, therefore, arises.

As stated, this work constitutes one of the first attempts to detail the hot streaks migration in the presence of an engine representative flow field and draw general conclusions regarding its behaviour and possible design issues. Beside, it provides experimental data in a CFD-friendly domain, characterized by a integer vortex-to-vane ratio, that numerical codes can be compared against. In detail the comparison of different kind of codes to the experi-

mental data is necessary to understand the requirements that these kinds of unsteady flow fields impose to the numerical evaluation. Early CFD comparisons with the present experimental database, carried out outside of this Ph.D. work, showed that, while industrial applications normally relies on Reynolds-Averaged Navier-Stokes (RANS) models for the characterization of the turbine behaviour, they introduce a substantial inaccuracy in the prediction of the thermal loads of the high-pressure turbine. On the other hand, the importance to shift to scale-resolving models was highlighted, together with the necessity of an integrated approach that considers both combustor and turbine together, to take into account the effect of flow unsteadiness on turbulent mixing.

Annex

Appendix 1 - Details of five hole probe data post-processing

In this section some additional details of the five hole probe data post-processing will be provided. As explained in Chapter 5, the classic five hole probe post-processing method, developed by Treaster and Yocum [124], was not found to provide good results in the angular range to be investigated.

It was, then, decided to adopt a different approach, defined by Paul et al. [128], in order to extend the angular validity of the probe response. This method consists of a sectoring scheme, which selects combinations of holes for which the flow is attached, to avoid singularities. Five different *zones* are defined depending on the port where the maximum pressure is recorded. Fig. 37 reports a sketch of the five hole probe head together with the definition of the non-dimensional coefficients, for each zone; the figure also shows where each zone is selecting, depending on pitch and yaw angles.

With these definitions, the results reported in Fig. 5.11. While the outcome is good in terms of angular validity and accuracy, it was necessary to define some procedure that allows to identify and discard the acquisitions that fall out from the calibration range or, better, out from the range where the experimental uncertainty stays within 2°. As the flow angle is not known before the measurement take place, as it was, on the other hand, for the procedure that brought to build Fig. 5.11, it was necessary to rely on the values of the non-dimensional coefficients. In fact, relevant errors arise when the measured angles are such that the coefficients shows limited change for further variation of the flow angles or singular trends.

Fig. 38 reports these trends for Zone 1. Fig. 38a depicts a 2D contour plot

that shows the actual flow angles in terms of calculated coefficients; Fig. 38b, on the other hand, reports the same information in terms of 1D profiles, for some selected flow angles. It is possible to see that a smooth gradient is achieved; the 1D profiles, in fact, do not show any singular trends and the curves for different flow angles always stay distinct one from the other. As a result of this, measurements that fall in Zone 1 always presents a good reliability.

Different outcomes are achieved when the outer zones are concerned, as they are valid when higher flow angles are encountered. Only results for Zone 3 will be reported here, as they are qualitatively similar for all the other ones. Fig. 39 shows the 2D contour plot: it is clear that a steep gradient occurs, both for pitch and for yaw angle. It means that relevant flow angle variations are achieved with very poor, or even absent, variations of the coefficients values. These conclusions are confirmed by 1D profiles reported in Fig. 40 for pitch and yaw angles separately; it is clear that, at certain flow angles, the non-dimensional coefficient collapse on very similar

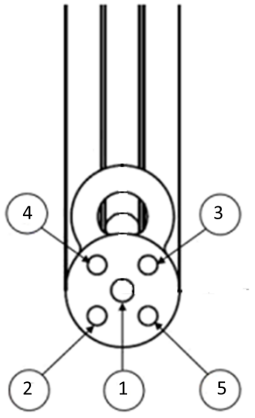

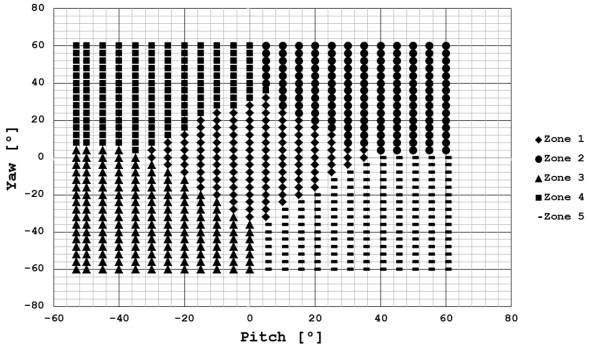

Zone 1:

- $P_m = \frac{P_2+P_3+P_4+P_5}{4}$
- $D = P_1 - P_m$
- $K_p = \frac{P_4-P_5}{D}$
- $K_y = \frac{P_3-P_2}{D}$
- $K_{pt} = \frac{P_1-P_{tot}}{D}$
- $K_{ps} = \frac{P_m-P_{stat}}{D}$

Zone 2:

- $P_m = \frac{P_1+P_4+P_5}{3}$
- $D = P_2 - P_m$
- $K_p = \frac{P_4-P_5}{D}$
- $K_y = \frac{P_1-P_2}{D}$
- $K_{pt} = \frac{P_2-P_{tot}}{D}$
- $K_{ps} = \frac{P_m-P_{stat}}{D}$

Zone 3:

- $P_m = \frac{P_1+P_4+P_5}{3}$
- $D = P_3 - P_m$
- $K_p = \frac{P_4-P_5}{D}$
- $K_y = \frac{P_3-P_1}{D}$
- $K_{pt} = \frac{P_3-P_{tot}}{D}$
- $K_{ps} = \frac{P_m-P_{stat}}{D}$

Zone 4:

- $P_m = \frac{P_1+P_2+P_3}{3}$
- $D = P_4 - P_m$
- $K_p = \frac{P_4-P_1}{D}$
- $K_y = \frac{P_3-P_2}{D}$
- $K_{pt} = \frac{P_4-P_{tot}}{D}$
- $K_{ps} = \frac{P_m-P_{stat}}{D}$

Zone 5:

- $P_m = \frac{P_1+P_2+P_3}{3}$
- $D = P_5 - P_m$
- $K_p = \frac{P_1-P_5}{D}$
- $K_y = \frac{P_3-P_2}{D}$
- $K_{pt} = \frac{P_5-P_{tot}}{D}$
- $K_{ps} = \frac{P_m-P_{stat}}{D}$

Figure 37: Non-dimensional coefficients definition and validity

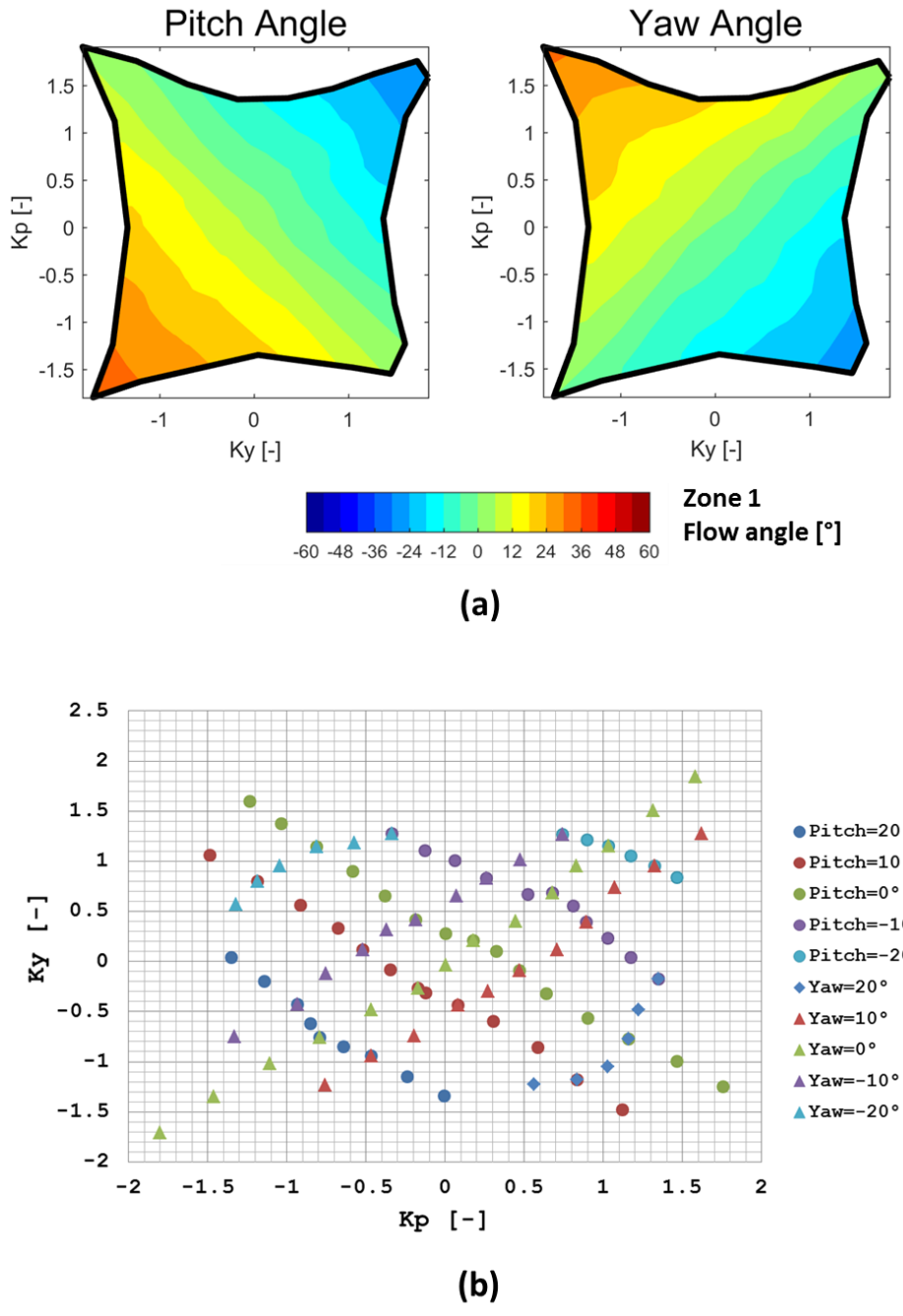

Figure 38: Non-dimensional coefficients trends in Zone 1: 2D contour plot (a) and 1D profiles (b)

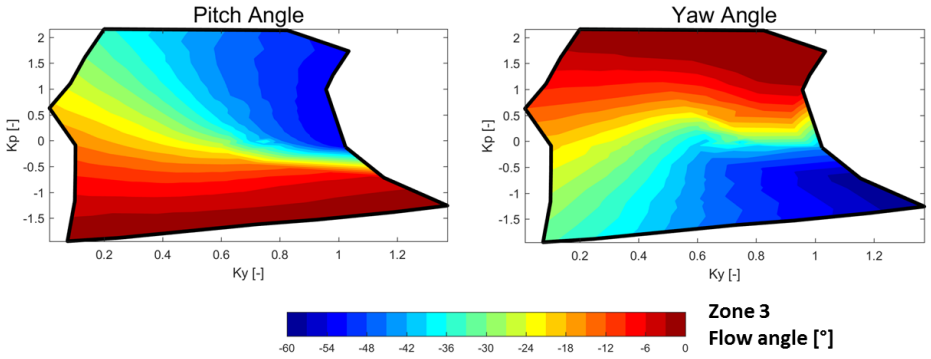

Figure 39: Non-dimensional coefficients trends in Zone 3: 2D contour plot

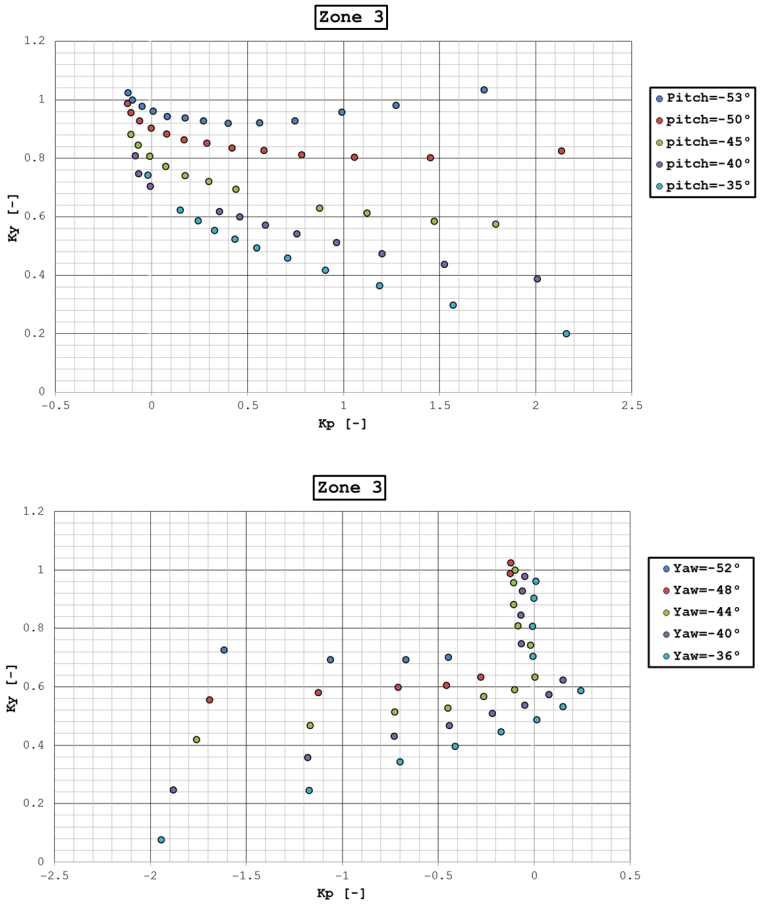

Figure 40: Non-dimensional coefficients trends in Zone 3: 1D profiles

values, even for different flow angles, or present singularities that preclude from obtaining a good interpolation of the flow angles values. Once all these positions, in terms of non-dimensional coefficient values, have been identified, the post-processing tool is able to evaluate if the acquired point falls in one of these areas and, eventually, discard it.

As a short summary, a quick list of the post-processing tool functioning is reported below:

1. Load flow angles and non-dimensional coefficient from calibration for each Zone and for each Mach number set
2. Load pressure acquisitions for each acquired mesh point of the test
3. Identify the Zone to be considered and calculate K_y and K_p from the equations reported in Fig. 37
4. Select a starting Mach number calibration set (according to expected Mach number to be measured)
5. Calculate Pitch and Yaw angles from interpolation of the calculated K_y and K_p on the selected calibration set
6. Calculate K_{pt}, K_{ps} and recovery factor (RF) from interpolation of the calculated Pitch and Yaw angles on the selected calibration set
7. Calculate P_{tot}, P_{stat}, T_{tot}, T_{stat} and Mach number from the calculated K_{pt}, K_{ps}, RF and the acquired temperature
8. Evaluate if the calculated Mach number falls in the same range of the selected calibration set: if it doesn't, go back to point 4 and select the new calibration set; if it does, go on to point 9
9. Evaluate if the non-dimensional coefficients fall in areas of singularity for the selected calibration set: if they do, discard the acquired point; if they do not, accept the calculated results

Appendix 2 - Details of hot wire probes calibration and data post-processing

In this section a detailed description used for HWA probes calibration and data post-processing will be given, in order to complement what was already stated in Section 5.3.2 and report all the adopted relations. The calibration and post-processing procedures will be described one after the other.

Mass-flux calibration

The first part of the calibration procedure is aimed at finding the relation that links the HWA response to mass-flux of the airflow. The $Nu - Re$ approach was used in order to scale the effect of flow compressibility and of the air temperature; to do so it was also necessary to evaluate the temperature of the sensors.

1) Acquisition of different points on the calibration hardware at $pitch = 0°$, $yaw = 0°$. Points have been acquired at different air velocity and total temperature, known through the monitoring instrumentation on the calibration hardware. For each point the average HWA output (E_1, E_2) have been recorded.

2) Calculation of the calibration flow Reynolds number for each acquired

point, through the following relations:

$$\rho = \frac{P_{stat}}{R \cdot T_{stat}} \tag{4a}$$

$$\mu = 4.03 \cdot 10^{-7} \cdot T_0^{0.675} \tag{4b}$$

$$Re = \frac{\rho \cdot V \cdot d_w}{\mu} \tag{4c}$$

3) Calculation of the Nusselt number for each acquired point, through the following relations; the resistance and the geometrical parameters of the sensor wire have been omitted, as they are constant through calibration/tests:

$$Kn = \frac{1.5871 \cdot 10^{-8}}{\rho \cdot d_w} \tag{5a}$$

$$\eta^* = \frac{Kn^{1.193}}{0.493 + M^{1.193}} \tag{5b}$$

$$\eta_{fc} = \frac{0.2167 \cdot M^{2.8}}{0.8521 + M^{2.8}} \tag{5c}$$

$$\eta_c = 1 - \frac{0.5 \cdot M^{3.5}}{1.175 + M^{3.5}} \tag{5d}$$

$$\eta = \eta^* \cdot \eta_{fc} + eta_c \tag{5e}$$

$$k = 0.026 \cdot (\frac{T_0}{300})^{0.7} \tag{5f}$$

$$Nu = \frac{E_1^2 + E_2^2}{k \cdot (T_w - \eta \cdot T_0)} \tag{5g}$$

As explained in Section 5.3.2, T_w was evaluated as the value that made all the points collapse on an exponential curve (i.e. maximum R^2). Results of the mass-flux calibration at $pitch = 0°$ and $yaw = 0°$ are reported in Fig. 41. Wire temperatures of 485 and 495 K were found for probes R56 and R57 respectively.

4) Once the wire temperature was known, the mass-flux calibration was repeated changing the flow angles. This calibration was carried out only with an ambient temperature airflow. It was verified that the influence of the flow angle in the plane perpendicular to the wire (i.e. pitch angle for R56 and

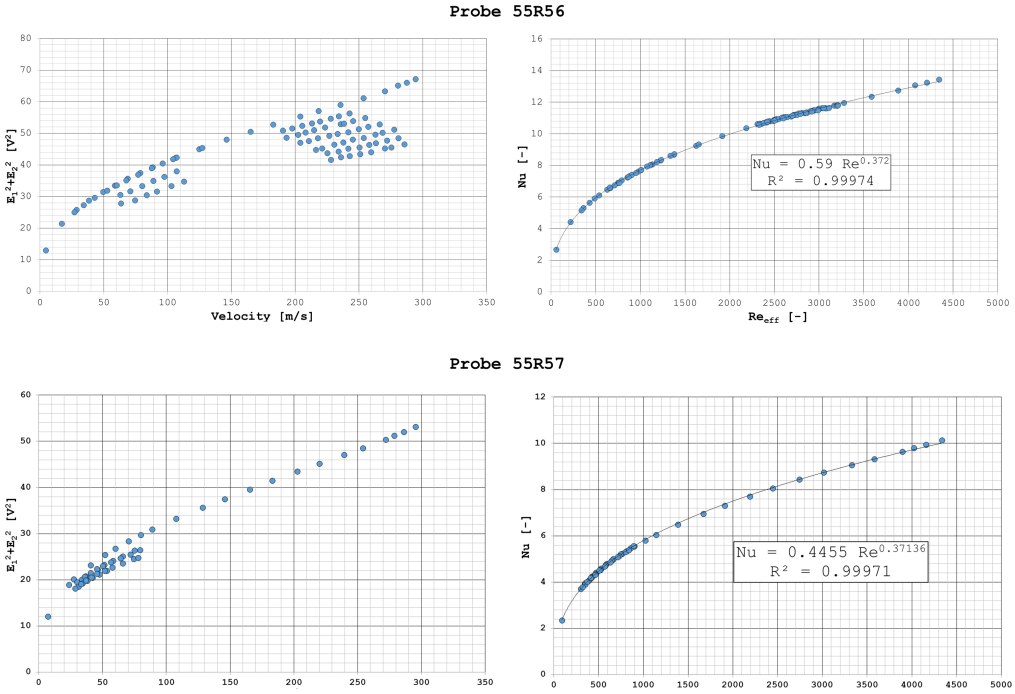

Figure 41: Mass-flux calibration at $pitch = 0°$ and $yaw = 0°$ for probes R56 and R57

yaw angle for R57) was negligible as the sum of the voltages showed very reduced variations. Different mass-flux calibration curves were, therefore, built varying the second flow angle (i.e. yaw angle for R56 and pitch angle for R57). Each curve relates the Nusselt number, calculated through Eq. 5g, to the *effective Reynolds number*, calculated considering only the velocity components that lay in the plane orthogonal to the probe wire. Results are reported in Fig. 42.

Angular calibration

Concerning the angular calibration, it was decided to relate the flow angle, in the plane perpendicular to the wire (i.e. pitch angle for R56 and yaw angle for R57), to either the ratio Re_1/Re_{eff} or Re_2/Re_{eff}. Re_{eff} was evaluated as specified previously (Point 4); Re_1 and Re_2 were calculated using the same exact $Nu - Re$ relation adopted for Re_{eff} (i.e. for that specific second flow angle), using either E_1^2 or E_2^2 in Eq. 5g, for the calculation of the Nusselt number (Nu_1, Nu_2), instead of $E_1^2 + E_2^2$. As expected, the relation between

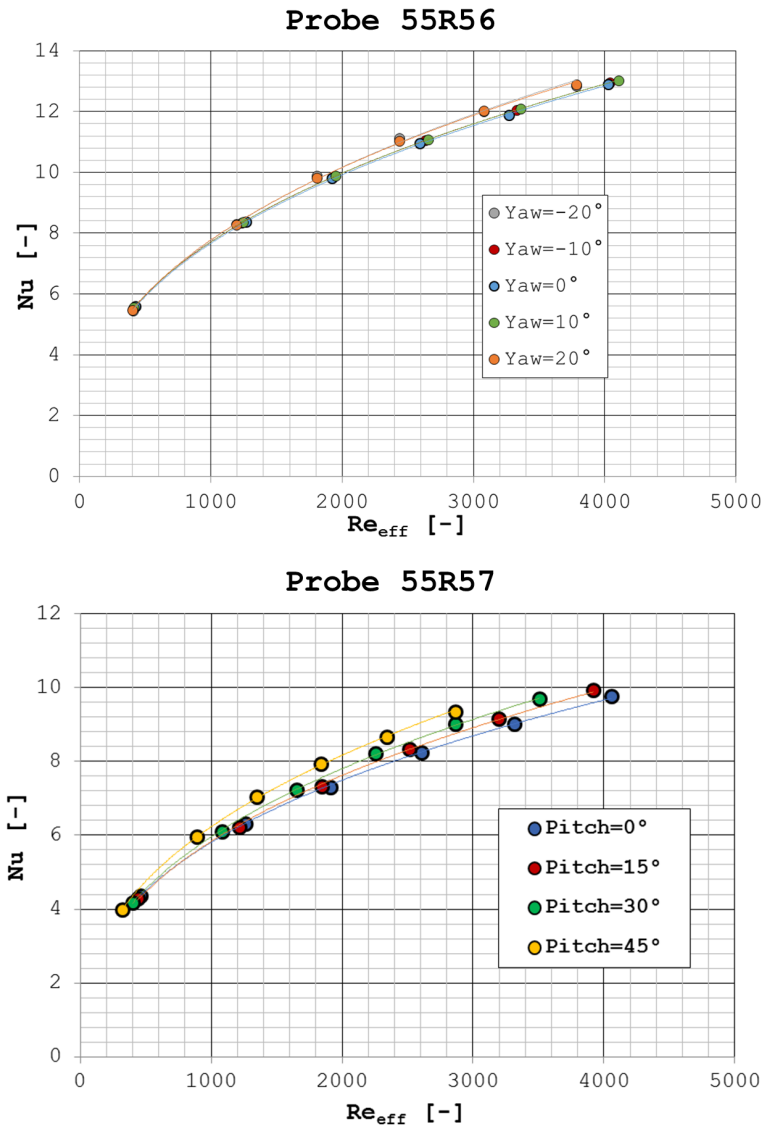

Figure 42: Mass-flux calibration for probes R56 and R57

the flow angle and these parameters was affected by both the second flow angle and the flow Reynolds number; therefore, different angular calibration curves had to be considered for different values of these parameters. Fig. 43 reports examples of these curves, for both probes.

Test execution and Data post-processing

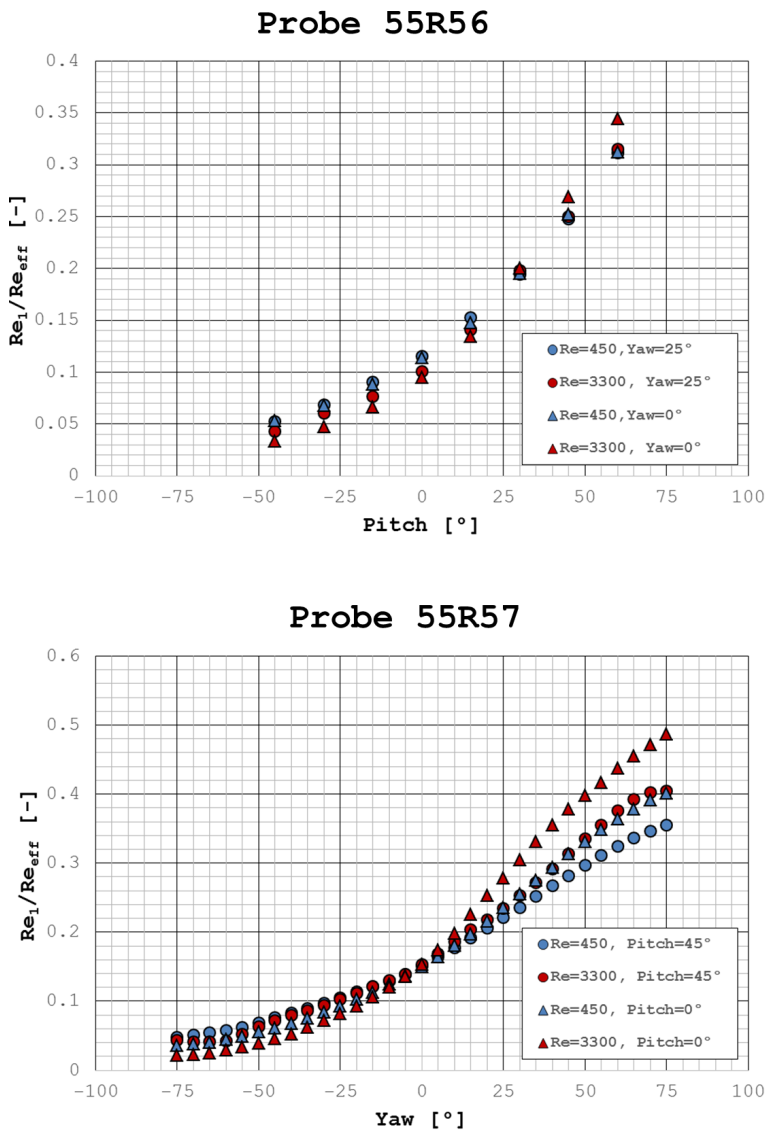

Figure 43: Angular calibration for probes R56 and R57

5) First of all the test with probe R56 was carried out; a preswirl equal to the time-average swirl angle felt by the probe, for each measurement position, was imposed, according to five hole probe results. In this way it was possible to post-process the acquired using only the calibration curves developed for $yaw = 0°$.

The Nusselt number was evaluated, through Equation 5g, starting from E_1

and E_2 (HWA probe output), T_0 (measured by the thermocouple upstream the swirlers), $T - w$ (known from the calibration) and η (calculated from Eqs 5a-e, using five hole probe results for Mach number and static pressure values). $Re_{eff,56}$ was, therefore, calculated through the mass-flux calibration curve for $yaw = 0°$ (Figs. 41 and 42). The angular calibration curves (Fig. 43) were, then, used to evaluate the pitch angle, starting from Re_1 or Re_2, calculated as explained at Point 4. At the end of this first step, $Re_{eff,56}$ and the pitch angle were known and, therefore, $\rho V_{ax,56}$ and ρV_y, through the following equations:

$$Re_{ax,56} = Re_{eff,56} \cdot cos(pitch) \tag{6a}$$

$$Re_y = Re_{eff,56} \cdot sin(pitch) \tag{6b}$$

$$\rho V_{ax,56} = \frac{\mu \cdot Re_{ax,56}}{d_w} \tag{6c}$$

$$\rho V_y = \frac{\mu \cdot Re_y}{d_w} \tag{6d}$$

It must be reminded that directions ax, x and y change from point to point, depending on the probe preswirl. Since these parameters were evaluated for all the 30000 points acquired in the 3 seconds acquisition interval (Section 5.3.2), it was also possible to evaluate their mean and rms values for each measurement position (i.e. mesh point).

6) Afterwards the test with probe R57 was carried out; the same procedure, using the calibration curves for the pitch angles found from R56 results (Figs. 42 and 43), was adopted; the values of $Re_{eff,57}$ and of the swirl angle were, therefore, calculated. Similar relations to Eqs. 6 were used to calculate

the mass-flux in axial and axial and x directions:

$$Re_{ax,57} = Re_{eff,57} \cdot cos(swirl) \tag{7a}$$

$$Re_x = Re_{eff,57} \cdot sin(swirl) \tag{7b}$$

$$\rho V_{ax,57} = \frac{\mu \cdot Re_{ax,57}}{d_w} \tag{7c}$$

$$\rho V_x = \frac{\mu \cdot Re_x}{d_w} \tag{7d}$$

The same considerations taken at Point 5 regarding directions ax, x and y also stand here. It was also verified that the time averaged values of $Re_{ax,57}$ and $Re_{ax,56}$ poorly differed from each other.

7) It was finally possible to use Equation 5.8 to evaluate the turbulence intensity.

After the overall procedure has been described, it is useful to provide some verifications that have been carried out. First of all, in the base procedure,

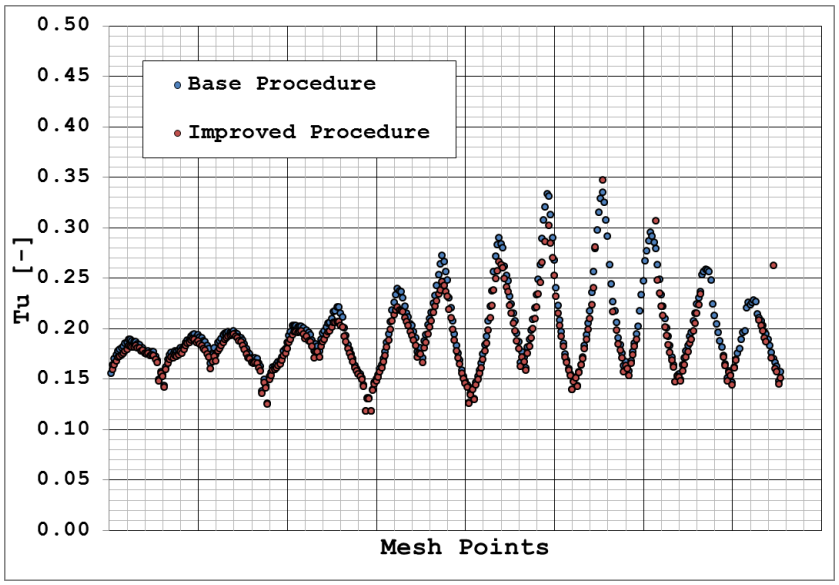

Figure 44: Measured turbulence intensity on Plane 40: comparison between base and improved procedure

only the time averaged flow angle value, is passed from R56 test results to R57 test post-processing, to select the correct calibration curve. An improved procedure was also tried, where the instantaneous value of the pitch angle, different for each of the 30000 acquisitions, was passed to R57 test post-processing. The procedure had to be made iterative, in order to re-select the R56 calibration curves, since significant deviations could occur between the time-averaged pre-swirl value and the instantaneous swirl evaluation. Fig. 44 shows the results of the two procedures in terms of measured turbulence intensity on Plane 40. Very limited differences can be found, showing up for the reliability of the base procedure. It must be also considered that, since two different acquisitions were carried out for R56 and R57, the two outputs are not synchronized together. Therefore, it is not straightforward to pass instantaneous information from one set to the other. For a limited number

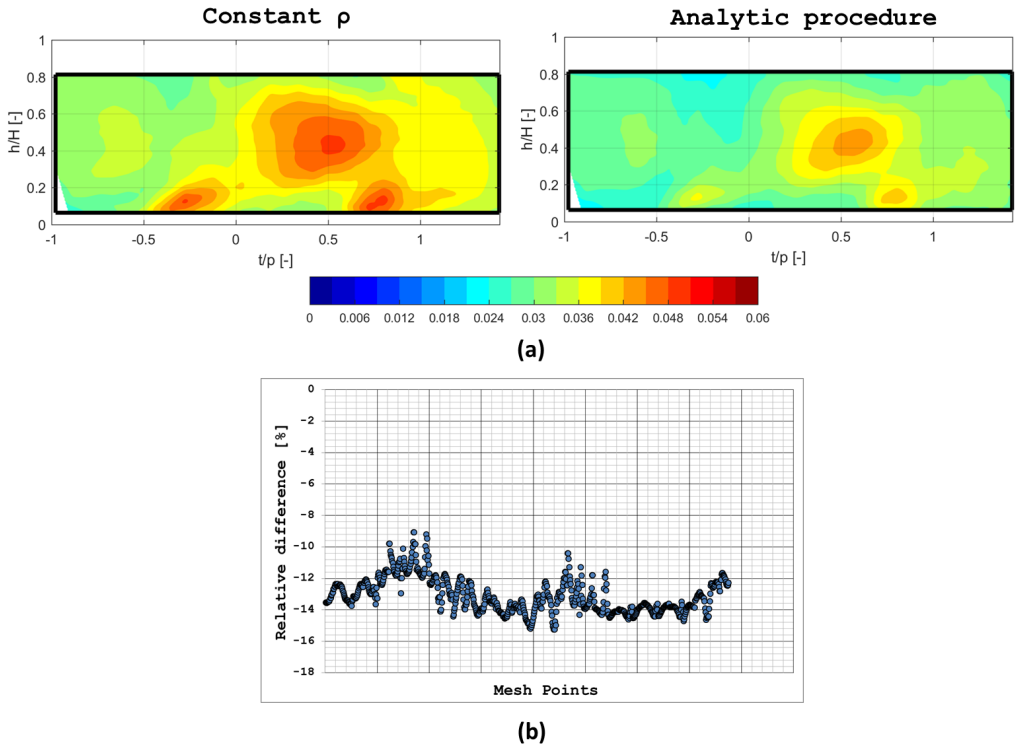

Figure 45: Measured turbulence intensity on Plane 41: comparison between adopted and analytic [150] approaches

of mesh points, different kind of synchronizations between the output signals (i.e. different time lags) were tested. The differences between the results were always negligible.
A further verification was aimed at evaluating the impact of using Equation 5.8, that corresponds to the classical definition only in the case of constant density. The topic has been discussed in Section 5.3.2. A comparison between the adopted procedure (constant density) and an analytic procedure [150], used to to discern between density and velocity effects, is provided here. It must be also added that the latter approach is developed for transonic and supersonic flows, that is not the case of the present treatment. Fig. 45 reports the comparison for Plane 41 results ($W = 0\%$), in terms of turbulence intensity maps (Fig. 45a) and relative difference $(Tu_{analytic} - Tu)/Tu$ (Fig. 45b).

It can be noted that the analytic approach provide a lower value of turbulence intensity. Nevertheless the turbulence field morphology is the same and the quantitative differences are mostly limited to 15%. The maximum measured Tu goes from 5% for the adopted approach, to 4.3% for the analytic one.

Bibliography

[1] D. Ballal and J. Zelina. Progress in aeroengine technology (1939-2003). *Journal of Aircraft*, 41:43–50, 2004.

[2] International Air Transport Association. Press release n° 57. Technical report, October 2014.

[3] Advisory Council for Aeronautics Research in Europe. Strategic research agenda. Technical report, ACARE, 2000.

[4] X. Zhao and T. Gronstedt. Aero engine intercooling optimization using a variable flow path. *ISABE*, 2015.

[5] W. Camilleri, E. Anselmi, V. Sethu, P. Laskaridis, T. Gronstedt, X. Zhao, A. Rolt, and P. Cobas. Concept description and assessment of the main features of a geared intercooled reversed flow core engine. *J Aerospace Engineering*, 2014. doi: 10.1177/0954410014557369.

[6] G. Wilfert, J. Sieber, A. Rolt, N. Baker, A. Touyeras, and S. Colantuoni. New environmental friendly aero engine core concepts. *Proceedings of the 18th ISABE conference*, ISABE-2007(1120), 2007.

[7] S. Kaiser, A. Seitz, S. Donnerhack, and A. Lundbladh. A composite cycle engine concept with hecto-pressure ratio. *51st AIAA/SAE/ASEE Joint Propulsion Conference - Propulsion and Energy Forum*, 2015.

[8] Technology innovation and exploitation : innovative technologies for future gas-turbine core-engines / lemcotec, low emmissions core-engine technologies. Technical report, 2017.

[9] S.M. Correa. A review of nox formation under gas-turbine combustion conditions. *Combustion Science and Technology,*, 7(1-6):329–362, 1993. doi: 10.1080/00102209208947221.

[10] Y. Zeldovich, D. Frank-Kamenetskii, and P. Sadvnikov. Oxidation of nitrogen in combustion. *Publ. House of the Acad of Sciences of USSR*, 1947.

[11] A. H. Lefebvre and D.R. Ballal. *Gas Turbine Combustion.* Taylor & Francis, 2010.

[12] Rolls-Royce. *The Jet Engine.* Rolls-Royce plc, 5th edition, 1996.

[13] A.M. Mellor. *Design of Modern Gas Turbine Combustors.* Academic Press, 1990.

[14] S.M. Correa. Carbon monoxide emissions in lean premixed combustion. *Journal of Propulsion and Power*, 8(6):1144–1151, 1992.

[15] R. Banck, C. Berat, Cazales M, and S. Hardling. Organisation of european aeronautic ultra-low nox combustion research. *25TH INTERNATIONAL CONGRESS OF THE AERONAUTICAL SCIENCES*, 2006.

[16] M. Kern, S. Marinov, P. Habisreuther, N. Zarzalis, A. Peschiulli, and F. Turrini. Characteristics of an ultra-lean swirl combustor flow by les and comparison to measurements. *ASME Conference Proceedings*, GT2011(45300), 2011.

[17] S. Marinov, M. Kern, K. Merkle, N. Zarzalis, A. Peschiull, and F. Turrini. On swirl stabilized flame characteristics near the weak extinction limit. *ASME Conference Proceedings*, GT2010(22335), 2010.

[18] C. L. Ford, J. F. Carrotte, and A. D. Walker. The impact of compressor exit conditions on fuel injector flows. *Journal of Engineering for Gas Turbines and Power*, 134:111504–111504, 2012. doi: 10.2514/3.11455.

[19] D.G. Lilley. Swirl flows in combustion: a review. *AIAA J.*, 5(8), 1977.

[20] J.M. Beer and N.A.Chigier. *Combustion aerodynamics*. Applied Science Publishers, London, 1974.

[21] O. Lucca-Negro and T. O'Doherty. Vortex breakdown: a review. *Progress in Energy and Combustion Science*, 27(4)(ISSN 0360-1285): 431–481, 2001.

[22] B. F. Hall, K. S. Chana, and T. Povey. Design of a non reacting combustor simulator with swirl and temperature distortion with experimental validation. *Proc. ASME Turbo Expo*, (GT2013-95499), 2013.

[23] Y.Huang and V.Yang. Dynamics and stability of lean-premixed swirl-stabilized combustion. *Progress in Energy and Combustion Science*, 5(4):293–364, 2009.

[24] A Andreini, B. Facchini, R. Becchi, A. Picchi., and F.Turrini. Effect of slot injection and effusion array on the liner heat transfer coefficient of a scaled lean-burn combustor with representative swirling flow. *J. Eng. Gas Turbines Power*, 138(4):041501-041501-10, 2015. doi: 10.1115/1.4031434.

[25] A Andreini, B. Facchini, L. Mazzei, R. Becchi, A. Picchi., and F.Turrini. Adiabatic effectiveness and flow field measurements in a realistic effusion cooled lean burn combustor. *J. Eng. Gas Turbines Power*, 38(3):031506-031506-11, 2015. doi: 10.1115/1.4031309.

[26] A. Andreini, R. Becchi, B. Facchini, L. Mazzei, A. Picchi, and A. Peschiulli. Effusion cooling system optimization for modern lean burn combustor. *ASME Conference Proceedings*, GT2016-57721, 2016. doi: 10.1115/GT2016-57721.

[27] M. Berrino, F. Satta, M. Ubaldi, P. Zunino ans S. Colantuoni, and P. Di Martino. Experimental characterization of the flow-field downstream of an innovative ultra low nox injection system. *ASME Conference Proceedings*, (GT2014-25459), 2014.

[28] M. Berrino, D. Legnani, F. Satta, M. Ubaldi, P. ZunP. Zunino. Colantuoni, and P. Di Martino. Investigation of the dynamics of an ultra low nox injection system by pod data post-processing. *ASME Conference Proceedings*, (GT2015-42638), 2015.

[29] S. Wang, V. Yang, G. Hsiao, S. Hsieh, and C. Mogiah. Large eddy simulations of gas-turbine swirl injector flow dynamics. *J. Fluid Mech*, 583:99, 2007.

[30] S Roux, G. Lartigue, and T.Poinsot. Studies of mean and unsteady flow in a swirled combustor using experiments, acoustic analysis, and large eddy simulations. *Combustion and Flame*, 141(1-2):40–54, 2005.

[31] L.Selle, G. Lartigue, and T.Poinsot. Compressible large eddy simulation of turbulent combustion in complex geometry on unstructured meshes. *Combustion and Flame*, 137(4):489–505, 2004.

[32] C.M. Cha, S. Hong, P.T. Ireland, P. Denman, and V. Savarianandam. Experimental and numerical investigation of combustor-turbine interaction using an isothermal, nonreacting tracer. *J. Eng. Gas Turb. Power*, 134, 2012.

[33] M.J. Wankhede, N.W. Bressloff, A.J. Keane, L. Caracciolo, and M. Zedda. An analysis of unstable flow dynamics and flashback mechanism inside a swirl-stabilised lean burn combustor. *ASME Conference Proceedings*, GT2010-22253, 2010.

[34] T. Povey and I. Qureshi. Developments in hot-streak simulators for turbine testing. *ASME J. Turbomach.*, 131(3):031009–031009, 2009. ISSN 0889-504X.

[35] T. Povey and I. Qureshi. A hot-streak (combustor) simulator suited to aerodynamic performance measurements. *Proceedings of the Institution of Mechanical Engineers, Part G: Journal of Aerospace Engineering*, 2008.

[36] I. Qureshi and T. Povey. A combustor-representative swirl simulator for a transonic turbine research facility. *Proceedings of the Institution of Mechanical Engineers: Journal of Aerospace Engineering*, 2011.

[37] P. Ligrani. Aerodynamic losses in turbines with and without film cooling, as influenced by mainstream turbulence, surface roughness, airfoil shape, and mach number. *International Journal of Rotating Machinery*, (957421), 2012. doi: http://dx.doi.org/10.1155/2012/957421.

[38] D.G. Ainley and G.C.R. Mathieson. An examination of the flow and pressure losses in bladeade rows of axial-flow turbines. Technical report, Aeronautical Research Council Reports and Memoranda, 1955.

[39] L.S. Langston, M.L. Nice, and R.M. Hooper. Three-dimensional flow wiwith a turbine cascade passage. *Engineering for Power*, 99, 1977.

[40] J.H. Horlock. Losses and efficiencies in axial-flow turbines. *Int. J. Mech. 8ci. Pergamon Press*, 2:48–75, 1959.

[41] O. Zweifel. *The Spacing of Turbo-Machine Blading Especially with Large Angular Deflection.* Brown Boveri Review, 1945.

[42] B. Lakshminarayana and J.H. Horlock. Review: secondary flows and losses in cascade and axial flow turbomachines. *Int. J. Mech. 8ci. Pergamon Press*, 5:287–307, 1962.

[43] L.S. Langston. Secondary flows in turbines-a review. *Ann. N.Y. Acad. Sci.*, 934:11–26, 2001.

[44] I. Qureshi, A. Smith, and T. Povey. Hp vane aerodynamics and heat transfer in the presence of aggressive inlet swirl. *ASME J. Turbomach.*, 135(2):021040–021040, 2012. ISSN 0889-504X.

[45] L. S. Langston. Crossflows in a turbine cascade passage. *ASME Journal of Engineering for Power*, 102:866–874, 1980.

[46] C.R.B. Day, M.L.G. Oldfield, and G.D. Lock. Aerodynamic performance of an annular cascade of film cooled nozzle guide vanes under

engine representative conditions. *Experiments in Fluids*, 29:117–129, 2000.

[47] L. Giller and H.P. Schiffer. Interactions between the combustor swirl and the high pressure stator of a turbine. *Proc. ASME Turbo Expo*, (GT2012-69157), 2012.

[48] H. Prumper. Application of boundary layer fences in turbomachinery. *AGARD-AG-164*, pages 311–331, 1972.

[49] H. Matsuda, F. Otomo, H. Kawagishi, A. Inomata, Y. Niizeki, and Takashi Sasaki. Influence of surface roughness on turbine nozzle profile loss and secondary flows. *ASME Conference Proceedings*, (GT2006-90828), 2006. doi: 10.1115/GT2006-90828.

[50] G.D. MacIsaac, S.A. Sjolander, and T. J. Praisner. Measurements of losses and reynolds stresses in the secondary flow downstream of a low-speed linear turbine cascade. *ASME Journal of Turbomachinery*, 134 (061015-1), 2012.

[51] G. Barigozzi, G. Franchini, A. Perdichizzi, and M. Quattrore. Endwall film cooling effects on secondary flows in a contoured endwall nozzle vane. *Journal of Turbomachinery*, 132(041005-1), 2010. doi: 10.1115/1.3192147.

[52] P. Schupbach, R.S. Abhari, M.G. Rose, T. Germain, I. Raab, and J. Gier. Improving efficiency of a high work turbine using nonaxisymmetric endwalls-part ii: Time-resolved flow physics. *Journal of Turbomachinery*, 132(021008-1), 2010. doi: 10.1115/1.3103926.

[53] J. Han, S. Dutta, and S. Ekkad. *Gas Turbine Heat Transfer and Cooling Technology*, pages 129–249. Taylor & Francis, 2000.

[54] M. R. L'Ecuyer and F. O. Soechting. A model for correlating flat plate film cooling effectiveness for rows of round holes. In *AGARD Heat Transfer and Cooling in Gas Turbines 12p (SEE N86-29823 21-07).*

1985. Provided by the Smithsonian/NASA Astrophysics Data System .

[55] W.J. Mick and R.E. Mayle. Stagnation film cooling and heat transfer, including its effect within the hole pattern. *Journal of Turbomachinery*, 110(1):66–72, 1988. doi: 10.1115/1.3262169.

[56] A. B. Mehendale and J.C. Han. Influence of high mainstream turbulence on leading edge film cooling heat transfer. *Journal of Turbomachinery*, 114(4):707–715, 1992. doi: 10.1115/1.2928023.

[57] A. Martin and S. J. Thorpe. Experiments on combustor effusion cooling under conditions of very high free-stream turbulence. *ASME Conference Proceedings*, (GT2012(68863)), 2012.

[58] S.V. Ekkad, J.C. Han, and H. Du. Detailed film cooling measurements on a cylindrical leading edge model: Effect of free-stream turbulence and coolant density. *Journal of Turbomachinery*, 120:799–807, 1998.

[59] D.P. Narzary, K.C. Liu, A.P. Rallabandi, and J.C. Han. Influence of coolant density on turbine blade film-cooling using pressure sensitive paint technique. *Journal of Turbomachinery*, 134(3), 2010. doi: 10.1115/1.4003025.

[60] S.Ito, R.J.Goldstein, and E.R.G. Eckert. Film cooling of a gas turbine blade. *ASME Journal of Engineering for Power*, 100:476–481, 1978.

[61] S.G. Schwarz and R.J. Goldstein. The two-dimensional behavior of film cooling jets on concave surfaces. *ASME Journal of Turbomachinery*, 111:124.130, 1989.

[62] D.R. Pedersen, E.R.G. Eckert, and R.J.Goldstein. Film-cooling with large density differences between the mainstream and secondary fluid measured by the heat-mass transfer analogy. *ASME journal of Heat Transfer*, 99:620–627, 1977.

[63] D.L. Schmidt and D.G. Bogard. Pressure gradient effects on film cooling. *International Gas Turbine and Aeroengine Congress and Exposition*, (95-GT-18), 1995.

[64] G. Barigozzi, S. Ravelli, A. Armellini, C. Mucignat, and L. Casarsa. Effects of injection conditions and mach number on unsteadiness arising within coolant jets over a pressure side vane surface. *International Journal of Heat and Mass Transfer*, 67:1220–1230, 2013.

[65] J.R. Schwab, R.G. Stabe, and W.J. Whitney. Analytical and experimental study of flow through an axial turbine stage with nonuniform inlet radial temperature profiles. *NASA Technical Memorandum Report*, AIAA Paper No. 83-1175, 1983.

[66] R.G. Stabe, W.J. Whitney, and T.P. Moffit. Performance of a high-work low aspect ratio turbine tested with a realistic inlet radial temperature profile. *NASA Technical Memorandum Report*, AIAA Paper No. 84-1161, 1984.

[67] T.L. Butler, O.P. Sharma, H.D. Joslyn, and R.P. Dring. Redistribution of inlet temperature distortion in an axial flow turbine stage. *J. Propul. Power*, 5(1):64–71, 1989.

[68] H.D. H.D. Joslyn.P. Dring. A trace gas technique to study mixing in a turbine stage. *ASME J. Turbomach.*, 110(1):38–43, 1988.

[69] C. Hadelman. An experimental study of radial temperature profile effects on turbine tip shroud heat transfer. *MS thesis, Aeronautical and Astronautical Engineering, MIT, Cambridge MA*, 1989.

[70] M. D. Barringer, K. A. Thole, and M. D. Polanka. Experimental evaluation of an inlet profile generator for high pressure turbine tests. *Proceedings of ASME TURBOEXPO 2006: Power for Land, Sea, and Air*, (GT-2006-90401), 2006.

[71] M. D. Barringer, K. A. Thole, M. D. Polanka, J. P. Clark, and P. J. Koch. Migration of combustor exit profiles through high pressure turbine vanes. *ASME J. Turbomach.*, (021010-1), 2009.

[72] M. D. Barringer, K. A. Thole, and M. D. Polanka. Effects of combustor exit profiles on vane aerodynamic loading and heat transfer in a high pressure turbine. *ASME J. Turbomach.*, 131(2):021008–021008, 2009. ISSN 0889-504X.

[73] S. C. Jenkins and D. G. Bogard. Superposition predictions of the reduction of hot streaks by coolant from a film-cooled guide vane. *ASME J. Turbomach.*, 131(4):041002–041002, 2009. ISSN 0889-504X.

[74] S. Jenkins, K. Varadarajan, and D. G. Bogard. The effects of high mainstream turbulence and turbine vane film cooling on the dispersion of a simulated hot streak. *ASME J. Turbomach.*, 126(1):203–211, 2004.

[75] G. Barigozzi, S. Mosconi, A. Perdichizzi, and S. Ravelli. The effect of hot streaks on a high pressure turbine vane cascade with showerhead film cooling. *International Journal of Turbomachinery Porpulsion and Power*, (44), 2017.

[76] R. M. Mathison, C. W. Haldeman, and M. G. Dunn. Aerodynamics and heat transfer for a cooled one and one-half stage high-pressure turbine - part iii: Impact of hot-streak characteristics on blade row heat flux. *ASME J. Turbomach.*, 134(1):011008–011008, 2011. ISSN 0889-504X.

[77] A. Krichbaum, H. Werschnik, M. Wilhelm, H.PH.P. Schiffer, and K. Lehmann. A large scale turbine test rig for the investigation of high pressure turbine aerodynamics and heat transfer with variable inflow conditions. *ASME Conference Proceedings*, (GT2015-43261), 2015.

[78] G. Schmid, A. Krichbaum, H. Werschnik, and H.P. Schiffer. The impact of realistic inlet swirl in a 1-1/2 stage axial turbine. *ASME Conference Proceedings*, (GT2014-26716), 2014.

[79] H. Werschnik, M. Schneider, J. Herrmann, D. Ivanov, H.P. Schiffer, and C. Lyko. The influence of combustor swirl on pressure losses and the propagation of coolant flows at the large scale turbine rig (lstr): Experimental and numerical investigation. *International Journal of Turbomachinery Porpulsion and Power*, (139), 2017.

[80] H. Werschnik, J. Hilgert, M. Wilhelm, M. Bruschewski, and H.P. Schiffer. Influence of combustor swirl on endwall heat transfer and film cooling effectiveness at the large scale turbine rig. *Journal of Turbomachinery*, 139(8), 2017. doi: 10.1115/1.4035832.

[81] S. Jacobi, C. Mazzoni, B. Rosic, and K. Chana. Investigation of unsteady flow phenomena in first vane caused by combustor flow with swirl. *Journal of Turbomachinery*, 139, 2017.

[82] M.D. Turrell, P.J. Stopford, K.J. Syed, and E. Buchanan. Cfd simulation of the flow within and downstream of a high-swirl lean premixed gas turbine combustor. *ASME Conference Proceedings*, (GT2004-53112), 2004.

[83] K.S. Chana, J.R. Hurrion, and T.V. Jones. The design, development and testing of a non-uniform inlet temperature distortion generator for the qinetiq transient turbine research facility. *ASME Conference Proceedings*, (GT2003-38469), 2003.

[84] I. Qureshi, A. Beretta, and T. Povey. Effect of simulated combustor temperature nonuniformity on hp vane and end wall heat transfer: An experimental and computational investigation. *ASME J Eng Gas Turb Power*, 133(3):031901–031901, 2010. ISSN 0742-4795.

[85] B.F. Hall and T. Povey. Experimental study of a non-reactiing low nox combustor simulator for scaled turbine experiments. *ASME Conference Proceedings*, (GT2015-43530), 2015.

[86] B. Killoros, R. Lubbock, P. Beard, F. Goenaga, A. Rawlinson, E. Janke, and T. Povey. Ecat: An engine component aerothermal facility at the university of oxford. *ASME Conference Proceedings*, (GT2017-64736), 2017. doi: 10.1115/GT2017-64736.

[87] B. Khanal, L. He, J. Northall, and P. Adami. Analysis of radial migration of hot-streak in swirling flow through high-pressure turbine stage. *Journal of Turbomachinery*, 135, 2013.

[88] A.C. Nix, A.C. Smith, T.E. Diller, W.F. Ng, and K.A. Thole. High intensity, large length-scale freestream turbulence generation in a transonic turbine cascade. *ASME Conference Proceedings*, (GT-2002-30523), 2002.

[89] S. Nasir, J. S. Carullo, W.-F. Ng, K. A. Thole, H. Wu, L. J. Zhang, and H. K. Moon. Effects of large scale high freestream turbulence and exit reynolds number on turbine vane heat transfer in a transonic cascade. *ASME J. Turbomach.*, 131:021021–021021, 2009.

[90] R. W. Radomsky and K. A. Thole. Flowfield measurements for a highly turbulent flow in a stator vane passage. *ASME J. Turbomach.*, 122(2): 255–262, 1999.

[91] G.J. Van Fossen and R.S. Bunker. Augmentation of stagnation heat transfer due to turbulence from a dln can combustor. *Journal of Turbomachinery*, 123:140–146, 2001.

[92] F.E. Ames. Experimental study of vane heat transfer and aerodynamics at elevated levels of turbulence. *NASA Contractor's Report 4633*, 1994.

[93] F.E. Ames. The influence of large-scale high-intensity turbulence on vane heat transfer. *Journal of Turbomachinery*, 9(1):23–30, 1997.

[94] C.M. Cha, P.T. Ireland, P.A. Denman, and V. Savarianandam. Turbulence levels are high at the combustor-turbine interface. *ASME Conference Proceedings*, (GT2012-69130), 2012.

[95] R.J. Lubbock and M.L.G. Oldfield. Turbulent velocity and pressure fluctuations in gas turbine combustor exit flows. *Proc IMechE Part A: J Power and Energy*, 0(0):1–13, 2017.

[96] C. Battisti, F. Kost, N. Atkins, W. Playford, M. Orain, G. Caciolli, L. Tarchi, M. Mersinligil, and J. Raffel. Full aerothermal combustor turbine interaction research. *Proceedings of the EASN workshop on Flight Physics and Propulsion*, 2012.

[97] G. Caciolli. A close investigation on the aerothermal behaviour of modern aeroengine combustors. *PhD thesis, University of Florence*, 2014.

[98] A. Andreini, G. Caciolli, B. Facchini, A. Picchi, and F. Turrini. Experimental investigation of the flow field and the heat transfer on a scaled cooled combustor liner with realistic swirling flow generated by a lean-burn injection system. *ASME J. Turbomach.*, 137(3):031012–031012, 2014.

[99] B. Wurm, A. Schulz, H.J. Bauer, and M. Gerendas. Impact of swirl flow on the cooling performance of an effusion cooled combustor liner. *ASME J Eng Gas Turb Power*, 134(12):121503–121503, 2012. ISSN 0742-4795.

[100] U. Meier, J. Heinze, M. Schroll, C. Hassa, S. Bake, and T. Doerr. Optically accessible multisector combustor: Application and challenges of laser techniques at realistic operating conditions. *ASME Conference Proceedings*, (GT2015-43391), 2015. doi: 10.1115/GT2015-43391.

[101] C. Koupper, G.a Caciolli, L. Gicquel, F. Duchaine, G. Bonneau, L. Tarchi, and B. Facchini. Development of an engine representative combustor simulator dedicated to hot streak generation. *ASME J. Turbomach.*, 136(11):111007–111007, 2014. ISSN 0889-504X.

[102] T. Bacci, G. Caciolli, B. Facchini, L. Tarchi, C. Koupper, and J.L. Champion. Flowfield and temperature profiles of a combustor simulator dedicated to hot streaks generation. *Proc. ASME Turbo Expo*, (GT2015-42217), 2015.

[103] ASME. Measurement uncertainty. *Instrument and Apparatus, Vol. ANSI/ASME PTC 19.1-1985 of Performance Test Code*, 1985.

[104] S. J. Kline and F. A. McClintock. Describing uncertainties in single sample experiments. *Mechanical Engineering*, 1953.

[105] K.S. Hermanson and K.A. Thole. Effect of mach number on secondary flows characteristics. *International Journal of Turbo and Jet Engines*, 17:179–196, 2000.

[106] F. Zhong and C. Zhou. Effects of tip gap size on the aerodynamic performance of a cavity-winglet tip in a turbine cascade. *Journal of Turbomachinery*, 2017. doi: 10.1115/1.4036677.

[107] D.M. Vogt and T.H. Fransson. A new turbine cascade for aeromechanical testing. *The 16th Symposium on Measuring Techniques in Transonic and Supersonic Flow in Cascades and Turbomachines*, 2002.

[108] S. P. Lynch, N. Sundaram, K.A. Thole, A. Kohli, and C. Lehane. Heat transfer for a turbine blade with nonaxisymmetric endwall contouring. *Journal of Turbomachinery*, 2011. doi: 10.1115/1.4000542.

[109] T. Povey, T.V. Jones, and M.L.G. Oldfield. On a novel annular sector cascade technique. *Journal of Turbomachinery*, 129(175), 2007.

[110] L.A. El-Gabry, R. Saha, J. Fridh, and T. Fransson. Measurements of hub flow interaction on film cooled nozzle guide vane in transonic annular cascade. *Journal of Turbomachinery*, 137, 2015.

[111] A.B. Shaukat. Parametric study of operating conditions in an annular turbine sector cascade. *KTH Industrial Engineering and Management, Master of Science Thesis*, 2013.

[112] A. Andreini, T. Bacci, M. Insinna, L. Mazzei, and S. Salvadori. Hibrid rans-les modeling of the aero-thermal field in an annular hot streak generator for the study of combustor-turbine interaction. *Proc. ASME Turbo Expo*, (GT2016-56583), 2016.

[113] M. Raffel, C. E. Willert, and J. Kompenhans. *Particle Image Velocimetry - A pratical guide*. Springer, 1997.

[114] C. Tropea, A. Yarin, and J.F. Foss. *Springer Handbook of Experimental Fluid Mechanics*. 2007.

[115] A. Spencer, D. Hollis, and J. Carrotte. Piv measurements of combustor turbulence fields. *Proc. ASME Turbo Expo*, (GT2007-28050), 2007.

[116] A. Spencer, D. Hollis, and S. Gashi. Investigation of the unsteady aerodynamics of an annular combustor using piv and les. *Proc. ASME Turbo Expo*, (GT2008-50277), 2008.

[117] H.P. Schiffer M. Kegalj and. Endoscopic piv measurements in a low pressure turbine rig. *14th Int Symp on Applications of Laser Techniques to Fluid Mechanics*, 2008.

[118] U. Dierksheide, P. Meyer, T. Hovestadt, and W. Hentschel. Endoscopic 2d particle image velocimetry (piv) flow field measurements in ic engines. *Experiments in fluids*, 33:794–800, 2002.

[119] S.M. Soloff and R.J. Adrian anc Z.C. Liu. Distortion compensation for generalized stereoscopic particle image velocimetry. *Meas. Sci. Technol.*, 8:1441–1454, 1997.

[120] N. J. Lawson M. Reeves. Evaluation and correction of perspective errors in endoscopic piv. *Experiments in Fluids*, 36:701–705, 2004.

[121] W. Xiong and W. Merzkirch. Piv experiments using endoscope for studying pipe flow. *Journal of Flow Visualization and Image Processing*, 6:167–175, 1999.

[122] J. Westerweel. Fundamentals of digital particle image velocimetry. *Meas. Sci. Technol.*, 8:1379–1392, 1997.

[123] J. Westerweel. and F. Scarano. Universal outlier detection for piv data. *Experiments in fluids*, 39:1096–1100, 2005.

[124] A. L. Treaster and A. M. Yocum. *The Calibration and Application of Five-Hole Probes*. The Pennsylvania State University Institute for Science and Engineering, 1978.

[125] E. O. Doebelin. *Measurement systems: application and design*. McGraw-Hill, 1990.

[126] A.J. Pisasale and N.A. Ahmed. A novel method for extending the calibration range of five-hole probe for highly three-dimensional flows. *Flow Measurement and Instrumentation*, 13(23-30), 2002.

[127] C. Ostowari and W.H. Wentz Jr. Modified calibration technique of a five-hole probe for high flow angles. *Experiments in Fluids*, 1983.

[128] A.R. Paul, R.R. Upadhyay, and A. Jain. A novel calibration algorithm for five-hole pressure probe. *International Journal of Engineering, Science and Technology*, (2), 2011.

[129] J. D. Crawford. *Design and Calibration of Seven Hole Probes for Flow Measurement*. Queen's University, Department of Mechanical and Materials Engineering, 2011.

[130] H.T. Hoenen, R. Kunte, P. Waniczek, and P. Jeschke. Measuring failures and correction methods for pneumatic multi-hole probes. *ASME Conference Proceedings*, (GT2012-68113), 2012.

[131] P.M. Ligrani. Spatial resolution and downwash velocity corrections for multiple-hole pressure probes in complex flows. *Experiments in fluids*, 7, 1989.

[132] F. Laurantzon, N. Tillmark, and P.H. Alfredsson. What does the hot-wire measure? *KTH Mechanics, Technical Report*.

[133] A.E. Perry. *Hot-wire anemometry*. 1982.

[134] M. Hultmark and A. Smits. Temperature corrections for constant temperature and constant current hot-wire anemometers. *Meas. Sci. Technol.*, 21(105404), 2010.

[135] L.V. King. On the convection of heat from small cylinders in a stream of fluid: determination of the convection constants of small platinum wires, with applications to hot-wire anemometry. *The Royal Society's physical sciences research journal*, 1914.

[136] L. Meyer. Calibration of a three-wire probe for measurements in non-isothermal flow. *Experimental Thermal and Fluid Science*, 5:260–267, 1992.

[137] T.J. Gieseke and Y.G. Guezennec. An experimental approach to the calibration and use of triple hot-wire probes. *Experiments in Fluids*, 14:305–315, 1993.

[138] N. P. Cheremisinoff. *Flow Measurement for Engineers and Scientists*. 1987.

[139] M. Samet and S. Einav. A hot-wire technique for simuitaneous measurement of instantaneous velocities in 3d flows. *Journal of Physics E: Scientific Instruments*, 20, 1986.

[140] G. Kergourlay, S. Kouidri, G.W. Rankin, and R. Rey. Experimental investigation of the 3d unsteady flow field downstream of axial fans. *Flow Measurement and Instrumentation*, 17:303–314, 2006.

[141] E.L. Huu and C. Beguier. Velocity measurements in 3d turbulent flows by means of a rotating x-wire probe. *Meas. Sci. Technol.*, 6:843–850, 1995.

[142] S. Russ and T.W. Simon. On the rotating, slanted, hot-wire technique. *Experiments in Fluids*, 12:76–80, 1991.

[143] F.L. Pena and T. Arts. The rotating slanted hot wire anemometer in practical use. *Proceedings of the 2nd International Conference on Experimental Fluid Mechanics*, 1994.

[144] G. Buresti and N.R. Di Cocco. Hot-wire measurement procedures and their appraisal through a simulation technique. *Journal of Physics E: Scientific Instruments*, 20, 1987.

[145] Dantec Dynamics. Split-fiber probes for 2-dimensional flow field measurements - information sheet.

[146] L. Helle. The use of a split-fiber probe for aerodynamic research. *Dantec Information*, 12, 1993.

[147] J. Lepicovsky. Measurements with a split-fiber probe in complex unsteady flows. *NASA Contractor's Report 2004-213065*, 2004.

[148] T. Ishihara, K. Hibi, and S. Oikawa. A wind tunnel study of turbulent flow over a three-dimensional step hill. *Journal of Wind Engineering and Industrial Aerodynamics*, 83:95–107, 1999.

[149] B. Cukurel, S. Acarer, and T. Arts. A novel perspective to high-speed cross-hot-wire calibration methodology. *Experiments in Fluids*, 53:1073–1085, 2012.

[150] F. Motallebi. A review of hot-wire technique in compressible flows. *TU-Delft, Faculty of Aerospace Engineering, Laboratory of High Speed Aerodynamics, Report LR-724*, 1993.

[151] R. Meyer, K. Knobloch, and S. Hakansson. Hot-wire measurements in a direct driven high speed turbo fan (ddtf) rig. *11th European Conference on Turbomachinery Fluid dynamics and Thermodynamics*, (ETC2015-234), 2015.

[152] K.R. Navarra. Development of the pressure-sensitive-paint technique for turbomachinery applications. *Virginia Polytechnic Institute and State University*, 1997.

[153] T.V. Jones. Theory for the use of foreign gas in simulating film cooling. *International Journal of Heat and Fluid Flow*, 20:349–354, 1999.

[154] R.J. Goldstein and H.H. Cho. A review of mass transfer measurements using naphthalene sublimation. *Experimental Thermal and Fluid Science,*, 10(4):416–434, 1995. doi: 10.1016/0894-1777(94)00071-F.

[155] R.L. Simpson and R.L. Field. A note on the turbulent schmidt and lewis numbers in a boundary layer. *International Journal of Heat and Mass Transfer*, 15:177–180, 1972.

[156] D. Charbonnier, P. Ott, M. Jonsson, F. Cottier, and T. Kobke. Experimental and numerical study of the thermal performance of a film cooled turbine platform. *ASME Conference Proceedings*, (GT2009(60306)), 2009.

[157] G. Caciolli, B. Facchini, A. Picchi, and L. Tarchi. Comparison between psp and tlc steady state techniques for adiabatic effectiveness measurement on a multiperforated plate. *Experimental Thermal and Fluid Science*, 48(0)(ISSN 0894-1777):122–133, 2013.

[158] A. Picchi. Experimental investigatio of effusion cooling systems for lean burn aero-engine combustors. *University of Florence, PhD Thesis*, 2014.

[159] M. Jonsson. Application of photoluminescent measurement techniques for quantitative assessment of turbine film cooling. phd thesis. *Ecole Polytechnique Federale De Lausanne*, 2010.

[160] J.C. Han and A.P. Rallabandi. Turbine blade film cooling using psp technique. *Frontiers in Heat and Mass Transfer (FHMT)*, 2010. doi: 10.5098/hmt.v1.1.3001.

[161] S.B. Pope. *Turbulent Flows*. Cambridge University Press, 2000.

[162] A. Andreini, T. Bacci, M. Insinna, L. Mazzei, and S. Salvadori. Modelling strategies for the prediction of hot streak generation in lean burn aeroengine combustors (under review). *Aerospace Science and Technology*, 2017.

[163] C. Koupper, G Bonneau, T. Bacci, B. Facchini, L. Tarchi, L. Gicquel, and F. Duchaine. Experimental and numerical calculation of turbulent timescales at the exit of an engine representative combustor simulator. *J. Eng. Gas Turbines Power*, 138, 2015.

[164] A.P. Weiss and L. Fottner. The influence of load distribution on secondary flow in straight turbine cascade. *International Gas Turbine and Aeroengine Congress and Exposition*, (93-GT-86), 1993.

[165] V. Dossena, A. Perdichizzi, M. Ubaldi, and P. Zunino. Turbulence measurements downstream of a turbine cascade at different incidence angles and pitch-chord ratios. *ASME Conference Proceedings*, 1993.

[166] R.J. Boyle, B.J. Lucci, and R.G. Senyitko. Aerodynamic performance and turbulence measurements in a turbine vane cascade. *ASME Conference Proceedings*, (GT2002-30434), 2002. doi: 10.1115/GT2002-30434.

[167] J. Steelant and E. Dick. Prediction of by-pass transition by means of a turbulence weighting factor - part i: Theory and validation. *ASME Conference Proceedings*, (99-GT29), 1999.

[168] D. Contini, G. Manfrida, V. Michelassi, and G. Riccio. Measurements of vortex shedding and wake decay downstream of a turbine inlet guide vane. *Flow, Turbulence and Combustion*, 64:253–278, 2000.